THE UNIVERSITY *of* EDINBURGH

Title	3D phase contrast MRI- velocity-field visualisation and wall shear rate calculation in major arteries
Author	Kohler, Uwe
Qualification	PhD
Year	2000

Digitisation Notes:

Page 205 is missing from original

3D Phase Contrast MRI — Velocity-Field Visualisation and Wall Shear Rate Calculation in Major Arteries

Uwe Köhler

PhD
University of Edinburgh
2000

Harald Köhler

*** 12.07.1941 — † 24.02.2000**

Danke für alles!

Abstract

Approximately half of all deaths in the developed world arise from cardiovascular disease, primarily caused by the deposition of atheroma within major arteries. It has been observed that atheroma is deposited preferentially in regions along the outer wall of bifurcations, and along the distal part of the inner wall of bends. These are regions associated with disturbances of the blood flow that display abnormal shear rate (spatial velocity gradient at the vessel wall).

Thus, in order to facilitate clinical diagnoses, it is important to visualise the structure and haemodynamic properties of arteries and veins. Magnetic resonance imaging (MRI) is well suited for volume imaging and can be made sensitive to flow. Quantitative velocity measurements are possible using phase contrast (PC) MRI.

The aim of this project was the provision of a method that provides information on wall shear rate vectors using MRI. To handle the large number of images acquired in PC MRI, automated flow detection algorithms were developed. Three different algorithms were identified: one operating on magnitude MR images only and two methods which additionally use the velocity information generated from *in vivo* and *in vitro* acquisitions. These algorithms are based on an edge detection method and were tested on phantoms.

The post-processing steps necessary to calculate wall shear stress involved the fitting of smooth functions to the velocity data, the detection of vessel walls and the calculation of the wall shear rate vector based on that information. Fitting a smooth function

removed residual noise and allowed the calculation of spatial derivatives. The velocity data was satisfactorily described by a segmented fifth order polynomial function. One method of vessel wall reconstruction was based on the fitted velocity field, while another one utilised the detected flow regions. Using the surface position and normals, the wall shear rate was calculated from the shear stress tensor. All post-processing steps were integrated in a purpose built program that enabled graphical user interactions.

The calculated wall shear rate values were quantitatively verified with experiments on various phantoms and simulations, and qualitatively compared with computational fluid dynamics calculations. It is shown that a method to calculate reliably wall shear rate directly from time averaged PC MRI acquisitions has been established.

Contents

List of Figures

List of Tables

1. Introduction

Approximately half of all deaths in the developed world arise from cardiovascular disease, primarily caused by the deposition of atheroma within major arteries. This process, atherosclerosis, is characterised by changes in the innermost layer of an artery, the intima. The disease process starts in early life [SKC97, Hee93], but the onset of symptoms might be delayed until 50-70 years of age. A number of risk factors have been established such as high blood pressure, smoking, high cholesterol levels in the blood, obesity and lack of sufficient exercise [Hee93]. Though there have been many studies of atherosclerosis, the fundamental mechanisms are not well understood. However, certain criteria of the disease process have been established. The first of these is that atherosclerosis is a local process. The disease occurs predominantly along the outer wall of bifurcations, and along the distal part of the inner wall of bends [KGZG85, YCGN88, GZGK88, Hee93]. Also, the process is strongly affected by lipids (especially cholesterol). Transportation and metabolisation of the lipids in the blood stream seem to play an important role. Another effect influencing atherosclerosis is the physical and chemical events that cause aggregation of blood platelets [Hee93]. The level of nitric oxide (NO) has been implicated as one influence on the aggregation [DDGQ98]. Inflammation of the intima has also been indicated in the atherosclerosis [Ale95].

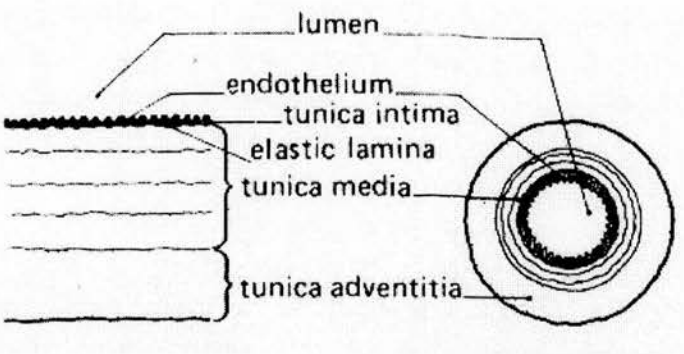

Figure 1.1.: *Transverse section through an artery. (Taken from [Mar96])*

The morphology of atherosclerotic lesions is complicated and changes over time [Hee93]. Children as young as ten start showing "fatty streaks" which consist of smooth muscle cells invading the intima (Figure 1.1) surrounded by intra- and extracellular lipids. These progress to "fibrous plaque" not earlier than the age of 15 - 20. These clearly bulge into the vessel lumen; however, the innermost cell layer, the endothelium, is still intact. From the early stages of intimal thickening there can be progression of disease over many years with the formation of plaque and narrowing of the artery in "complicated lesions". Possible consequences include reduction of flow rate, thrombus formation and break-up, plaque rupture, and complete vessel occlusion. The importance of these events depends on which vascular system is considered. In this project we are primarily concerned with stroke, and therefore it is the carotid arteries which are of interest [SE71, Str92].

A number of metabolic hypotheses characterising the disease process can be distinguished [Hee93]. The innermost layer of cells in an artery, the endothelium (Figure 1.1), might respond to injury possibly assisted by the formation of a thrombus. Another hypotheses assumes that low - density lipoprotein (LDL) receptors decrease under the influence of a high cholesterol intake and the LDL metabolism is reduced. Also, mutation or ageing of the smooth muscle cell in the arterial wall might lead to a migration of smooth muscle cells into the intima. Under certain circumstances the bioelectric repulsion between the arterial wall and the constituents of blood might break down. The chemical substance homocystine can cause damage to the endothelium and trigger the atherosclerotic process.

It has been observed that atheroma is deposited preferentially in regions along the outer wall of bifurcations, and along the distal part of the inner wall of bends [KGZG85, YCGN88, GZGK88]. These are regions associated with disturbances of the blood flow that display abnormal shear rate (blood velocity gradient at the vessel wall). In a recent review [GZG93], it was noted that wall shear stress is normally in the range 1-2 N/m^2. The endothelium is in direct contact with the blood. It consists of a monolayer of cells that are normally about 50 μm long and 5 μm wide. The long axis is normally aligned with the streamlines of the blood flow. In abnormal flow regions, however, the shape of the endothelium cells is irregular. This change in shape of the cells suggests that structural elements of these cells are related to mechanical properties of the local blood flow. It has been shown that endothelium cells change their orientation to align with a flow that has been rotated experimentally by 90^o within 5 to 10 weeks [Hee93].

Two parameters influence the behaviour of a viscous fluid: the pressure field and shear stress. The pressure field couples to the inertia (mass) of the fluid whereas the shear stress originates in the friction between layers of fluid and/or the vessel wall, which equalises the velocity of neighbouring regions of flow. The pressure acts normal to the vessel wall, whereas the shear stress acts tangential. The physical background of fluid dynamics and wall shear stress is explained in detail in Chapter 4. Clearly, the orientation of endothelium cells along streamlines indicates a strong influence of wall shear stress.

A number of possible mechanisms by which wall shear stress can influence atherosclerotic disease are listed in [Hee93]. The "convection – diffusion theory" is based on mechanisms that bind platelets to damaged parts of the endothelium. Platelets are the constituents that form a thrombus by adhesion. Looking at the convection and diffusion of platelets in the vessel wall and blood stream, the theory tries to predict the platelet flux to the wall. The theory was extended to take account of the distribution of blood constituents across the vessel cross-section along with stirring effects. However, it does not provide a straightforward prediction of stenosis formation sites.

Experimental observation of flow fields deviating from well defined laminar flow lead to the "stagnation point hypotheses" [Hee93]. Blood flow in general is laminar, but in regions where the formation of stenosis is frequently observed the flow deviates from this

behaviour. Secondary flows will lead to recirculation and points of stagnation. Although these points of stagnation might move under the influence of a pulsed flow field, they provide regions where the reaction times between blood constituents and the vessel wall are prolonged.

The "high shear rate hypotheses" is based on the change of protein transport in the arterial wall with shear rate [Hee93]. Shear rates which are high enough to damage the endothelium have yet to be demonstrated convincingly.

The "low shear rate hypotheses" is based on the observation that in humans stenosis sites are strongly correlated to sites of low wall shear stress [Hee93]. Low wall shear rate was used as an indicator for the risk of stenosis formation in [KWO+97].

"Oscillatory shear index (OSI)" is a quantitative measure of the oscillation of wall shear stress [KGZG85]. Over a cardiac cycle the index equates to the negative area of the wall shear stress versus time curve in relation to the whole area.

An alternative parameter used to predict stenosis formation is the "wall shear stress gradient", used directly or incorporated into a dimensionless parameter Π [LKT95]. This parameter is claimed to correlate more closely with sites of stenosis formation than OSI.

A detailed summary of the measurement of wall shear stress can be found in Section 4.5.

Currently, clinical intervention takes place relatively late in the development of the disease, usually once plaque has developed. Medical treatment or surgical removal of the plaque (endarterectomy) may be performed. It would be of potential importance to develop a non-invasive technique to measure blood flow patterns, and particularly wall shear stress, in order to (i) predict those patients most at risk of further development of atherosclerotic disease and (ii) to assess treatment. Such techniques would be applicable to the investigation of arterial disease in other arteries such as the aorta, femoral and renal arteries in addition to the carotid arteries (Figure 1.2).

Thus, in order to facilitate clinical diagnoses, it is important to visualise the structure and haemodynamic properties of arteries and veins. Magnetic resonance imaging (MRI) uses the spin of nuclei to acquire information about the molecular environment (Chapter 2).

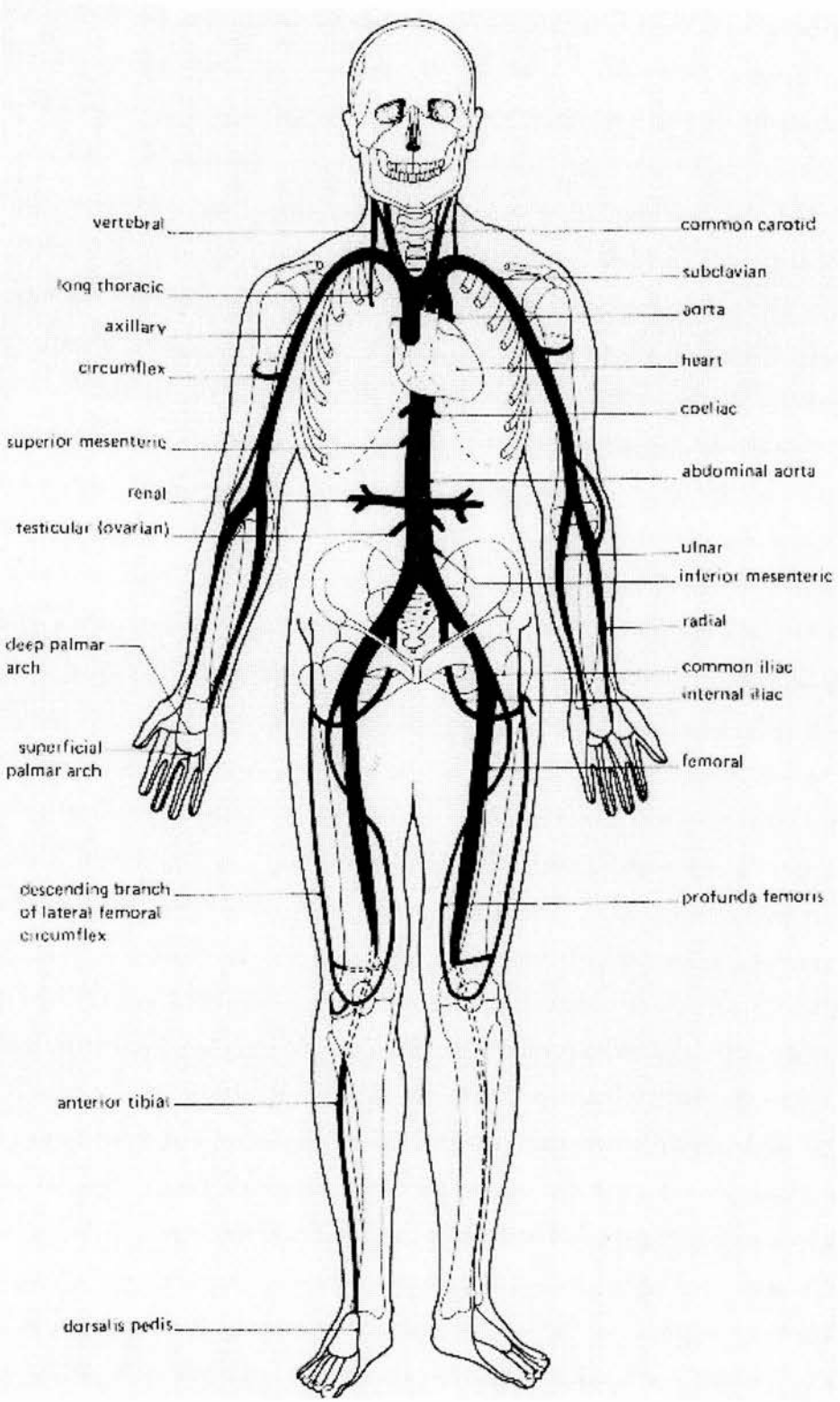

Figure 1.2.: *Principal arteries of the body. (Taken from [Mar96])*

When used on a human subject, various contrast mechanisms can be applied providing valuable diagnostic information. MRI is also well suited for volume imaging and can be made sensitive to flow (Chapter 3). Three different approaches have been used in MRI to visualise blood flow. Bolus tracking excites the nuclei within a well defined volume and monitors their progress by rapidly imaging these spins. This method produces intuitive flow information, but the edges of the tracked bolus are indistinct and the only quantitative information that can be safely extracted is the flow rate [SMS+86, EMKS89].

Time-of-flight (TOF) magnetic resonance angiography (MRA) is a routine clinical tool for the visualisation of vascular structure. MR imaging sequences have been developed in which the moving spins demonstrate high signal intensity (white blood MRA) [BS95] or low signal intensity (black blood technique) [EMKS89]. Recently, contrast agents have been used to reduce flow void artefacts due to turbulent flow conditions [PYK+93, Pri94]. Quantification of the velocity is, however, not reliable, due to the lack of a simple relationship between intensity and velocity.

Phase contrast (PC) MRI is a third method to study the 3D motion of fluids [BPFL84, FNK+87, FNKL90, PSL+94]. A bipolar gradient pulse is used to introduce a phase shift that is proportional to velocity. This information is then used to construct velocity maps. It can be used in a quantitative investigation of the detailed haemodynamics of arterial blood flow.

The aim of this project was the provision of a method that provides information on wall shear stress using MRI. To handle the large number of images acquired in PC MRI, automated flow detection algorithms were developed. Three different algorithms were differentiated: one operating on conventional MRI images only [Köh99a] along with two methods that use velocity information generated with *in vivo* [Köh99c] and *in vitro* [Köh99b] acquisitions, respectively. A detailed description with examples and verification experiments can be found in Chapter 6.

A number of phantoms were constructed to undertake the *in vitro* experiments. The flow was provided by a programmable pump, where the compatibility of the device with the MRI environment was ensured by the construction of a purpose built shield [RKM99a, RKM99c, RKM00].

The resulting flow information enabled the validation of the velocity data against known values before further post-processing was attempted. The post-processing steps necessary to calculate wall shear stress involve various fits of smooth functions to the velocity data [KR00], two methods to detect the vessel walls and the calculation of the wall shear rate vector based on that information [KRMH00]. All of these steps are explained in detail and the advantages of the different approaches are discussed in Chapter 7.

Theoretical work on pulsatile flow in tubes with circular cross-sections was undertaken to provide verification of the wall shear rate calculation and experimental procedures [RKM99b, RKHM99, RKHM00].

Subsequently, these methods were applied to a variety of phantoms (Chapter 8) and volunteers (Chapter 9). It is shown that a method to calculate accurately wall shear stress directly from time-averaged PC MRI acquisitions has been established.

2. Magnetic Resonance Imaging

2.1. Introduction

Nuclear Magnetic Resonance utilises a property of the nucleus, namely the magnetic moment. The most commonly used nucleus in magnetic resonance imaging is the proton ${}^{1}_{1}H$. Its abundance and high density in human tissue makes it ideal for imaging. Also, intrinsic properties of this nucleus produce a large signal.

Although magnetic resonance uses a physical property of the nucleus, the energies involved are considerably lower than those common in nuclear physics, and hence it leaves the properties of the nucleus unchanged. The application of magnetic resonance involves the use of electromagnetic energies which are well below the optical spectrum; single quanta in this regime are not able to break molecular bonds.

It follows that the risks involved in a magnetic resonance imaging examination are different from those using ionising radiation. One potential for danger can be seen in the strong magnetic field involved: ferromagnetic materials are attracted and can fly across the room like projectiles. The second possible source of danger for the patient can be seen in the high frequency radio waves: these can lead to the heating of the body.

A simple explanation of magnetic resonance starts with the magnetic moment of the nuclei. Hydrogen nuclei (protons), for example, exhibit a strong magnetic moment.

This property of the nucleus leads to a behaviour similar to a small permanent magnet in a magnetic field. The magnetic moments orient themselves parallel and anti-parallel to the external field. Mathematically, magnetic moments in an external field are similar to a gyroscope in the gravitational field; like gyroscopes a magnetic moment in a field will precess with a resonant precessional frequency. Applying an external electromagnetic field oscillating at exactly this precessional frequency excites the spins to start nutating. The spins continue to precess for some time after the external field has been switched off; during this process a weak electromagnetic signal is emitted that can be detected in a receiver coil introduced in a plane orthogonal to the main field. Since this phenomenon is based on the resonance of the nuclei under examination the method is called nuclear magnetic resonance (NMR).

Human tissue consists mainly of water. The hydrogen nuclei contained in this water content can be used to produce a strong NMR signal. To allow imaging, the signal that is emitted by the nuclei has to be correlated to its position within the subject. To achieve this, the normally homogeneous magnetic field is modulated by magnetic gradient fields creating a dependence of the resonance frequency on the location. To achieve spatial resolution in all directions three different magnetic gradient fields in the directions of space are applied in conventional imaging. The appropriate application of radio frequency pulses, gradient fields and signal detection to produce the image is known as a pulse sequence.

Using these pulse sequences the signal can be detected with spatial resolution. On its own this would not really allow us to distinguish between different tissues. In this simple view, all nuclei emit a signal of the same strength; only the population of protons relative to the position in the subject would be detected. However, the signal detected depends on a variety of additional parameters: the density of water and two relaxation times to be explained later. Other quantities like flow and diffusion can strongly influence the signal, as well. The variance of these parameters in human tissues can be used to distinguish different pathology. The signal from different tissues depends on the local proton density and the magnetic resonance tissue parameters. The differing signal intensities are shown as corresponding brightness values (grey scales), so that the brightness varies between different tissues.

A good introduction to nuclear magnetic resonance and magnetic resonance imaging can be found in the following texts [Eng85, Har85, Kol96, Cal91, BS95, Sli78]. A very good text on the physics of the nucleus is [MK84].

2.2. Spins in a Magnetic Field

2.2.1. Basic Physical Principles

Magnetic Field: An external magnetic field is described by the vector $\vec{H}$. A measurement inside the magnetic field leads to the magnetic induction vector $\vec{B}$. The relationship between the two properties is $\vec{B} = \mu_0 \mu_r \vec{H}$. The relative permeability μ_r, is a dimensionless characteristic of the material under investigation. Its value is unity in vacuum. $\mu_0 = 4\pi \cdot 10^{-7}\mathrm{Hm}^{-1}$ is the magnetic field constant. The dimension of $\vec{B}$ is Tesla (T). The natural magnetic induction on earth is about 0.0005 T whereas the fields used in clinical magnetic resonance imaging are around 1 T. The property $\vec{B}$ is commonly known as magnetic field, as well.

Electromagnetic Spectrum: The electromagnetic spectrum covers a range from the radio frequency (about 10^6 Hz (medium wave) to 10^8 Hz (VHF)) via microwave (10^9 Hz) and visible light (10^{15} Hz) up to Röntgen radiation (X-rays, 10^{19} Hz). Higher frequencies and energies are created in particle accelerators and occur in cosmic background radiation. For magnetic resonance imaging high frequency waves of about 10 MHz = 10^7 Hz to about 80 MHz are commonly used.

By applying Planck's equation $E = h\nu$ (E : energy, $h = 6.62 \cdot 10^{-34}\,\mathrm{Ws}^2$: Planck's constant, ν : frequency) the corresponding energy can be calculated. The binding energy of molecules corresponds to a frequency of 10^{15} Hz.

2.2.2. Resonance Condition

The spin of an elementary particle is a quantum mechanical property. The spin of a particle can be thought of as an "eigen" angular momentum. The important point is the coupling with a magnetic moment. Indeed, this holds true for electrons as well as nucleons. It turns out that all spins have multiples of half integer values. A particle with spin I can adopt $2I + 1$ different states m with values $-I, -I + 1, ..., +I$. This quantisation (m can only adopt discrete values) is important for the calculation of energy levels later. Figure 2.1 shows the different levels for an $I = 1/2$ system (e.g. electrons, protons, etc.).

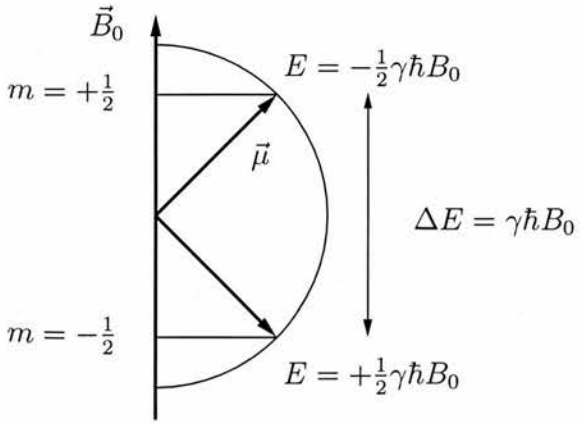

Figure 2.1.: *Quantisation of energy levels illustrated for the quantum mechanical description of a spin 1/2 nucleus oriented in a magnetic field* $\vec{B}_0$.

The magnetic moment $|\vec{\mu}|$ of a nucleus with spin I is given by:

$$|\vec{\mu}| = \frac{\gamma h I}{2\pi} \tag{2.1}$$

with the magnetic moment μ, the gyromagnetic ratio γ of the particle and Planck's constant h. With the exception of the unstable nucleus tritium the hydrogen nucleus has the highest magnetic moment amongst the nuclei.

Electrons have a spin, too. It's symbol is usually S. Free electrons have a massively higher gyromagnetic ratio (about 1000 times) than nuclei. However, only for the understanding of contrast agents do electron spins have to be considered, since in chemical bonds the electron spins are neutralised pairwise and no net electron spin is observed.

Only nucleons with an odd number of neutrons or protons exhibit a resulting spin. Several nuclei, which exhibit an NMR signal, are clinically important. These are, in addition to the proton ^1H, the nucleons lithium ^7Li, carbon ^{13}C, fluorine ^{19}F and phosphorus ^{31}P.

The energy of a magnetic moment $\vec{\mu}$ in an external magnetic field with magnetic induction $\vec{B}$ is:

$$E_{pot} = -\vec{\mu} \cdot \vec{B}. \tag{2.2}$$

Aligning the z-axis of the coordinate system with the direction of the external magnetic field of strength B_0 simplifies the expression to:

$$E_{pot} = -\mu_z \cdot B_0 \tag{2.3}$$

with μ_z the z-component of the magnetic moment. If the magnetic moment originates from a spin, it can have $2I + 1$ distinct values.

$$E_m = -\gamma \frac{h}{2\pi} \cdot B_z \cdot m. \tag{2.4}$$

The result is a distribution of discrete energy levels (Figure 2.1). This effect is known as the nuclear Zeeman effect. The energy difference between the two neighbouring levels in a magnetic field is $\Delta E = \gamma(h/2\pi)|\vec{B}|$. The selection rules allow transitions between neighbouring energy levels ($\Delta m = \pm 1$), only. During the transition from one energy level to the next an energy quant ΔE is either absorbed or emitted. Using Planck's equation this energy is related to a frequency ν:

$$E = h \cdot \nu \tag{2.5}$$

or expressed in the cycle frequency ω:

$$E = \hbar\omega \tag{2.6}$$

with $\hbar = {}^{h}/_{2\pi}$.

The frequency of radiation to initiate a transition between neighbouring energy levels, the resonance condition, is therefore given by the Lamor frequency:

$$\nu = \frac{\gamma}{2\pi} \cdot B_0 \quad \text{or} \quad \omega = \gamma B_0. \tag{2.7}$$

The resonance frequency ν for a given nucleus is therefore proportional to the magnetic induction B. The gyromagnetic ratio γ is a characteristic property of the atom under investigation and can be used to calculate ν for a specific B_0. For a direct calculation of the frequency in Hertz (Hz), ${}^{\gamma}/_{2\pi}$ is tabulated rather than γ (Table 2.1).

Isotope	Spin I	Gyromagnetic ratio $\gamma/2\pi$ in MHz/T	Natural abundance in %
^{1}H	1/2	42.577	99.9
^{13}C	1/2	10.708	1.1
^{19}F	1/2	40.077	100
^{23}Na	3/2	11.268	100
^{31}P	1/2	17.256	100

Table 2.1.: *Properties of important isotopes for magnetic resonance imaging and spectroscopy [Kol96, Eng85, Har85].*

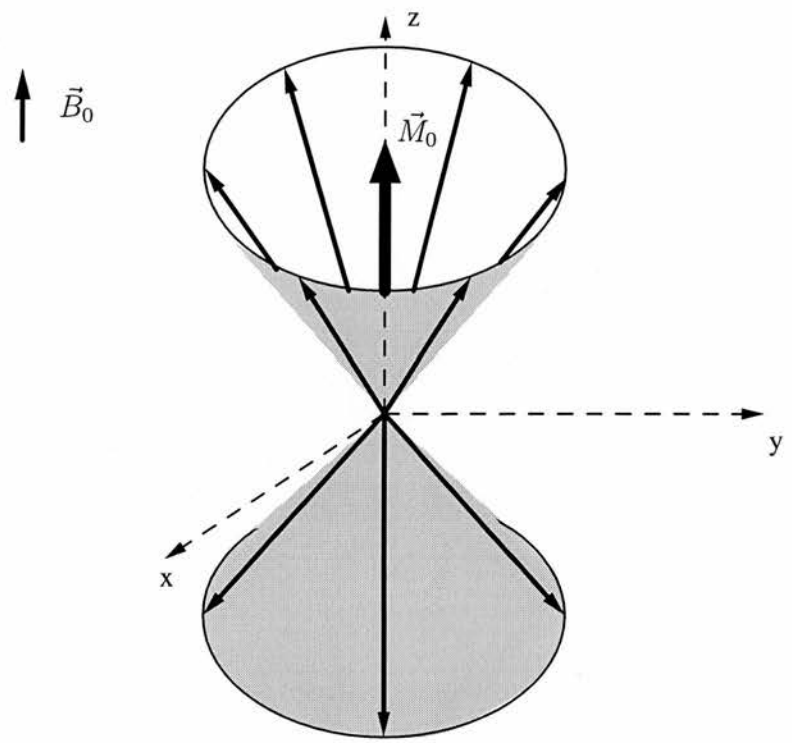

Figure 2.2.: *Illustration of the net magnetisation $\vec{M}_0$ resulting from an ensemble of protons precessing in a magnetic field $\vec{B}_0$. Slightly more protons align themselves parallel to $\vec{B}_0$ than anti-parallel.*

During the transition between neighbouring energy levels an amount of energy that corresponds to the resonance condition is required. Practically, however, there is a large population of available nuclei taking part in the process (1 cm^3 water contains about $7 \cdot 10^{25}$ protons). In addition the thermal energy kT ($k = 1.38 \cdot 10^{-23}$ Ws/K Boltzmann constant, T absolute temperature) of the atoms has to be taken into account. Combined, this leads to an initial occupation of the energy levels following the Boltzmann statistic. The ratio of occupation of two energy levels is (illustrated in Fig. 2.2):

$$N_2/N_1 = e^{\left(\frac{\Delta E}{kT}\right)}. \tag{2.8}$$

For the energy difference between two nuclear spin levels ($E = \gamma h B/2\pi$), the ratio of occupation for room temperature ($T = 300\,K$) and a typical magnetic field for clinical MRI ($B = 1.5\,T$) is about 0.99999; this means that the difference in occupation is only 10^{-5}. To express it differently: only every 100 000th nucleus contributes to a net magnetisation at conventional magnetic fields. Magnetic resonance imaging is thus a very insensitive method.

A simplified, classical view of this net moment would be a small bar magnet that aligns with an external magnetic field and precesses around the main axis at the resonance frequency. This net moment is not only a microscopic property, but it can be detected macroscopically: moving magnets induce a voltage. It is always important to remember that the net moment is the average over many particles. Quantum mechanically, the net moment $\vec{m}$ follows from:

$$|\vec{m}| = N \cdot I(I+1)\gamma^2 \cdot \left(\frac{h}{2\pi}\right)^2 \frac{B_z}{3kT} \tag{2.9}$$

with N the number of spins that contribute to the net moment. The magnetisation $\vec{M}$ is often used; it incorporates the sample volume V, such that $\vec{M} = \vec{m}/V$.

2.2.3. Radio Frequency Pulses

Manipulation of the spins can be achieved with radio frequency (RF) pulses. At equilibrium the magnetisation aligns with the external magnetic field after some time. An excitation using a periodic magnetic field orthogonal to the main field can change the magnetisation of the spins considerably. The frequency of the excitation has to match the resonance frequency of the spins, however.

For the correct description of the magnetisation in this case, a rotating coordinate system (x', y', z') is commonly used; the coordinate system is rotating round the z-axis with the resonance frequency. This simplifies the calculation significantly. All of the following diagrams relate to this rotating coordinate system.

A periodic, magnetic field applied at the resonance frequency $\vec{B_1}$ is a vector fixed in the rotating coordinate system. The convention has this vector in the x-direction of the rotating coordinate system. Hence, the precessing magnetisation is fixed in the rotating coordinate system. In analogy to the precession of the magnetisation around the main magnetic field $\vec{B_0}$ there is a precession around the local magnetic field $\vec{B_1}$ with a frequency of $\omega_1 = \gamma B_1$.

This leads to a movement of the magnetisation into the x-y-plane under the influence of the additional $\vec{B_1}$ field. As the B_1 fields are usually a lot smaller than the static magnetic field B_0, this rotation is slower. The frequency ν_1 is typically around 50 Hz rather than the 40 MHz of ν_0. Using careful timing of the B_1 field duration, the rotation of the magnetisation can be precisely chosen. The rotation angle φ follows in analogy from the rotation frequency ω_1 and the application time t: $\varphi = \omega_1 t$. Taking a typical value for medical imaging $\nu_1 = 100\,\text{Hz}$ a full turn takes 10 ms and a 90^o flip into the x-y-plane 2.5 ms. The effect of this very common pulse (switching of radio frequency signal), also known as a 90^o-pulse, is illustrated in Figure 2.3. A 180^o-pulse will turn the magnetisation from the z-direction into the negative z-direction. These high frequency fields are transmitted by coils within the magnet that are driven by high frequency amplifiers.

The linear field $\vec{B_1}$ can be understood as a linear combination of two cyclic fields with opposing direction of rotation. One of them will have the same direction of rotation as the precessing spins and enables interaction of the magnetic field with the rotating spins.

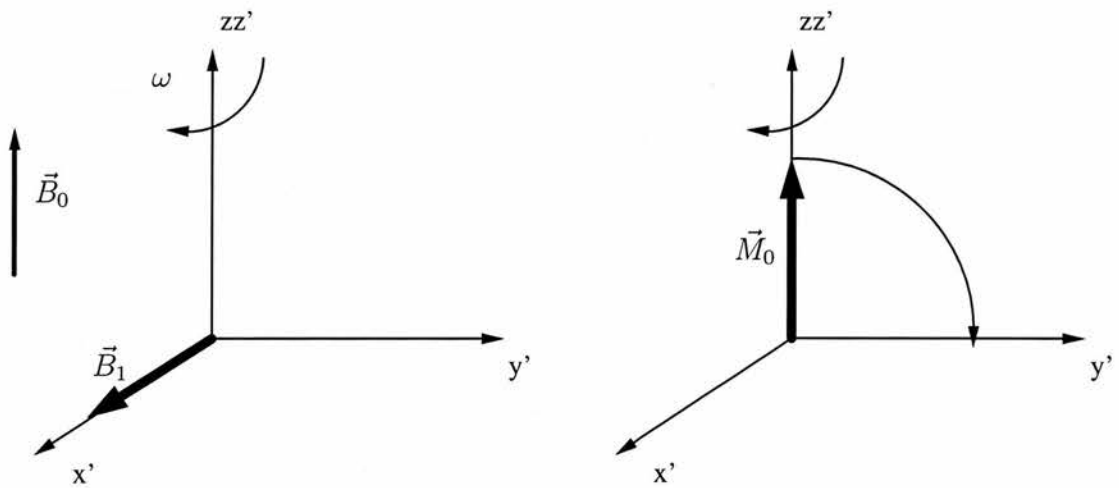

Figure 2.3.: *Diagram illustrating how the net magnetisation $\vec{M}_0$ is rotated about a magnetic field $\vec{B}_1$ applied along the x' axis in a frame of reference rotating at resonance such that $\omega = \omega_0 = -\gamma \vec{B}_0$*

2.2.4. Relaxation

The temporal changes of magnetisation are covered by a number of relaxation processes. Starting from equilibrium a distortion is introduced from the outside. This can happen, for example, through radio frequency excitation. It results in a temporal change in magnetisation:

$$\frac{\mathrm{d}\vec{M}}{\mathrm{d}t} = \gamma \cdot \vec{M} \times \vec{B}. \tag{2.10}$$

This equation is following basic mechanics: the right hand side describes the torque and the left hand side the rate of change in angular momentum.

This equation leads to a precession equation: a precession with the angular frequency ω: $\omega = \gamma \cdot B_z$ or expressed as a frequency:

$$\nu = \frac{\gamma}{2\pi} B_z. \tag{2.11}$$

It can be assumed that the system will return (relax) to equilibrium state after a certain amount of time. A coordinate system is chosen with the z-axis parallel to the external magnetic field. The equilibrium magnetisation will adjust to the same direction. Furthermore, the equilibrium state magnetisation M_0 lies purely in z-direction and has no components in the x-y plane. This simplifies Equation 2.10 to the following equations for the three components which are known as the Bloch equations:

$$\frac{\mathrm{d}M_x}{\mathrm{d}t} = \gamma \cdot \left(\vec{M} \times \vec{B}\right)_x - \frac{M_x}{T_2} \tag{2.12}$$

$$\frac{\mathrm{d}M_y}{\mathrm{d}t} = \gamma \cdot \left(\vec{M} \times \vec{B}\right)_y - \frac{M_y}{T_2} \tag{2.13}$$

$$\frac{\mathrm{d}M_z}{\mathrm{d}t} = \gamma \cdot \left(\vec{M} \times \vec{B}\right)_z + \frac{M_0 - M_z}{T_1}. \tag{2.14}$$

These Bloch equations form the basis for many calculations and descriptions of the bulk magnetisation during pulse sequences. The longitudinal relaxation time T_1, governs the return of the magnetisation back to the original value M_0 along the z-axis. The transverse relaxation time T_2, describes the decay of the magnetisation component in the x-y-plane to zero.

The longitudinal relaxation is connected to an energy transfer. The surplus energy has to be transferred to the surroundings. This process is very important in solid state physics. Here, the energy is transferred to the surrounding lattice. This leads to the other name for this process: spin-lattice-relaxation. The key to the efficient transfer of energy is the presence of a molecular motion (e.g. rotation) with a matched resonance frequency.

The process of transverse relaxation does not transport energy out of the spin system. This always happens quicker than longitudinal relaxation: $T_1 \geq T_2$. It can be explained using spin flips that conserve the overall energy of the system. The magnetisation vectors of the individual spins diverge in the x-y-plane and the x-y-component of the magnetisation $\vec{m}$ dephases. The magnetisation is exchanged between spins in this case: spin-spin-relaxation. This is in part due to molecular motion and rotation but also magnetic field inhomogeneities. Contributions to the inhomogeneity can be recovered with certain pulse sequences. Inhomogeneities in the local magnetic field generally shorten the transverse relaxation time considerably and are due to main-field inhomogeneity, magnetic susceptibility effects in the tissue and poorly designed imaging gradient. Another relaxation time constant was introduced to take these effects into account $T_2^\star$ [Kol96, BS95]:

$$\frac{1}{T_2^\star} = \frac{1}{T_2} + \frac{1}{T_{2M}} + \frac{1}{T_{2SM}}. \tag{2.15}$$

Where T_{2M} is the time constant due to inhomogeneities in $\vec{B}_0$ and T_{2SM} is attributed to susceptibility artefacts.

The Bloch equations are first order differential equations. For simple starting and boundary conditions, the solutions are exponential functions. If the magnetisation is changed in a simple case from M_0 in z-direction at the start ($t = 0$) to a value of 0, the resulting time course takes the following form:

$$M_z = M_0 \cdot \left(1 - e^{-t/T_1}\right) \tag{2.16}$$

and the magnetisation in x-direction starting from M_{x0} at $t = 0$:

$$M_x = M_{x0} \cdot e^{-t/T_2}. \tag{2.17}$$

These two cases illustrate the importance of the time constants, T_1 and T_2, again.

2.2.5. Nuclear Magnetic Resonance: Free Induction Decay

The simplest nuclear magnetic resonance experiment follows directly from the aforementioned principle. A sample is introduced into a static magnetic field. After some time the magnetisation in the sample will align with the external magnetic field.

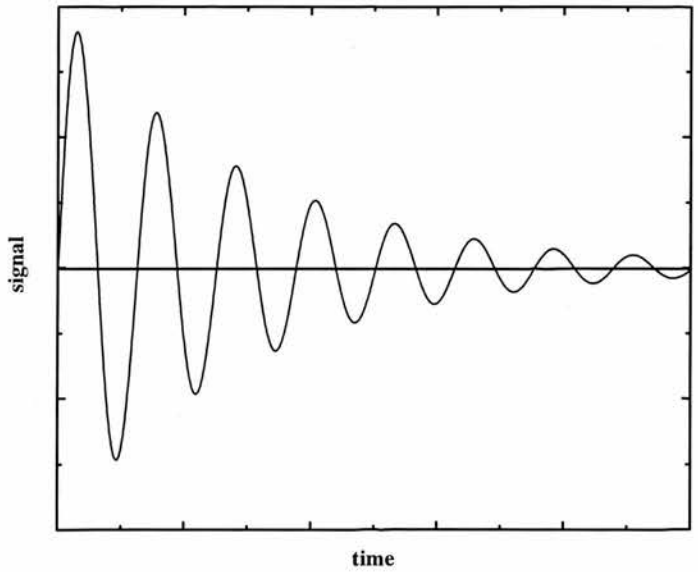

Figure 2.4.: *An illustration of the general signal received from an NMR experiment after a 90° RF excitation pulse. This signal is known as a free induction decay (FID).*

A high frequency antenna, placed in the magnet, creates a periodic magnetic field B_1 orthogonal to B_0. This antenna is sensitive to periodic fields in the x-y-plane. The antenna is used to introduce a 90°-pulse that turns the magnetisation, in the rotating coordinate system, into the y'-direction. In the static coordinate system the magnetisation vector rotates in the x-y-plane. This is the plane of sensitivity of the high frequency antenna. The rotating magnetisation creates a weak electromagnetic field. The antenna is now used as a receiver rather than a transmitter. The weak signal is detected as a periodic voltage across the antenna and can be amplified and displayed. The signal will have the general form displayed in Figure 2.4.

The signal exhibits a high frequency ω_0. The decay is due to the transversal relaxation (T_2) that reduces the component of the magnetisation in the x-y-plane. The magnetisation is the sum of many components that fan out in the x-y-plane reducing the net magnetisation as illustrated in Figure 2.5.

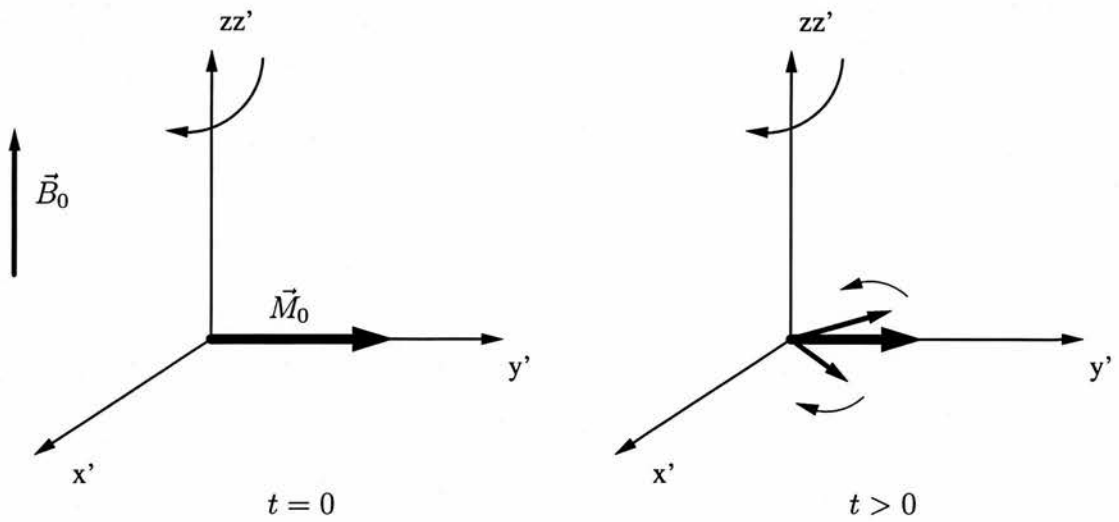

Figure 2.5.: *An illustration of the effect of T_2: the precessing net magnetisation vector on the left creates the signal. Under the influence of T_2 the spins contributing to the net magnetisation will dephase and the net magnetisation decreases. Only two spin isochromats contributing to the bulk magnetisation are presented.*

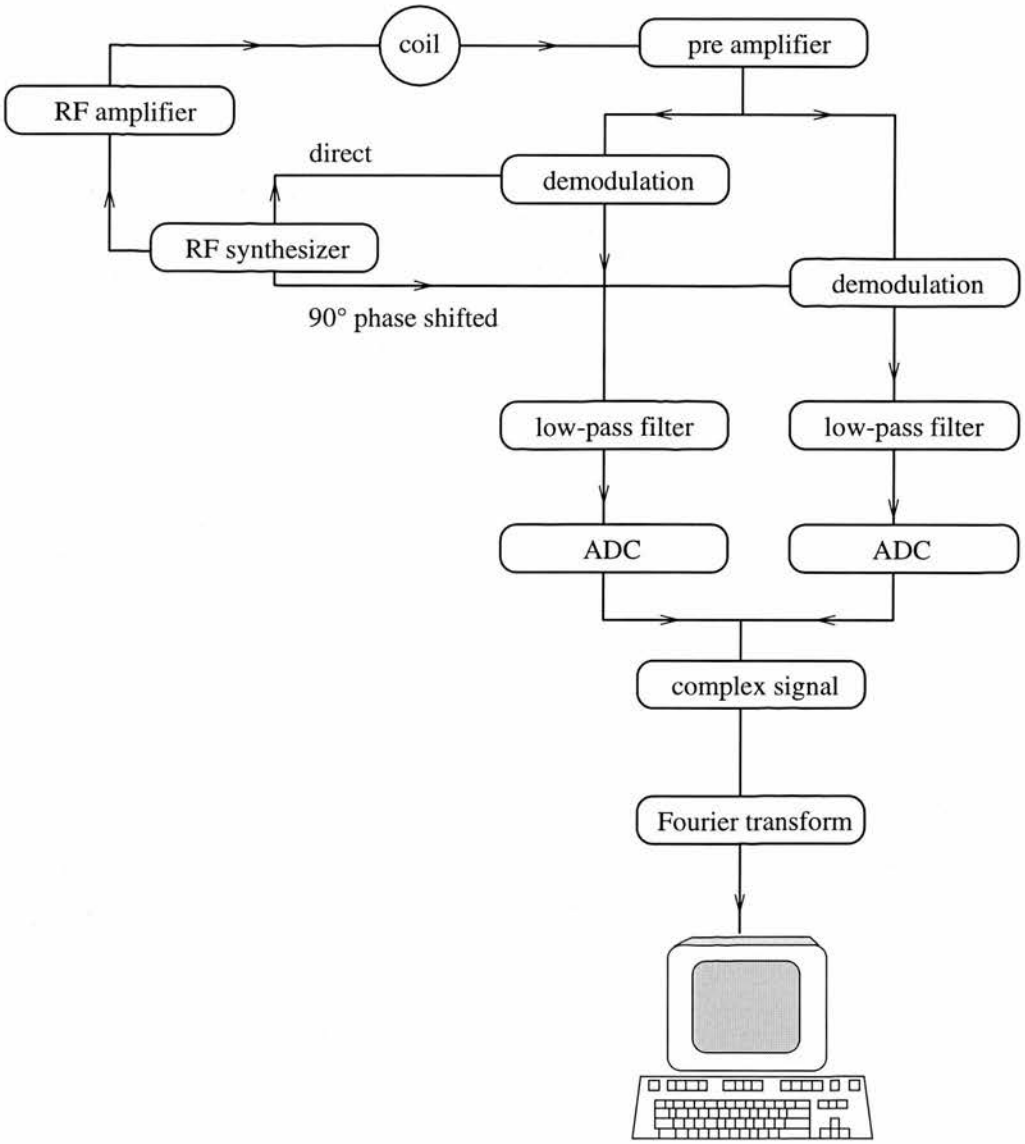

Figure 2.6.: *An illustration of the signal path in a commercial MRI scanner. The resonant RF signal created in the syntheziser is transmitted via the coil to the sample where it leads to a rotation of the net magnetisation. The coil then receives the resulting signal induced by the rotating magnetisation. This signal is amplified and demodulated with the original signal sent to the coil. The resulting high frequency components are filtered out and the complex signal (with magnitude and phase) is digitised by analogue to digital converters (ADCs). The complex signal is collected and Fourier transformed on a computer.*

In practice the signal is demodulated to low frequency as illustrated by Figure 2.6. At these lower frequencies, filtering and digitisation using analogue to digital converters (ADCs) are easier to realise. Quadrature detection enables the measurement of a complex signal with magnitude and phase information. This is the simplest nuclear magnetic resonance (NMR) experiment, also known as a free induction decay (FID). It is rarely used in imaging, due to problems with the switching from transmit mode to receive in the RF circuits. This time delay, the dead time, does not allow the acquisition of an actual full FID with imaging equipment.

Another simple NMR experiment is known as the spin-echo-experiment [Hah50]. A 90^o-pulse is applied followed after a certain time τ by a 180^o-pulse. After another period of τ a signal forms, the so called spin-echo. The period between the 90^o-pulse and the echo is called echo time $t_e = 2\tau$.

The spin-echo forms after the dephasing of the individual spins is reversed (Figure 2.7). In more detail: the 90^o-pulse brings the magnetisation into the x-y-plane. The individual spins have slightly different resonance frequencies due to their different environments and $\vec{B_0}$ field inhomogeneities. In the rotating coordinate system these spins fan out in the x-y-plane. Following τ the y-components of the individual spins are reversed with a 180^o_x pulse. The fans return to the x-y-plane and the spins continue to disperse. After the rotation, the direction of the dispersion is towards each other rather then apart. The magnetisation returns to a maximum after the dispersion of the spins with T_2 has been recovered at 2τ.

2.3. Spatial Resolution: Magnetic Resonance Imaging

The creation of an NMR signal has been explained. Using large enough magnets and coils this can be applied to the human body. However, spatial information is still to be discussed. This section aims to explain the modification to the experiments to use nuclear magnetic resonance to form images of the human body.

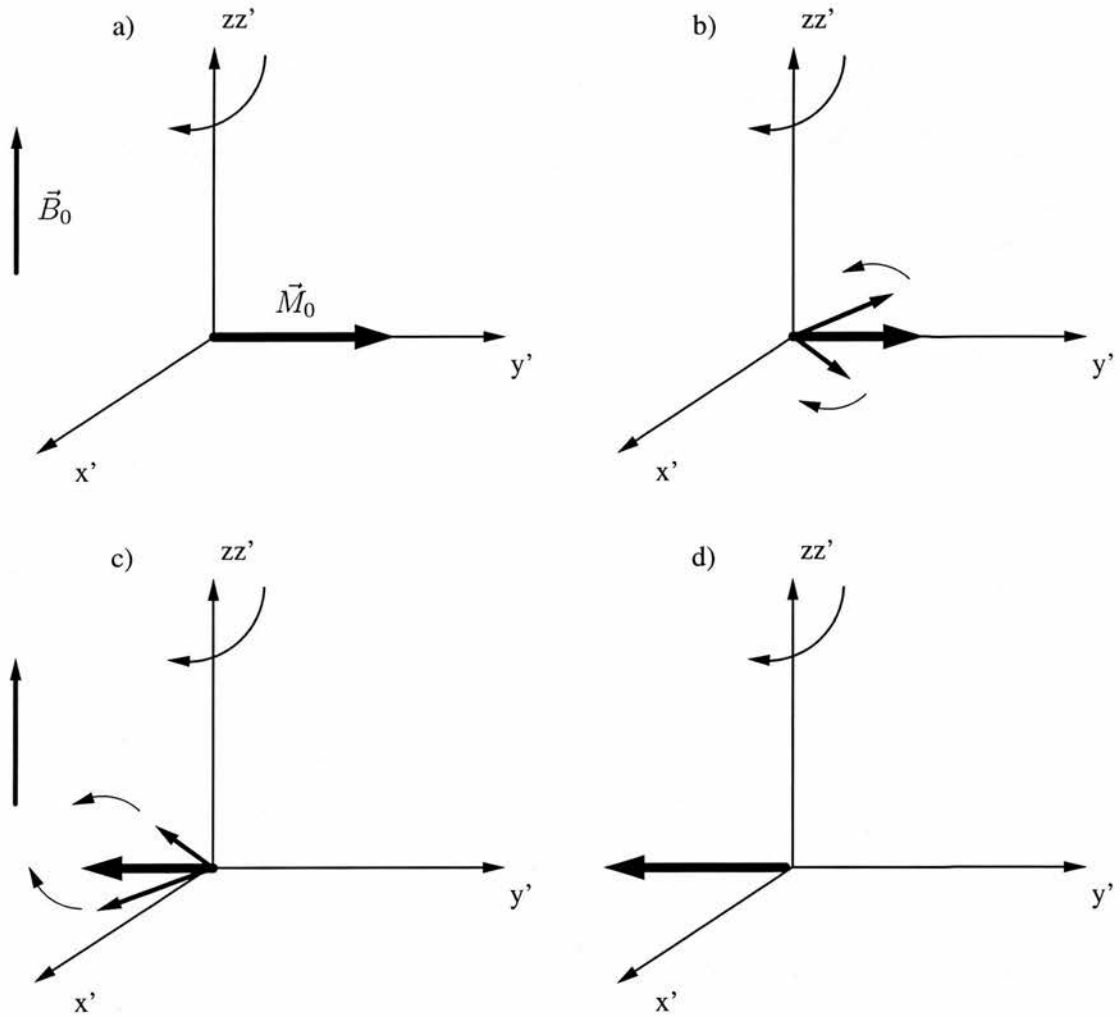

Figure 2.7.: *The formation of a spin echo: a) after the application of a 90° RF pulse the net magnetisation $\vec{M}_0$ lies along the y' - axis of the rotating frame of reference. b) The spins contributing to the net magnetisation dephase for a time period τ. c) Application of a 180° RF pulse mirrors the spins around the origin. This also changes their direction of dephasing. d) After another τ the continued rephasing leads to the formation of an echo. Only two of the isochromats contributing to the bulk magnetisation are presented.*

2.3.1. Magnetic Field Gradients

The principle behind image formation from NMR signals is similar for all the methods subsequently described. The homogeneous magnetic $\vec{B}_0$ field is spatially modulated using magnetic gradient coils. The aim is to vary the magnetic field linearly in space. According to $\omega = \gamma B$ this leads to a linear variation in the resonance frequency.

The modulated magnetic field should remain parallel to the original homogeneous magnetic field. The x- and y-components remain negligible for moderate gradient strengths while the component in z-direction varies in space. Based on gradients there are three principal localisation methods: slice selection, frequency encoding and phase encoding.

2.3.2. Slice Selection

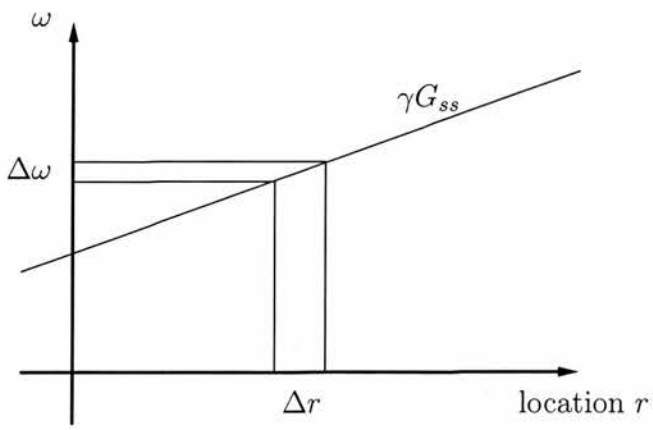

Figure 2.8.: *Correlation between slice thickness Δr and frequency bandwidth $\Delta\omega$ through the slice selection gradient G_{ss}.*

Application of an RF pulse with a magnetic field gradient allows the selection of a slice from the sample for excitation. The application of the magnetic gradient varies the magnetic field and the NMR resonance frequency accordingly as shown in Figure 2.8. The application of a frequency band rather than a single frequency will now excite a slice of space.

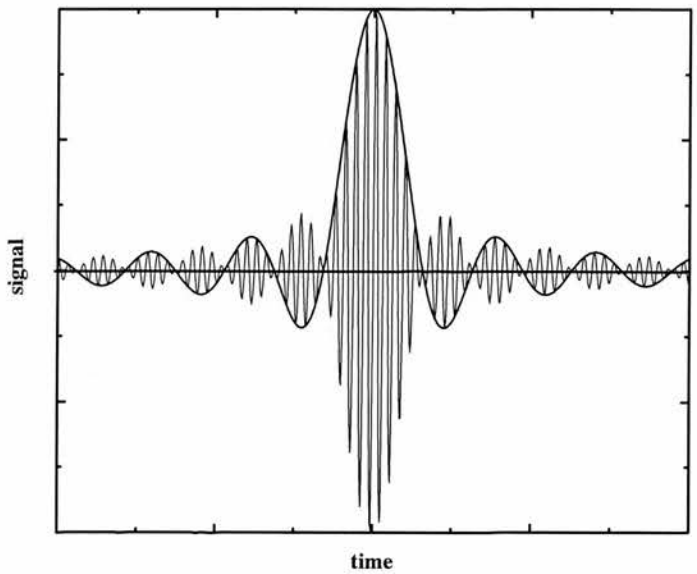

Figure 2.9.: *An illustration of a sinc RF pulse used for rectangular slice excitation.*

The connection between the distribution of frequencies in the RF pulse and the slice profile is approximately governed by the Fourier transform [Cal91] for small flip angles. This mathematical operation returns the harmonic analysis $I(\nu)$ of an arbitrary signal $s(t)$.

$$I(\nu) = \frac{1}{\sqrt{2\pi}} \int_{-\infty}^{\infty} s(t) \cdot e^{-i2\pi\nu t} dt. \tag{2.18}$$

A rectangular slice profile, for example, is generated by a $\mathrm{sinc}((\omega - \omega_0)t) = \frac{\sin((\omega-\omega_0)t)}{(\omega-\omega_0)t}$ frequency envelope (Figure 2.9).

Slice selection is presented in a pulse diagram as shown in Figure 2.10. The slice selection gradient is first switched on. As very high currents have to be switched, the required value will only be available after a short time. Subsequently the RF pulse is applied and then the gradient is switched off.

The envelope of a slice selection RF pulse to excite a rectangular slice profile is a sinc function as shown in Figure 2.9. For a truly rectangular excitation, the sinc pulse needs to be applied for a very long time covering many zero crossings. In practical applications,

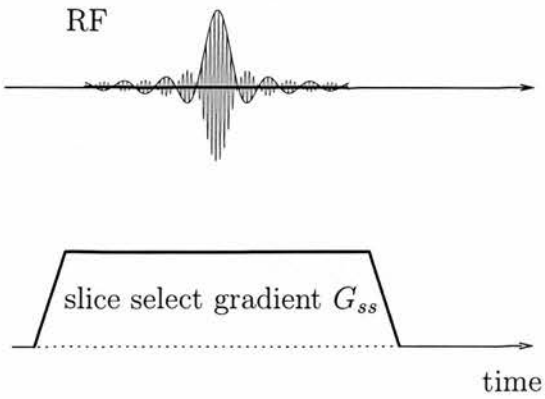

Figure 2.10.: *The presentation of a slice selection pulse in a pulse sequence program.*

the slice profile is chosen as a compromise between acquisition time and deviation from a rectangular profile. The inverse slice thickness is given by

$$\frac{1}{D} = \frac{\gamma}{2\pi} G_{ss} t_0 \tag{2.19}$$

with G_{ss} the strength of the gradient pulse (usually in mT/m) and t_0 the time from maximum to the first zero crossing in the sinc function. The slice profile improves with the number of zero crossings of the sinc function covered, but practically four to five zero crossings prove sufficient. Other envelope forms for the excitation RF pulse have been proposed [Cal91].

According to equation 2.19 there are two possibilities to change the slice profile: the form of the RF pulse envelope and the gradient strength G_{ss}. Changing the form of the envelope will also change the shape of the slice profile.

The slice position is given by the frequency of the RF pulse. When the frequency of the RF pulse coincides with the spin resonance ω_0 a slice corresponding to zero gradient field is selected. The slice position S can be calculated from the difference between the RF pulse and ω_0: $\Delta\nu = (\gamma/2\pi)\Delta B$ and ΔB is given by $S \cdot G_{ss}$. The frequency shift needed to localise a slice at S is therefore given by

$$\Delta\nu = \frac{\gamma}{2\pi} G_{ss} S. \tag{2.20}$$

2.3.3. Frequency Encoding

Frequency encoding is another way to use gradients to correlate NMR signals to a coordinate in space. A gradient is applied during the readout period. This gradient is therefore known as the readout gradient.

The underlying principle, again, is that the resonance frequency depends on the location during the application of a gradient. In the presence of a gradient during the readout period the signal will contain frequency components that can be assigned to a coordinate in space. A Fourier transformation of the temporal signal measured will assign the signals to their location.

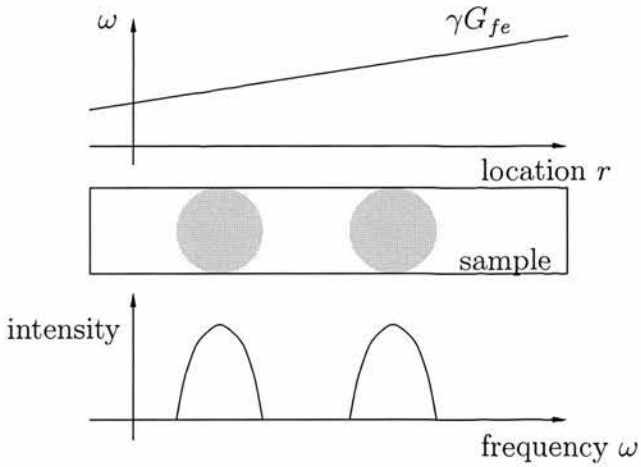

Figure 2.11.: *An illustration of frequency encoding. A sample with two water filled tubes in a linear gradient field G_{fe} will produce a signal after Fourier analysis that looks like the one shown at the bottom.*

As an example, a phantom consisting of two tubes filled with water (Figure 2.11) is used. During the readout of the signal a gradient pulse is applied in a way that the two samples have different resonance frequencies. The resulting signal is highly complex. After Fourier transformation the intensity will display an NMR signal wherever there is water in the projection onto the gradient direction. Spatial resolution has been achieved in one direction. The Fourier transform of just one signal already achieves spatial resolution in one direction.

To calculate the strength of the readout gradient the readout time t_{read} (the time during which the signal is sampled) has to be known. The field of view (FOV) in the readout direction and the number of image pixels in that direction, N, defines the spatial resolution. The frequency bandwidth of the sampling is given by $\Delta\nu = 1/t_{dwell}$, where t_{dwell} is the time between two sampling points. The readout time is then given by $t_{read} = Nt_{dwell}$. The bandwidth can be calculated from the resonance condition (Eq. 2.7), such that: $\Delta\nu = (\gamma/2\pi)G_{fe}\text{FOV}$. Both equations together give:

$$G_{fe} = \frac{N}{(\gamma/2\pi)} \cdot \text{FOV} \cdot t_{read}. \tag{2.21}$$

As a consequence, spatial resolution can be achieved with a weak gradient but a long readout. This reduces the bandwidth of the sampling which allows for better noise filtering. However, the acquisition time will increase and the signal might vary during the readout due to T_2 relaxation. Also, field inhomogeneities become more important when a lower gradient is used.

Another effect to take into account is the chemical shift. In the absence of gradients more than one frequency may be detected in the signal. The main components of the NMR signal in humans are water and fat, which are separated by approximately 220 Hz at 1.5 T. Assuming a 3 mT/m readout gradient and 26 cm FOV the chemical shift will correspond to 2 pixels. Any bigger shifts will result in more distinct artefacts (chemical shift artefact) and should be avoided.

2.3.4. Phase Encoding

To achieve phase encoding a pulsed gradient is employed. This gradient is switched on neither during the RF excitation, like the slice selection gradient, nor during the readout, like the readout gradient. Instead this gradient is applied between those two pulses. It assigns a spatially varying phase to the spins, i.e. the magnetisation vectors at different locations point in different directions.

While the phase encoding gradient G_{pe} is applied the precessional frequency of the protons either increases or decreases depending on their spatial position (Figure 2.12). Once G_{pe} is turned off, the protons precess at their original frequency, but will be either

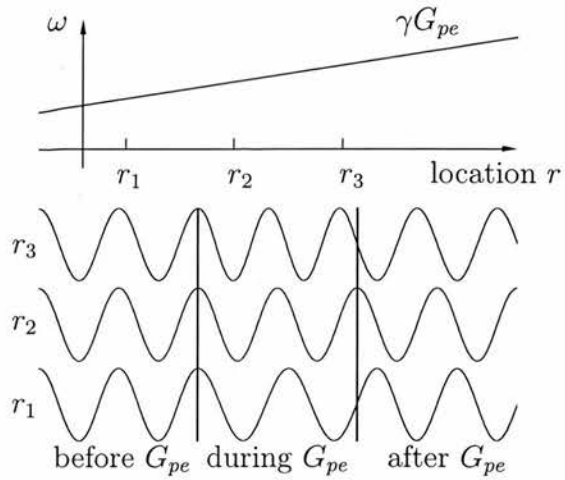

Figure 2.12.: *Illustration of the evolution of the phase of spins at different locations during the application of a phase encoding gradient. Spins at r_1 and r_3 lose or gain phase while the gradient is switched on and continue with their normal precession afterwards.*

ahead or behind in phase relative to the protons which experience $G_{pe} = 0$. The phase shift induced by G_{pe} will de determined by the magnitude and duration of G_{pe} such that

$$\varphi(y) = \gamma \left(\int G_{pe} dt \right) \cdot y \tag{2.22}$$

with the accumulated phase angle φ. Intuitively, it is clear that the integral of the gradient with respect to time governs the amount of phase difference accumulated. The term $\int G dt$ is used frequently and often denoted with k (for gradients in x- , y- and z-direction k_x, k_y and k_z respectively). This will later lead to the introduction of "k-space" in Section 2.3.6. In practice, the "k-space" corresponds to the "space" of raw data.

An important point of phase encoding is the fact that the experiment has to be repeated with several values for the phase encoding gradient. In this case the number of steps determines the spatial resolution. These repetitions do increase measurement time, but on the other hand they increase the signal to noise ratio (SNR). The repetitions increase the SNR in a similar way to a straight forward accumulation of signals. Due to the differences in the phase encoding gradient, the improvement in SNR is about 13 % less than the ideal square root of the number of repetitions [Kol96].

The phase difference over a FOV should be 2π. With a given length of the phase encoding gradient t_{phase} the phase difference $\Delta\varphi$ can be calculated from $\Delta\varphi = \Delta\omega t_{phase}$. $\Delta\omega$ is determined by the resonance condition (Eq. 2.7) and the strength of the phase encoding gradient G_{pe}:

$$\Delta\omega = \gamma G_{pe}\mathrm{FOV}. \tag{2.23}$$

A phase shift of 2π requires therefore:

$$2\pi = \gamma G_{pe}\mathrm{FOV}t_{phase}. \tag{2.24}$$

For a given number N of image pixels within the FOV, the gradient strength is given by:

$$G_{pe,max} = \frac{N/2}{(\gamma/2\pi)\cdot \mathrm{FOV}\cdot t_{phase}}. \tag{2.25}$$

2.3.5. Nyquist Theorem

The combination of digitising the signal at discrete time points and Fourier transformation leads to a maximum frequency that can be sampled relative to the centre frequency. This is known as the Nyquist frequency ω_{Nq}:

$$\omega_{Nq} = N/(2\cdot t_{read}) \tag{2.26}$$

where N is the total number of sampling points. The Nyquist frequency in MR can be 0.5-50 kHz, depending on the combination of sampling time and number of data points. To exclude frequencies greater than the Nyquist limit prior to digitisation, a low-pass filter is employed to improve the signal to noise ratio by removing noise and signal in a frequency range that cannot be sampled. This also helps to reduce aliasing.

2.3.6. K-Space

The concept of reciprocal k-space was briefly introduced in Section 2.3.4 to simplify the Fourier analysis of a spin system in the presence of a magnetic field gradient. It was also demonstrated that, under the application of a magnetic field gradient, the precessional frequency becomes proportional to the position in the field. With the introduction of a reciprocal space $k = \int G dt$ as given in Section 2.3.4, the Fourier transform relationship between time and frequency is transported into a relationship between reciprocal space and real space. As such $\vec{r}$ and $\vec{k_r}$ are Fourier transform pairs, in the same way as ω and t. This concept is the same as that used in solid state physics and especially in crystallography.

The central portion of k-space, corresponding to low amplitude G and the central region of the readout data, contains most of the signal content and provides the majority of the image contrast, while the edges of k-space provide the fine detail from high frequency components. The k-space data has a Hermitian symmetry due to the positive and negative G values introducing opposite phase shifts to the proton resonance. This symmetry can be exploited by using half Fourier techniques to reduce the acquisition time [Kol96]. The half Fourier approach samples approximately 60 % of k-space, corresponding to the negative phase encoding values and the first few positive values. The regions of k-space corresponding to the positive G values can be reconstructed using the symmetry properties of the data, while the additional acquired positive k-space lines are used for phase correction and contrast. Half Fourier imaging techniques result in the same spatial resolution and FOV, but reduce the acquisition time by around 40 %. However, the SNR is reduced and the method is more sensitive to artefacts arising from the duplication of data.

The k-space formalism results in a convenient description of the different sampling methods used to acquire the raw data matrix. The traditional method sequentially fills each line of k-space, each corresponding to a different phase encoding step.

2.4. Imaging Sequences

2.4.1. Spin Echo

To put all these techniques into context a typical sequence to acquire an MRI image is examined. All three methods to achieve spatial resolution, as described, are employed. The sequence presented here uses the spin echo (Section 2.2.5) to create a signal that is sampled.

As previously mentioned, imaging with a spin - echo utilises all three encoding methods: slice selection, frequency encoding and phase encoding. The sequence diagram of such a sequence will be developed here step by step.

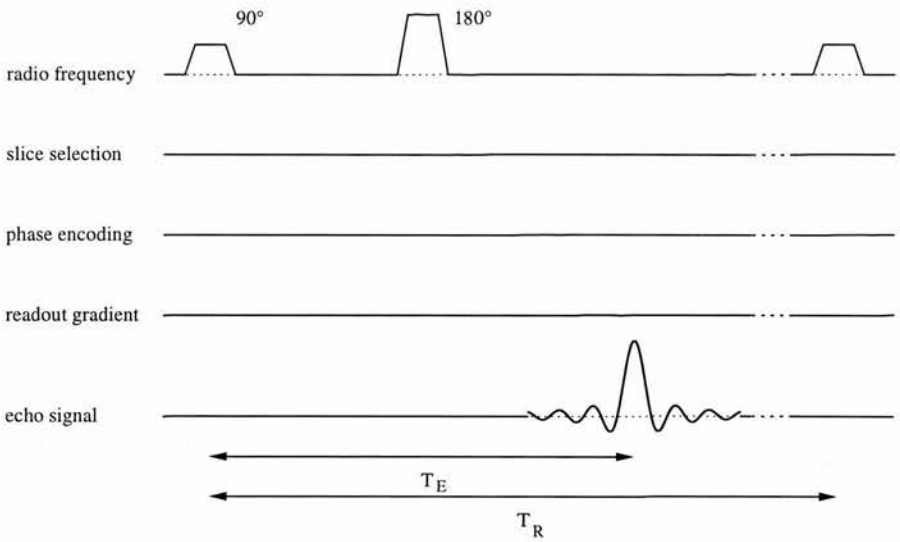

Figure 2.13.: *A spin echo NMR experiment. The RF pulses are not slice selective, yet. This experiment is repeated after T_R.*

Starting with the basic NMR experiment (Section 2.2.5, page 22) only the RF pulses and the readout interval are portrayed (Figure 2.13). The RF pulses are not marked as slice selective, yet. The area under the 180^o pulse is twice the 90^o pulse indicating twice the B_1 strength. This leads to a rotation of the bulk magnetisation through twice the angle for the 180^o pulse. Exactly after the time between the two pulses has elapsed again, the rephasing is accomplished, the echo is fully formed and the signal is acquired

during this period. The centre of the RF pulses is important for the calculation of the exact echo time T_E. This experiment will be repeated after a period T_R, the repetition time, during which the bulk magnetisation will relax.

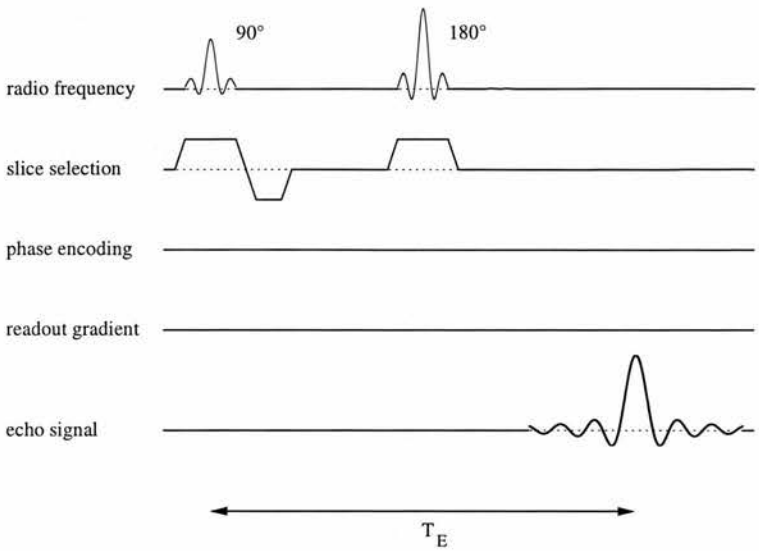

Figure 2.14.: *A spin echo experiment with slice selection gradients.*

In the next step (Figure 2.14), slice selection is added. The slice is chosen to be orthogonal to the z-direction: the slice normal points along the z-axis. Slice selective RF pulses are chosen during the application of a z-gradient. During the application of the slice selection gradient and the RF pulse, the spin isochromats gather a net phase shift that varies through the slice width. A small correction has to be applied at this point. A 90^0 pulse in conjunction with a gradient leads to a distribution of magnetisation in the x-y-plane. This can be compensated for by applying a gradient pulse in the opposite direction. The area of this pulse is the same as the gradient pulse from the centre of a symmetric RF pulse to the end.

To achieve spatial resolution in the next direction, frequency encoding is applied in the x-direction (Figure 2.15). In principle it would be enough to apply this pulse during the readout interval. This, however, leads to a phase shift that is compensated by the application of a gradient pulse, half the area of the readout gradient, before the 180^o RF pulse. This leads to an accumulation of phase in the x-direction that is then

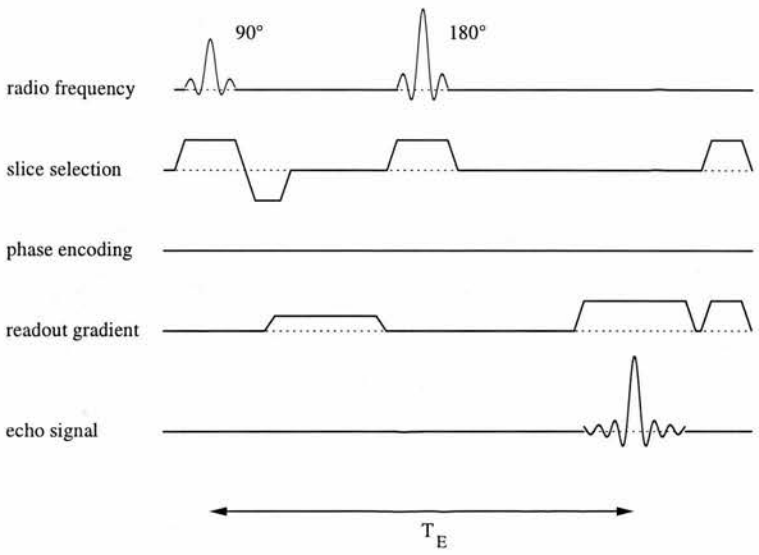

Figure 2.15.: *Spin echo MRI with slice selection and readout spatial encoding.*

mirrored by the 180^o pulse. At the point where the readout gradient is applied, the phase accumulation is inverted and all phases in this direction end up synchronised at the centre of the echo. This shifts the acquisition of the centre of k-space well away from the gradient pulse leading edge. Gradient pulses at the end of the sequence have been added to the slice and readout directions to dephase all unwanted transverse magnetisation before the sequence is repeated. These gradient or RF pulses are known as spoiler or crusher pulses.

Finally, phase encoding is added to achieve spatial resolution in the y-direction (Figure 2.16). The experiment has to be repeated with many different values for the phase encoding gradient. The repetition time T_R between two such experiments should be long compared to the echo time T_E to achieve relaxation of the spins back to a pseudo equilibrium state. The signal measured with a spin echo sequence depends on T_E, T_R and the tissue properties:

$$S = S_0 \cdot e^{-T_E/T_2} \cdot \left(1 - e^{-T_R/T_1}\right) \tag{2.27}$$

where S_0 is a constant.

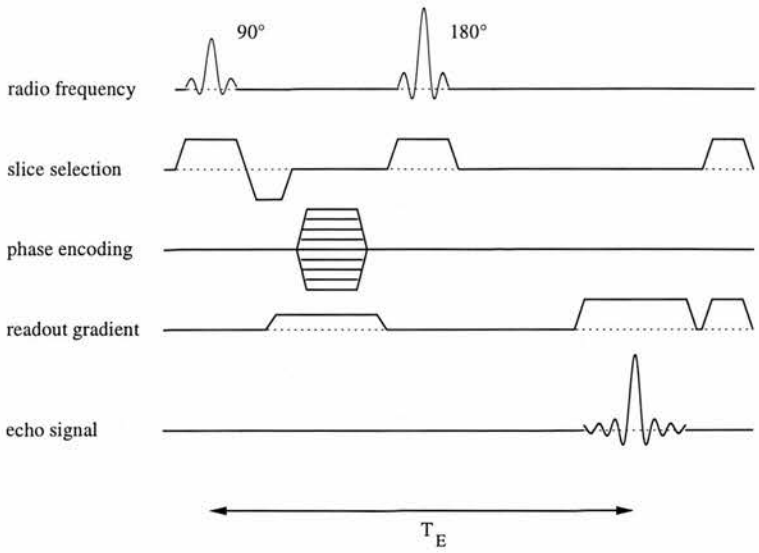

Figure 2.16.: *Spin echo MRI with slice selection, phase and readout spatial encoding.*

After the echo has been sampled, crusher gradients are used to dephase all the remaining net magnetisation in order to prepare the sample for the next excitation (Figure 2.16).

The choice of z-direction for slice encoding, y-direction for phase encoding and x-direction for frequency encoding are arbitrary. The three directions of space are obviously linearly independent. Consequently, the gradients are labelled slice-, encode- and readout-direction. This enables the acquisition of oblique and double oblique slices to improve visualisation of an organ in the body.

2.4.2. Gradient Echo

The gradient echo technique (Figure 2.17) uses a gradient pulse to dephase and subsequently rephase the magnetisation. The 180^o RF pulse used in the spin echo technique to rephase the spins is not applied. In spin echo experiments the rephasing due to the 180^o RF pulse and the gradient echo are timed to coinside. The gradient echo technique is faster and deposits less RF power in the patient. However, the 180^o RF pulse in the spin echo technique refocuses dephasing spins due to local field distortions. The signal in the gradient echo therefore decays with the shorter $T_2^\star$ rather than T_2.

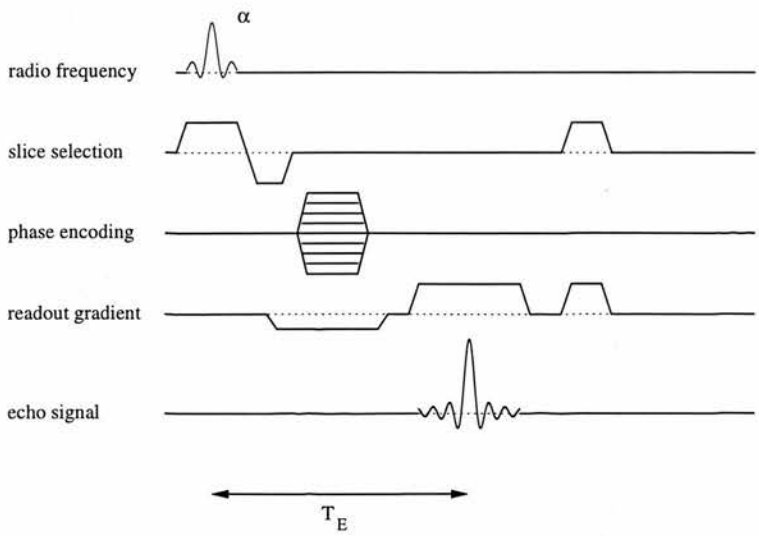

Figure 2.17.: *Gradient echo MRI with slice selection and phase and readout spatial encoding.*

Since the gradient echo technique does not use the time intensive 180° RF pulse the echo time T_E and repetition time T_R can be shorter. When T_R is chosen to be shorter than T_1 the magnetisation is left with insufficient time to relax between the successive excitations. This leads to a saturation of magnetisation and the detected signal is decreased. This can be avoided by using flip angles α of less than 90°. The signal S of a gradient echo sequence may be calculated as follows:

$$S = S_0 \cdot \left(1 - e^{-(T_R/T_1)}\right) \cdot e^{-(T_E/T_2^*)} \frac{\sin(\alpha)}{1 - \cos(\alpha) \cdot e^{-T_R/T_1}} \tag{2.28}$$

with S_0 the maximum possible signal. The signal can be maximised by choosing the Ernst angle:

$$\alpha_{ernst} = \cos^{-1}\left(e^{-T_R/T_1}\right). \tag{2.29}$$

2.4.3. 3D Acquisition

By adding an additional phase encoding table, the pulse sequence can be extended to a 3 dimensional acquisition. Since the gradient echo sequence is faster this is usually

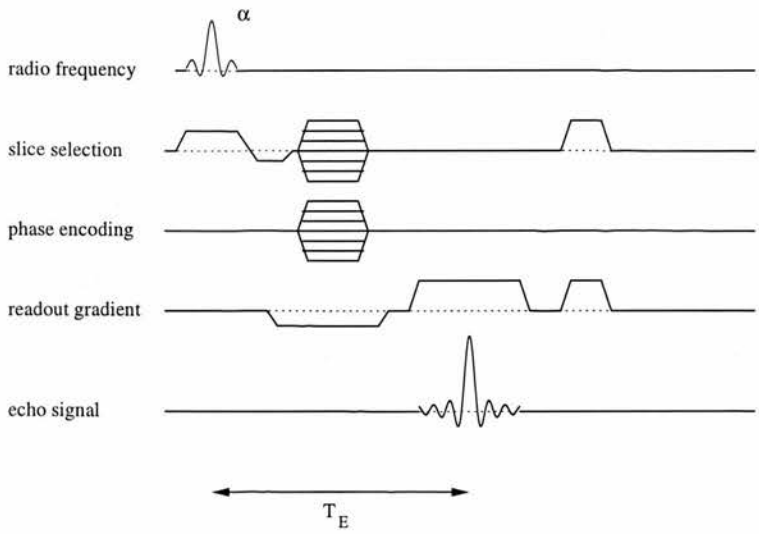

Figure 2.18.: *3D Gradient echo MRI with slice selection and readout spatial encoding. Two phase encoding tables allow for encoding in two dimensions.*

chosen for 3D acquisitions, as seen in Figure 2.18. With this method the selected slab is rather thick and spatial resolution within that slab is achieved by the second phase encoding table. Since the signal of the entire slab is collected, the signal to noise ratio improves over the acquisition of separate slabs. This allows for the acquisition of thinner slices and the data can be resliced in arbitrary directions retrospectively.

2.4.4. Contrast in MR Images

The signal intensity, using spin echo sequences (Eq. 2.27), depends on T_E and T_R which are set during the acquisition, and also T_1 and T_2 that are given by the tissue sampled. Some typical values of T_1 and T_2 are given in Table 2.2.

Choosing a T_E shorter than any T_2 relaxation times of the tissues and a T_R between the T_1 times of two tissues in a region of interest, the T_1 of tissue is the parameter with the main influence on the signal intensity. Small changes in T_1 lead to large changes in image intensity and this case (short T_E and short T_R) is therefore called T_1-weighting (Figure 2.19 (a)).

Tissue	T_1 in ms	T_2 in ms
Brain: grey matter	810	101
Brain: white matter	680	92
Muscle	730	47
Heart	750	57
Liver	420	43
Kidney	590	58
Fat	240	84
Blood	1300	185
Water	3000	1400

Table 2.2.: *T_1 and T_2 relaxation times for a variety of tissues at 1 T [Kol96].*

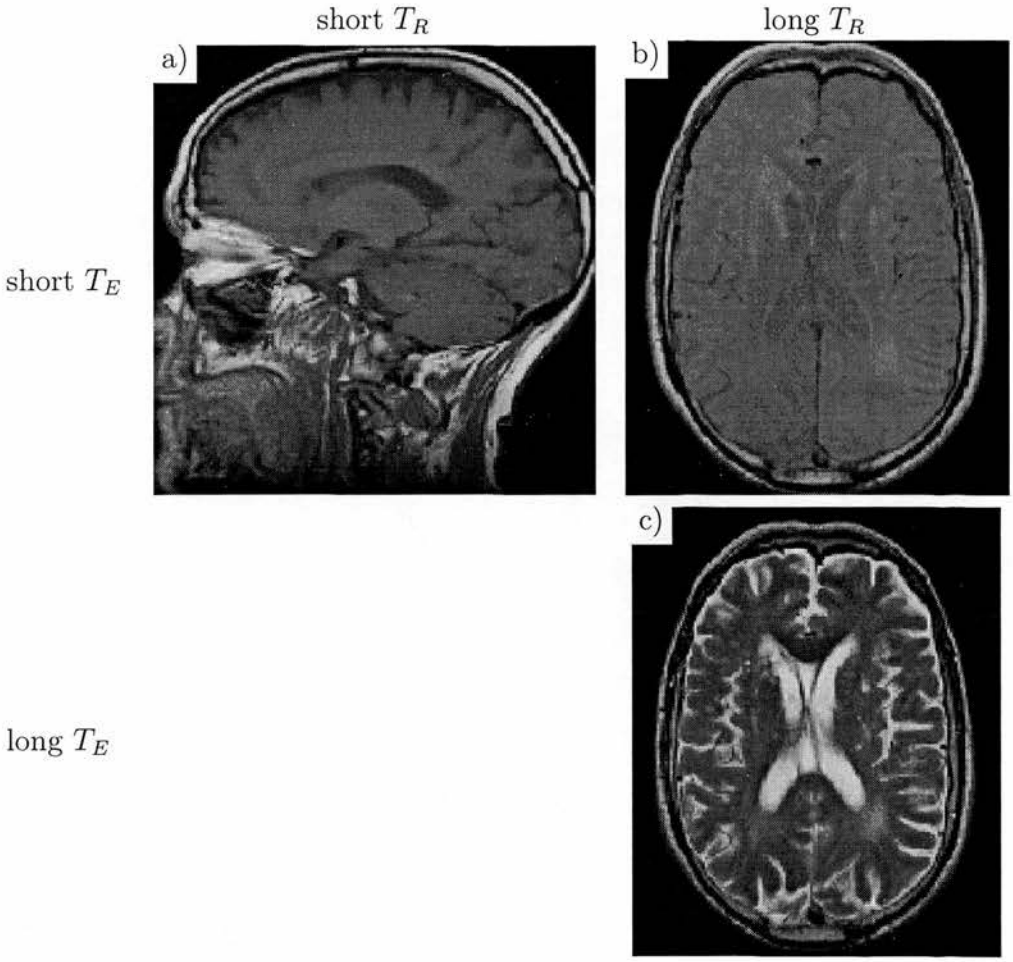

Figure 2.19.: *Examples of the different types of image contrast possible using MRI techniques showing: a) T_1-weighted sagittal image, b) Proton density axial image and c) T_2-weighted axial image.*

Choosing a long T_E and a long T_R, however, allows the spins to relax completely between repetitions and T_1 has a small influence on the signal intensity. If T_E is comparable to the T_2 of the tissues under investigation, good contrast that depending on T_2 is achieved (T_2-weighting) (Figure 2.19 (b)).

With a short T_E and a long T_R the constant S_0 in the formula (Eq. 2.27) becomes the most important factor. This constant depends mostly on the density of spins in the sample and the contrast achieved is proton density-weighting (Figure 2.19 (c)). Similar rules apply to gradient echo sequences. However, since no 180^o RF pulse is used for refocussing, a $T_2^\star$ contrast is achieved.

2.4.5. Image Artefacts

One source of image artefacts is the aliasing of information outside of the FOV into the image. The main reason for this is the limit imposed by the discrete sampling of the signal (Section 2.3.5, Eq. 2.26). In general this occurs when the FOV is smaller than the sensitive area of the receiving coil. Spins outside the FOV produce a signal and in the direction of the phase encoding these signals will have a phase outside the 2π region. Due to the cyclic nature of the phase, this is projected back into the 2π region. These signals appear folded back into the image. In the frequency encoding direction the restriction of the FOV corresponds to a limit of receiver bandwidth. These frequencies are still present in the signal and are projected back when the sampling rate is too low.

In the frequency direction the sampling rate can be doubled and the surplus data points are ignored after Fourier transform. This can be done without lengthening the acquisition time or degrading SNR. The same approach can be taken in the phase direction for 2D as well as 3D acquisitions. In this case, however, there is a significant time penalty, since the acquisition has to be repeated for every extra line or slice. Due to the larger excited volume, the increased SNR will improve the resulting images.

Another class of artefacts is due to movement of the imaging object, i.e. breathing motion or blood flow. The frequency and phase encoding direction will show different effects in this case. In the frequency encoding direction the image will be blurred with the extent of the movement. However, the phase encoding direction demonstrates a wide distribution of the moving contours along the phase direction (ghosting). Depending

on the timing of the movement the phase information of the signal is distorted and the unique relation between location and phase is destroyed.

It is best to avoid all movement during acquisition of MRI data. In cases where this is impossible, the moving part can be selectively saturated and thereby prevented from contributing to the signal. For cardiac and breathing motion, a gating approach can be adopted, where the acquisition is restricted to periods with little, or no, movement. This can be done prospectively for cyclic motion once the pattern is known. Data is only sampled during a certain time after a trigger pulse is detected. The other approach is to sample continuously and record the trigger timing. The data can then be reordered retrospectively. This approach usually takes longer, but it is more robust and will cover the cardiac cycle completely.

Ferromagnetic materials introduce a strong artefact in the images. These materials significantly distort the local magnetic field making any imaging in their proximity impossible. A smaller effect can be introduced at interfaces of materials of differing susceptibility μ_r. This has been ignored, since its value is about 1 for most materials. Some sequences are sensitive to the distortion introduced in the phase information due to the small change in magnetic field at the interface.

2.4.6. Contrast Agents

Contrast agents in MRI provide another possible contrast method. Intravenous agents make up the majority of agents in clinical practice today. They work by shortening T_1 locally. This is achieved by metal ions with one or more unpaired electrons that are chemically shielded to prevent poisoning the patient. Unpaired electron spins couple to the spins of protons via a dipole interaction. This interaction leads to a relaxation of the proton spins in the vicinity of the metal ion. The electron spin is left unchanged by the interaction and can cause further spins to relax as a catalyst. Therefore the metal ions work as a relaxation sink for the water protons. As mentioned in section 2.2.4 (page 17), T_1 relaxation depends on the "lattice" absorbing the energy. In the presence of contrast agents, all water molecules diffusing into the vicinity of the metal ions will relax faster. This diffusion process is rapid and the dosage of contrast agent needed is low. A specific use for contrast agents is discussed later in section 3.2.1.

3. MRI and Flow

3.1. Historical Outline and Methods

The detrimental influence of blood flow on conventional magnetic resonance imaging (MRI) was noticed very early in the development and techniques to suppress this artefact were consequently established (Section 3.3.4, page 53). A historical outline of the use of phase shifts in MRI to measure flow has been published [FNKL90, PSL+94].

A phase shift in the nuclear magnetic resonance (NMR) signal due to slow coherent motion (flow) was noticed as early as 1954 [CP54]. That effect was used to present a blood flow meter based on nuclear magnetic resonance [BK59] and to introduce a phase shift to the signal of flowing sea water [Hah60]. Along with other methods in NMR, further improvements of flow measurement utilised the use of pulsed gradients for diffusion measurements in 1965 [ST65] and was subsequently applied for the pipeline industry in 1968 [Bat68]. Subsequently gradient pulses and phase differences were utilised for velocity phase mapping [BPFL84] (1984). In 1971 [GS71] and 1974 [Gar74] an alternative technique was developed with a gradient applied in the flow direction and a Fourier analysis of multiple spin-echo signals to give a plot of the velocity distribution.

The development from these non imaging studies to MRI velocity experiments concentrated on the effect of flow on the signal intensity (magnetic resonance angiography –

MRA) rather than its phase. Only in 1982 was it suggested to introduce bipolar velocity phase encoding pulses to the three axes of a standard spin echo imaging sequence [Mor82]. Several methods based on the phase shift induced by flow were subsequently presented.

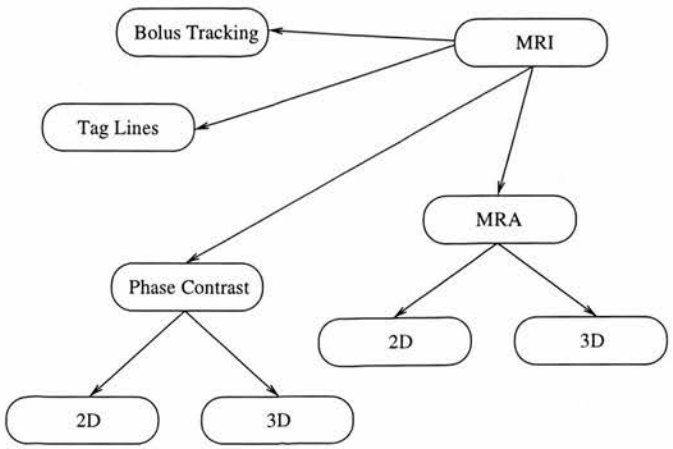

Figure 3.1.: Some of the methods developed to analyse flow using MRI

Magnetic resonance imaging is inherently non-invasive and 3 dimensional. No tracers or probes have to be inserted into the flow and therefore the velocity field can be studied undisturbed. Flow fields, like other vector fields, are six dimensional (three location dimensions and three dimensions for the vector field) or even seven dimensional in the case of time-varying fields. Methods like Doppler ultrasound and laser Doppler anemometry conventionally allow access to a subspace of the complete vector field. However, full acquisition methods have now been developed.

A variety of methods have been developed to study flow using MRI (Figure 3.1) and these are subsequently described. However, only MRA and to a limited extent phase contrast MRI have found a place in routine clinical practice. MRA is the standard tool to visualise vasculature, while PC MRI is the only method that allows reliable flow quantification.

Phase Mapping – Phase Contrast MRI: Phase mapping techniques were demonstrated twice in 1984 [Dij84, BPFL84]. These methods were more useful clinically,

partly because of the use of gradient echo sequences [YBP86, RS86] and, most importantly, because of the introduction of velocity-compensated gradient waveforms [NFL86]. The improvements enabled the sequence to be repeated rapidly and prevented the characteristic signal loss due to shear flow when uncompensated gradient waveforms were employed (Section 3.3.2). The technique has been validated *in vivo* [FNK+87] and has provided useful information in clinical and physiological flow studies [UFK+87, KFU+87]. The bipolar velocity encoding gradient pulse has been combined with several standard imaging sequences, but the most promising for the examination of pulsatile flow is the gradient echo sequence because of its relatively high speed and low number of artefacts. Since the present project is mostly concerned with this method, it will also be described in detail below (Section 3.3).

Fourier Flow Analysis: The use of several flow encoding steps was first demonstrated in 1984 [RNJH84]. Only those parts of the image that contain a certain velocity were shown and the combination of several steps allowed the mapping of the velocity distribution for each pixel. Although the technique was improved in 1986 [FCS+85], 1988 [HMBF88] and 1991 [DSHA91], it is not widely used, since it takes a relatively long time to acquire the images. One image is required for every velocity step. The major advantage of this method is the absence of signal loss in turbulent flow regions and the measurement of velocity distributions in a pixel.

Alternatives using Phase Information: A method based on a string of 180^o pulses was described in 1984 for non-spatially resolved measurement of flow in plant stems [ASJK84]. Another method that depends on the dependence of the signal magnitude on the phase shift was suggested in 1986 [DH86]. A constant signal from flowing blood would be essential for this method to work.

Bolus Tracking: The principle is essentially similar to colour, heat or nuclide bolus tracking methods [Mat82, Kon96], but with improved spatial and temporal resolution. A volume of fluid (bolus) is marked and its progress through the vessel is then monitored. The MRI method selectively excites a bolus of spins. This method produces intuitive flow information, but the edges of the tracked bolus appear indistinct and the only quantitative information that can safely be extracted is

the total flow [FCS+85, SMS+86, EMKS89]. A typical procedure employs a bolus of presaturated spins that is tracked using a FISP (rapid gradient echo) pulse sequence [EMKS89]. The vessel will normally be imaged in plane. Only the bolus of spins excited in an orthogonal plane will contribute any signal in the imaging plane.

Tag Lines: In the tagging method, sample magnetisation is nulled in an orthogonal grid pattern using the DANTE technique, prior to imaging [MF78]. This grid appears in the form of black lines on the image. A delay between the preparation and imaging sections is incremented during a series of measurements [NGD+97]. This permits the distortions of the grid with time to be observed.

Magnetic Resonance Angiography (MRA): This technique is also known as a time of flight method, since it is based on spins flowing in and out of the imaging plane. This partial or complete exchange of spins in the imaging plane has a drastic influence on the magnitude of the signal. The slice orientation in MRA is generally orthogonal to the vessel. Since the method is well established in clinical applications and provides valuable information on regions with flow present, it will be described in a little more detail below (Section 3.2).

3.2. MR – Angiography

For spin echo sequences, the spins need to receive both the 90^o and the 180^o pulses to form an echo and hence produce a signal. During the period of time between the excitation and the 180^o pulses, flowing blood moves from the imaging plane and is replaced with unexcited spins (Fig. 3.2 a, b and c). This phenomenon occurs with various standard sequences and is routinely applied in clinical practice. However, the signal intensity is difficult to predict, since it depends on a number of factors ([BS95, Chapter 10]). If the blood is replaced with spins that have yet to be excited, the intensity will decrease up to a maximum velocity, when all the blood is replaced. Flowing blood will therefore give a lower signal than stationary tissue. This is the so-called "black-blood„ technique.

Saturation of spins with a number of pulses generally leads to lower signal intensity. If the surrounding tissue is saturated, the inflowing blood which is unsaturated gives a

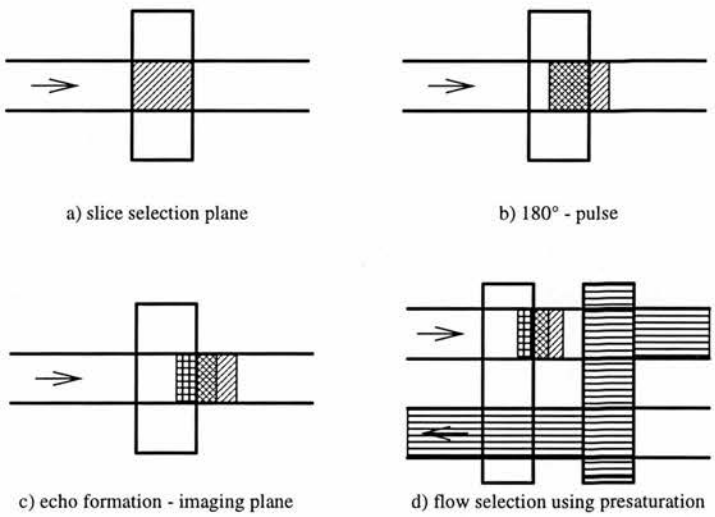

Figure 3.2.: *The basic time-of-flight experiment. During slice selection a bolus of blood is marked (a). This bolus moves during the time period leading to the 180° pulse and only part of the bolus receives both pulses (b). By the time the echo is formed, part of the bolus of excited spins has left the slice (c). Using a presaturation plane, one flow direction can be suppressed (d).*

higher signal than the surrounding tissue. This is the basic principle behind "white-blood„ time of flight MR Angiography. Saturation can also be used to suppress one flow direction, by decreasing the signal from blood flowing in one direction. A saturation plane is placed close to the imaging plane on one side (Fig. 3.2 d) to achieve this effect.

Using computational fluid dynamics (CFD) a better understanding of the signal intensity of complex flow patterns has been achieved [JvTBS96], but the computing time needed for such intensive calculations renders it impractical for everyday use. A study has compared phantom images of stenotic flow with CFD for pre- and post-stenotic flow [SOPK95, SOPK96, SOPK97], with good agreement. The method gives an intuitive representation of flow that can be acquired quickly, but for quantitative studies, the relationship between signal intensity and velocity is prohibitively complex.

With an analytical approach, the signal dependence from both laminar and plug flow on spin echo parameters has been calculated [GSW88]. This allows optimisation of the sequence parameters to achieve good results with a simple model.

3.2.1. Contrast Enhanced MRA

Intravenous contrast agents injected as a bolus change the T_1 of the blood (Section 2.4.6). This bolus of blood with short T_1 travels to the heart and from there through the arteries in the body. Due to the short T_1, this bolus of contrast agent demonstrates a high intensity when compared to the saturated background of stationary tissue. This effect is independent of the motion of the blood and is therefore less influenced by intra-voxel dephasing in areas of turbulent flow, so called flow voids. Timing the acquisition of the centre of k-space correctly, the arterial phase of contrast arrival can be distinguished from the venous phase where both kinds of vessels show up brightly. This method [PYK+93, Pri94], although more expensive due to the cost of the contrast agent, is reliable and is now established as a routine clinical tool.

3.3. Velocity Measurement using MRI: Phase Contrast

3.3.1. Basic Principle

Comprehensive introductions to the principle of phase contrast MRI include [PSL+94, FCS+85, NFL86, SPL+90, NGD+97, O'D85, PLEO96]. These articles introduce the basic principles and deal with the design of pulse sequences, problems with flow integration and various applications of the technique.

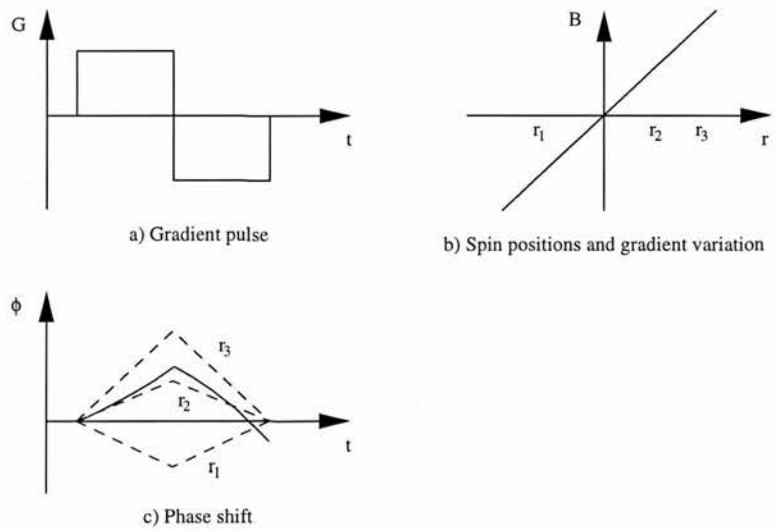

Figure 3.3.: *Phase shift with bipolar gradient lobe. The influence of a bipolar gradient lobe (a) on spins at the following positions in relation to its spatial orientation (b) is shown in graph (c). The static spins r_1 to r_3 gather no net phase shift (dashed lines), unlike spins moving form r_2 to r_3 (solid line).*

As mentioned in the introduction, phase contrast MRI is based on the effect that stationary spins do not gather any net phase shift under the application of a bipolar gradient pulse, unlike spins moving in the direction of the gradient (Figure 3.3). A bipolar gradient pulse with no net area is applied in the velocity encoding direction and varies linearly in space (a). Under the influence of the bipolar gradient lobe the three static spins at positions r_1 to r_3 are left with no net phase shift. Spins moving from r_2 to r_3 during the application of the gradient pulse, however, gather a net phase shift.

The frequency offset of spins under an arbitrary gradient $G(t)$, moving position $r(t)$ in the direction of G at time t is $\gamma G(t)r(t)$. The phase shift at the echo time T_E results from integration (Eq. 2.22)

$$\phi = \gamma \int_0^{T_E} G(t)r(t)dt.$$

For first order motion, i.e. $r = vt$, and a gradient pulse with zero net area, e.g. a bipolar lobe, this simplifies to

$$\phi = v(\gamma M_1) \tag{3.1}$$

with the first moment of the gradient pulse given by

$$M_1 = \int_0^{T_E} G(t)tdt. \tag{3.2}$$

Since many other processes, e.g. eddy currents, field inhomogeneities and pulse sequence tuning, influence the phase of the spins, subtracting two phase images recorded with different first moments should leave only the influence of motion.

$$\Delta\phi = v(\gamma \Delta M_1). \tag{3.3}$$

Applying a velocity encoding gradient in three different (preferably orthogonal) directions and subtracting each from an acquisition without flow encoding allows measurement of the complete vector field with all its components.

Two main choices of bipolar lobes can be found. The first method inverts the velocity encoding gradient pulse to acquire two images with different first moments. The second acquires images with and without velocity encoding. In addition, the latter version produces a standard magnitude image. This is the simple PC gradient echo pulse sequence reproduced in Fig. 3.4. Here, the solid lines represent the standard gradient echo pulse sequence and dashed lines show the changes necessary in all three directions to add a bipolar lobe for first order velocity phase encoding. The sequence is flow compensated to avoid ghosting of the signal originating from flowing spins. One acquisition is needed for every velocity component examined in addition to a reference scan.

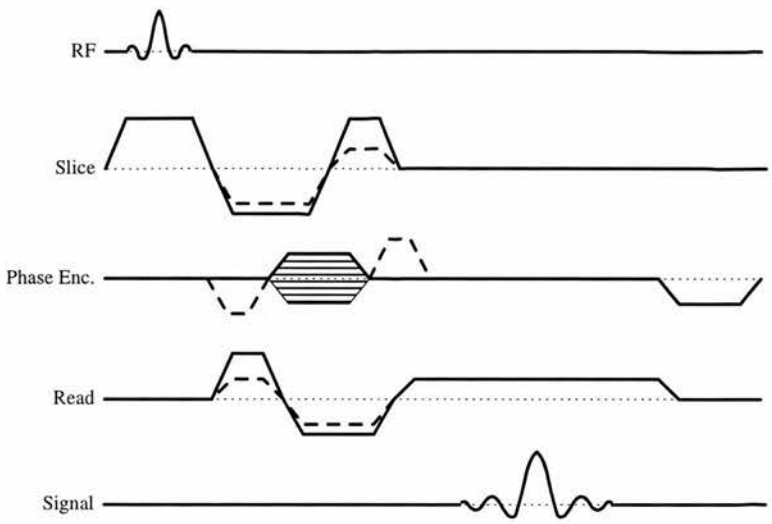

Figure 3.4.: *Gradient echo phase contrast pulse sequence based on the gradient echo sequence presented in Fig. 2.17. The solid lines represent the sequence without velocity encoding. First order velocity encoding is presented for all three directions by dashed lines.*

The cyclic nature of the phase leads to a problem called phase wrapping. The velocity is not an unambiguous function of phase. Basically, velocity is uniquely defined only in a window of 2π. This window need not be symmetric around zero phase shift, but it can take any value (Section A.4.3). For an ensemble of velocities which are dominant in one direction this approach can increase the dynamic range. The ambiguous nature of the phase leads to the introduction of the maximum velocity $v_{enc} = \pi/(\gamma \Delta M_1)$ which aims to limit the range of phases recorded to 2π. The interpretation of the maximum velocity can be confusing in the light of asymmetric windows and for phase unwrapping. The change in phase per change in velocity is a much better parameter to describe the correlation.

3.3.2. Artefacts in Phase Contrast Data

Apart from phase wrapping, which has been described earlier, other artefacts may appear in images acquired with phase contrast methods.

Misalignment of Flow Encoding

For the measurement of the velocity field using three flow encoding directions, the alignment of the slice or slab with the vessel is of very little importance. In clinical practice, however, PC MRI is often used to measure volume flow rate in a vessel. For this purpose, a slice orthogonal to the vessel is chosen and the velocity is only measured in the slice direction. It turns out that the errors of a misalignment of the slice and the vessel cancel each other. The velocity is proportional to the cosine of the angle between the vessel and the surface normal of the slice, while the area is inversely proportional. For the volume flow rate these two values are multiplied and the effect cancels out. The angle should be as low as possible when considering noise in the image. A velocity error is associated with every velocity measurement and the total error is minimised for a low number of pixels across the vessel. Another important argument for a low angle between the surface normal of the slice and the vessel is that of signal intensity discussed below.

Partial Volume Averaging of Flow Data through the Slice

The contribution of isochromats to the signal from a voxel is based on a vector addition and can lead to distortions called partial volume effects. So far, it was implicitly assumed in this text that the isochromats adding up to the signal from a voxel all have the same signal magnitude and just differing phases. In that case, the measured phase difference is equal to the average of the contributing phases and will represent the average velocity in the voxel. This assumption is fulfilled for voxels with a narrow velocity distribution. However, for larger voxels the velocity distribution might be large enough for the magnitude signal to depend significantly on the velocity of the spins. Significant partial volume effects are also evident in voxels with a mixture of stationary and moving isochromats. The stationary spins are saturated and contribute a low signal with no phase shift. In contrast, the moving spins have a higher magnitude signal and in the voxel average these is dominant. In general, the velocity in voxels containing contributions from the vessel wall is overestimated. The best method to overcome this problem is the reduction of voxel size.

Another area where this effect becomes important is in regions of turbulent flow. A wide and often unsteady distribution of velocities is found in these voxels. This can lead to a

complete destruction of the phase coherence for that voxel and the signal in this voxel is reduced during reconstruction. This effect is not only visible for PC MRI, but also in MRA.

In the carotid arteries flow voids appear in regions downstream of stenotic disease. This can make diagnosis quite complicated for the clinically significant value of 70 % stenosis, though the presence of a flow void can be used as a vital diagnostic indication. Since contrast enhanced MRA does not depend on moving spins, this effect poses less of a problem for this technique.

Misregistration Effects

As the spins move during the period between the different encoding pulses, the correlation between their location and the encoding is distorted. Hence, the blood might be positioned incorrectly in the reconstructed images. Two problems result from this: first, the blood signal cannot be compared with features from stationary tissue because it might be positioned incorrectly and, second, if the signal from blood is misregistered into regions with contributions from stationary tissue it leads to an additional partial volume effect. A comparison between geometric parameters of the flow in question from acquisitions, with and without flow (a technique easily achieved for phantoms), must be treated with caution.

Phase Errors Due to Higher Order Motion

The fundamental relationship between signal phase and velocity (Eq. 3.1) was derived from the general expression (Eq. 2.22) for constant velocity ($r = vt$). A more general approach could be based on a Taylor series of the displacement:

$$r(t) = r(0) + r'(0)t + r''(0)t^2/2! + \cdots + r^{(n)}(0)t^n/n!. \tag{3.4}$$

The phase subtraction employed normally in PC MRI, however, removes most of the error resulting from the acceleration because the phase shifts introduced in the encoded and unencoded sequence are similar. For time resolved studies, problems might occur for interleaved acquisitions of encoded and reference acquisitions. The difference is not really between coincidental signals and acceleration will affect the result.

Signal Loss

There is a strong correlation between complex signal magnitude and phase. Obviously, the phase of a signal with no magnitude is indeterminate and the error in the phase measurement decreases with signal magnitude. In detail, it depends on the values for the components of the complex measurement. As a consequence, the signal intensity of flowing spins in phase contrast studies should be maximised.

In 3D PC MRI studies, the inflowing spins are subjected to a number of RF pulses on their progress downstream. This leads to an increasing saturation of the flowing spins and consequently signal loss. The choice of T_R and T_E (Section 3.3.3) can help to minimise this effect.

In-plane flow in 2D PC MRI acquisitions show no inflow effect, since the flowing spins are already saturated, and therefore possess a low signal. An exception is spins entering the FOV from outside the excited volume. The slice should consequently be orientated orthogonal to the vessel of interest wherever possible.

Intra-voxel phase dispersion in turbulent flow regions and regions with high shear (high spatial change of velocity) destroy the phase coherence and the signal is reduced during image reconstruction. The use of a symmetric gradient waveform [FNKL90] minimises the effect of odd order motion on the signal without increasing T_E. Choosing the shortest possible echo time minimises the effect of the even order derivatives.

3.3.3. Guidelines for PC MRI

Concentrating on 3D acquisitions, a number of guidelines can be given to improve the quality of the data set. To minimise partial volume effects at the vessel wall, the voxel size should be as low as possible. This also minimises intra-voxel dephasing due to velocity distributions within the vessel. However, the desire to minimise the voxel size has to be balanced against acquisition time and SNR. Intra-voxel dephasing is also reduced by minimising T_E, with the side effect that the misregistration is reduced. T_R and the flip angle have a major influence on the contrast between stationary tissue and flow. A short T_R and high flip angle increase the saturation of stationary tissue and increase the flow signal relative to background ratio for *in vivo* acquisitions. However,

the inflowing spins are saturated faster. This leads to a downstream signal loss in the flow. For the *in vitro* phantoms this does not pose a problem, since the flow is usually surrounded by material that does not give any signal (e.g. plastic and air). Loading the coils with additional saline bags can improve the signal to noise ratio for *in vitro* acquisitions. In these cases a flip angle of 22^o and a long T_R gave the best results at the price of very long acquisition times. For *in vivo* studies a flip angle of about 25^o and the shortest possible T_R produced the best results.

3.3.4. Consequences for Sequence Design

Since it is important that the basic pulse sequence is insensitive to flow, in order to get a good magnitude signal that defines the phase, the theoretical considerations on the suppression of flow artefacts are very important [MB92]. The theoretical approach to the influence of sequence parameters, in a spin-echo acquisition, on the signal magnitude from flowing spins [GSW88], is helpful in understanding the appearance of different flow types. Additional methods to improve the acquisition with MRA pulse sequences have been discussed (Section 3.2, page 46).

Detailed analyses of the influence of gradient parameters on phase contrast MRI have been presented [PLEO96, KHS95]. These include a detailed analysis of the influence of the gradient form on the phase shift. Gradient echo sequences utilising even echo rephasing to avoid signal loss due to higher order motion have been designed [NFL86].

There are conflicting aims in pulse sequence design: the pulse shape should be symmetrical to minimise effects of even order derivatives of displacement, but the first moment of the gradients should be nulled to minimise flow artefacts. Overall the echo time should be kept as short as possible. For steady flow, aliasing from flow artefacts should be relatively small and for low flow rates regions of turbulent flow should remain small. This leads to a basic implementation of the PC MRI sequence for work with steady flow phantom. For high resolution *in vivo* studies, the total acquisition time dictates a short T_R and T_E. This does not allow the optimisation of the pulse sequence except the overall length.

Another complication is the introduction of concomitant, or Maxwell, gradient terms. Whenever a desired linear magnetic field gradient is activated, additional magnetic fields

with non-linear spatial dependencies result. This is a consequence of the Maxwell equations for the divergence and curl of the magnetic field [MHJ97, BZKG97, KGZB97, BZP+98]. It has been shown that this effect is minimised for PC MRI by avoiding overlap between velocity encoding and other gradient pulses. The effect of the other gradients on the velocity measurement is eliminated when the phase difference is taken. Fast gradient edges, however, cause eddy currents. These can distort the velocity measurements and should be avoided.

In general, the design of the pulse sequences should try to achieve the following aims: the underlying imaging sequence should be flow compensated as in Figure 3.4 and the sequence has to be fast to avoid trouble with misregistration artefacts and the pulsatility of the flow.

4. Flowing Fluids: Hydrodynamics

4.1. Introduction

Classical mechanics deals with infinitesimally small points of finite mass and their combinations in ideal solids. These ideal solids do not deform under applied forces. Real materials, however, are readily deformed when forces are applied. The nature of the deformation is quite different for the two classes of deformable material investigated in this chapter: solids and fluids (including gases). A fluid is a substance which may flow; that is, its constituent elements may easily change their positions and their neighbours. Moreover, the constituent elements offers no lasting resistance to their displacement, however great, of one layer over another. In a resting fluid no shear forces (forces tangential to a surface) exist. A solid, however, can resist shear forces. As a result, a solid can maintain its overall form under external forces while a fluid will always fill the bottom of its container. This distinction, although it might sound clear, is not always distinct for substances that show abnormal behaviour (e.g. non-linear elasticity and high viscosity). The theory derived in this chapter is valid only for a linear approximation with small relative displacements (linear deformation). Under these simplifying assumptions the distinction is clearly made.

Dealing with a large number (10^{23}, Avogadro's constant) of particles brings a number of conceptual difficulties. The concept of looking at an infinitesimally small point makes no sense given the make-up of molecules or atoms. It is completely impractical to derive the behaviour of every particle for a material of any considerable size. More commonly the detailed behaviour of a single particle is unimportant and average properties convey the desired information. This leads to the introduction of a small unit volume. This is small enough to be considered homogenous but sufficiently large to average the contributions of individual particles. The local form of continuum mechanics used in this chapter has to be understood against the background of this small unit volume.

Throughout this chapter vectors will be indicated by the parameter with a single subscript or an arrow above the parameter i.e. $(x_i, \vec{x})$ and tensors (matrices) are indicated by further subscripts or an underline per level of the tensor e.g. $(a_{ij}, \underline{a})$.

Like classical mechanics, the theory is independent of the coordinate system chosen. This means that all the formulae presented, including any derivatives, have to be transferred into the desired coordinate system before their application. At the end of the chapter (sections 4.4.3 and 4.5) concrete examples of this transition are presented. The location vector $\vec{r}$ will be used as either $\vec{r} = (x_1, x_2, x_3)^c$ or $\vec{r} = (x, y, z)^c$. Here, the $()^c$ operation transforms a row vector into a column vector. The first version is better for summations and avoids the misconception of a Cartesian coordinate system. The second version, however, is often easier to understand in complex formulae. In analogy, there are two representations of the velocity vector: $\vec{v} = (v_1, v_2, v_3)^c = (u, v, w)^c$. Many calculations in multi-dimensional spaces involve several levels of summation over the same indices. To simplify the formulae Einstein's summation convention is used. It assumes that, if a subscript appears twice in a variable or across a product of variables, then summation is implied over that subscript in its range. For example, under this convention:

$$\begin{aligned} A_{ij}B_{jkl} &\equiv \sum_j A_{ij}B_{jkl} \\ u_i v_i &\equiv u_1 v_1 + u_2 v_2 + \cdots + u_N v_N \\ A_{ii} &\equiv A_{11} + A_{22} + \cdots + A_{NN} \equiv \mathrm{tr}\,\underline{\underline{A}} \end{aligned}$$

with tr the trace (tr) of a matrix. The vector or matrix nature of an expression is determined by the number of its free indices, that is, the indices that appear only once. For example, $A_{ij}U_j$ is a vector, whereas $u_i u_j$ and $u_i A_{ijl}$ are two dimensional matrices.

Standard introductions to continuum and fluid dynamics are [vMF71, Poz97, MWS98]. A second year theoretical physics lecture by Dr. Mayer zur Capellen, Universität-GH Paderborn, Germany was also used as a basis for this chapter.

4.2. Deformation Theory

4.2.1. Linear Deformation

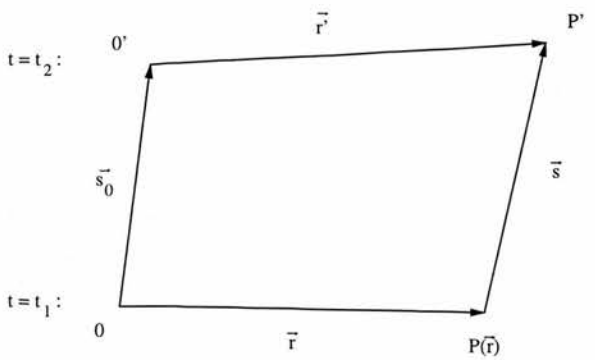

Figure 4.1.: *First order deformation: definition of terms.*

To understand the physics of deformable materials and the movement of fluids, a different approach to classical mechanics has to be adopted. Under the influence of a force, individual points of the sample will experience a translation $\vec{s}$ from P to P'. For closely related points this results in the situation illustrated in Figure 4.1 with a translation of the origin $\vec{s}_0$ from O to O', or mathematically:

$$\vec{r}\,' = \vec{r} + \vec{s} - \vec{s}_0. \tag{4.1}$$

Using the Taylor series of a general function $\vec{f}$ [BS79]

$$\vec{f}(\vec{r}) = \sum_{n=0}^{\infty} \left. \frac{\vec{r} \cdot \nabla^n \vec{f}}{n!} \right|_{\vec{r}=O} \tag{4.2}$$

and neglecting second and higher order terms leads to the linear approximation:

$$\vec{f}(\vec{r}) = \vec{f}(\vec{0}) + (\vec{r} \cdot \nabla)\, \vec{f}\,\big|_{\vec{r}=O} . \tag{4.3}$$

For $\vec{f} = \vec{s}$ this results in a linear deformation:

$$\vec{s} = \vec{s}_0 + (\vec{r} \cdot \nabla)\, \vec{s}\,|_O . \tag{4.4}$$

Defining the translation tensor $\underline{\underline{a}}$ such that $(\vec{r} \cdot \nabla)\vec{s} = \underline{\underline{a}} \cdot \vec{r}$ with $a_{ij} = {}^{\partial s_i}/_{\partial x_j}|_O$ and leaving out the argument (in the present case O), equation 4.4 simplifies to:

$$\vec{s} = \vec{s}_0 + \underline{\underline{a}} \cdot \vec{r}. \tag{4.5}$$

Every second degree tensor can be split into a symmetric and antisymmetric contribution:

$$a_{ij} = \frac{1}{2} \underbrace{(a_{ij} - a_{ji})}_{antisymetric} + \frac{1}{2} \underbrace{(a_{ij} + a_{ji})}_{symetric} = \phi_{ij} + \epsilon_{ij}$$

leading to

$$\vec{s} = \vec{s}_0 + \underline{\underline{\phi}} \cdot \vec{r} + \underline{\underline{\epsilon}} \cdot \vec{r}. \tag{4.6}$$

The first term on the right hand side of the equation describes the translation, the second the rotation and the last the deformation. The tensor $\underline{\underline{\epsilon}}$ is known as the deformation tensor with components $\epsilon_{ij} = {}^1/_2 \left({}^{\partial s_i}/_{\partial x_j} + {}^{\partial s_j}/_{\partial x_i}\right)$.

Defining the vector $\vec{\varphi}$

$$\vec{\varphi} := \begin{pmatrix} -\phi_{23} \\ \phi_{13} \\ -\phi_{12} \end{pmatrix} \tag{4.7}$$

the rotation becomes

$$\underline{\underline{\phi}} \cdot \vec{r} = \vec{\varphi} \times \vec{r} = \frac{1}{2} \nabla \times \vec{s}. \tag{4.8}$$

The diagonal elements ϵ_{ii} of the deformation tensor $\underline{\underline{\epsilon}}$ describe the change in length of a sample under an arbitrary force while the off-diagonal elements $\epsilon_{ij}(i \neq j)$ describe the shearing of the sample. The volume dilatation can be derived from the deformation tensor, such that: $V = V(1 + \mathrm{tr}\,\underline{\underline{\epsilon}}) = \nabla\vec{s}$.

The deformation tensor can be split into two components:

$$\epsilon_{ij} = \left(\epsilon_{ij} - \frac{1}{3}\mathrm{tr}\,\underline{\underline{\epsilon}}\delta_{ij}\right) + \frac{1}{3}\mathrm{tr}\,\underline{\underline{\epsilon}}\delta_{ij} \tag{4.9}$$

$$= d_{ij} + s_{ij} \tag{4.10}$$

with the deviator d_{ij} and the sphere tensor s_{ij}. The deviator describes a deformation with constant volume and the sphere tensor a deformation which maintains the original shape.

4.2.2. Velocity and Acceleration Field

The velocity of a particle passing the location $\vec{r}$ at a point in time is defined as

$$\frac{\mathrm{d}\vec{s}}{\mathrm{d}t} = \vec{v}(\vec{r}, t). \tag{4.11}$$

It follows from Eq. 4.6 and 4.8 that the velocity of a particle can be expressed as

$$\vec{v} = \vec{v}_0 + \vec{\omega} \times \vec{r} + \underline{\underline{\dot{\epsilon}}} \cdot \vec{r}; \tag{4.12}$$

the first term on the right hand side is the translational velocity, the second the rotational velocity and the third involves the rate of deformation tensor $\underline{\underline{\dot{\epsilon}}}$ or the temporal derivative of $\underline{\underline{\epsilon}}$. The trace of this tensor is the dilatation velocity and vanishes for incompressible media:

$$\nabla \cdot \vec{v} = 0. \tag{4.13}$$

As continuum mechanics involves a large ensemble of particles moving through space with time, three cases for the acceleration have to be distinguished:

Fixed particle: $\vec{r} = \vec{r}(\vec{r}_0, t)$ describes the path of a fixed particle that started from $\vec{r}_0$ at $t = t_0$. The acceleration on this particle at a certain time will be

$$\vec{a}(\vec{r}_0, t) = \frac{\mathrm{d}\vec{v}(\vec{r}_0, t)}{\mathrm{d}t}. \tag{4.14}$$

It is also known as substantial acceleration.

Fixed location: The change in velocity at a fixed point $\vec{r}$ in space at a certain time t is

$$\vec{a}(\vec{r}, t) = \frac{\partial\vec{v}(\vec{r}, t)}{\partial t}. \tag{4.15}$$

This is called the local acceleration.

A specific particle $\vec{r}_0$ passing the point $\vec{r}$ at time t:

$$\begin{aligned}
\vec{v} &= \vec{v}(\vec{r}, t) = \vec{v}(\vec{r}(\vec{r}_0, t), t) && (4.16)\\
&= \vec{v}(x(\vec{r}_0, t), y(\vec{r}_0, t), z(\vec{r}_0, t) && (4.17)\\
\Rightarrow \frac{d\vec{v}}{dt} &= \frac{\partial\vec{v}}{\partial x}\underbrace{\frac{dx}{dt}}_{v_1} + \frac{\partial\vec{v}}{\partial y}\underbrace{\frac{dy}{dt}}_{v_2} + \frac{\partial\vec{v}}{\partial z}\underbrace{\frac{dz}{dt}}_{v_3} + \frac{\partial\vec{v}}{\partial t} && (4.18)\\
&= \frac{\partial\vec{v}}{\partial t} + \underbrace{\left(\sum_{i=1}^{3} v_i \frac{\partial}{\partial x_i}\right)}_{\vec{v}\cdot\nabla}\vec{v} && (4.19)\\
\Rightarrow \frac{\mathrm{d}\vec{v}}{\mathrm{d}t} &= \frac{\partial\vec{v}}{\partial t} + (\vec{v}\cdot\nabla)\vec{v}. && (4.20)
\end{aligned}$$

The last equation (Equation 4.20) is known as the material derivative and describes the effect of convectional acceleration. The material derivative holds true for all properties (scalar and vectorial) and depends on the velocity gradient tensor $(\vec{v}\cdot\nabla)\vec{v}$.

4.3. Continuum Mechanics

4.3.1. Balance Equations

Continuum mechanics involves looking at a material volume in a moving medium; i.e. a volume with a smooth surface that is moving with the particles. Within this volume the additional property ψ can be calculated from its density ϕ:

$$\psi(t) = \int_{V(t)} \phi(\vec{r}, t) \mathrm{d}V$$

The substantial derivative of this property is given by Reynolds' transport theorem:

$$\frac{\mathrm{d}\psi}{\mathrm{d}t} = \int_{V(t)} \left[\frac{d\phi}{dt} + \phi(\nabla \cdot \vec{v}) \right] dV \tag{4.21}$$

$$= \int_{V(t)} \left[\frac{d\phi}{dt} + \nabla \cdot (\phi \vec{v}) \right] dV \tag{4.22}$$

Applying Gauss' theorem [BS79]

$$\int_V \nabla \cdot \vec{a} \mathrm{d}V = \int_{\partial V} \vec{a} \cdot \mathrm{d}\vec{A} \tag{4.23}$$

this equation can also be expressed as:

$$\frac{d\psi}{dt} = \int_{V(t)} \frac{d\phi}{dt} + \int_{\partial V} \psi \vec{v} \cdot d\vec{A}. \tag{4.24}$$

Choosing $\phi = \rho(\vec{r}, t)$, the material density, the conservation of mass is used to arrive at the continuity equation:

$$\frac{d}{dt} \int_V \rho(\vec{r}, t) dV = 0 \tag{4.25}$$

$$\Leftrightarrow \frac{d\rho}{dt} + \rho(\nabla \cdot \vec{v}) = 0. \tag{4.26}$$

Forces which act on deformable media can be distinguished as mass or volume forces $\vec{f}$ (e.g. gravity and electromagnetic forces) and surface forces $\vec{t}$ (e.g. stress, pressure and friction). The total force $\vec{F}$ acting on the sample is:

$$\vec{F} = \int_V \rho \vec{f} dV + \int_{\partial V} \vec{t} dA. \tag{4.27}$$

At equilibrium the surface forces cancel each other out. On an arbitrary surface, with surface normal $\vec{n}$, there is a linear relationship between the surface normal and the surface forces $\vec{t}$. This relationship is expressed through the stress tensor $\underline{\underline{\sigma}}$ with the components σ_{ij}:

$$\vec{t} = \underline{\underline{\sigma}} \cdot \vec{n}. \tag{4.28}$$

In general, there are normal components of the surface forces (pressure) and tangential components (shear). The normal surface forces are contained in the diagonal elements of the tensor σ_{ii}, the normal stresses, and the tangential surface forces in the off-diagonal elements $\sigma_{ij} (i \neq j)$, the shear stresses. Since the stress tensor is symmetric ($\underline{\underline{\sigma}} = \underline{\underline{\sigma}}^T$), only six components of the tensor are independent (the diagonal and three off-diagonal elements).

Again, applying Gauss' theorem (Eq. 4.23) the surface integral can be expressed as:

$$\int_{\partial V} \vec{t} dA = \int_{\partial V} \underline{\underline{\sigma}} \cdot \vec{n} dA = \int_V \nabla \cdot \underline{\underline{\sigma}} dV \tag{4.29}$$

where the components of $\nabla \cdot \underline{\underline{\sigma}} = {}^{\partial \sigma_{ij}}/_{\partial x_i}$, using Einstein's summation convention.

The second Newtonian axiom has to hold for deformable media:

$$\frac{d\vec{p}}{dt} = \vec{F} \tag{4.30}$$

with the net impulse $\vec{p}$. Using $\rho\vec{v}$, the impulse density, it follows from Equation 4.27 that

$$\frac{d}{dt} \int_V \rho \vec{v} dV = \int_V \rho \vec{f} dV + \int_{\partial V} \vec{t} dA \tag{4.31}$$

or with Eq 4.21 and 4.23:

$$\int_V \rho \frac{d\vec{v}}{dt} dV = \int_V \rho \vec{f} dV + \int_V \nabla \cdot \underline{\underline{\sigma}} dV \tag{4.32}$$

in the local form

$$\rho \frac{d\vec{v}}{dt} - \nabla \cdot \underline{\underline{\sigma}} = \rho \vec{f}. \tag{4.33}$$

Using the material derivative (Eq. 4.20) and the definition $\nabla \cdot (\rho\vec{v} \otimes \vec{v}) = (\rho\vec{v} \cdot \nabla)\vec{v} + \vec{v}\nabla \cdot (\rho\vec{v})$ the local form can be alternatively expressed as

$$\frac{\partial(\rho\vec{v})}{\partial t} + \nabla \cdot (\rho\vec{v} \otimes \vec{v} - \underline{\underline{\sigma}}) = \rho \vec{f} \tag{4.34}$$

with the impulse density $\rho\vec{v}$ and impulse stream density $\rho\vec{v} \otimes \vec{v}$, which is a tensor with the components $\rho v_i v_j$.

4.3.2. Material Equations

In summary, knowledge of the volume force density $\vec{f}$ and the geometry of the problem have been assumed. The behaviour of the sample has been described by the continuity equation 4.25 and the impulse balance (Eq. 4.33).

Hence, the properties of interest are the density field $\rho(\vec{r},t)$, velocity field $\vec{v}(\vec{r},t)$ and stress tensor $\sigma_{ij}(\vec{r},t)$. As there are four equations that describe the problem, but ten unknown variables, additional information has to be provided. So far the properties of the sample in question have not been taken into account. These properties are contained in the material equation.

The general form of the equation needed is:

$$f(\underline{\underline{\sigma}}, \underline{\underline{\epsilon}}, \dot{\underline{\underline{\epsilon}}}, \ldots) = 0. \tag{4.35}$$

This equation correlates the stress tensor $\underline{\underline{\sigma}}$ with the deformation tensor $\underline{\underline{\epsilon}}$ and/or rate of deformation tensor $\dot{\underline{\underline{\epsilon}}}$.

Hooke's Law

One example of an equation of state is Hooke's law for elastic deformation:

$$\underline{\underline{\sigma}} = \underline{\underline{\underline{\underline{C}}}} \cdot \underline{\underline{\epsilon}} \tag{4.36}$$

The term $\underline{\underline{\underline{\underline{C}}}}$ is a fourth level elasticity tensor, which possesses 81 components. Symmetry considerations reduce this number considerably and the equation can be simplified to

$$\underline{\underline{\sigma}} = \lambda(\mathrm{tr}\,\underline{\underline{\epsilon}})\underline{\underline{1}} + 2\mu\underline{\underline{\epsilon}} \tag{4.37}$$

with λ and μ the Lamé elasticity constants and the identity tensor $\underline{\underline{1}}$.

Stress Tensor in Fluids

Materials that do not resist deformation (with constant volume) are called fluids; i.e. $\sigma_{ij}(i \neq j)$ vanishes. Application of Hooke's Law (Eq. 4.37) shows this can only happen for $\mu = 0$. Hence, fluids with vanishing μ are called ideal fluids. Equation 4.37 simplifies, for an ideal fluid, to

$$\tau_{11} = \tau_{22} = \tau_{33} = \lambda(\mathrm{tr}\,\underline{\underline{\epsilon}}) = -p. \tag{4.38}$$

This only holds for resting fluids. The extension to the stress tensor for moving fluids is

$$\underline{\underline{\sigma}} = -p\underline{\underline{1}} + \underline{\underline{R}}(\underline{\underline{\dot{\epsilon}}}). \tag{4.39}$$

The tensor $\underline{\underline{R}}$ contains the dependence of the stress tensor on the rate of deformation tensor.

With a linear approximation $\underline{\underline{R}} \sim \underline{\underline{\dot{\epsilon}}}$, Hooke's law is valid for isotropic fluids:

$$\underline{\underline{\sigma}} = -p\underline{\underline{1}} + 2\eta\underline{\underline{\dot{\epsilon}}} + \eta'(\mathrm{tr}\,\underline{\underline{\dot{\epsilon}}})\underline{\underline{1}} \tag{4.40}$$

with the dynamic viscosity, η, and kinematic viscosity, η'. This linear approximation goes back to Newton and consequently fluids with a linear relationship between stress and rate of deformation are called Newtonian fluids.

As a consequence of this relationship, additional pressure is created in moving fluids can be used to measure the velocities (e.g. in planes). Since $\mathrm{tr}\,\underline{\underline{\dot{\epsilon}}} = \nabla \cdot \vec{v} = 0$ for incompressible fluids, the stress tensor simplifies to

$$\underline{\underline{\sigma}} = -p\underline{\underline{1}} + 2\eta\underline{\underline{\dot{\epsilon}}}. \tag{4.41}$$

This equation is only valid for incompressible, Newtonian fluids. This specific case is regularly adopted, because it simplifies the mathematics of the problem considerably. Many real fluids can be adequately described as incompressible, Newtonian fluids. For these fluids the shear stress is proportional to the first derivative of the velocity and the viscosity is independent of the shear rate.

A basic property that can be used to describe the viscosity of fluids is the attraction between the molecules. This in turn leads to friction between layers of fluid passing each other at different speeds. Gases also exhibit viscosity. In this case, the average separation between the molecules is too large to explain the viscosity by the attraction between the molecules.

A Gedanken-experiment helps to clarify the concept of viscosity, by examining two layers of fluid passing each other at two different velocities. If individual particles in this stream were followed, a single particle might migrate between layers due to diffusion. This diffusion is driven by the thermal energy of the fluid and governed by Brownian motion. Obviously, the individual particles carry their momentum from one layer to the next. Within a layer the frequent collisions between particles equilibrate the differences in the momentum between the individual particles. Hence, the migration of particles between layers leads to the effects of viscosity.

4.4. Hydrodynamics

4.4.1. Constituent Equations

Applying the linear elasticity theory to the behaviour of fluids for a given geometry under known external forces is called "hydrodynamics". The following equations form the basic frame for this field of theoretical physics.

- Continuity equation (Eq. 4.25):

$$\frac{d\rho}{dt} + \rho(\nabla \cdot \vec{v}) = 0.$$

- Impulse balance (Eq. 4.33):

$$\rho \frac{d\vec{v}}{dt} = \rho \vec{f} + \nabla \cdot \underline{\underline{\sigma}}.$$

- Material equation for incompressible fluids (Eq. 4.41):

$$\underline{\underline{\sigma}} = -p\underline{\underline{1}} + 2\eta\dot{\underline{\underline{\epsilon}}}.$$

- Equation of state (EOS) for a barotropic fluid where the pressure is a function of density alone:

$$\rho = \rho(p) \Leftrightarrow p = p(\rho). \tag{4.42}$$

Combining the material equation (Eq. 4.41) and the impulse balance (Eq. 4.33) leads to the well known Navier-Stokes Equation:

$$\frac{d\vec{v}}{dt} = \frac{\partial \vec{v}}{\partial t} + (\vec{v} \cdot \nabla)\,\vec{v} \tag{4.43}$$

$$= \vec{f} - \frac{1}{\rho}\nabla p + \frac{\eta}{\rho}\Delta\vec{v}. \tag{4.44}$$

Experimental evidence leads to the assumption that the fluid velocity at the vessel wall is zero, the non-slip condition. In general this approximation is valid, and independent of the chemical composition of the fluid and the wall.

4.4.2. Wall Shear Stress

The interaction between the vessel wall and the flow is defined through the stress which can be calculated from the stress tensor $\underline{\underline{\sigma}}$ and the surface normal $\vec{n}$. This extracts the stress vector at that particular location and surface normal from the stress tensor (Eq. 4.28):

$$\vec{t} = \underline{\underline{\sigma}} \cdot \vec{n}$$

For an incompressible Newtonian fluid this stress (Eq. 4.41) contains two main components: a component due to the hydrostatic pressure and a second component due to viscosity. The component in the surface due to viscous forces at the vessel wall is known as wall shear stress (WSS). It can be calculated from the shear stress tensor $\underline{\underline{\tau}}$, which is the viscous component of the stress tensor

$$\underline{\underline{\tau}} = 2\eta\underline{\underline{\dot{\epsilon}}}. \tag{4.45}$$

and the surface normal $\vec{n}$. The components of the rate of deformation tensor are given by $\epsilon_{ij} = 1/2\,(\partial v_i/\partial x_j + \partial v_j/\partial x_i)$. To extract the normal component of a vector, the dot-product

of the two vectors is multiplied with the surface normal: $\vec{f}^N = (\vec{f} \cdot \vec{n})\vec{n}$. To extract the tangential component a series of cross-products is used: $\vec{f}^T = \vec{n} \times (\vec{f} \times \vec{n}) = \vec{f} - \vec{f}^N$. For the coordinate system independent expression of wall shear stress the following expression is left:

$$\vec{w} = \vec{n} \times \left[\left(2\eta \underline{\underline{\dot{\epsilon}}} \cdot \vec{n} \right) \times \vec{n} \right]. \tag{4.46}$$

For Newtonian fluids, the relationship between wall shear stress $\vec{w}$ and wall shear rate $\vec{w}_{rate}$ is linear and governed by the viscosity η: $\vec{w} = \eta \cdot \vec{w}_{rate}$ or

$$\vec{w}_{rate} = \vec{n} \times \left[\left(2\underline{\underline{\dot{\epsilon}}} \cdot \vec{n} \right) \times \vec{n} \right]. \tag{4.47}$$

4.4.3. Poiseuille Flow

Constant Pressure

Pressure-driven flow of an incompressible fluid through a cylindrical vessel was first considered by Hagen and Poiseuille, the latter in his treatise of blood flow [Poi46]. The problem is simplified considerably by the use of cylindrical polar coordinates. Writing the Navier-Stokes Equation (Eq. 4.43) in cylindrical polar coordinates (z, r, ϕ) and ignoring gravity ($\vec{f} = \vec{0}$):

$$\begin{aligned} &\frac{\partial u}{\partial t} + u\frac{\partial u}{\partial z} + v\frac{\partial u}{\partial r} + w\frac{1}{r}\frac{\partial u}{\partial \phi} \\ &\quad = -\frac{1}{\rho}\frac{\partial p}{\partial z} + \frac{\eta}{\rho}\left[\frac{\partial^2 u}{\partial z^2} + \frac{1}{r}\frac{\partial}{\partial r}\left(r\frac{\partial u}{\partial r} \right) + \frac{1}{r^2}\frac{\partial^2 u}{\partial \phi^2} \right] \end{aligned} \tag{4.48}$$

$$\begin{aligned} &\frac{\partial v}{\partial t} + u\frac{\partial v}{\partial z} + v\frac{\partial v}{\partial r} + w\frac{1}{r}\frac{\partial v}{\partial \phi} - \frac{w^2}{r} \\ &\quad = -\frac{1}{\rho}\frac{\partial p}{\partial r} + \frac{\eta}{\rho}\left[\frac{\partial^2 v}{\partial z^2} + \frac{\partial}{\partial r}\left(\frac{1}{r}\frac{\partial (rv)}{\partial r} \right) + \frac{1}{r^2}\frac{\partial^2 v}{\partial \phi^2} - \frac{2}{r^2}\frac{\partial w}{\partial \phi} \right] \end{aligned} \tag{4.49}$$

$$\begin{aligned} &\frac{\partial w}{\partial t} + u\frac{\partial w}{\partial z} + v\frac{\partial w}{\partial r} + w\frac{1}{r}\frac{\partial w}{\partial \phi} + \frac{vw}{r} \\ &\quad = -\frac{1}{\rho}\frac{1}{r}\frac{\partial p}{\partial \phi} + \frac{\eta}{\rho}\left[\frac{\partial^2 w}{\partial z^2} + \frac{\partial}{\partial r}\left(\frac{1}{r}\frac{\partial (rw)}{\partial r} \right) + \frac{1}{r^2}\frac{\partial^2 w}{\partial \phi^2} + \frac{2}{r^2}\frac{\partial w}{\partial \phi} \right]. \end{aligned} \tag{4.50}$$

Away from the entrance region, where the flow profile is fully developed, it follows from symmetry considerations that flow is only possible along the unit vector in the

z-direction, but not in the r- or the ϕ-directions, i.e. $v = w = 0$. The system is also rotationally symmetric around the z-axis, i.e. $u(z, r, \phi) = u(z, r)$. Once established, the flow should not change along the axis of the vessel, i.e. $u(z, r) = u(r)$. Hence, Equations 4.48 – 4.50 simplify to

$$\frac{\partial u}{\partial t} = -\frac{1}{\rho}\frac{\partial p}{\partial z} + \frac{\eta}{\rho}\left[\frac{1}{r}\frac{\partial}{\partial r}\left(r\frac{\partial u}{\partial r}\right)\right] \tag{4.51}$$

$$0 = -\frac{1}{\rho}\frac{\partial p}{\partial r} \tag{4.52}$$

$$0 = -\frac{1}{\rho}\frac{1}{r}\frac{\partial p}{\partial \phi}. \tag{4.53}$$

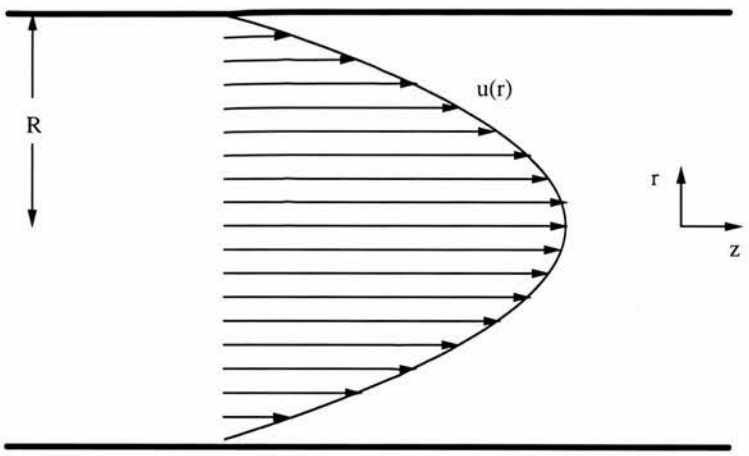

Figure 4.2.: *Poiseuille flow in a straight vessel with circular cross section.*

As expected there is no change in pressure along the r- and ϕ-directions. The remaining differential equation for $u = u(r)$ is readily solved with the non-slip boundary condition $u|_{r=R} = 0$ and the radius of the vessel R. The solution is a parabolic flow profile:

$$u = \frac{\Delta p}{4L\eta}\left(R^2 - r^2\right) = \frac{V_{max}}{R^2}\left(R^2 - r^2\right). \tag{4.54}$$

The maximum velocity, $V_{max} = {}^{\Delta p}/_{4L\eta}R^2$, occurs at the centre of the flow ($r = 0$) and Δp, the pressure drop, along the vessel of length L. The resulting parabolic flow profile is illustrated in Figure 4.2. Integration over the vessel cross-section determines the volume flow rate:

$$Q = \frac{\pi R^4 \Delta p}{8L\eta}. \tag{4.55}$$

From the volume flow rate the mean velocity can be calculated:

$$V_{mean} = \frac{Q}{\pi R^2} = \frac{\Delta p}{8L\eta}R^2 = \frac{V_{max}}{2}. \tag{4.56}$$

Initially, it was assumed that the displacement of the flowing particles was small and could be described linearly. It was German engineer G. H. L. Hagen who discovered that the type of flow in a straight tube of circular cross-section changes relatively suddenly with the flow rate. This transition depends on the viscosity. Reynolds showed that the transition was associated with a change in the behaviour of streamlines. At low flow rates all stream lines align with the axis of the vessel. When increasing the flow rate this changes to random, complex streamlines. These two types of flow are called laminar and turbulent respectively. Turbulent flow has not been found in the blood stream of healthy volunteers outside the ascending aorta [NO90]. The main location of turbulent flow in human arteries is located downstream from stenotic sites. In addition, laminar flow is re-established, by the viscosity found near the vessel wall, in a boundary layer.

Reynolds found that the transition almost occurred systematically and is connected to a dimensionless constant, the Reynolds number:

$$Re = \frac{\rho l v}{\eta} \tag{4.57}$$

with a characteristic length l and velocity v. For a straight cylindrical vessels the characteristic length is approximately the diameter and the characteristic velocity the mean velocity. The flow will be laminar for $Re < 2000$ and turbulent for $Re > 4000$. Between those two values the state of the flow could be either type, or a mixture of both, and is in general difficult to predict.

As mentioned previously, the steady flow profile is established by a boundary layer growing into the vessel lumen from the wall. For straight, cylindrical vessels experimental results show that laminar flow is established within an entrance length $0.06R \cdot Re$ of the vessel inlet [CPSS78].

The wall shear stress can be calculated from this parabolic flow profile. Expressing the wall shear stress (Equation 4.46) in cylindrical polar coordinates leads to

$$\begin{aligned}
\vec{w} &= \vec{n} \times \left[\left(2\eta\dot{\underline{\underline{\epsilon}}} \cdot \vec{n}\right) \times \vec{n}\right] \\
&= \vec{n} \times 2\eta[\\
&\quad \left(\begin{pmatrix} \frac{\partial u}{\partial z} & \frac{1}{2}\left(\frac{\partial u}{\partial r} + \frac{\partial v}{\partial z}\right) & \frac{1}{2}\left(\frac{\partial w}{\partial z} + \frac{1}{r}\frac{\partial u}{\partial \phi}\right) \\ \frac{1}{2}\left(\frac{\partial u}{\partial r} + \frac{\partial v}{\partial z}\right) & \frac{\partial v}{\partial r} & \frac{1}{2}\left(r\frac{\partial}{\partial r}\left(\frac{w}{r}\right) + \frac{2}{r}\frac{\partial v}{\partial \phi}\right) \\ \frac{1}{2}\left(\frac{\partial w}{\partial z} + \frac{1}{r}\frac{\partial u}{\partial \phi}\right) & \frac{1}{2}\left(r\frac{\partial}{\partial r}\left(\frac{w}{r}\right) + \frac{2}{r}\frac{\partial v}{\partial \phi}\right) & \frac{1}{r}\frac{\partial w}{\partial \phi} + \frac{1}{r}v \end{pmatrix} \cdot \vec{n}\right) \\
&\quad \times \vec{n}] \qquad (4.58)
\end{aligned}$$

For this case, the surface normal always points opposite to the direction of the unit vector in the r-direction $\vec{n} = -e_r = -(0,1,0)^c$ (inwards). The equation for the wall shear stress (Eq. 4.58) simplifies to

$$\begin{aligned}
\vec{w} &= \begin{pmatrix} 0 \\ -1 \\ 0 \end{pmatrix} \times 2\eta \left[\left(\left(\begin{pmatrix} 0 & \frac{1}{2}\left(\frac{\partial u}{\partial r}\right) & 0 \\ \frac{1}{2}\left(\frac{\partial u}{\partial r}\right) & 0 & 0 \\ 0 & 0 & 0 \end{pmatrix} \cdot \begin{pmatrix} 0 \\ -1 \\ 0 \end{pmatrix}\right) \times \begin{pmatrix} 0 \\ -1 \\ 0 \end{pmatrix}\right] \\
&= \begin{pmatrix} 0 \\ -1 \\ 0 \end{pmatrix} \times 2\eta \left[\begin{pmatrix} \left(\frac{1}{2}\frac{\partial u}{\partial r}\right) \\ 0 \\ 0 \end{pmatrix} \times \begin{pmatrix} 0 \\ -1 \\ 0 \end{pmatrix}\right] \\
&= -\eta\frac{\partial u}{\partial r}\vec{e_z}. \qquad (4.59)
\end{aligned}$$

Frequently, only the magnitude of the wall shear stress (Eq. 4.59) is reported in the literature, often without any derivation. This approach is found in Doppler ultrasound literature, where normally only one component of the velocity field can be measured.

Oscillatory Pressure

If an oscillating pressure gradient is applied to a long cylindrical vessel of length L and radius R, the flow will slow down, stop and reverse direction, accelerate in that direction, then slow down again. If this takes place gradually enough the flow will always have the parabolic flow profile that resulted from the steady pressure gradient (Eq. 4.54). However, if the frequency of the oscillation increases, the velocity profile becomes progressively distorted. The inertia of the fluid in the central core prevents the core from following the applied pressure gradient and the amount by which it lags increases as the frequency of the oscillation is raised.

Oscillatory flow in straight vessels is a very important first model for blood flow in arteries. The solution for a sinusoidal pressure gradient $A\sin(\Omega t)$ is given by the real part of the Fourier-Bessel series:

$$u(r,t) = -\frac{A}{\rho\Omega} e^{-i\Omega t}\left(1 - \frac{J_0((-i\rho\Omega/\eta)^{1/2}r)}{J_0((-i\rho\Omega/\eta)^{1/2}R)}\right). \tag{4.60}$$

The square root with the negative real part $(-i)^{1/2} = e^{3\pi i/4}$ has to be chosen. The angular frequency is often expressed in terms of the Womersley number $N_W = {}^1/_2R(\rho\Omega/\eta)^{1/2}$. At low values of N_W, steady Poiseuille flow is obtained, whereas at high values the flow profile is composed of a plug-flow core and an axisymmetric boundary layer.

The Navier-Stokes Equation (Eq. 4.43) is linear with respect to the applied pressure, i.e. $NSE(ap_1 + bp_2) = aNSE(p_1) + bNSE(p_2)$ where NSE represents the Navier-Stokes Equation. Complex pressure profiles can therefore be split into several components and the solutions of the simpler problems add up to the total solution. For pulsatile pressures, a Fourier analysis allows the calculation of the individual contributions for the separate harmonics of the pressure profile [RKM00]. The velocity profile can then be calculated from a series of contributions of the form given in Equation 4.60.

4.5. The Measurement of Wall Shear Stress

Blood is, to a good approximation, a Newtonian fluid [CFGS71]. A detailed discussion of the linearity between shear rate and shear stress can be found in [BHHR95]. Although over a wide range of shear rates the connection is not linear, for the physiological range, blood can be assumed to be a Newtonian fluid with a viscosity $\eta = 0.003$ Ns/m^2 [BHHR95]. In this regime the theory laid out in this chapter can be applied.

The expression for wall shear stress $\vec{w}$ has been derived (Equation 4.46)

$$\vec{w} = \vec{n} \times \left[\left(2\eta\dot{\underline{\underline{\epsilon}}} \cdot \vec{n}\right) \times \vec{n}\right]$$

The measurement of wall shear stress therefore involves the determination of the position of the wall, the surface normal $\vec{n}$ and the knowledge of the velocity derivatives that make up $\underline{\underline{\epsilon}}$.

Three major approaches have been used to provide information on the local wall shear stress in arteries: (i) experiments in realistic and simplified models of arterial sections, (ii) *in vivo* measurements mainly using Doppler ultrasound and (iii) computational fluid dynamics (CFD).

The streamlines of flows in realistic models have been studied using dyes [IK98] and hydrogen bubbles [GZGK88]. Although these methods provide an intuitive understanding of the flow field, it is very difficult to quantify the data.

An approach that is only applicable *in vitro* is laser Doppler anemometry (LDA). Laser light is scattered by particles suspended in the fluid at a localised point. The scattered light undergoes a frequency shift, which after electro-optic pre-processing can be interpreted as velocity information of the particles. The method requires a translucent fluid with particles suspended in it. Transparent models of arteries have to be constructed before velocity fields can be measured [LM84, LMB92, KG87, BHHR95]. LDA has also been used to study wall shear stress in a compliant model of the human carotid artery [AJG$^+$94]. The influence of the input flow waveform on wall shear rate has been studied in a realistic model of the human carotid artery using LDA [GK87].

A method that has *in vitro* and *in vivo* capabilities is Doppler ultrasound. It uses ultrasound to depict the different acoustical properties of various tissues and blood. Using the

Doppler shift it can be used to measure velocities. Introductory texts on state-of-the-art cardiovascular ultrasound can be found in [HFS+94, Hos96a, Hos96b, Hos97, HFMM98]. Using independent beam directions, more than one velocity component can be measured. In 1991 a comparative study on different signal analysis techniques with Doppler ultrasound was published [MK91]. They found a good correlation between theoretical and ultrasound velocities ($r \approx 0.97$). Five different approaches to the calculation of wall shear stress were taken: (i) the wall and the velocity at the first measured position next to the wall, (ii) the wall and two points, (iii) the wall and three points, (iv) two points without the wall and (v) three points without the wall. These results were then compared to theoretical predictions of wall shear stress based on Poiseuille flow, i.e.

$$|\vec{w}| = \frac{4\eta\bar{v}}{R} \tag{4.61}$$

with $\bar{v} = 0.5v_{max}$ as the average velocity. For turbulent flow, the Blasius empirical relationship was used for comparison [Sch79]:

$$|\vec{w}| = \frac{1}{8} \cdot \frac{0.316}{Re^{0.25}} \rho \bar{v}^2. \tag{4.62}$$

Using method (iii) minimised the error of the measured wall shear stress against the theoretical one. However, linear regression and not a parabolic function was used. A similar method to Eq. 4.61 has previously been used [GIC+97] for measurements in the carotid artery.

The importance of deconvolution with the spatial resolution when measuring with a specific resolution in a tube of a fixed diameter has been discussed [HH93]. The Doppler signal obtained is formed from the weighted average of velocities in the sample volume. The sample volume is defined by the equipment used. For a parabolic flow profile, the distribution of velocities in the sample volume means that the point of peak velocity is shifted away from the transducer, but deconvolution with the sample volume shape can correct for this effect. In addition, the problems concerning the reliability of the wall point are discussed. The error in the position of the wall must be taken into account for any subsequent calculations. Various fit methods were tested to determine the wall shear stress and by far the best fit was a least-squares parabolic fit to the data, which

produced a mean difference of only 1%. This result is better than a linear fit applied to the theoretical Poiseuille velocity profile (Eq. 4.54).

Examining flow profiles measured with Doppler ultrasound for one velocity component allows an estimate of WSS. It has been applied to phantoms [GZG93, BHHR95] and the human common carotid artery [SWB+97].

For a non-Newtonian fluid, the relationship between shear rate and viscosity is non-linear and a plot of a measurement for blood has been published [BHHR95]. It shows a slightly non-linear relationship. During the experiments they were able to show a reversal in sign of the wall shear rate in the femoral artery during the cardiac cycle, but not in the common carotid artery. The distension of the vessel during the cardiac cycle was also considered. A comparison with laser Doppler anemometry showed quite good agreement for an *in vitro* study.

A purpose built transducer for wall shear measurements using Doppler ultrasound has been developed [KNN+95]. This device uses three transducers mounted in one head and is time gated to sample three radial velocities needed to fit the wall shear stress. However, only a few of the devices could be produced and the method is invasive, since the transducer head has to be placed directly next to the vessel wall. With further technological development this might prove to be a good prospect in the future for an easy wall shear stress measurement based on ultrasound.

The method used to measure velocity fields non-invasively using MRI was introduced in Chapter 3. One application is in the visualisation of flow fields in human arteries. Application in the aortic arch [KYM+93] proved the usefulness of flow pattern visualisation. Flow information was acquired in one slice with Cine gating. The results showed a helical flow pattern in the aortic arch and an end-systolic retrograde flow. These results corresponded to the behaviour of the flow in a simple tube model of the aortic arch [KYM+93]. This work was extended to the thoratic aorta and pulmonary arteries [MYK94]. This study included patients with dilated great vessels as well as healthy volunteers and proved the existence of very complex flow patterns in aneurysms. Additional validation studies were undertaken using a double loop tube phantom. These results were confirmed for flow patterns in infrarenal aortic aneurysms [LPOP95].

An extension of the acquisition of flow information from a plane to a 3D slab has been described in [WSW96]. The acquisition time was cut by adding a segmented k-space capability to a standard 3D phase contrast sequence on a GE scanner. Image construction was performed off-line with dedicated software. This added very valuable information to the visualisation of the velocity fields. Application to the heart has recently allowed time resolved particle traces to be reconstructed [WEAF+99].

Although these studies did not measure wall shear rate or wall shear stress they still allowed the visualisation of the velocity field. Regions of stagnation and reverse flow became apparent and this might be enough to indicate locations predisposed to stenosis formation. The value of wall shear stress tends to be very low close to these regions of stagnation.

In the discussion on ultrasound measurements it was mentioned that the determination of wall shear stress is difficult since it involves the determination of the derivative of data on a grid and the uncertainty in the wall position. Several approaches with a varying number of pixels next to the wall that were included in the calculation have been presented [MK91]. This work was repeated for MRI [MFU+99] with the same result. The flow profile was assumed to be parabolic in shape near the vessel wall. Measurements based on a linear approach to calculating the shear stress have been published for the abdominal aorta [OPR+97]. A study for the same vessel has been previously published [MXG+94], but no detailed description of the wall shear stress calculation was provided.

A more consistent method based on parabolic fits has been published [ORP+97, ORK+98]. A second order surface $(a(x^2 + y^2) + bx + cy + d)$ was fitted to data points within a ring of pixels close to, but not touching, the vessel wall. The original second order surface used [ORP+97] was rotationally symmetric. However, this approach is not able to describe more complex geometries. Instead of extending the surface to a general second order surface, this group decided to split the region of interest into radial sections and execute a fit for each. This method has been successfully applied to a variety of vessels [WRS+00, OP00]. A comparison of these results with computational fluid dynamic simulations shows limited agreement [PWF+00].

Though fitting a surface to the velocity components is a significant advance, the approach taken in [ORP+97, ORK+98] is limited. A general mathematical solution to the problem

with rotational symmetry would have been a general second order surface. This includes one more term in xy instead of needing five parameters per radial segment. For small vessels, the ratio between the number of fitted parameters and data points contained within the narrow ring used in that method is small and could approach unity. This method does not allow for any smoothing of the data and all velocity noise will influence the calculated wall shear stress. Since a 2D slice is acquired, only one component of the wall shear stress orthogonal to the plane can be determined. For complex geometries this will lead to significant systematic errors which are only enhanced by the use of relatively thick slices ($> 4\,\mathrm{mm}$).

In this project, that work was extended in several respects. First, 3D velocity data sets were used. This allowed a much lower slice thickness to be acquired due to the intrinsically better SNR in 3D MR. Fits for these measurements were based on segments including seven slices out of the complete data set instead of just a ring close to the vessel surface. For complex flow profiles, higher order polynomials were used, but the fit was stabilised by the core flow data. Noise elimination was achieved by using a smooth function with 56 parameters fitted to approximately 300 data points per segment. The new method is introduced in detail in Chapter 7.

Computational fluid dynamic (CFD) studies have been undertaken for simple geometric models and models of human arteries based on *in vivo* measurements. Studying tubes with one or more bends, and deviations from in-plane bends, the behaviour of flow in the aortic arch has been approximated [BHHR95]. In the aortic arch, a single pronounced helical vortex has been found using MRI [KYM+93]. This flow pattern could be simulated using a relatively simple geometric model.

Studying a number of simple geometric branches, the sites of stenosis formation have been predicted by looking at the local changes in the calculated wall shear stress (or Π - value) [LKT95]. A comparison of the prediction with the stenosis found in an excised carotid artery showed good agreement. The model geometry was reconstructed from angiograms. However, it is questionable whether the original vessel geometry can be reconstructed from the angiogram of a diseased vessel. Simple geometric branches and a simplified model of a carotid artery have also been studied [XC94].

Using data from a biplanar angiographic system to generate the surface mesh of the artery, CFD has been used to study wall shear stress in human coronary arteries [KWO+97]. The results were then correlated to the curvature of the vessel and the wall thickness. Evidence was found for an inverse relationship between wall thickness and shear stress.

Using MRI data to construct the vessel wall mesh for human carotid arteries and the measured velocity profiles as the entrance and exit conditions, blood flow in the carotid artery has been simulated [XLC+99]. Adding an approximately straight model of the superior thyroid artery, branching from the external carotid artery to the model, at various distances from the bifurcation allowed the study of the influence of this artery on the blood flow in the carotid bifurcation [ZXC+99].

A comparison of MRI flow rate measurements and CFD predictions for a realistic model of the human carotid bifurcation has shown agreement in principle between the results [BRS+00].

The basic CFD approach has been extended to include the effects of distensibility of arterial walls on the flow patterns [ZYC98a, ZYC98b].

5. Experimental Detail

5.1. MRI Pulse Sequences

5.1.1. PC MRI Sequence on the Siemens Scanner

Initial tests of PC MRI sequence were conducted using a 1.5 Tesla SIEMENS 63SP Magnetom (SIEMENS Medizintechnik, Erlangen, Germany) with the pulse program provided by the manufacturer. The acquisition was restricted to a single slice oriented to a maximum oblique angle of 45°.

This initial period served mainly to get acquainted with the method and select materials for phantom construction. None of the data was used in the final thesis.

5.1.2. PC MRI Sequence on the Elscint Scanner

Most of the experiments were carried out on a 1.9 Tesla Elscint Prestige scanner (Elscint-GE, Haifa, Israel) with progressive versions of the software. None of the software versions permitted the reconstruction of the velocity data from the images saved by the scanner. Hence, image reconstruction from the raw data was implemented. Gating was restricted to one slice and retrospective "Cine" gating. In this case, the scanner acquired one line

of k-space for a pre-calculated number of times (calculated from the average heart rate of the subject) and proceeded to the next line of k-space after a certain time has elapsed from the last detected heart beat. The number of times a k-space line was acquired was saved together with a time offset as a table for every line in the raw data file. This allowed for off line reconstruction of time frames from the raw data (see Section A.4). Despite significant effort, the precise meaning of the offset time table remained unknown to us, as well as Elscint.

A limited amount of pulse programming was allowed on the Elscint scanner. The timing of all pulses and the strength of pulses that was not calculated internally could be changed. However, no additional pulse could be added.

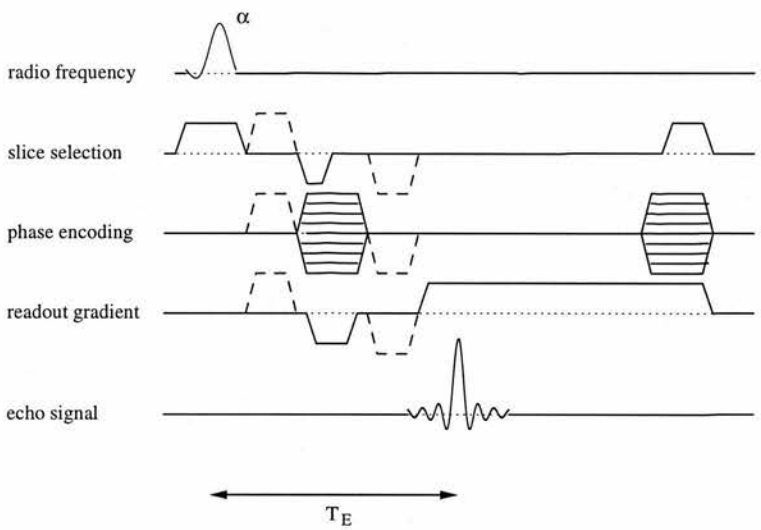

Figure 5.1.: *Gradient - echo phase contrast pulse sequence as used on the Elscint scanner. The solid lines represent the sequence without velocity encoding. First order velocity encoding is presented for all three directions by dashed lines.*

The original 2D sequence had a minimum slice thickness of 11.02 mm. The pulse program (Figure 5.1) was changed to allow the acquisition of thinner slices. The slice thickness (FWHM) was theoretically calculated as 1.8 mm (Figure 5.2), but this value was verified experimentally to be 2.1 mm. The sequence demonstrated a number of features which minimised the echo time. The RF excitation pulse was a minimised version of a sinc pulse. For this pulse, the refocusing gradient was less than half of that during the

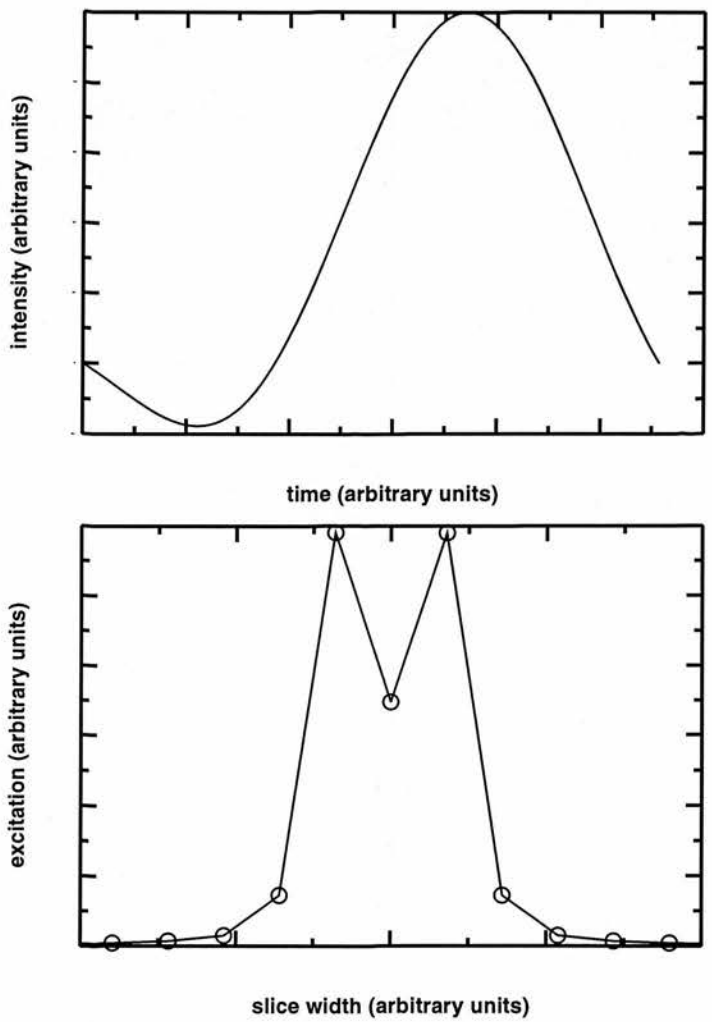

Figure 5.2.: *Excitation pulse used for the gradient - echo phase contrast pulse sequence. The graph on the top shows the RF pulse shape and the graph on the bottom the slice profile as defined by the Fourier transform of the RF pulse.*

excitation. Also, the first part of the echo was not sampled. For the 3D sequence another phase encoding pulse was required.

None of the velocity encoding gradient pulses overlaps any other gradient pulse. This avoids problems due to Maxwell gradient terms (Section 3.3.4). The observation of these effects is rather unlikely.

The v_{enc} for an acquisition was determined by acquiring a number of 2D PC slices across the volume of interest. The highest velocity was found in the velocity maps plus some extra allowance was made to avoid phase wrapping.

5.1.3. PC MRI Sequence on the GE Scanner

On the 1.5 Tesla GE Signa LX scanner the standard PC MRI sequence was used. This is based on a gradient echo sequence, similar to the one provided with the Elscint scanner. Both 2D and 3D velocity sequences are provided, but only the 2D sequence can be gated.

The 3D sequence provided the main data sets for this work. It has a fixed echo time, but the repetition time may be chosen, as well as the flip angle. The choice of frequency encoding and phase encoding steps is limited to certain ratios. Another limit is the number of slices that can be acquired. The maximum number of slices that can be reconstructed per acquisition is 512. With the magnitude, collapsed velocity and three velocity component images plus a number of projections normally created, this limit is reached quickly. For thick regions of interest the slice thickness in a single 3D slab will be higher than desired.

During the setup of the sequence, it is important to enable velocity quantification to avoid filtering, which does not allow the absolute velocity values to be calculated. For clinical imaging purposes, the velocity images are normally multiplied by the magnitude images to remove the noise from undefined phases in low intensity regions. Although it is possible to reverse this process offline, it is desirable to switch this feature off. In research mode, the control variable (CV) "mag_mask" is set to 0. Combined, these allow the measurement of velocities directly on the screen in mm/s.

Normally, a few 2D slices were quickly acquired across the volume of interest in order to choose the right encoding velocity v_{enc}. The highest velocity was found in the velocity maps plus some extra allowance was made to avoid phase wrapping. It is important to remember that v_{enc} has to be entered in cm/s while the velocities on the screen are given in mm/s.

5.2. Scanner Specific Artefacts

5.2.1. Elscint

Due to a rather broad slice and slab profile, the position of saline bags used for the loading of the coil on the Elscint scanner had to be chosen very carefully. Immersing the phantoms in water or gel would have created even bigger problems, since the phase wrapping artefacts would not allow the acquisition of thin slabs around the tubes.

Figure 5.3.: *An example of the Elscint stripe artefact in a 12 mm diameter tube. The magnitude image is shown in (a) and the velocity in the z - direction in (b).*

Another, seemingly random, problem appeared in the form of stripes in the flow areas (Figure 5.3). These stripes were always restricted to areas with flow and never detected in stationary samples. We were unable to remove the artefact by changing any of the scan parameters within reasonable limits. Reducing the tip angle seemed to improve the situation, but Figure 5.3 shows the artefact that was left after such a reduction. It is clear that not only the magnitude images were affected (Figure 5.3 (a)), but also the velocity maps (Figure 5.3 (b)). The artefact always appeared perpendicular to the frequency direction, suggesting a modulation of the signal amplitude. A thorough investigation of the problem was prevented by the decommissioning of the scanner.

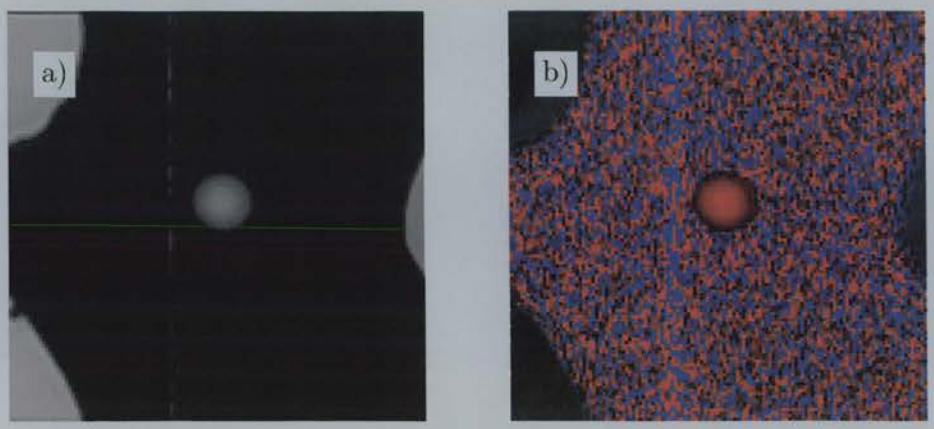

Figure 5.4.: *An example of the EMI experienced with the GE scanner for the 3D PC MRI acquisition. The magnitude image is shown in (a) and the velocity in the z - direction in (b).*

5.2.2. GE

Both 2D and 3D PC acquisitions on the GE scanner suffer from electromagnetic interference (EMI). Figure 5.4 shows an example of the EMI in a 3D acquisition. This stripe is not visible on the magnitude image (Figure 5.4 (a)) [1], but becomes clear on the velocity image (Figure 5.4 (b)). However, in the grey scale used on the scanner for velocity images, the stripe is far more difficult to make out.

The situation for 2D phase contrast acquisitions (Figure 5.5) is similar. This example shows the interference on the magnitude image (Figure 5.5 (a)), but not on the velocity image (Figure 5.5 (b)). In general, the EMI appeared in both types of images at the same time. At the time of writing, the cause of these artefacts is not clear. It has been seen on structural brain scans without any additional equipment in the scanner room. This rules out the pump as a cause. Changing the scan parameters within reason did not appear to affect the artefact. The problem is presently under investigation by GE.

[1] The interference is not visible on computer screens with linear scaling of the grey scale, but the printers (HP LaserJet and HP DeskJet) seem to use a non-linear grey scale

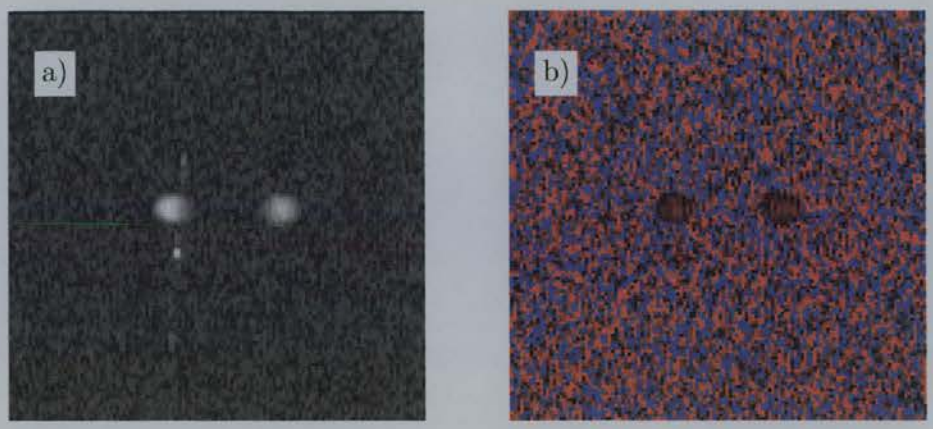

Figure 5.5.: *An example of the EMI experienced with the GE scanner for the 2D PC MRI acquisition. The magnitude image is shown in (a) and the velocity in the z - direction in (b).*

5.3. Phantoms

5.3.1. Mains Pressure Driven Phantom

The first phantom used water directly from a mains tap situated near the scanner. The flow rate was regulated using the tap and measured with a stopwatch and a volume measure. During experiments this measurement was frequently repeated and the volume flow rate was found to remain constant during a single acquisition within the experimental error.

The mains water driven phantom (Figure 5.6) consisted of rigid plastic pipes connected in series by flexible PVC tubing. An approximately 2 m long tube (5 mm inner radius) was used as the inlet into this phantom. This was sufficient to ensure well developed flow profiles, which were qualitatively ascertained from the velocity maps. Subsequently, pipes of 5 mm and 3 mm inner radius were linearly connected by U-bends within the case. This phantom was only used in flow detection verification and has been succeeded by pump based phantoms.

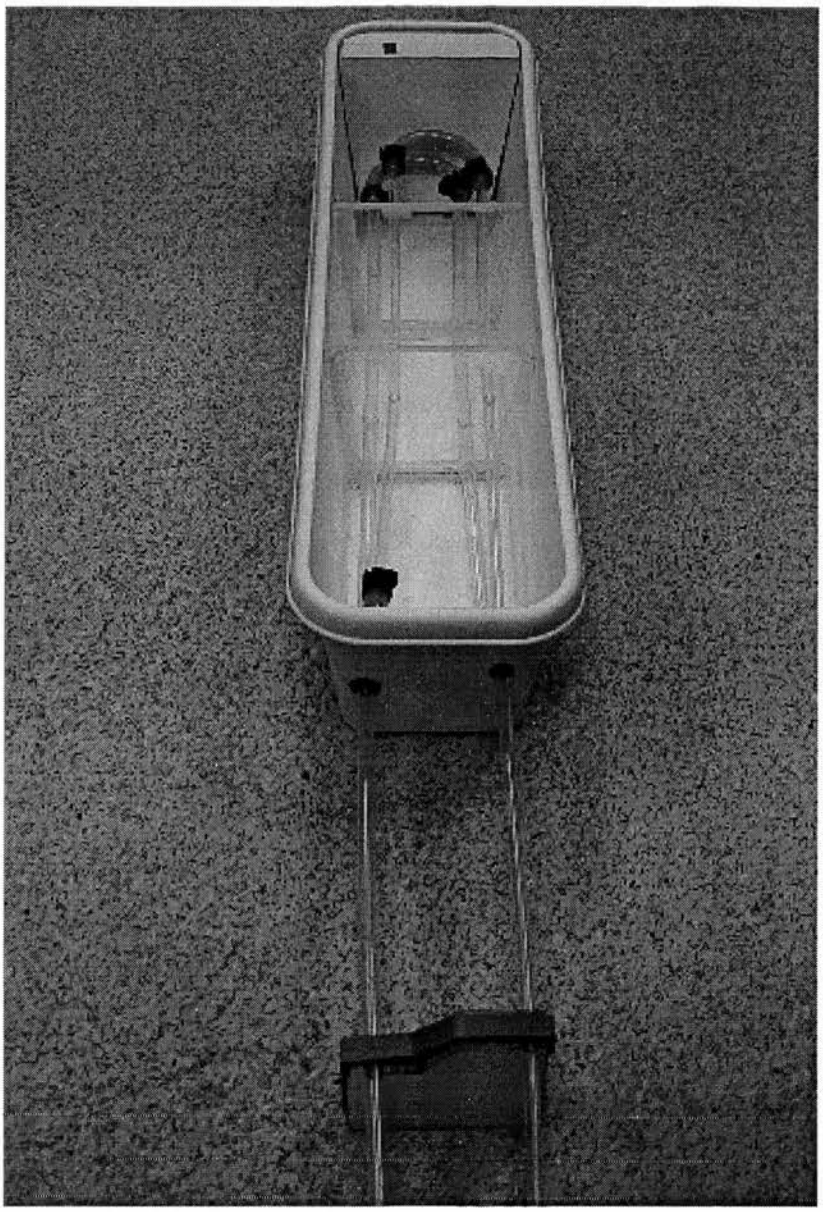

Figure 5.6.: *A photo of the custom-built mains driven flow phantom.*

5.3.2. MR Compatible Pump

The flow simulator used for this project was the two-unit MR-compatible UHDC system (Shelley Medical Imaging Technologies, Ontario, Canada). To the best of our knowledge, this is the only MR-compatible pump capable of producing accurate physiological waveforms that is commercially available. It is designed to ensure the positive displacement pump can be positioned in close proximity to the magnet bore. Control of the pump is through a computer that is positioned further from the magnet. The two units are connected through cables that control the motor and additional electronics.

The flow simulator consists of an anodised aluminium piston within an acrylic cylinder. The piston is translated by a lead-screw situated along the cylinder axis and connected to a stepping motor. An electronically controlled valve ensures that flow from the fluid ports to the test objects remains unidirectional through the phantom when the piston changes direction at the end of the cycle. Both the stepping motor and the valve are under computer control. The use of a stepper motor enables the precise definition of waveforms by the use of simple displacement tables that control the shaft rotation. The frequency of the waveform can be controlled by choosing the time interval between two steps in the range from 2 ms to 50 ms. A trigger point can be defined in the waveform table and an ECG trigger is delivered to an interface that allows the connection to conventional MR-compatible ECG leads.

The volume flow rate accuracy of the pump is specified to $\pm$ 1 % over a flow range of 0.1 - 35 ml/s. Calibration controls undertaken at regular intervals confirmed this accuracy. The volume flow rate is assumed to be known exactly for all following calculations.

The equipment as provided was found to be unsuitable for the use in our MR environment. An unacceptable level of electromagnetic interference (EMI) was produced that rendered the MR images useless. The signal to noise ratio of gradient echo localiser images was reduced from 100:1 to 4:1 as soon the pump unit was connected and switched on. A custom-built RF shield (Picture 5.7) was constructed [RKM99a, RKM99c, RKM00] from 1 mm sheet aluminium. The dimensions of the shield (410 mm$\times$585 mm$\times$255 mm) were selected to comfortably house the pump, allowing for sufficient air circulation around the pump motor to prevent heating. Apertures were left in the shield for the fluid input and output tubes and the vent tube from the fluid reservoir. Motor and control

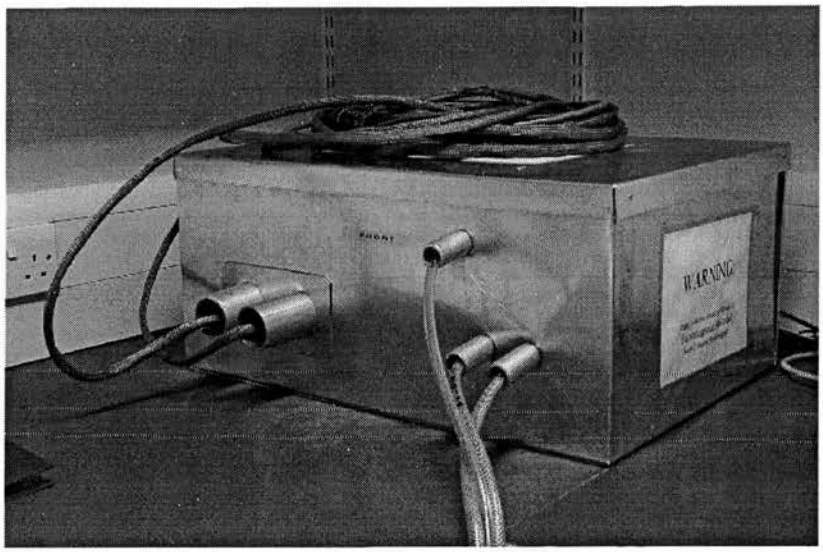

Figure 5.7.: *A photo of the custom-built RF shield.*

cables from the pump to the host computer were shielded using a braided cable sheath (RS, Northants, UK). Connectivity of the shield and cables with ground was verified through testing the electrical resistance.

The connection between the pump and the phantoms was provided by reinforced PVC hose of 6.3 mm inner diameter (RS, Northants, UK). The connection between tubes was provided by all plastic, acetal CPC couplings (Tom Parker Ltd, Preston, UK) similar to the ones supplied with the pump.

5.3.3. Blood Mimicking Fluid

A blood mimicking fluid (Shelley Medical Imaging Technologies, Ontario, Canada) was supplied with the UHDC pump . It has been designed to resemble blood as closely as possible. The kinematic viscosity given in the specifications is 2.5 cSt and the density is 1.03 g·cm^{-3} resulting in a dynamic viscosity of 0.0026 Ns/m^2. The fluid's relaxation times of $T_1 = 1300$ ms and $T_2 = 185$ ms at 1.5 T resemble those of blood. It can also be provided with appropriate ultrasound properties.

However, during the course of this project two problems appeared. A minor one was the strong smell of the fluid. It is advisable to take appropriate precautions when

handling it. A more significant problem seems to be the increase in fluid viscosity over time. Simulations performed with computational fluid dynamics indicate the later experiments were carried out with a viscosity up to five times higher than the quoted value. In hindsight, it was noted that the pump could not deliver flow rates higher than 25 ml/s during the later experiments. A viscosity measurement carried out following British Standard BS 3900 : Part A6 : 1971 yielded 0.0206 Ns/m^2. The viscosity was measured after all MRI acquisitions were finished. The result is outside the calibration range and therefore has to be treated with caution.

5.3.4. 180° Bends

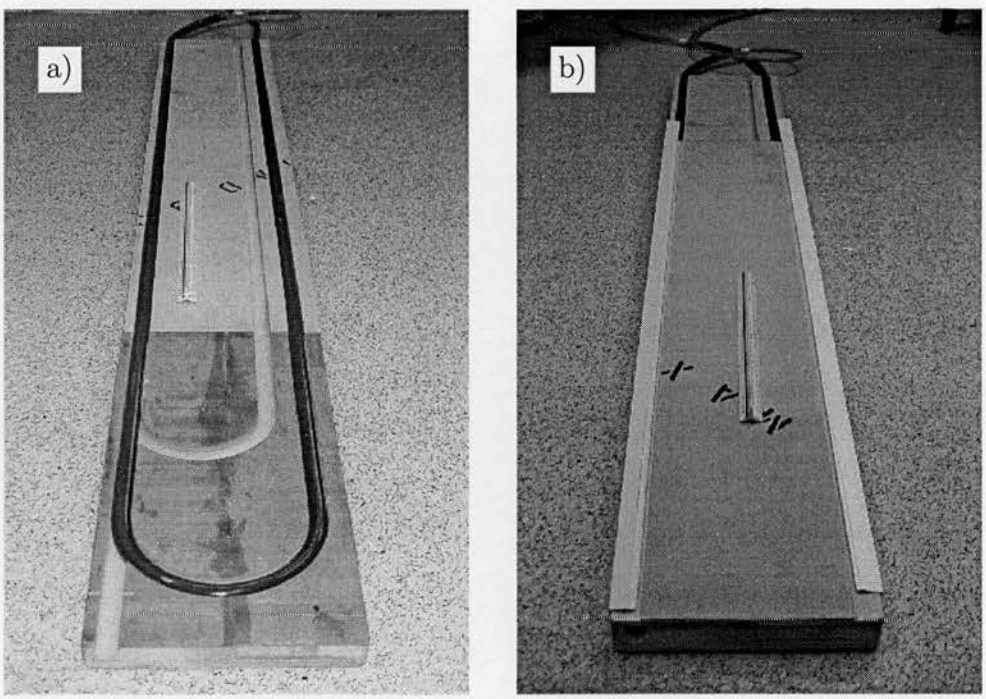

Figure 5.8.: *Photos of the 180° bend phantom open (a) and closed (b). The ruler placed on the phantom is 32 cm long.*

Bending a tube tends to change the cross sectional shape. To avoid this problem, a wooden board (Figure 5.8 (a)) with tight fitting grooves served as a mould for the flexible tube to form 180° bends. A tight fitting lid (Figure 5.8 (b)) for the board forced the tubes to retain their cylindrical cross section. The long, straight inflow regions ensure

fully developed parabolic flow at the entrance to the bend. The centre of the bend was marked with small, water filled vials, that show up on the MRI scans. Unreinforced PVC hose (RS, Northants, UK) with an inner diameter of 12 mm was inserted into either the bigger bend of 90 mm radius or the smaller one with 70 mm radius. Adapters were fitted to the end of this bigger tube to connect to to the reinforced PVC tubing to connect to the pump.

5.3.5. Simple Bifurcation Models

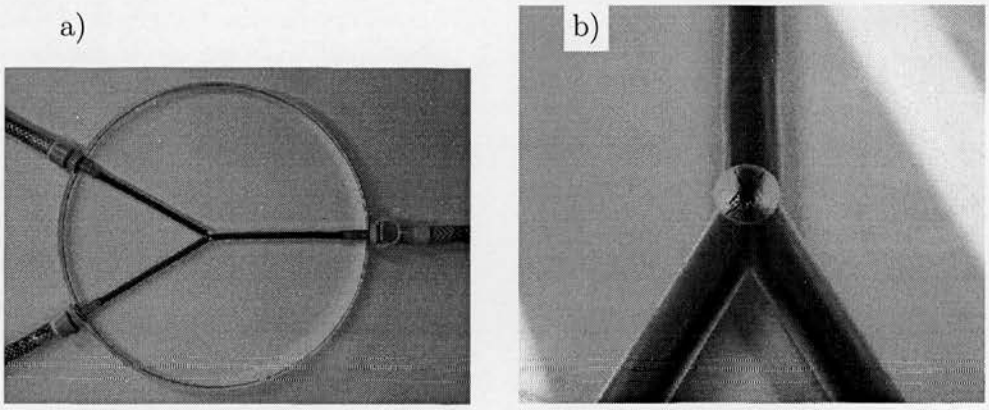

Figure 5.9.: *Photos of the 60° bifurcation phantom in an overview (a) with connectors and in detail (b).*

A perspex disk of 200 mm diameter and 18 mm thickness was used to construct a simple bifurcation model (Figure 5.9). Holes of 6 mm diameter were drilled towards the centre of the disk. The three holes met in the centre to form a 60° forward bifurcation. Threaded versions of the acetal connectors were fitted to the phantom for connection to the pump hoses. Although the inlet length in this phantom was shorter, parabolic flow profiles were found experimentally in the inlet tube.

5.3.6. Human Carotid Bifurcation Models

An anthropomorphic carotid phantom (Shelley Medical Imaging Technologies, Ontario, Canada) was used for more realistic *in vitro* studies. These phantoms are designed to accurately mimic complex physiological vascular geometry of the carotid bifurcation

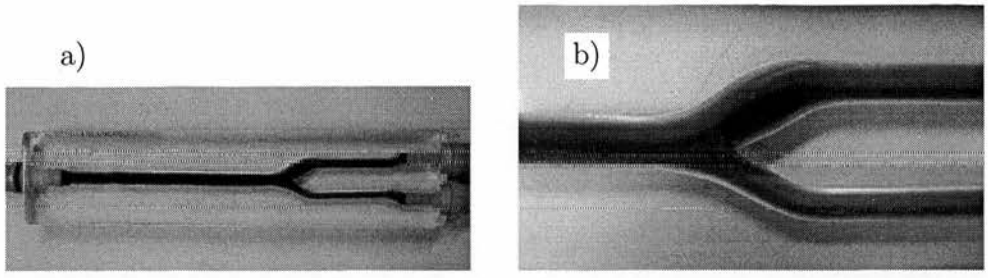

Figure 5.10.: *Photos of the human bifurcation phantom in an overview (a) with connectors and in detail (b).*

[FGR+93]. An acrylic block with connectors for the rigid tubing (Figure 5.10 (a)) holds the realistic model. The geometry of the phantom was chosen to resemble an average human carotid artery [FGR+93, SRFR96]. The branches remain in plane throughout the phantom. The common carotid vessel has a diameter of 8 mm, the post-sinus internal carotid diameter is 5.55 mm and the outflow diameter of the external carotid vessel is 4.65 mm.

6. Automatic Flow Detection

6.1. Introduction:

In white blood MRA and PC MRI the proton signal from blood appears brighter than the surrounding tissue. Fresh spins contained in the inflowing blood are excited through successive radio frequency (RF) pulses, but stationary tissue saturates and appears dark in the images. The detection of flow regions is performed by the selection of the high intensity pixels and rejection of regions containing noise.

Regions which exhibit flow in these images are usually determined, and subsequently indicated, by radiologists. However, an automated approach gives a more accurate result for the measurement of flow rates and less inter-observer variability [BFWE92]. The automated approach may be extended to global thresholding, where each pixel above a predetermined intensity is considered to be part of the flow region [Buo98]. A semi-automated seed growing algorithm [HVvR+95], with a threshold at the mean intensity between intra-luminal and the surrounding signal, has been successfully used [PSE+91, TBP93]. A modified version of the region growing procedure was also used in order to avoid leaks from incomplete boundaries [KKKW00]. All of these methods have been employed to determine volume flow rates in PC images.

Vessel walls have been modelled through a simple circle fitting procedure [Ham94]. The variation in the detected area introduced by the position of the centre of the circular lumen has been quantified [KKKW00]. Active contours, also known as snakes, introduce a flexible boundary to detect vessel walls [HRC+98]. Hence, the assumption that the lumen possesses a circular cross-section is dispensed with for a more flexible edge model. This method creates a smooth boundary but has difficulty handling complex (concave) edges. A commercial system has recently become available that detects arterial contours automatically after the user marks the centre [vdGNvdW+98].

In vessel wall voxels only some of the proton spins are mobile and their contributions are vectorially added to the contribution from stationary spins. This effect makes reliable flow detection, and consequently flow rate measurements, in Phase Contrast MRI quite difficult [FNKL90, PSL+94, HVvR+95, WERR93]. For the quantitative study of flow it is important not to include these errant velocity values in further calculations.

Here we present a method to efficiently detect flow areas in MRA and PC MRI with minimum input by the operator and only one interactive parameter. Three approaches were devised for specific input data: time of flight, *in vitro* and *in vivo* phase contrast MRI. These methods provide a reproducible and efficient way to provide data for haemodynamic studies. While region growing procedures [KKKW00] take into account the intensity of the pixel in question and its neighbours, the new edge detection based algorithm also incorporates the local variation in intensity. To avoid partial volume effects the inclusion of wall pixels is avoided. The detection of flow regions depends strongly on the resolution of the MRI scan. A minimum lumen diameter of at least three pixels has been quoted [HBV98]. The algorithm that has been developed was tested for lumen cross-section diameters of at least six pixels, well above this level. This work was submitted to Magn. Reson. Med. ([KRM]).

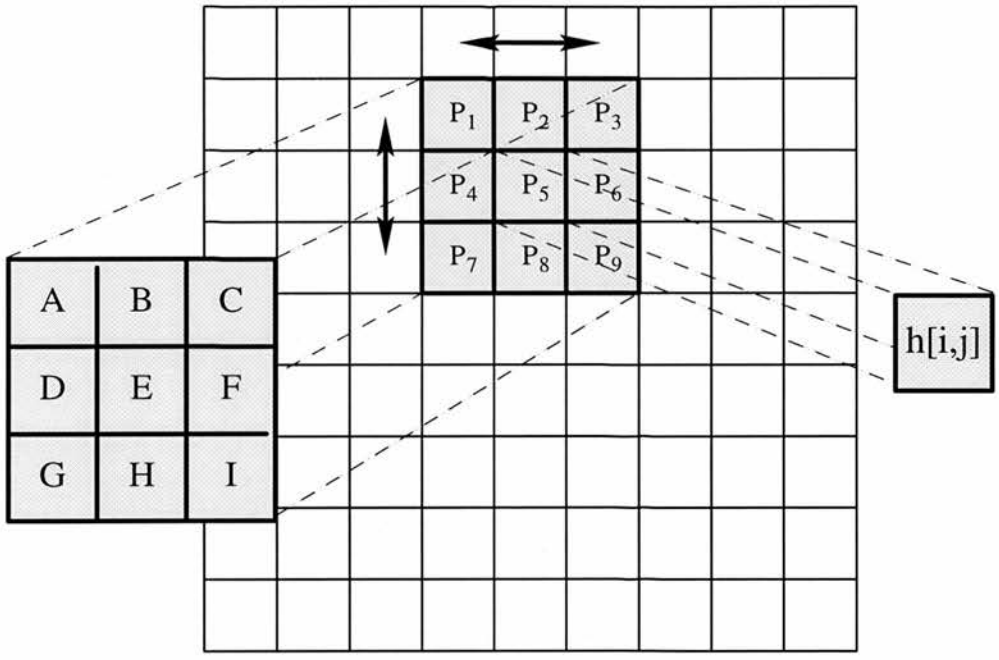

Figure 6.1.: *Convolution filters use a matrix to calculate the new value $h[i,j]$ at point P_5. This matrix is translated across the whole image to create the filtered version. See also Equation 6.1.*

6.2. Theory:

There are two main approaches to manipulate the data in an array representing an image: convolution masks and Fourier filters. Convolution in image space corresponds to a multiplication in Fourier space [Pra78, JKS95].

A convolution filter works by applying a smaller $n \times n$ array mask to every point in the image. The computation scales with $O(n^2)$ and therefore the smallest, sufficient convolution mask should be chosen. In general this will be a 3×3 array. Applying a general 3×3 convolution mask, defined by the matrix:

$$\begin{pmatrix} A & B & C \\ D & E & F \\ G & H & I \end{pmatrix},$$

to calculate the new value $h[i,j]$ for point P_5 that is situated in the local area defined by:

$$\begin{pmatrix} P_1 & P_2 & P_3 \\ P_4 & P_5 & P_6 \\ P_7 & P_8 & P_9 \end{pmatrix}$$

the following formula is applied (see also Figure 6.1):

$$h[i,j] = AP_1 + BP_2 + CP_3 + DP_4 + EP_5 + FP_6 + GP_7 + HP_8 + IP_9. \quad (6.1)$$

Choosing the parameters in the convolution matrix can create very different effects.

The definition of the algorithm results in a loss of information in the outermost frame of the original image. For a 3×3 kernel the first and last row and column remain undefined. Since images are normally chosen to be larger than the object of interest, this loss of information can be tolerated. A number of convolution filters have been used for this work: Gauss, Sobel, Laplace and Laplacian of Gaussian.

One important application of convolution filters is the smoothing of images. A successful algorithm to remove noise drawn from a normal distribution is the Gaussian filter. The

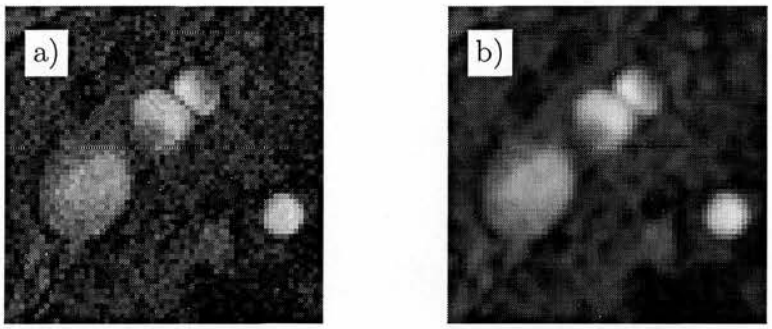

Figure 6.2.: *The effect of a Gaussian convolution filter. The original image is displayed in (a) and the filtered image in (b).*

full rotational symmetry of the Gaussian filter leaves the images undistorted. A common version, which was employed in this work is:

$$\text{Gauss} = \begin{pmatrix} 1 & 2 & 1 \\ 2 & 4 & 2 \\ 1 & 2 & 1 \end{pmatrix} /16. \tag{6.2}$$

The effect can clearly be seen in Figure 6.2 (b). All edges appear softer and noise levels are reduced. The original image shows the magnitude image reconstructed for a slice out of a 3D PC MRI study. The jugular vein, internal and external carotid arteries as well as the vertebral artery on right side of a volunteer's neck can be seen as bright regions.

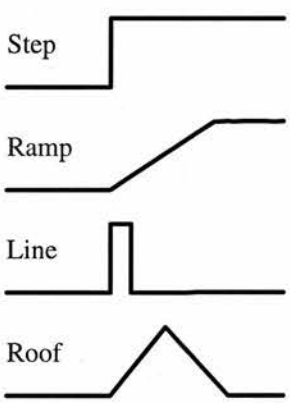

Figure 6.3.: *Possible types of edges in one dimension.*

An edge in an image is a significant local change in the image intensity, usually associated with a discontinuity in either the image intensity or the first derivative of the image

intensity [JKS95]. Discontinuities in the image intensity can be either *step* discontinuities or *line* discontinuities (Figure 6.3). Sharp discontinuities, such as these, rarely exist in real signals, because of low-frequency components or the smoothing introduced by most sensing and imaging devices. Step edges become *ramp* edges and line edges become *roof* edges. In both cases the intensity variation is not instantaneous but occurs over a finite distance. Noise in images, however, poses a problem. Essentially it is a local, but not significant, change in image intensity.

An edge in an image corresponds to an extremum of the first or a zero-crossing of the second derivative (Figure 6.3). The first derivative of an image can be calculated using Sobel filters. The determination of edge pixels for the result still needs some sort of a threshold value. Second derivatives, however, lead to zero-crossings and the value to look for is therefore fixed. Laplacian filters are convolution filters which are used to form the second derivative of an image. Noise, however, is another form of local change in image intensity.

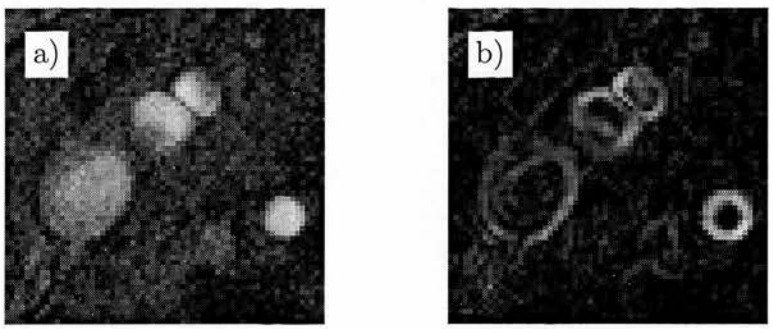

Figure 6.4.: *The effect of a Sobel convolution filter. The original image is displayed in (a) and the filtered image in (b).*

To detect an extremum in the first derivative, the Sobel filter uses two convolution masks: one to detect the gradient along the rows s_x and one along the columns s_y (see [JKS95]):

$$s_x = \begin{pmatrix} -1 & 0 & 1 \\ -2 & 0 & 2 \\ -1 & 0 & 1 \end{pmatrix} \qquad s_y = \begin{pmatrix} 1 & 2 & 1 \\ 0 & 0 & 0 \\ -1 & -2 & -1 \end{pmatrix}. \tag{6.3}$$

The magnitude of the slope is $M = \sqrt{s_x^2 + s_y^2}$, or a faster approximation $M = |s_x| + |s_y|$, since knowledge of the absolute value of the gradient is not always required. The result of Sobel filtering can be seen in Figure 6.4. Edge pixels display a high intensity after application of the Sobel filter. Due to the smoothness of the images, the edges appear rather thick.

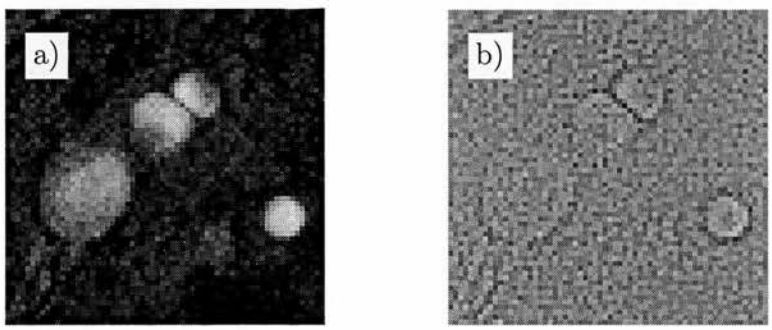

Figure 6.5.: *The effect of a Laplacian convolution filter. The original image is displayed in (a) and the filtered image in (b).*

Edge detection based on the first derivative has to use a threshold, to identify an edge pixel. This narrows down the edges and eliminates noise contributions. A local maximum in the first derivative corresponds to a zero crossing in the second derivative. This can be identified without the use of an additional threshold. The Laplacian, Δ, is the multi dimensional equivalent of the second derivative in one dimension. A common convolution filter representation, that was used in this work, is [JKS95]:

$$\Delta = \begin{pmatrix} -1 & -1 & -1 \\ -1 & 8 & -1 \\ -1 & -1 & -1 \end{pmatrix}. \tag{6.4}$$

The effect of the Laplacian filter is illustrated in Figure 6.5. The results are positive and negative numbers. These can be rendered to a colour scale or, as in this case, to a grey scale with the medium grey representing null. Around the edges a change from higher to lower intensity can be seen.

To eliminate noise, strong filtering before the use of the Laplacian filter is necessary. However, the application of a Gaussian convolution filter followed by a Laplacian filter

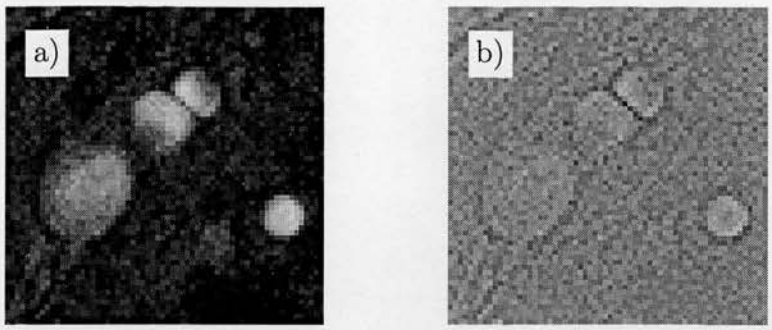

Figure 6.6.: *The effect of a Laplacian of Gaussian convolution filter. The original image is displayed in (a) and the filtered image in (b).*

is possible in one step with a Laplacian of Gaussian (LoG) filter. A 5×5 convolution filter [JKS95] representation, also used here, is:

$$\mathrm{LoG} = \begin{pmatrix} 0 & 0 & -1 & 0 & 0 \\ 0 & -1 & -2 & -1 & 0 \\ -1 & -2 & 16 & -2 & -1 \\ 0 & -1 & -2 & -1 & 0 \\ 0 & 0 & -1 & 0 & 0 \end{pmatrix}. \tag{6.5}$$

A comparison between Figure 6.5, the Laplacian filter, and Figure 6.6, the LoG filter, shows the reduction of noise in the resulting image.

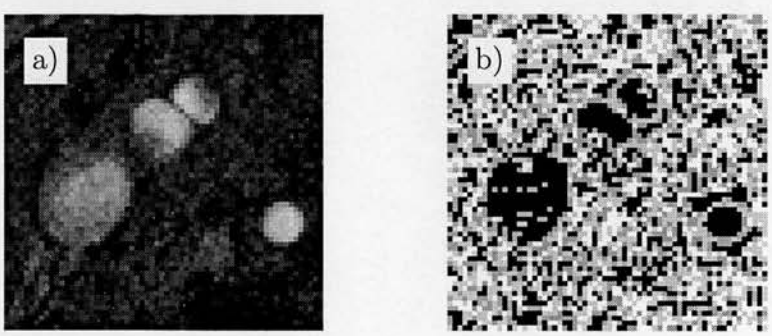

Figure 6.7.: *Edge detection in a Laplacian of Gaussian convolution filtered image. The original image is displayed in (a) and the filtered image in (b).*

The LoG filter produces a map with positive and negative pixel values. At the vessel wall the sign of the second derivative changes and edge detection is reduced to zero-crossing detection in the LoG image. Any pixel with between two and six nearest and

next nearest neighbours of a different sign is marked as part of an edge in the magnitude based edge map (Figure 6.7). A lower or higher number of changes in sign indicates the presence of a single pixel edge which must constitute noise. This edge map allows the detection of flow regions.

6.3. Materials and Methods:

6.3.1. Edge Map Generation

In this work we propose an image processing pipeline that uses the Laplacian of Gaussian (LoG) convolution filter [JKS95] for edge detection on 2D magnitude images and optionally takes the velocity information into account. 3D acquisitions are treated slice by slice. A flow diagram of the whole process is presented in Figure 6.8. Three cases can be identified: a purely magnitude image based approach (**Alg. 1**) and the use of velocity for *in vitro* (**Alg. 2**) and *in vivo* (**Alg. 3**) PC studies. These are followed by a common region filling algorithm. A convolution filter works by applying a smaller $n \times n$ array mask to every point in the image. The computation scales with $O(n^2)$ and therefore the smallest, sufficient convolution mask, a 3×3 array, was chosen.

The first step of the method examines the magnitude images (**Alg. 1**) starting by smoothing them using a 3×3 Gaussian convolution filter [Pra78, JKS95]. This step removes some of the noise in the images. The result is then used as the input to a 5×5 LoG filter [JKS95].

At this point, additional information obtained from the measured velocities can be included. For both *in vitro* (**Alg. 2**) and *in vivo* (**Alg. 3**) acquisitions the variance of the velocity maps is measured separately and combined in one array. For this work it was found that different approaches for the two types of study produced the best results.

A filter was constructed as a measure of local variance in the image based on differences between neighbouring pixel values. Executing a walk around the eight nearest and next nearest neighbour points, the filter sums up the absolute value of the difference between all the pixel pairs encountered and normalises by dividing by 8. The effects of this filter can be seen in Figure 6.9. It shows the velocity map in z-direction from the same acquisition used for the magnitude examples of the convolution filters. Flow towards the

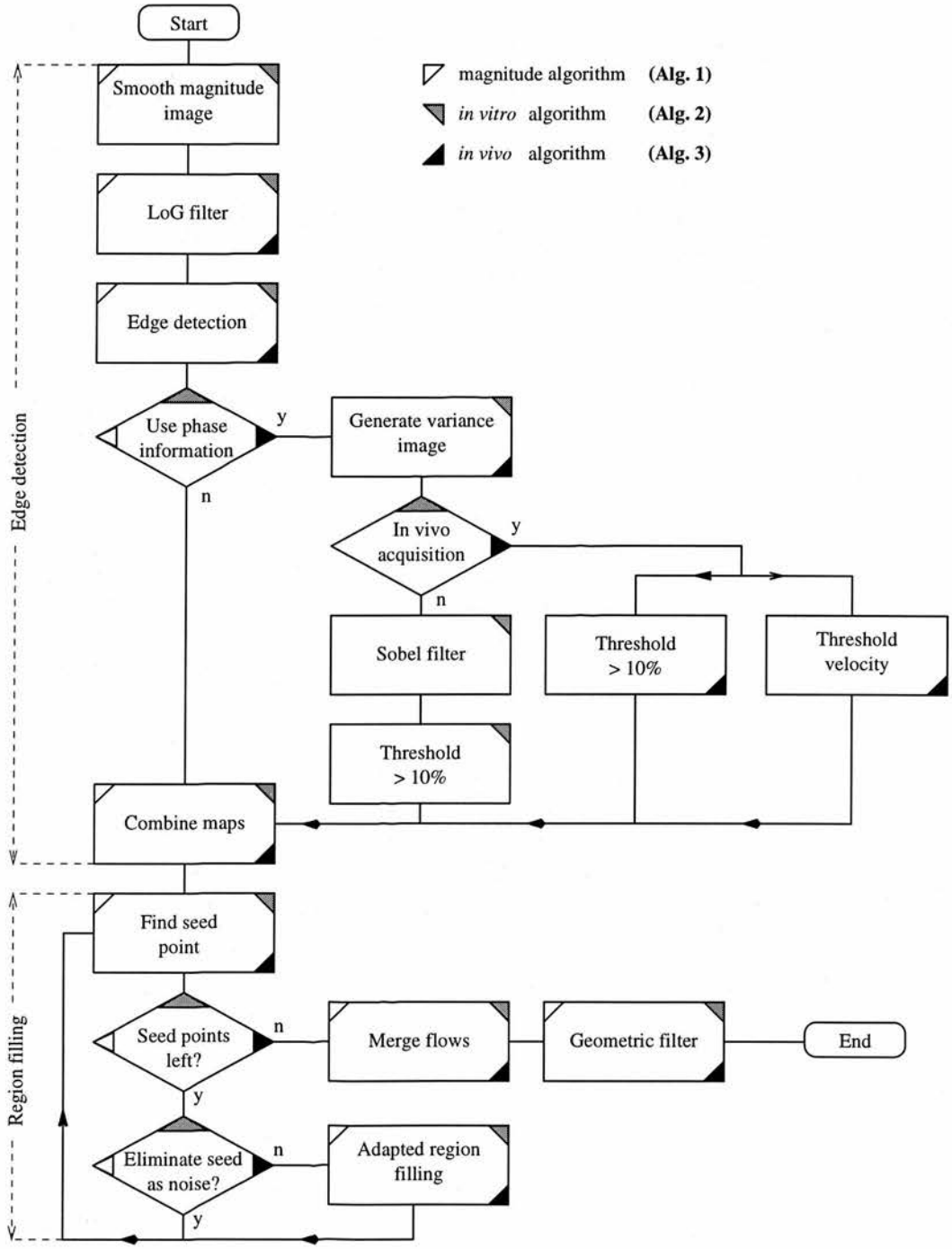

Figure 6.8.: *Flow diagram of the steps to identify flow pixels based on an edge detection based algorithm. (See text for details)*

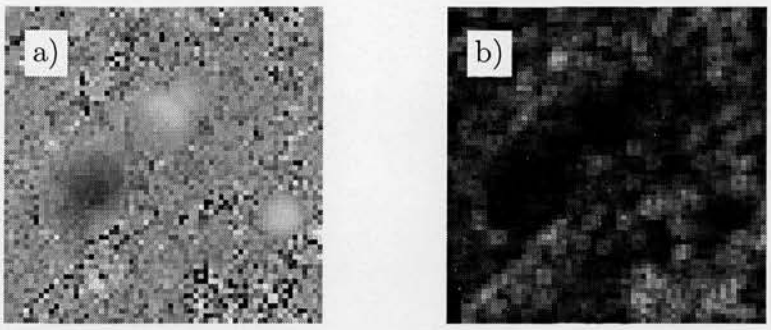

Figure 6.9.: *The effect of the local variance filter. The original image is displayed in (a) and the filtered image in (b).*

head shows up bright on the original image while flow in the opposite directions shows up black. A significant amount of noise can be seen in areas of low intensity on the magnitude image (Fig. 6.7 (a)). The variance filtered image shows low intensity in areas with no noise. Within the flow regions, the velocity is well defined and does not change much between pixels. These regions also exhibit low intensity. For *in vivo* acquisitions, the area outside the vessels does not exhibit a systematically high variance.

For complicated flow conditions a method entirely based on the intensity of the magnitude image can fail to detect the complete flow region. *In vitro* studies often involve fluids flowing in vessels that are surrounded by a material which gives a low MRI signal, such as air. Consequently, areas around such vessels show high phase (i.e. velocity) noise. For these studies (**Alg. 2**) a Sobel filter was used to enhance the edges and a simple threshold of greater than 10 % maximum was sufficient to extract a second edge map based on the velocity information. This map was combined with the magnitude based edge map to produce the final edge map that was used for region filling.

In vivo PC images are often noisy due to the thinness of the slices. In addition, the phase difference maps around blood vessels display a mixture of noise and consistently low values. This makes image segmentation quite difficult. Thresholding on the velocity variance and neglecting velocity data below the level of the acquisition noise provides a map that can stabilise the magnitude flow detection (**Alg. 3**). Since the wall separating blood vessels can be very narrow (one or two pixels), Sobel filtering of the variance data cannot be used to enhance the edges. A pixel was marked as an edge in the final mask when the magnitude mask and at least one of the two other masks indicated the presence of an edge.

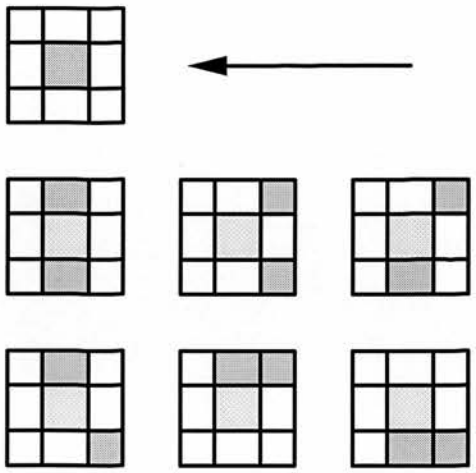

Figure 6.10.: *Boundary conditions for a filling along the row from right to left. The pictures show various stopping conditions for the pixel depicted in the centre (light grey). If the pixel examined is an edge pixel (dark grey) the fill is stopped (shown in the top left). The two rows below show conditions with two edge pixels stopping the fill while the pixel examined is not an edge pixel.*

6.3.2. Region Filling

Once the pixels of the edge had been determined, the region of flow was constructed. The area within each marked edge was filled. The high intensity associated with flow regions has only been used on a relative and local basis. However, pixels above a certain threshold can be employed as seed points for a region filling algorithm. Due to noise, the edge is not always completely closed, causing the filling algorithm to "spill out" from the region of interest. In this case the terminating condition of the filling process is not met, leading to the marking of pixels outside the region of interest.

The region filling employed here was restrictive to avoid including vessel wall pixels. Connected regions were merged after the filling process, and regions not filled from the first application of the algorithm should be filled from a subsequent one. Starting from the seed point, assumed to lie near the centre of the region, each pixel in adjacent rows was examined. This process was then repeated along the columns. Four different

stopping conditions can be identified corresponding to the left, top, right and bottom edge. Only the algorithm applied to horizontal filling towards the left is discussed, since the other cases follow from proper rotation. The filling in the row was stopped if the pixel under examination was marked as an edge pixel. In addition, the pixels situated above and below, as well as those positions in the column to the right, were checked. If more than one of those pixels had been marked as an edge pixel the filling was stopped. Figure 6.10 shows the terminating condition and the additional check with two other pixels marked as edge pixels. The region filling seed for each pass of the algorithm was the highest intensity pixel in the magnitude image, that was not marked as part of a flow region. If no seed with an intensity higher than a chosen threshold was left, the filling was stopped. This threshold is the only parameter that is interactive.

At the end of the filling step, the flow regions were represented by a collection of pixel coordinates. All detected flows in a data set were checked for connectivity at this point. Initially, for speed of computation, the bounding boxes were examined for overlap. Overlapping flows were then checked for connection of nearest neighbours and merged.

6.3.3. MRI

The Elscint Prestige 1.9 T MRI scanner (GE-Elscint, Haifa, Israel) was used to acquire imaging data sets in this study. A 2D phase contrast sequence was used for the phantom studies with a pixel size of 0.6 mm × 0.6 mm, 11 mm slice thickness and 256 × 256 matrix. The values selected for the timing parameters were repetition time $T_R = 20$ ms, echo time $T_E = 8.8$ ms and a flip angle = 30^o. All three velocity components were measured.

The 3D phase contrast *in vivo* studies were carried out with the following parameters: pixel spacing 0.6 mm × 0.6 mm, 1.5 mm slice thickness, 256 × 256 pixels image size in a slab of 36 slices. Slightly longer timing values were necessary: $T_R = 24$ ms, $T_E = 10.8$ ms and flip angle = 30^o. All three velocity components were measured.

The flow phantom (Section 5.3.1) consisted of rigid plastic pipes connected in series by PVC tubing. In all experiments presented here, a constant flow of water was used (up to 40 ml/s).

The 3D MRA studies of healthy volunteers followed a standard clinical protocol. The pixel size was 0.8 mm × 0.8 mm, with 1.2 mm slice thickness, for a 256 × 242 matrix in

a slab of 64 slices. The values used for the timings were $T_R = 38\,\text{ms}$, $T_E = 5.8\,\text{ms}$ and flip angle $= 28^o$ and a saturation band was placed superior to the region of interest to eliminate signal from veins.

Experiments were also carried out on the GE Signa 1.5 T MRI Scanner (GE, USA) using a straight PVC tube of 12 mm inner diameter. The tube was positioned parallel to the scanner axis at the iso-centre and moved about 6 cm horizontally. The standard 3D PC velocity sequence supplied on the GE scanner was used with a pixel size of $0.8\,\text{mm} \times 0.8\,\text{mm}$, 1.0 mm slice thickness and 256×128 matrix. The values selected for the timing parameters were repetition time $T_R = 30\,\text{ms}$, echo time $T_E = 8\,\text{ms}$ and a flip angle $= 30^o$. All three velocity components were measured.

6.4. Results and Discussion:

6.4.1. Magnitude Only Algorithm (Alg. 1)

Although MRA does not provide velocity maps, the magnitude based part of the algorithm (**Alg. 1**) can be applied to detect flow regions. In Figure 6.11 the results are presented from a 3D (TOF) MRA data set for a healthy volunteer's neck. Slices immediately inferior (Figure 6.11 (c) and (d)) and superior (Figure 6.11 (a) and (b)) to the carotid bifurcation were selected for presentation. The common, internal and external carotid artery as well as the vertebral artery show high intensity on the MRA slices. Flow regions detected by the magnitude image based algorithm (**Alg. 1**) are marked in Figure 6.11 (b) and (d).

As PC magnitude images resemble TOF MRA data, the algorithm works reliably in MRA data. As the detected area is restricted to a minimal approximation of the flow regions, the method presented here is ruled out for the detection of stenosis and unusual vessel cross-sections.

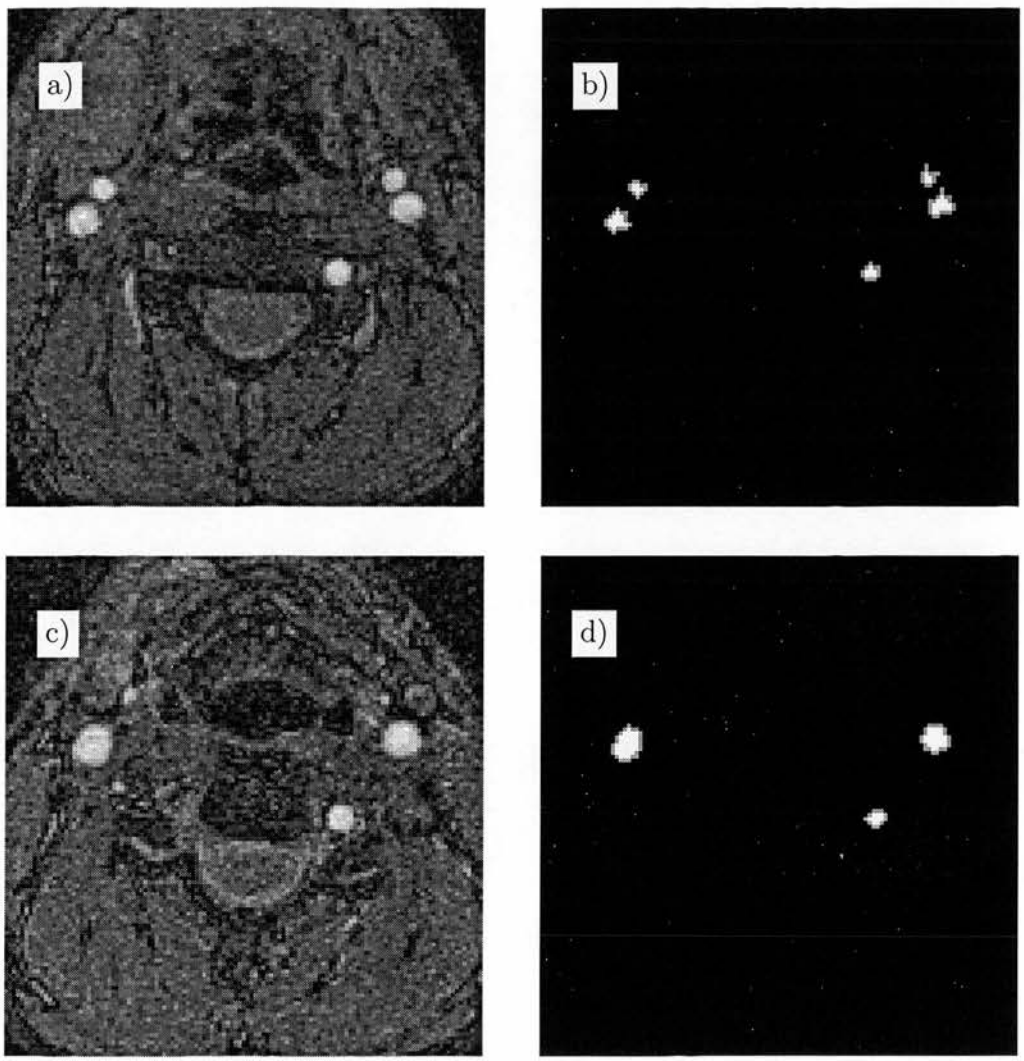

Figure 6.11.: *TOF MRA results superior to the carotid bifurcation (***a***) and (***b***) and inferior to the carotid bifurcation (***c***) and (***d***) in a volunteer's neck. Figures (***a***) and (***c***) show the magnitude images, while (***b***) and (***d***) show the flow detected with the purely magnitude based algorithm (***Alg. 1***).*

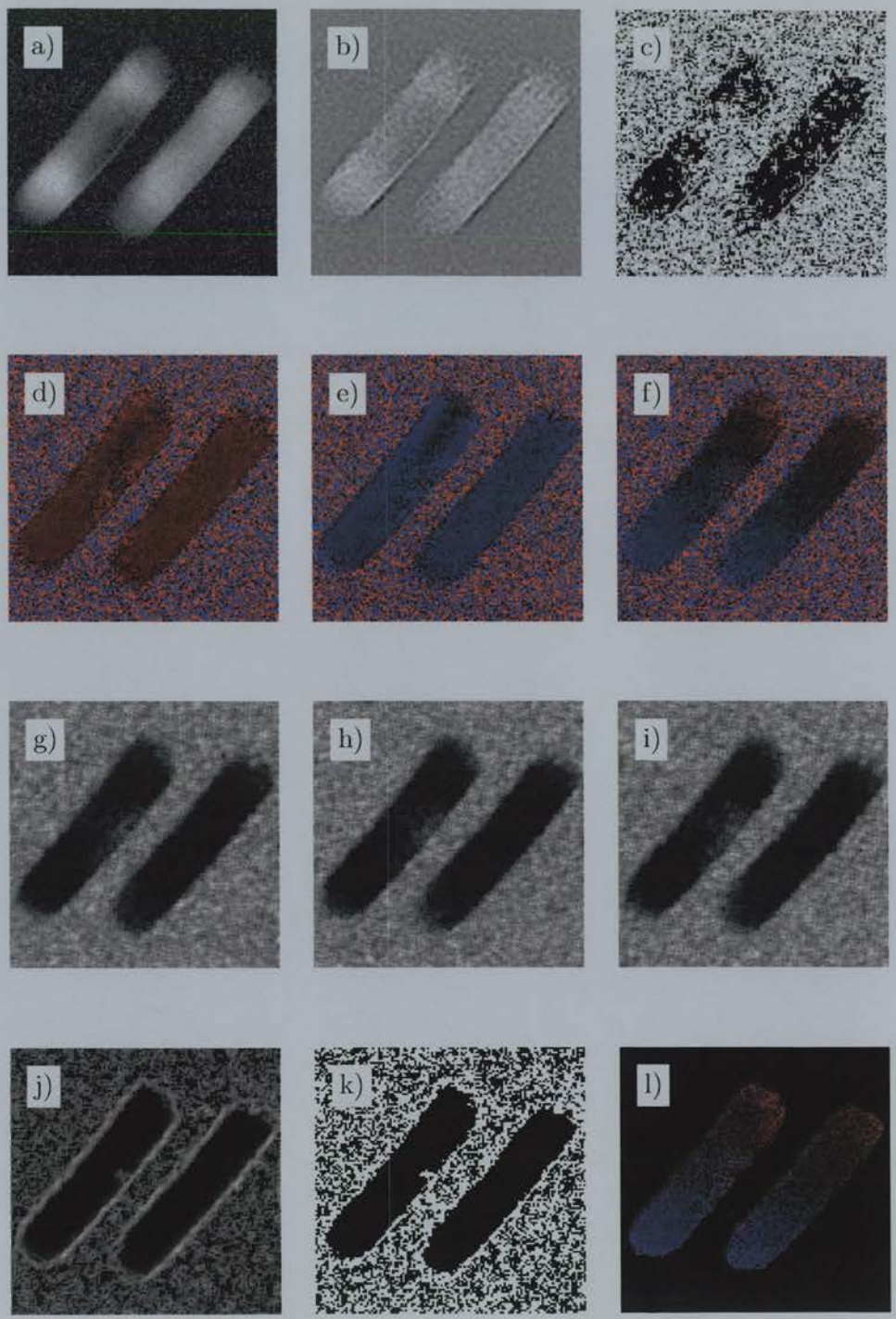

Figure 6.12.: *Velocity data for a slice through* 180° *bends acquired using phase contrast MRI: results of the different steps of the in vitro algorithm (***Alg. 2***) leading to the velocity mask in z-direction (l). For details see text.*

6.4.2. The Algorithm Step by Step: In Vitro Case (Alg. 2)

An example of the algorithm developed for *in vitro* PC acquisitions (**Alg. 2**) is shown for a complex flow in bends at a 45° degree angle to the frequency and phase encoding directions (Figure 6.12). The fluid enters the slice in both bends at the top right corner of the image and leaves it at the opposing side. As it is difficult to maintain a circular cross-section in bent tubes or pipes, the tubes in this phantom possessed an irregular shape. The resulting complex flow field was ideal to test the flow detection under these difficult conditions. The first row in Figure 6.12 shows the results of the individual steps of the part of the technique based purely on magnitude information (**Alg. 1**): the magnitude image (Figure 6.12 a); after the application of the Laplacian of Gaussian filter (Figure 6.12 b); and the resulting edge map following the detection of zero-crossing points (Figure 6.12 c). After application of a Laplacian of Gaussian filter, the centre of the grey scale in the image presented was assigned to null (seen in the background), positive values appear brighter and negative values darker. The application of a LoG filter to an image produces the second derivative and edges show up as regions which change in sign between positive and negative values. The edge map (Figure 6.12 c) represents the number of sign changes for every pixel with its neighbours (Figure 6.12 b). In order to eliminate noise, edge pixels with one, seven or eight sign changes are discarded.

The remaining images in Figure 6.12 represent the generation of the additional information from the phase difference maps (**Alg. 2**). Phase maps were acquired with velocity encoding for three orthogonal directions. These are shown in Figure 6.12 (d) - (f) for the x-, y- and z-direction respectively. Within the flow regions, the phase shift is proportional to the velocity, while outside, in air, the magnitude of the signal is very low, and the phase is essentially random. Consequently, the variance (noise) of the phase maps is low inside the region of flow (Figure 6.12 (g) - (i)) and high outside. To enhance the appearance of edges, the combination of the variances is treated with a Sobel filter (Fig. 6.12 (j)). The map created by the Sobel filter is a measure of the first derivative, where the edges show up brightly, if somewhat broad. Combining this information with the edge map for the conventional image (Fig. 6.12 (c)), using logical AND, generates a combined edge map (Fig. 6.12 (k)). Region filling results in the masked image for the phase difference in the z-direction (Figure 6.12 l).

To test the algorithms, a complex flow pattern that occurred in a bend with irregular cross-section was imaged. When the magnitude image (Figure 6.12 (a)) was compared with the phase difference maps (Figure 6.12 (d)-(f)) it was evident that the high intensity regions, due to the inflow effect, in the conventional image did not cover the complete flow region. However, the algorithm which combined the magnitude and velocity information (**Alg. 2**) detected the flow region reliably (Figure 6.12(l)). The increased stability of the detection is demonstrated in the number of pixels inside the flow region, that are not marked as an edge in the combined edge image (Figure 6.12 (k)) when compared to the initial edge image (Figure 6.12 (c)). The improvement in stability is well worth the additional time spent on the more complex calculation. However, phase wrapping has to be avoided when velocity information is used since this leads to a loss in dynamic range of the velocity data. An encoding velocity chosen too low leads to phase distortions that can only be unwrapped locally after flow detection. They would, however, appear as a high variance in the phase maps, and the edge maps based on the variance would contain false edges. The reliability of this method for this particular case of complex flow demonstrates the robustness of the algorithm.

6.4.3. The In Vivo Algorithm (Alg. 3)

Results from the *in vivo* method (**Alg. 3**) that uses the velocity variance and enforces a minimum velocity are presented for a healthy volunteer using a 3D PC sequence (Figure 6.13). The volunteer gave informed consent prior to the scan. The results were cropped to display the right part of the neck (left part of the image). The magnitude images show the carotid and vertebral arteries and the jugular vein with bright inflow effect. Slices in the carotid artery bifurcation (middle row), as well as slices superior (top row) and inferior (bottom row) to the bifurcation, were chosen from the 3D data set. After the application of the flow detection algorithm, only the detected velocities (right column) remain from the original phase maps in the centre column.

The detected flow regions were used to construct the surface of the vessel with VTK (Kitware Inc, Clifton Park NY, USA) and a surface rendered image of the reconstruction is presented (Figure 6.14). A magnitude image is displayed at the volume centre to aid

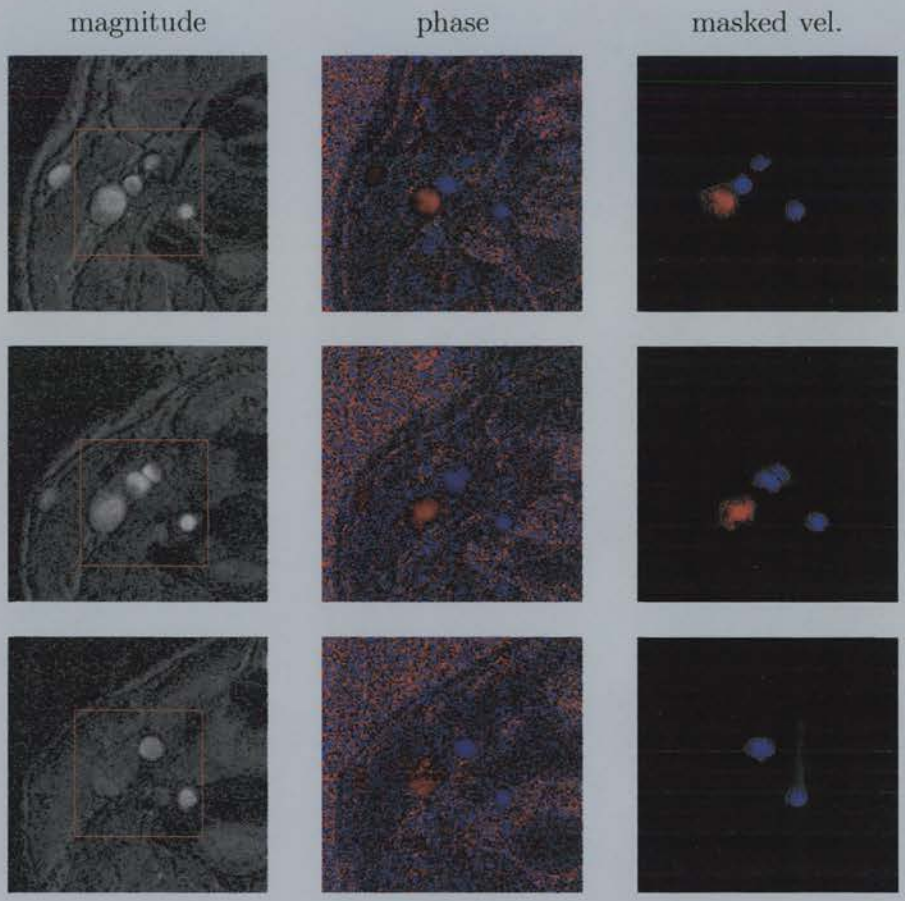

Figure 6.13.: *Flow detection in a PC MRI study of the vessels in the right hand side of a volunteer's neck showing the carotid arteries, the vertebral artery and the jugular vein. The magnitude, phase difference in the superior-inferior direction, and the final masked velocity images as detected by the in vivo algorithm (***Alg. 3***) are displayed. The jugular vein loses intensity in the magnitude images before it reaches the bottom of the volume of interest (indicated by the red squares) and is consequently not detected in the inferior slice.*

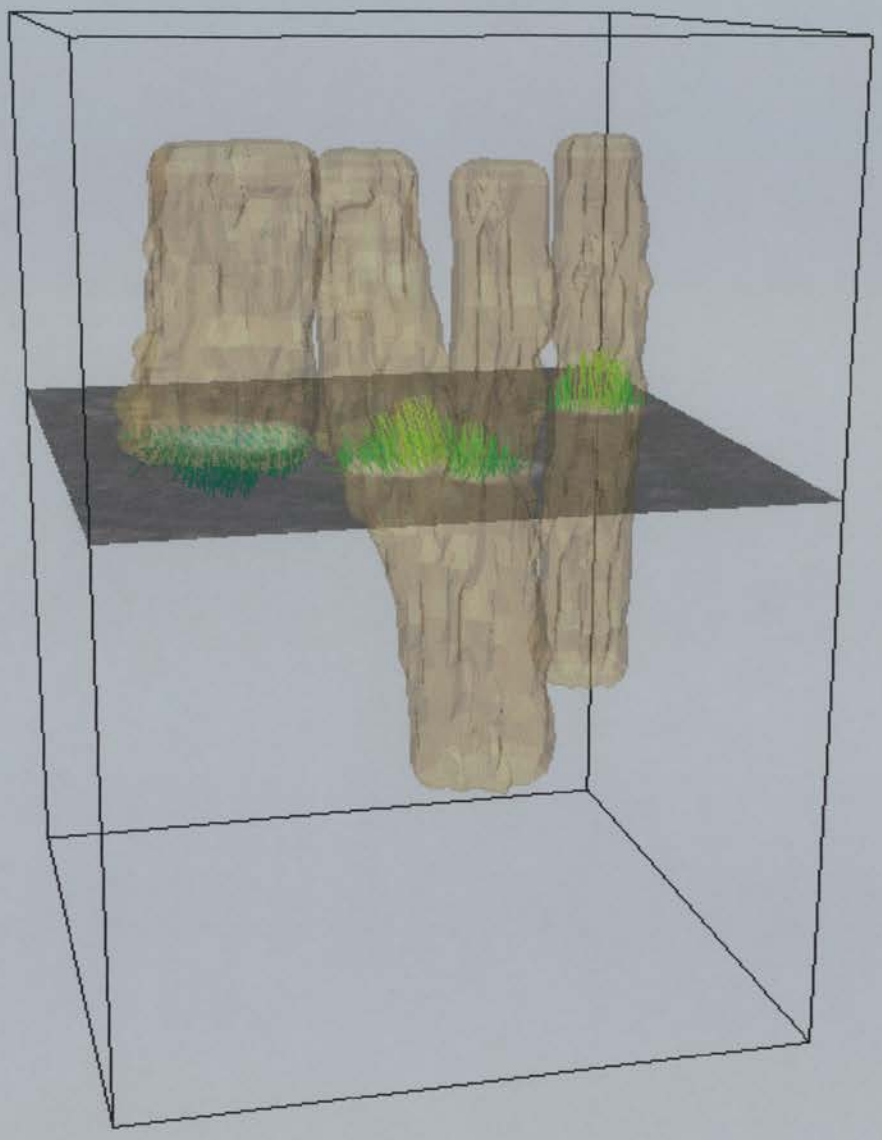

Figure 6.14.: *Reconstructed vessels in the right hand side of a volunteer's neck obtained using PC MRI. Transparent surface rendering of the detected vessels is displayed with a transparent magnitude image showing the slice bisecting the carotid bifurcation. The lines represent the time-averaged velocity vectors measured in the slice shown.*

orientation. Time averaged velocity vectors originating within the flow regions from that slice are also displayed.

When comparing the magnitude images with the phase difference maps (Figure 6.13) it is evident that the high intensity regions depend only slightly on the flow velocities. In the masked velocity map based on the *in vivo* algorithm, only the carotid arteries and the vertebral artery show up in all slices, as was specified for the final region filling. The low intensity and noisy signal associated with veins does not permit them to be easily distinguished from stationary tissue. This presents a huge detection challenge. To characterise venous flow, a lower flip angle could be used to avoid the saturation of spins in slow flowing blood. However, the algorithm combining phase and magnitude information reliably detects the arterial flow regions (Figure 6.13). The dynamic range of velocity measurement is limited, since the phase based part of the algorithm cannot handle phase wrapping.

6.4.4. Tuning and Validation

The effect of the threshold parameter used to choose seed points for the region filling algorithm is compared with simple thresholding using the same value (Figure 6.15). The results of a Phase Contrast MRI study on the neck of a healthy volunteer (Figure 6.13, middle slice) were used for the comparison (Figure 6.15). The *in vivo* (**Alg. 3**) algorithm was employed as the edge detection method. For region growing algorithms a threshold of the mean intensity between intra-luminal and the surrounding signal has been suggested [PSE+91, TBP93]. That value would correspond to about 40 % - 50 % of the maximum intensity in the image. Application of **Alg. 3** shows the masked velocities in the z-direction, with high intensities assigned to flow in the superior direction (arteries) and low values to inferior direction flows (veins). The images generated by simple thresholding show the pixels of the magnitude image for each threshold value.

The edge detection *in vivo* algorithm (**Alg. 3**) is more stable than simple thresholding above a certain value, as illustrated in Figure 6.15. A flow region is either found or remains undetected. Over a range of threshold values from 90% to 30% only a few pixels are added to the arterial flow region using the new algorithm. This helps to distinguish arteries from veins, which are only detected at lower threshold values. Arteries tend

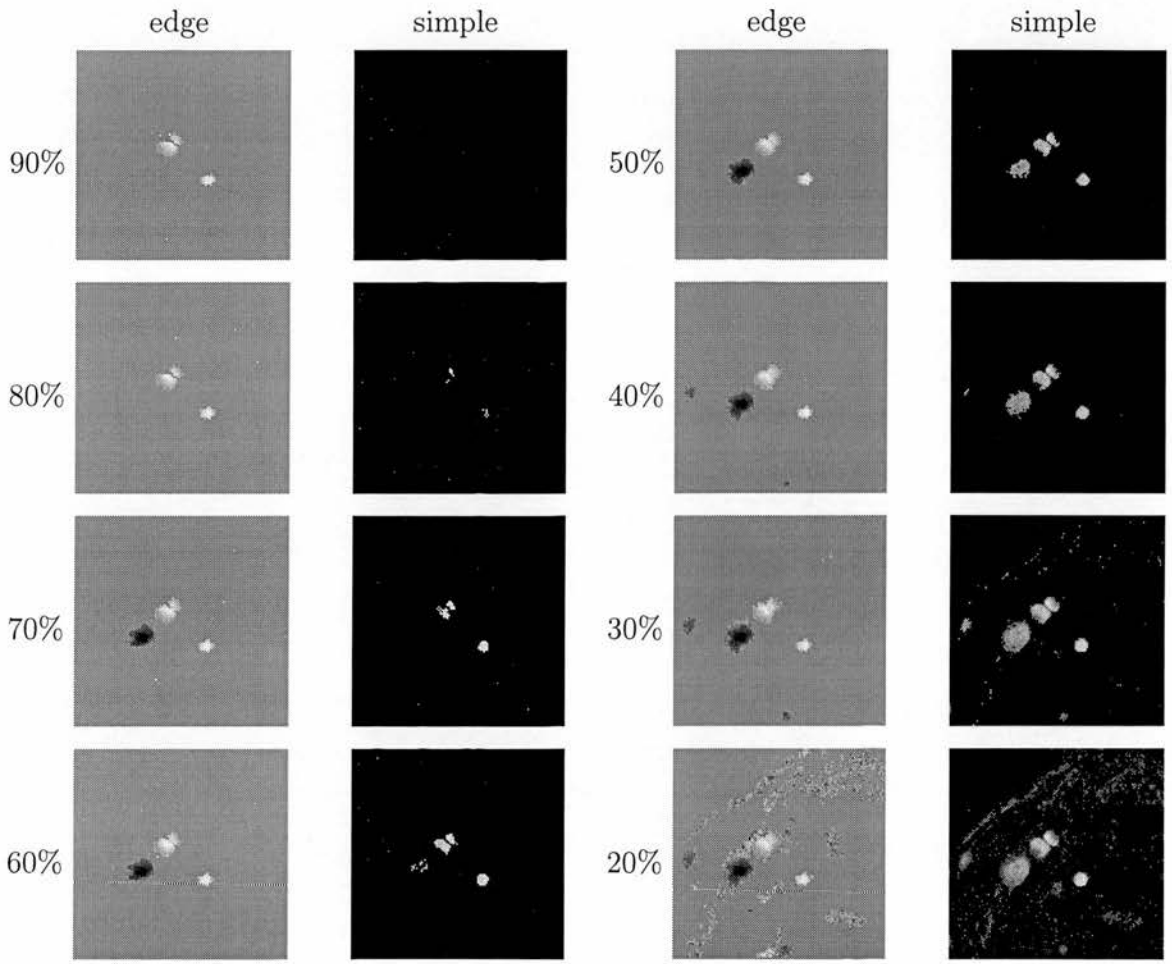

Figure 6.15.: *A direct comparison between values for the threshold parameter in the edge detection in vivo algorithm (***Alg. 3***) and a simple thresholding algorithm. All thresholds are from the given level to maximum intensity. The same slice was used in Figure 6.13 centre row.*

to have a higher maximum intensity within the cross-section than veins. It is these maximum values that are used as seed points in the region filling. Veins tend to change their maximum intensity throughout a 3D acquisition. This can clearly be observed in Figure 6.13 where the intensity of the jugular vein drops significantly from the superior slice to the inferior slice. This is due to increased saturation of spins in the slower venous blood during the passage of the 3D slab. The threshold value can be used to distinguish between arteries and veins in either single slices or as part of a 3D slab.

The quantitative analysis of the detected cross-sectional area was performed on a flow phantom with straight tubes and steady flow (Fig. 6.16). The distribution of areas detected by the new algorithm (**Alg. 1**) was studied for 70% threshold and compared to the expected area for a perpendicular plane through the (5 ± 0.1) mm radius plastic pipes. For the quoted resolution, the number of pixels completely and partially covered by the vessel cross-section is between 88 and 97 depending on the position of the grid centre. The histograms of the two independent series of experiments are shown for the same pipes (Fig. 6.16 outflow in black and inflow in white). The variation of the detected area with varying flow rates was examined using data from four tubes with two sizes: 3 mm and 5 mm inner radius. Constant flow was used during the acquisitions.

The histogram in Figure 6.16 (a) proves that the detected flow area is always smaller than the calculated maximum (vertical dashed line). Close visual inspection of the images shows that no pixel outside the area which is obviously flow in the magnitude image is detected. The algorithm (**Alg. 1**) returns a minimum approximation of the flow, as intended. A slight dependence on the flow volume can be seen in Fig. 6.16 (b). This is due to the decrease in the signal-to-noise ratio with decreasing flow rate. A conservative approach will always miss more pixels in low signal-to-noise images. However, the effect is small enough not to influence the studies of flow profiles. Again, the detected flow areas are all below the expected maximum value (horizontal dashed lines). It is interesting to note that the area of flow detected in outflow regions seems to be more stable. This was probably associated with the larger polarisation of the spins in these regions. The spins flowing into the phantom via the long (about 2 m) straight tubes spend approximately 1 s in the B_0 field before entering the slice of interest. For water, with $T_1 \approx 3$ s full polarisation is not be achieved. Spins in the outflow regions have spent more time in the magnetic field and an enhanced polarisation should be achieved.

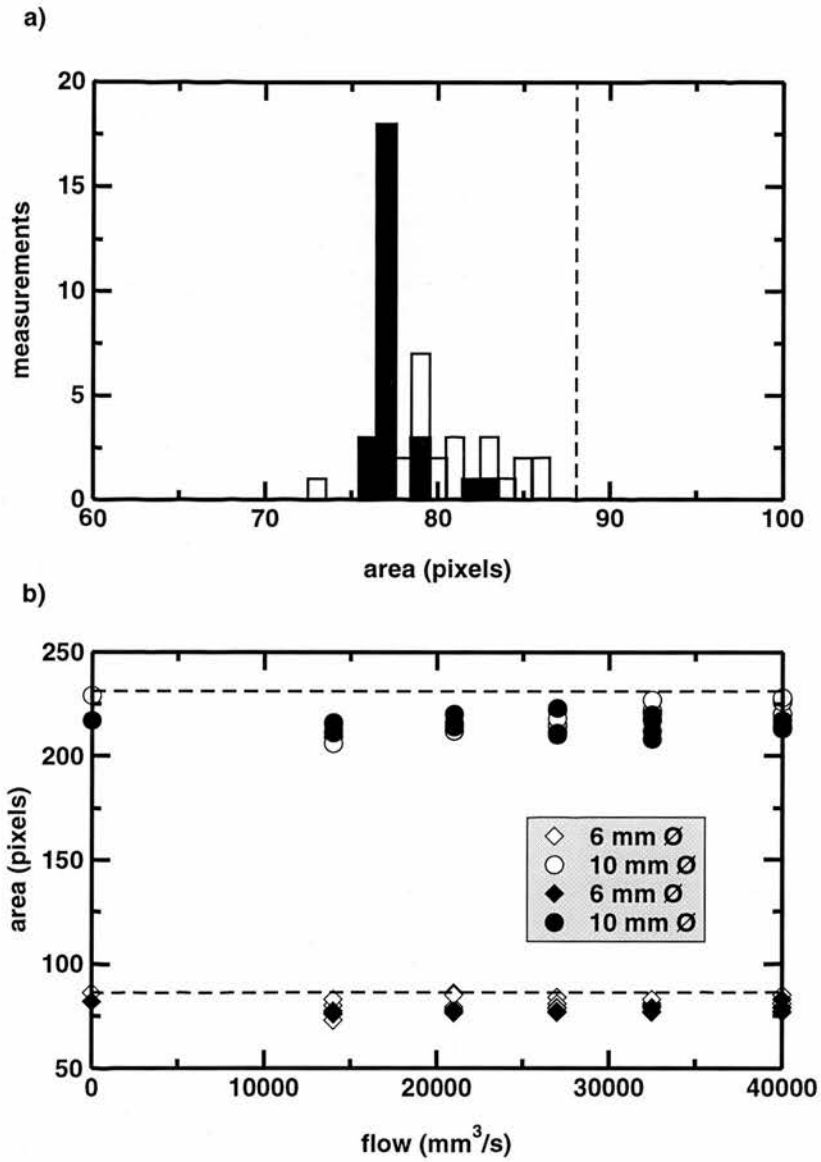

Figure 6.16.: *(a) Histogram of the area detected with the automated flow detection (***Alg. 1***) for two independent experiments on the same in vitro vessel. Measurements were performed at several different flow rates. The data for the inflow is presented in white and for the outflow in black. (b) The dependence of the flow detection algorithm (***Alg. 1***) on flow rate for four different tubes of two diameters. Open symbols represent the inflow and black symbols the outflow. The dashed lines represent the maximum expected number of pixels.*

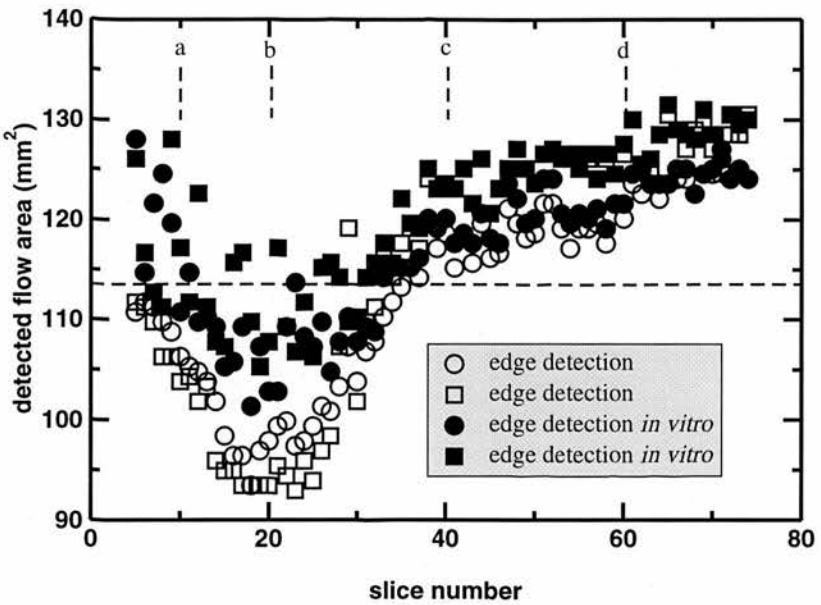

Figure 6.17.: *The variation of the detected flow area in a 12 mm inner diameter tube with slice number. Two different encoding velocities were used at the isocentre and offset horizontally. The areas detected by the purely magnitude based algorithm (***Alg. 1***) and the in vitro version (***Alg. 2***) are presented. The lines and letters mark the position of the example images shown in Figure 6.18*

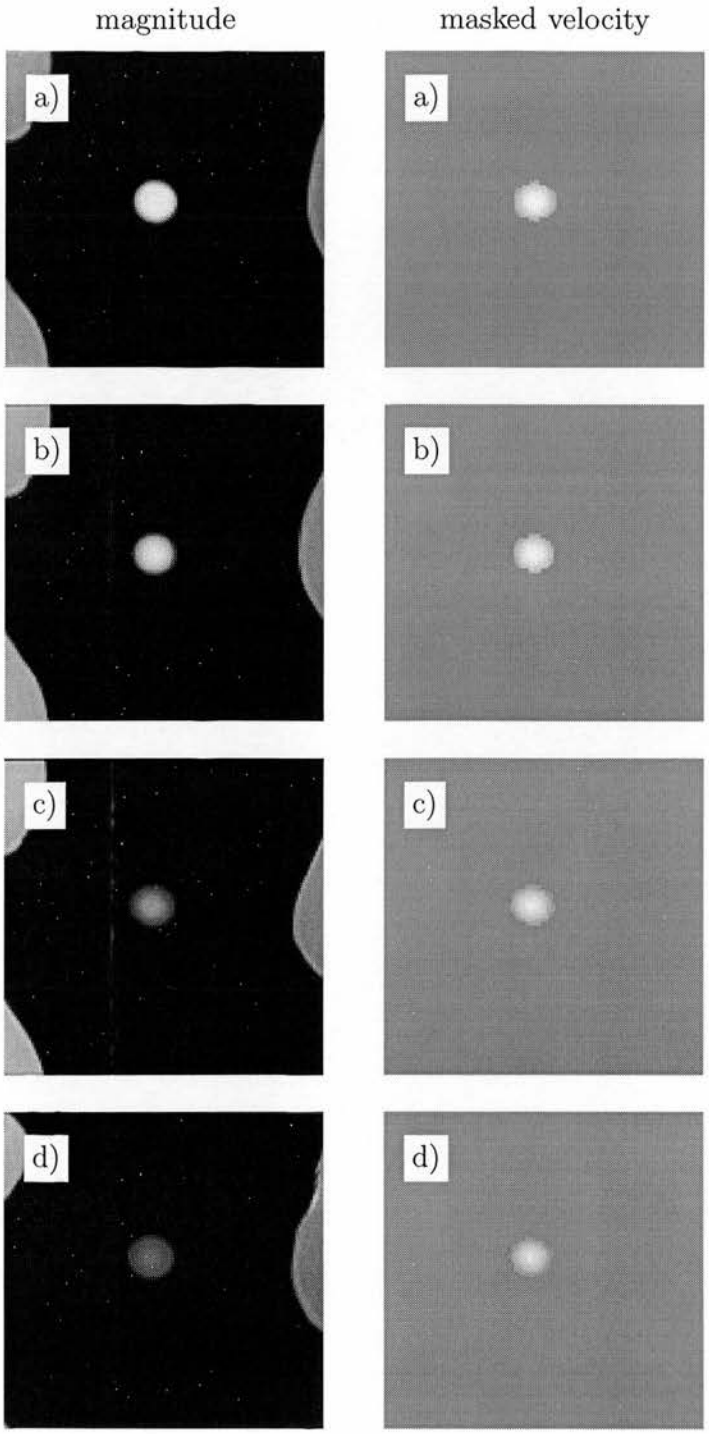

Figure 6.18.: *Selected magnitude and masked velocity component (in z-direction,* **Alg. 2***) images from a straight tube phantom. The flow area is presented in Figure 6.17.*

Using a straight tube phantom, the flow area can be verified. Figure 6.17 shows the variation of the detected flow area with slice number. The slice number corresponds to the position in superior / inferior direction. The theoretical value is shown as a dashed line. As expected, both the magnitude based algorithm (**Alg. 1**) and the *in vitro* method (**Alg. 2**) underestimate the area in the region of the well defined inflow artefact around slice 20. An example of the magnitude image and detected area are presented in Figure 6.18 b. The first slices might contain a slight phase wrapping contribution from the other end of the 3D slab leading to a slightly higher detected area. Slice ten is presented as an example (Fig. 6.18 a). Due to saturation effects, the intensity of the flow regions on the magnitude images decreases as the spins proceed through the excited slab. This leads to an increasingly difficult detection. The area increases as the definition of the edge against the noise becomes more difficult. In slice 40, the intensity of the flow region is already markedly reduced (Fig. 6.18 a) and in slice 60 the edge becomes difficult to differentiate when looking at the image (Fig. 6.18 d). This loss of intensity leads to a higher number of wall pixels being included in the detected area. These are easiest to spot in the masked velocity due to the fact that their velocity is not very well defined. Still, both algorithms return areas that are close to the theoretical value. The expected area for the true radius plus one pixel would be 132 mm^2, a value that is not exceeded by either method even for the very difficult higher slice numbers.

6.5. Conclusion:

The edge detection based algorithms for the identification of flow areas in MRA experiments works reliably on time of flight, *in vivo* and *in vitro* phase contrast MRA. Flow in arteries and rigid vessel phantoms is successfully detected when it exhibits an area with a diameter larger than 6 pixels and produces a bright inflow effect on the magnitude images. For complex flows, a method was developed that employed velocity information to stabilise the results. However, the dynamic velocity range is lost in these acquisitions, because phase unwrapping cannot be performed before the application of the flow detection. The method has only one variable parameter, which is insensitive. The result is stable for a variation in the parameter over a wide range of values. It can be determined for a given set of imaging parameters and subsequently kept fixed. The fully

automated procedure is completely reproducible and largely operator independent. The provision of a method that greatly reduces the work-load of the operator while detecting flow regions makes detailed haemodynamic studies of arteries significantly easier.

All image filters have been applied to 2D slices rather than 3D slabs. For voxels with similar dimensions in all three directions this could be extended to the use of 3D convolution filters. However, this approach was not implemented since it take considerably longer.

7. Wall Shear Rate Calculation

7.1. Velocity Validation

Before any post-processing was attempted, a check of the velocity measurement produced with the PC MRI sequences on the Elscint and GE scanner was carried out. This validation encompassed an estimate of the velocity noise per voxel and the precision of volume flow rate measurements.

Using the velocity offset and standard deviation in stationary material situated near the iso-centre of the magnet, the velocity noise per voxel was estimated. On the Elscint scanner a bottle of doped water was scanned as a part of other experiments at a variety of encoding velocities. The pixel size used was 0.58×0.58 mm in an 11.1 mm thick slice. The minimum $T_E = 8.8$ ms and $T_R = 20$ ms were combined with a tip angle of 30^o. All three velocity components were measured.

Figure 7.1 shows the dependence of the velocity offset and standard deviation of stationary water as a function of encoding velocity for the Elscint scanner. Systematic offsets, below the noise level, are demonstrated at all possible encoding velocities except at the lowest setting. A rough estimate of the velocity noise was made, where approximately 5% encoding velocity (v_{enc}) satisfactorily describes the data. Obviously, the noise increases in regions with very low intensity.

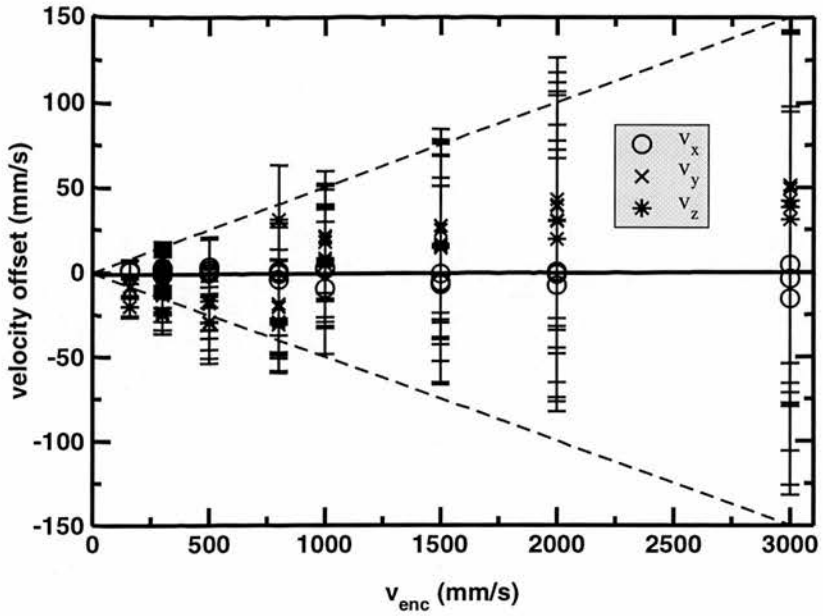

Figure 7.1.: *The variation of the velocity measured in stationary water with encoding velocity for the Elscint scanner. The dashed lines show 5% encoding velocity.*

Experiments on the GE scanner produced similar results for stationary water in a slice at the iso-centre of the coil, although the general trend is towards smaller errors (Figure 7.2). However, looking at the variation of the velocity offset with the slice number (i.e. z-position) for four independent regions of interest in each slice reveals a strong systematic error in the z-component of the velocity (Figures 7.3 and 7.4). The x- and y-components of the velocity appear to be independent of the slice position in z - direction. Figures 7.3 and 7.4 show the results for an encoding velocity of 200 and 1000 mm/s respectively. Plotting the velocity offset as a percentage of the encoding velocity against the slice number for several different encoding velocities (Figure 7.5), it became clear that the correlation between encoding velocity and offset is a non - trivial problem. However, the effect seems to get worse with low encoding velocities, i.e. high gradient strength, which suggests a problem with eddy currents or Maxwell terms.

Measuring the velocity offset in stationary material may not produce useful results. Another method to determine the spatial dependence of the velocity measurement is an examination of the experimental volume flow rate compared to the known flow rate. For the Elscint scanner (Figure 7.6), the bend phantom used with both bend radii

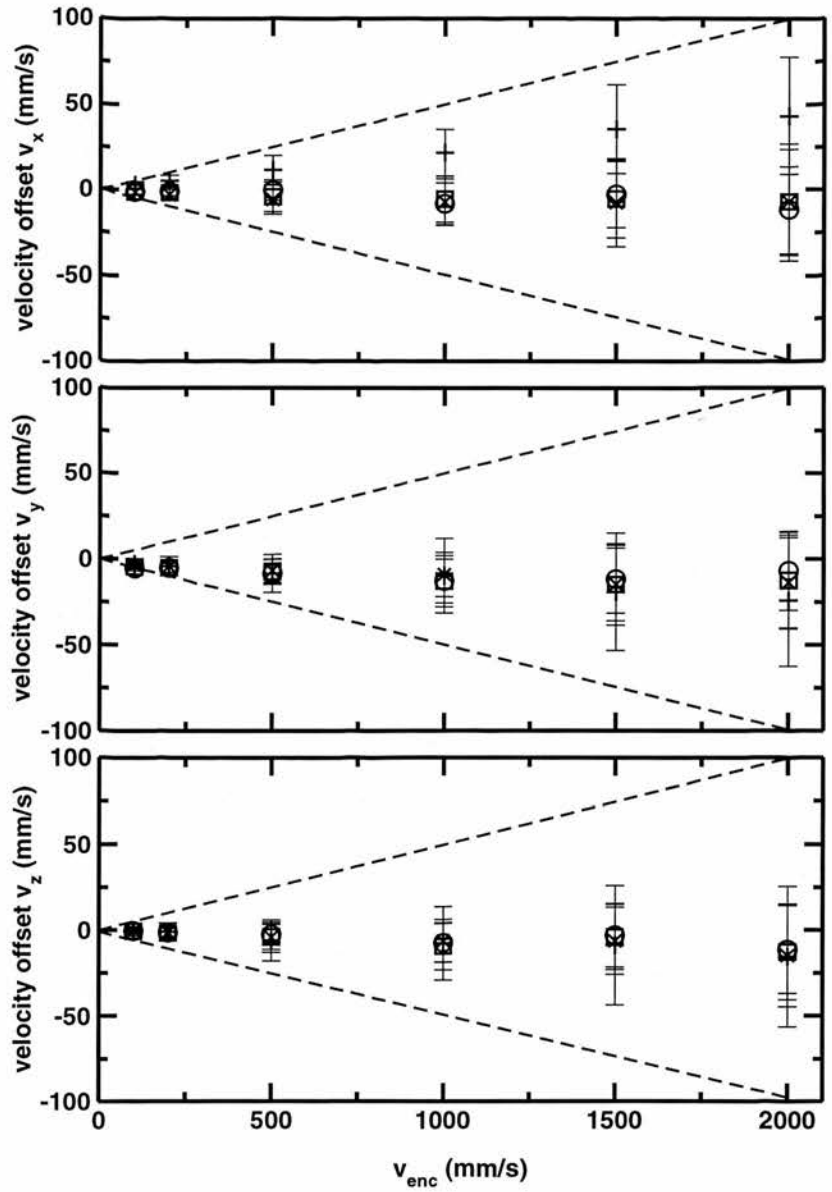

Figure 7.2.: *The variation of the velocity measured in stationary water with encoding velocity for the GE scanner. The dashed lines show 5% encoding velocity.*

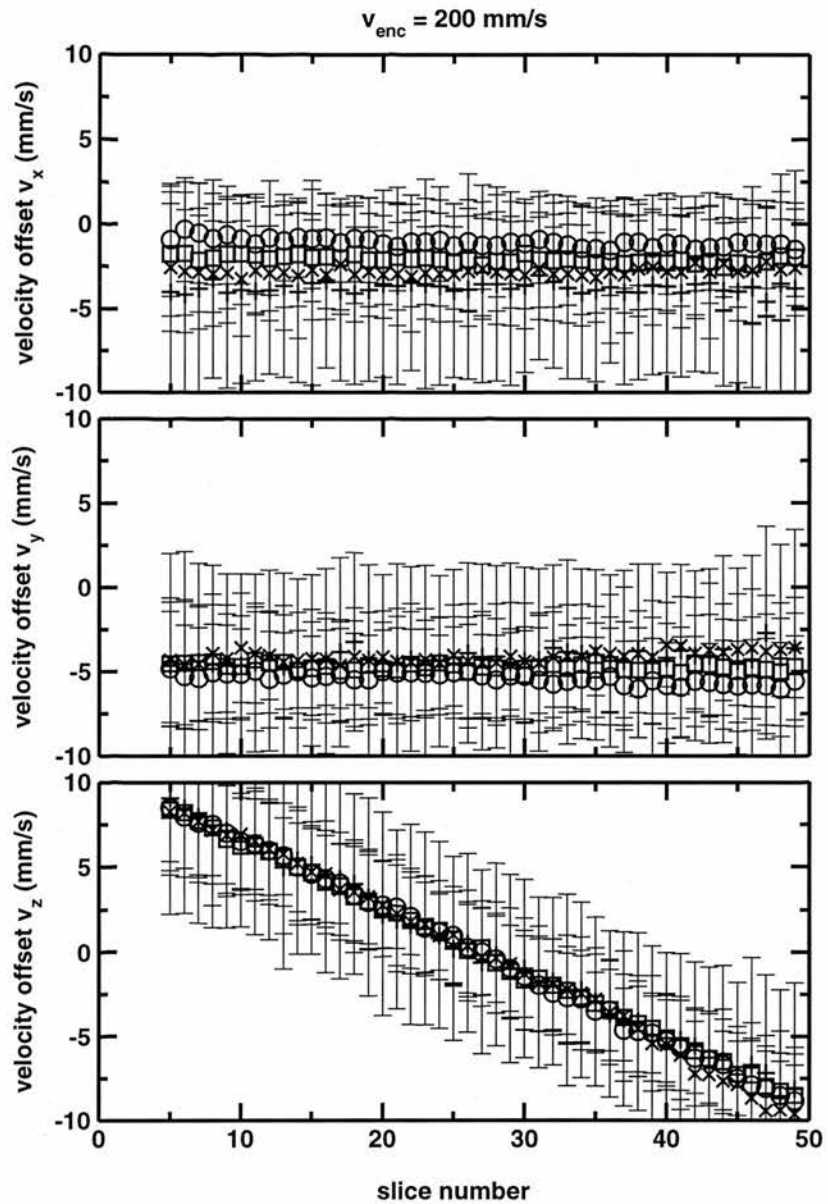

Figure 7.3.: *The variation of the velocity measured in stationary water with slice number (z-position) for the GE scanner. Four independent regions of interest (indicated by different symbols) are shown for an encoding velocity of 200 mm/s.*

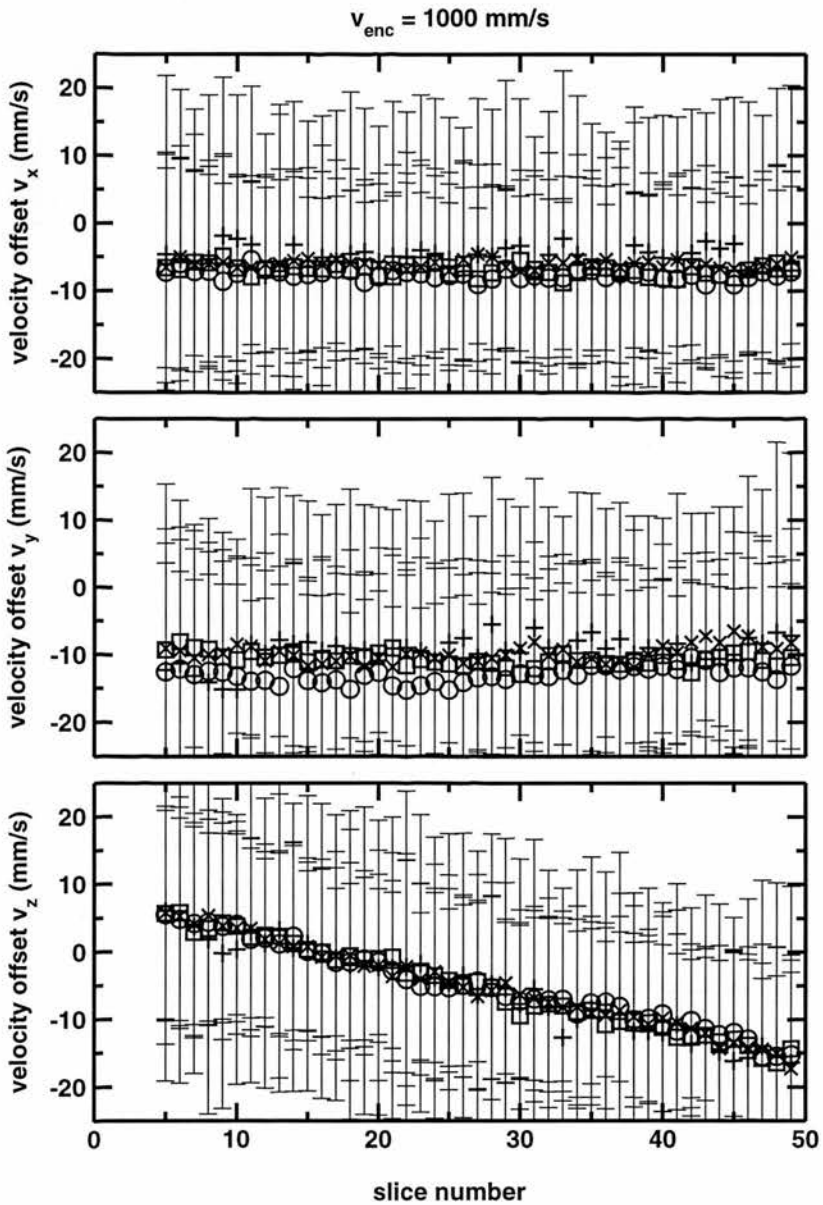

Figure 7.4.: *The variation of the velocity measured in stationary water with slice number (z-position) for the GE scanner. Four independent regions of interest (indicated by different symbols) are shown for an encoding velocity of 1000 mm/s.*

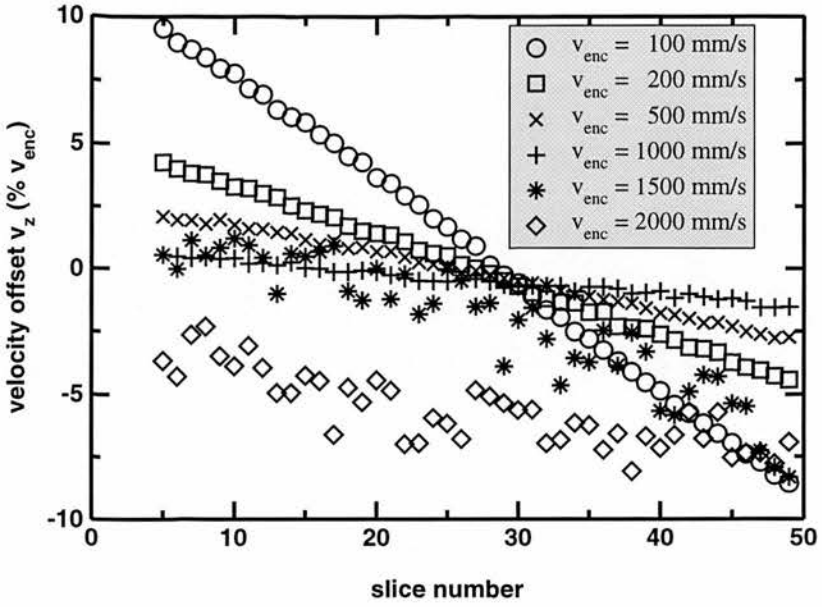

Figure 7.5.: *The variation of the velocity measured in stationary water with slice number (z-position) for the GE scanner. The results of measurements at different encoding velocities are shown.*

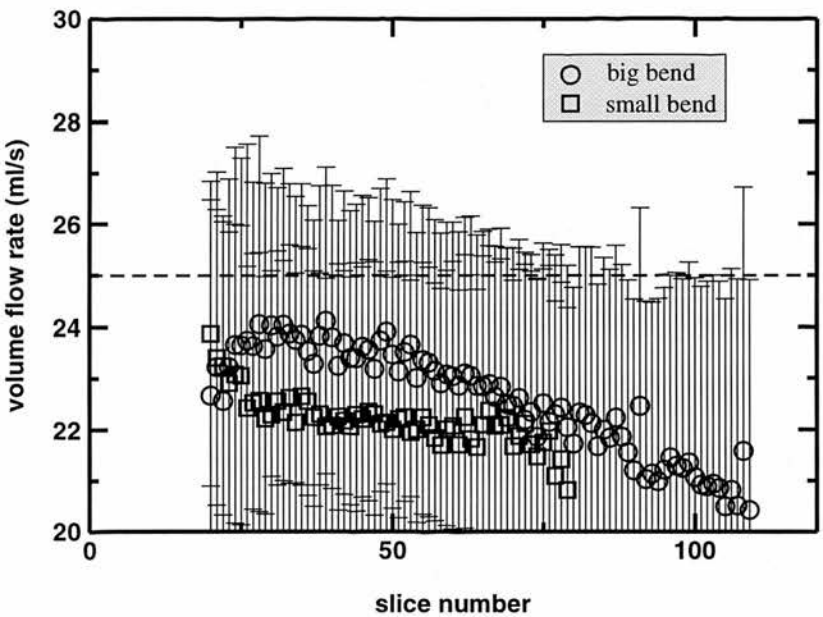

Figure 7.6.: *Variation of volume flow rate with slice number (z-position) for two independent acquisitions of a big and a small bend on the Elscint scanner. The dashed line marks the constant volume flow rate used in both experiments.*

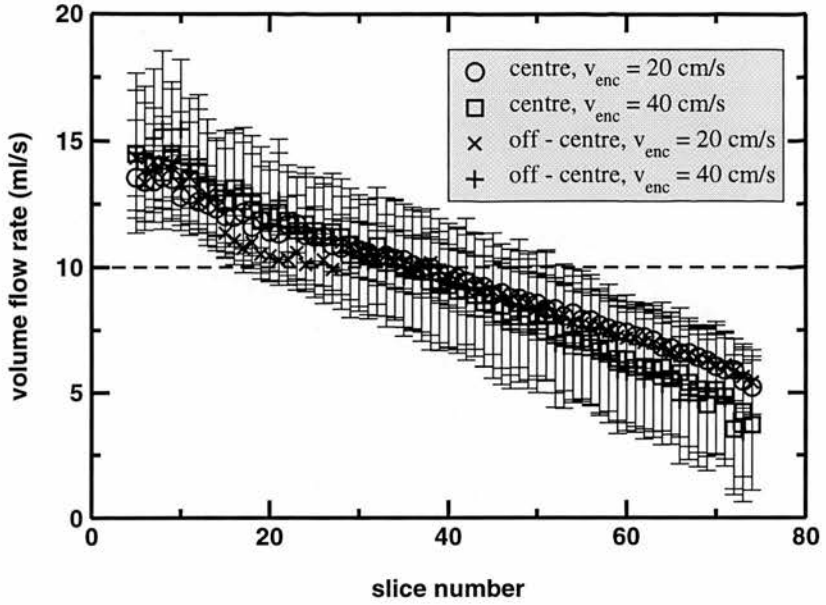

Figure 7.7.: *Variation of volume flow rate with slice number (z-position) for four independent studies on the GE scanner. A straight tube of 6 mm radius was supplied with a constant flow of 10 ml/s (dashed line).*

showed a slight underestimate of the volume flow rate (dashed line, 25 ml/s), but the results are consistent within the error bars. The underestimation of the volume flow rate was attributed to the conservative estimate of the cross-section by the flow detection algorithm (Chapter 6).

Figure 7.7 shows the change of measured flow rate with slice number (z-position) for the GE scanner. The results are derived from the same experiment that was used for Figure 6.17 and Figure 6.18. A 50% overestimate of the volume flow rate at low slice numbers changes to a 50% underestimate at high values, compared to the known volume flow rate (dashed line, 10 ml/s). The deviation seems to follow a linear relationship and to vanish at the iso-centre. Two values of the encoding velocity were used. A v_{enc} of 200 mm/s represents the optimum value for this experiment, but the acquisition was repeated with 400 mm/s to determine any effect of the encoding velocity on the results. The influence of the tube position in the scanner was tested by moving the tube about 5 cm away from the iso-centre horizontally. This variation of the flow encoding with the slice position in z-direction could be due to eddy-currents or Maxwell gradient terms (Section 3.3.4), and is currently under investigation by GE.

7.2. Flow Fitting

7.2.1. The Aim of Fitting

As has been shown in the previous section, the acquired velocity data has about 5 % v_{enc} noise associated with it. This makes the direct calculation of derivatives prone to large errors. As the data is only available on a grid, any prediction of the derivatives is difficult. The only information present is that of the neighbouring grid points, but there is no information of the behaviour between the grid points. One approach is to assume linear behaviour of the velocity between grid points, but it has been shown that this approach is not very effective [MK91, MFU+99]. Using the information from the next nearest neighbour and fitting a parabola yielded much better results. A fitted function includes more of the available data to predict the behaviour of the function between the grid points and additionally allows the calculation of the derivatives.

Another problem is that in principle there is very little information available to calculate wall shear stress or wall shear rate. It is known that pixels which contain a contribution from the wall will exhibit an unreliable velocity measurement due to partial volume effects. The other problem is the limit to a one - sided derivative since the velocity function is only defined inside the flow area. Again, fitted functions can help. By assuming that the function will exhibit a behaviour outside the flow area consistent with that inside, an extrapolation of the velocity profile towards the vessel wall is possible. However, any extrapolation has to be undertaken with care.

Any set of orthogonal functions can be used to approximate a mathematical function. Sinusoids and their harmonics, and Bessel functions are frequently used. Another approach is the use of polynomials. Since the solution of Poiseuille flow is a parabolic flow profile, polynomials seemed the most appropriate set of functions. Each of the velocity components is independent and can be treated separately. The returned fit defines a surface defined over a 3D parameter space. Function evaluation of polynomials is very efficient and this cuts down the calculation time.

Assuming incompressibility of the fluid ($\nabla \cdot \vec{v} = 0$) may stabilise the fit, but the velocity components would not remain independent and a vectorial fit would have to be used. With one predominant velocity component in most data sets (v_z) this approach may prove problematic.

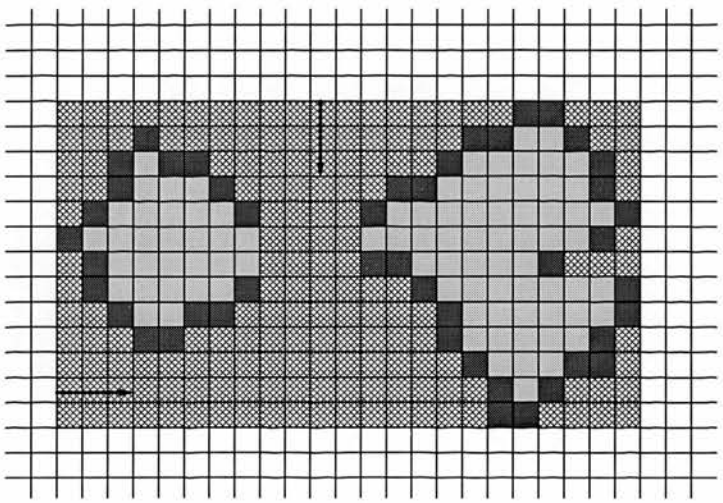

Figure 7.8.: *Illustration of the problem when marking the wall of complex, merged flow objects. The hashed area marks the bounding box of the merged flow object, that is connected in 3D. The arrows indicate the direction of wall pixel marking from the limits of the bounding box inwards. With this method, all dark grey pixels are marked in the flow. The other flow pixels remain untouched (light grey).*

7.2.2. Data Set Preparation

The points that are marked as detected by the flow detection algorithms (Chapter 6) are collected in lists per slice. The lists are merged at this point for the first time within a slice, since a flow region might be filled from several seed points. For each of the resulting lists, the outermost pixels are marked as the wall by setting the weight of the **UKFlowPoint**. Coming from the bounding box values inwards, the first pixel encountered in a row or column is assumed to be part of the wall. The next step is to merge all the lists within the volume of interest. This will collect all the data points for a flow in a complex geometry, e.g. bifurcation, into one list. Another step of wall marking should not be undertaken, since for example one branch of the bifurcation might prevent parts of the wall of the other branch from being marked as wall (see Figure 7.8). Here, the left arm of the bifurcation prevents a test for wall pixels from reaching the left side of the right arm and vice versa.

The slab selection pulse used by the Elscint scanner excited a significant number of spins outside the volume of interest, resulting in serious phase folding problems. Quite often, the velocity information within a flow was significantly wrong for single pixels within a flow. By checking the velocity components of every pixel against the mean of its neighbours, these pixels were eliminated. If any velocity component was outside the range of the neighbours mean $\pm$ 20 % v_{enc} the point was removed. Additionally, if v_{enc} was chosen to be too small, phase folded velocity data was eliminated by this step.

Despite all the checks built into the flow detection algorithm, leaking of the region filling algorithm may occur. Leaked flow points only have one or two neighbours. Filtering can also lead to the same phenomenon. To eliminate this problem, pixels with only one neighbour are removed during the velocity noise check and this procedure is repeated again afterwards. Care has to be taken to avoid eroding the flow volume by applying this filter too often.

The subsequent fits can take quite a lot of time and for large *in vivo* data sets this time can be cut down significantly by eliminating all flows that are directed in the negative z-direction. These flows stem from veins which are of limited interest in the study of atherosclerotic disease.

7.2.3. Polynomial Fit of the Whole Flow

One approach is to fit all the available data points in one process. For relatively small errors, this has the great advantage of providing lots of data points for a limited number of parameters, and the noise should be reduced. Several fit functions have been implemented for this project, where the inclusion of data points close to the vessel wall and the order of the polynomial that was to be fitted were considered. The easiest way to ensure that all possible terms in x, y and z have been included in the polynomial is to collect all the terms from the expansion of $(a + x + y + z)^n$, where n is the order of the polynomial. The resulting functions are:

$$\text{Zeroth-Order}(x, y, z) = p_0 \tag{7.1}$$

$$\text{First-Order}(x, y, z) = \text{Zeroth-Order}(x, y, z) + p_1 x + p_2 y + p_3 z \tag{7.2}$$

$$\text{Second-Order}(x, y, z) = \text{First-Order}(x, y, z) + p_4 xy + p_5 xz + p_6 yz$$

$$+p_7x^2 + p_8y^2 + p_9z^2 \tag{7.3}$$

$$\begin{aligned}\text{Third-Order}(x,y,z) &= \text{Second-Order}(x,y,z) + p_{10}x^2y + p_{11}x^2z \\ &+p_{12}xy^2 + p_{13}xz^2 + p_{14}y^2z + p_{15}yz^2 + p_{16}xyz \\ &+p_{17}x^3 + p_{18}y^3 + p_{19}z^3 \end{aligned} \tag{7.4}$$

$$\begin{aligned}\text{Fourth-Order}(x,y,z) &= \text{Third-Order}(x,y,z) + p_{20}x^2y^2 + p_{21}x^2z^2 \\ &+p_{22}y^2z^2 + p_{23}x^3y + p_{24}x^3y + p_{25}xy^3 + p_{26}y^3z \\ &+p_{27}xz^3 + p_{28}yz^3 + p_{29}x^2yz + p_{30}xy^2z + p_{31}xyz^2 \\ &+p_{32}x^4 + p_{33}y^4 + p_{34}z^4 \end{aligned} \tag{7.5}$$

$$\begin{aligned}\text{Fifth-Order}(x,y,z) &= \text{Fourth-Order}(x,y,z) + p_{35}x^4y + p_{36}x^4z \\ &+p_{37}xy^4 + p_{38}y^4z + p_{39}xz^4 + p_{40}yz^4 + p_{41}x^3yz \\ &+p_{42}x^3y^2 + p_{43}x^3z^2 + p_{44}xy^3z + p_{45}x^2y^3 \\ &+p_{46}y^3z^2 + p_{47}x^2z^3 + p_{48}y^2z^3 + p_{49}xyz^3 \\ &+p_{50}x^2y^2z + p_{51}x^2yz^2 + p_{52}xy^2z^2 + p_{53}x^5 \\ &+p_{54}y^5 + p_{55}z^5 \end{aligned} \tag{7.6}$$

As long as all the terms are included, a translation into another coordinate system leads to a redefinition of the parameters, but does not involve any additional terms. One set of parameters is stored per fit and velocity component.

With around 10 000 data points in a typical flow, this provides a very favourable data to parameter ratio. However, data that is obviously wrong, and has not been filtered out before the flow is fitted, will influence the fitted function across the whole volume of interest.

7.2.4. Segmented Polynomial Fit

One way of improving the fit even further is the use of higher order polynomials. However, errors in the parameters are already contributing with x^4, where x represents any coordinate. This is very significant, since x can be of the order of 100. It was noticed that the precision of floats on the Sun computers used was not enough to avoid significant rounding errors. It was therefore decided not to extend the system to include sixth order polynomial fits.

Splitting up the data set into segments decouples sections of the data set. The data set was split parallel to the original slice direction and fifth order fits were applied to each segment. For this purpose it was necessary to select seven neighbouring slices to provide enough information in the z - direction for a stable fit.

For complex geometries (e.g. bifurcations, bends, etc) there is little incentive for the fitted function to cross through zero at the wall. As an example, the two branches of a bifurcation possess similar values of velocities in close proximity to each other. The fit accommodates this situation by staying at a higher value rather than approaching zero in the gap between the branches. A good example of this situation is discussed for the data set acquired on Volunteer 1 (Figure 9.5). To improve the fit, the values associated with wall points were fixed to zero and given a weight of 40 %. This value was empirically determined.

The fitted velocity values are stored for the middle slice of the segment at every grid point defined by the original MRI acquisition. This includes the spatial derivatives of the velocity components. The segment is then translated by one slice. This allows the fitted values to be stored for every slice in sequence. However, the first and last 3 slices are problematic, since a lower number of slices contribute to the fit. Their data have to be treated with caution.

Care also has to be taken that there are more data points in every segment than parameters. If this condition is violated, the whole flow is removed from the list. Another important point concerns the extrapolation of the velocity information towards the vessel wall. As the flow detection has been proved accurate (Chapter 6), the surface is not assumed to be further than two pixels away from the detected flow volume. Fitted velocity information is stored for this extended volume.

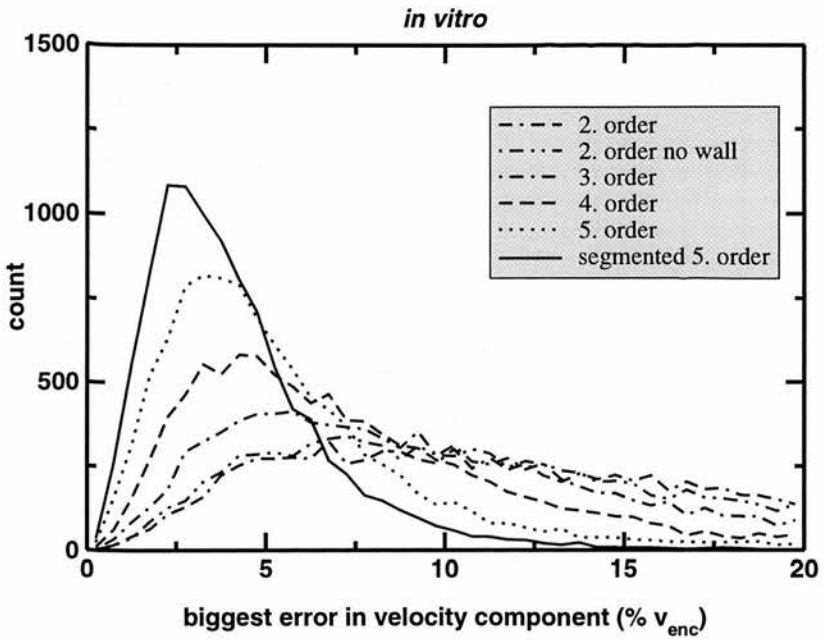

Figure 7.9.: *Difference between measurement and various fit methods for in vitro data. The 3D velocity field in a model of the human carotid artery was acquired. For every data point, the component with the biggest difference to the fit was chosen and the distribution of these values plotted.*

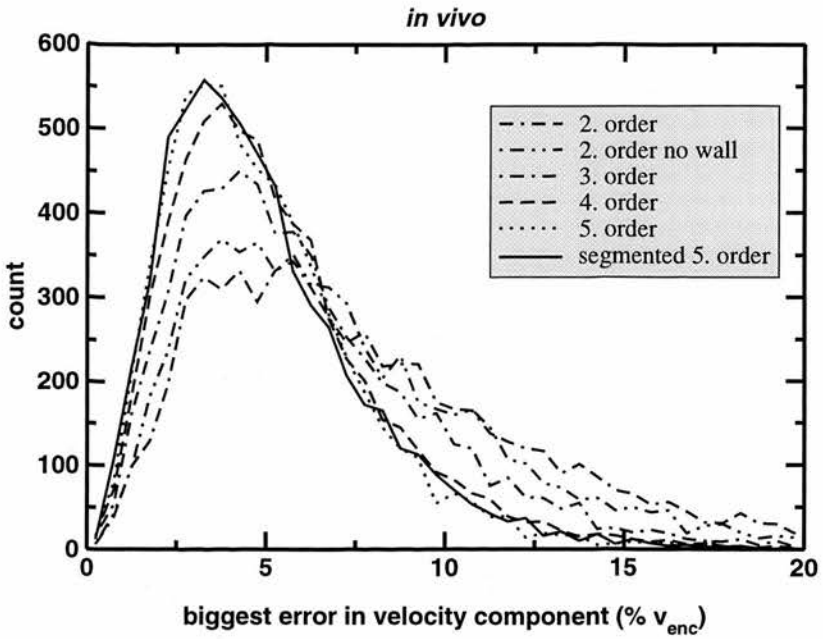

Figure 7.10.: *Difference between measurement and various fit methods for in vivo data. The chosen data set contained the carotid bifurcation, vertebral artery and jugular vein of a volunteer on both sides of the neck. For every data point, the component with the biggest difference to the fit was chosen and the distribution of these values plotted.*

7.2.5. Comparison of Fit Strategies

For a quantitative understanding of the fit quality, the component with the largest error was expressed as a percentage of v_{enc} and the results were collected for all the data points in a acquisition. Experiments using a model of a human carotid artery (Figure 7.9) and a volunteer data set (Figure 7.10) were chosen as examples. The peak error reduces with an increase in the fit order and improves further with the segmented fit ($\approx$ 3 % v_{enc}) in both the *in vitro* and *in vivo* cases. With an expected velocity noise of not more than 5 % v_{enc} a very good fit has been achieved. Any further improvement in the difference between the fit and the original data would indicate that noise is fitted rather than eliminated.

A qualitative, visual inspection of the fit is possibly as important as the quantitative assessment. It is possible to judge if the error is due to a bad fit or unreliable velocity data. Figures 7.11 and 7.12 show the difference between the fit and the original velocity data in the carotid bifurcation model and a volunteer respectively. The slice was chosen in the bifurcation, as the flow profile in this region is complex and difficult to fit. The original velocity vectors are presented as narrow, deep blue tubes, while the difference vectors are thicker tubes that are colour coded. First, the velocity component with the biggest difference between the fit and the experimental data is chosen for every data point. This difference is then expressed as a percentage of v_{enc} and the colour ranges from green (no difference) via yellow (5 % v_{enc} difference) to red (more than 10 % v_{enc} difference). The expected noise level in the velocity data is about 5 % v_{enc}.

A clear improvement of the fit with the order of the polynomial and the additional segmentation can be seen in the *in vitro* data (Figure 7.11). The main improvement can be seen at the internal wall of the external carotid artery (right hand side of the left flow) and in the carotid bulb (right hand side of the right flow). Complex flow patterns can be expected in the carotid bulb and the segmented fit manages to describe satisfactorily the experimental data.

The improvement in the *in vivo* data set (Figure 7.12) is more distinct in the carotid bifurcation than the jugular vein (left, downward flow) and the vertebral artery (right, upward flow). A fifth order segmented fit is necessary to describe adequately the experimental data.

In light of the clear advantage of the segmented fifth order fit, all further calculations were based on this method.

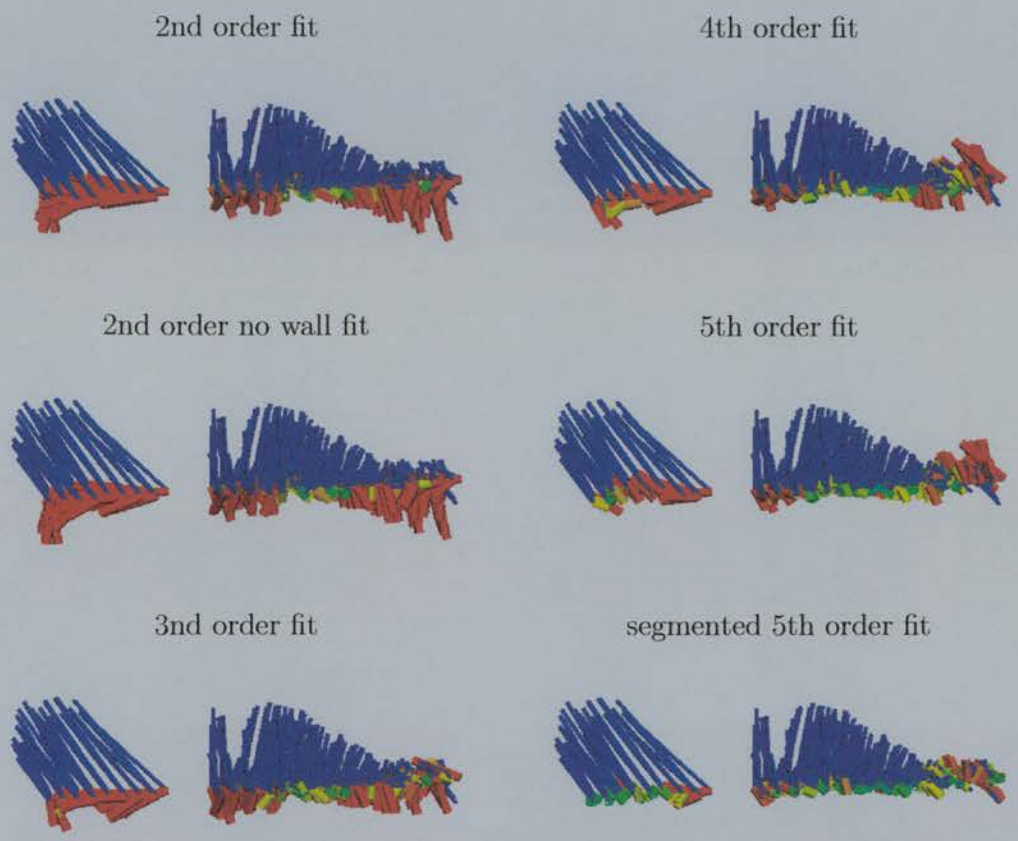

Figure 7.11.: *Visual representation of the difference between the measured velocity field and various fit methods for a slice selected from the in vitro data set used for Figure 7.9. The slice chosen was located in the carotid bulb, the area that exhibits the most complicated flow pattern. The thin blue tubes represent the measured velocity vectors, while the colour coded thicker tubes represent the difference vectors. The colour scale extends from green (no difference) via yellow (5 % v_{enc} difference) to red (more than 10 % v_{enc} difference). The colour is based on the velocity component with the biggest difference at every point. The expected velocity noise is approximately 5 % v_{enc}.*

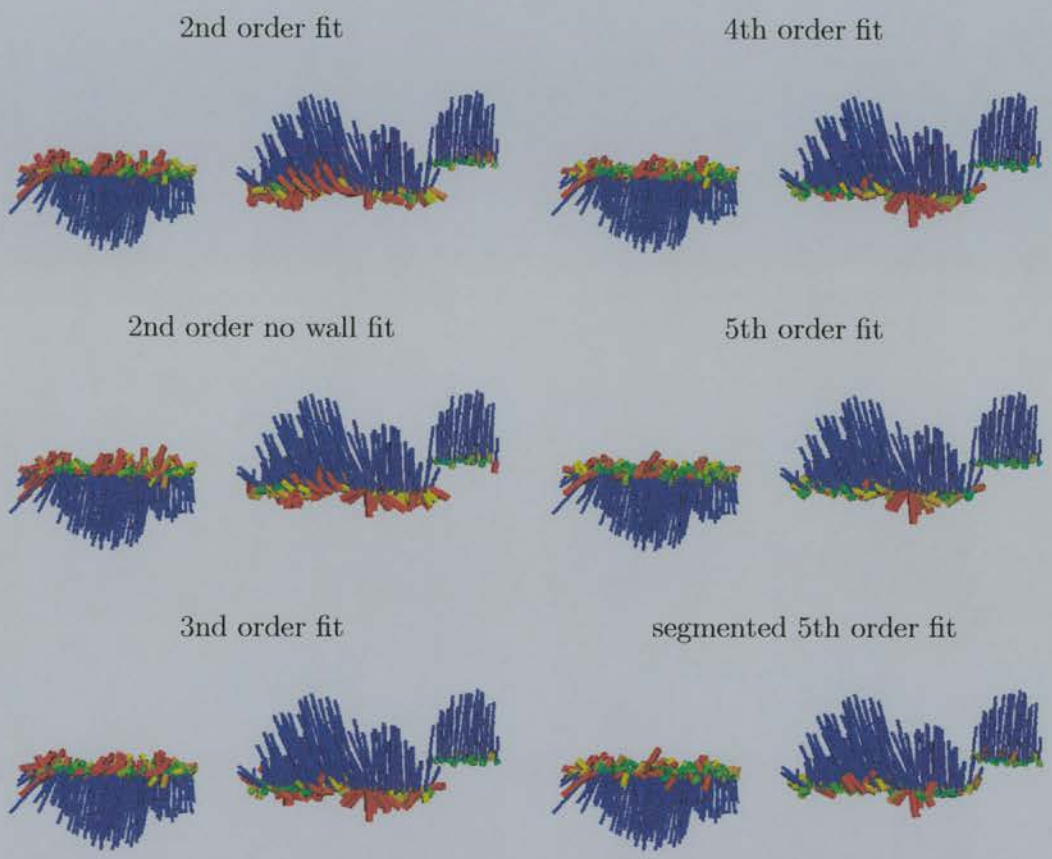

Figure 7.12.: *Visual representation of the difference between the measured velocity field and various fit methods for a slice selected from the in vivo data set used for Figure 7.10. The slice chosen was located in the carotid bulb, the area that exhibits the most complicated flow pattern. The jugular vein (left) and vertebral artery (right) can also be seen. The thin blue tubes represent the measured velocity vectors, while the colour coded thicker tubes represent the difference vectors. The colour scale extends from green (no difference) via yellow (5 % v_{enc} difference) to red (more than 10 % v_{enc} difference). The colour is based on the velocity component with the biggest difference at every point. The expected velocity noise is approximately 5 % v_{enc}.*

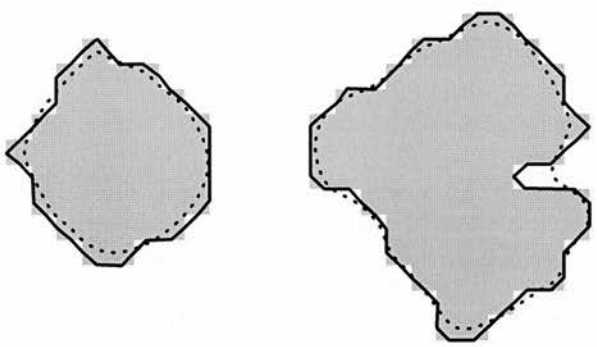

Figure 7.13.: *Illustration of the wall reconstructed from the wall that was used as an example in Figure 7.8. The solid line is reconstructed from the marked flow pixels and then smoothed (dotted line).*

7.3. Wall Reconstruction

7.3.1. Representation of a Surface

The general description of a surface needs more information than just the coordinates of points located on it. The relationship between this collection of points has to be defined as well. By defining connections between the points, the form of the surface is uniquely identified. Modern graphic cards have some hardware acceleration included for the handling of surfaces. This is normally restricted to sets of triangles. Every surface that is defined by a mesh of points can be expressed in triangles and this is the most general representation.

Defining surfaces therefore involves more than the definition of surface points. The determination of the relationships between the surface points can be difficult. For most cases, **VTK** provides the functionality required.

7.3.2. Detected Wall

Based on the accuracy of the flow detection presented in Chapter 6, this volume which contains flow pixels can be used to reconstruct the surface of the vessel. **VTK** supplies a filter to construct iso-surfaces. This filter is ideal for this purpose, since it returns the polygon data (the triangles) of the wall.

To apply the filter, a structured grid of the dimensions of the bounding box of the list of flows is created. All vertices in this structured grid are initialised with scalar values of nil, and assigned the absolute position of the voxel in mm. Iterating over all flows and all points within those flows, vertices that coincide with a flow point are assigned the new scalar value of one.

A "vtkContourFilter" is subsequently applied to the structured grid with a lower threshold of 0.4 and an upper threshold of 0.6. This filter returns the desired surface. Figure 7.13 illustrates the resulting wall as a solid line. Internally, **VTK** employs a marching cube filter. This filter examines every cell (made up of the vertices) and decides where the edges of the cell are intersected by the surface. The decision is based on the scalar value assigned to every vertex and the change between the vertices. If the scalar values cross the threshold range the edge is intersected and a surface point is placed half way along the edge. A more detailed description of the algorithm is given in [SML97]. The resulting surface cannot be represented as a structured grid (the vertices cannot be addressed like an array) and the grid lines were removed in Figure 7.13 to illustrate this fact.

The surface normals are used in subsequent calculations and it is important to create a smooth surface to represent satisfactorily the smooth vessel wall. The "vtkSmoothPolyDataFilter" provides a method to smooth surfaces. It calculates the mean position of all the neighbours of a vertex and a displacement vector from the current vertex. For every iteration, the vertex is moved a fraction of that displacement vector. This procedure is repeated for all points and over many iterations. This smoothing obviously shrinks the surface during this process and the right combination to produce smooth surfaces was empirically determined. The minimum displacement (8 %) and the minimum number of iterations (70) that return a qualitatively smooth surface were chosen.

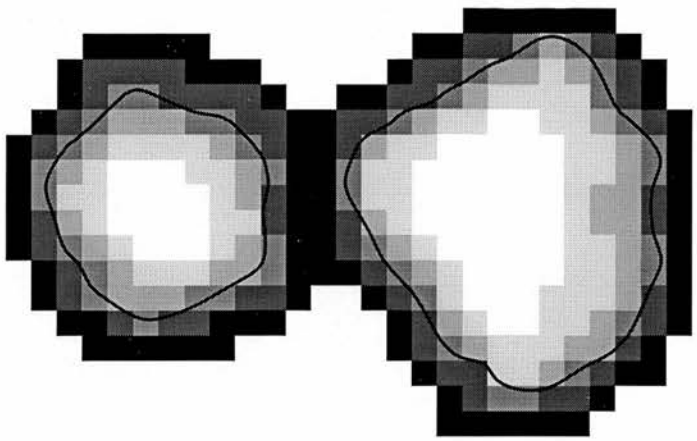

Figure 7.14.: *Illustration of the wall reconstruction based on the fitted velocity values for the flow example used in Figure 7.8. The grey scale resembles possible velocity values of the major component in this slice. The fitted velocity is defined in regions outside the flow region originally detected. An iso-surface on the change from positive to negative velocities (a medium grey in this example) defines the wall (solid line).*

7.3.3. Wall in Fitted Flow

For the calculation of wall shear stress, the velocity derivatives at the vessel wall are of interest. These derivatives are calculated from the function fitted to the velocity data. Initially, the wall predicted by the fit was chosen rather than the detected wall in order to minimise systematic errors. The non slip assumption (the velocity vanishes at the wall) provided the test condition. However, the velocity data is noisy and even the fitted function cannot be expected to vanish completely at the vessel surface. Since the fit provides information outside the detected flow area (in the case of the segmented fit this is limited to an additional two pixel area) a zero crossing of the major velocity component provides a better test.

By restricting the method to the main velocity component in a slice, the secondary velocity contributions are ignored. In most cases these have significantly lower velocities and are more susceptible to errors.

Analogous to the detected wall, a structured grid of the dimensions of the flow list bounding box is constructed. The vertices in this structured grid are all initialised with the scalar zero and existing flow points later assigned a scalar value of one. For the polynomial fit to the whole flow, the region is enlarged by assigning a scalar value of one to the (5×5) in-plane neighbourhood of every pixel, while for the segmented fit this enlargement is given by the use of the fitted flows. This enlargement of the detected region is necessary to compensate for the conservative flow detection. Within that conservative region, the velocity may not cross zero. The application of a "vtkThresholdFilter" with an upper value of 0.5 selects only vertices that might contain the wall when the position is restricted to a two pixel neighbourhood of the detected area. This filter returns an unstructured grid, since the position of the vertices in space is located on a grid, but they are no longer addressable as an array.

The threshold filter restricted the wall to positions that are trustworthy (that are close to the detected flow area). The value of the major velocity component per slice is then assigned to the scalar values of the remaining vertices. A "vtkContourFilter" reconstructs the surface from this unstructured grid. The threshold values used to detect a zero crossing are $\pm\, 5\,\%\ v_{enc}$, the expected noise level. Due to the nature of the fit function, the resulting surface is smooth and no further steps are necessary.

Figure 7.15.: *Vessel wall reconstruction for a straight tube (Figure 7.7). The detected wall (Section 7.3.2) is shown on the left and the fitted wall (Section 7.3.3) on the right. The flow direction is from the bottom to the top.*

7.3.4. Comparison of Wall Reconstructions

The straight tube experiment carried out for volume flow rate validation (Figure 7.7) provided a good test for the different methods of wall reconstruction. Figure 7.15 shows the surfaces for the detected wall on the left and the fitted wall on the right. Overall, the fitted wall appears smoother and has a smaller cross-section. However, close to the inflow, the fitted surface shows a hole on the right side. This region appears rougher on the detected wall, but a fully closed surface is reconstructed.

In Figure 7.16, cross-sections of the walls are presented for the region where the surface is correctly reconstructed (top row) and in the problematic region (bottom row). Both walls seems to deform into an elliptical geometry in the upstream region.

An explanation for this problem in the wall reconstruction can be found in the line profiles displayed in Figure 7.17. The line profiles were taken horizontally across a slice in the middle of the hole in the fitted wall. Whereas the magnitude image (circles) shows only a slight asymmetry, the velocity in z - direction exhibits a strong disturbance near the wall region. The flow area was detected with the flow sensitive *in vitro* algorithm and this disturbance influences the image segmentation. The velocity fit also has no incentive to approach zero with the upward turn in velocities near the vessel wall. In this case, the problem of wall reconstruction can therefore be traced back to the raw data rather than the algorithms.

7.4. Implementing Wall Shear Rate Calculation

7.4.1. The Calculation

The expression for the wall shear rate (WSR) has been previously derived (Equation 4.47, Section 4.4.2)

$$\vec{w}_{rate} = \vec{n} \times \left[\left(2\underline{\underline{\dot{\epsilon}}} \cdot \vec{n} \right) \times \vec{n} \right]$$

in terms of the velocity derivatives $\underline{\underline{\dot{\epsilon}}}$ and the surface normal $\vec{n}$. As the segmented fit provides by far the best results, the WSR calculation is restricted to that fit method. All the derivatives necessary to calculate $\underline{\underline{\dot{\epsilon}}}$ are stored for every location on the original

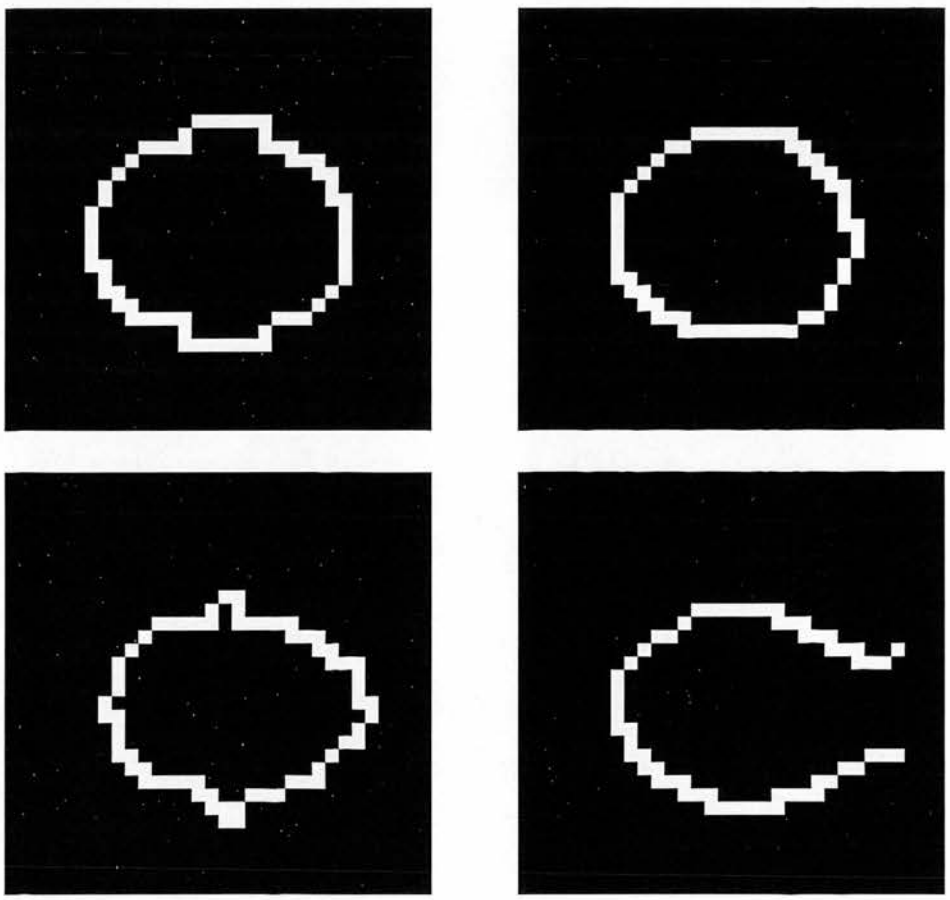

Figure 7.16.: *Cross-section of the reconstructed vessel wall for the straight tube (Figure 7.7). The detected wall is shown on the left and the fitted wall on the right. The top row are the results for the centre slice, while an upstream slice within the region of wall reconstruction problems is displayed in the bottom row.*

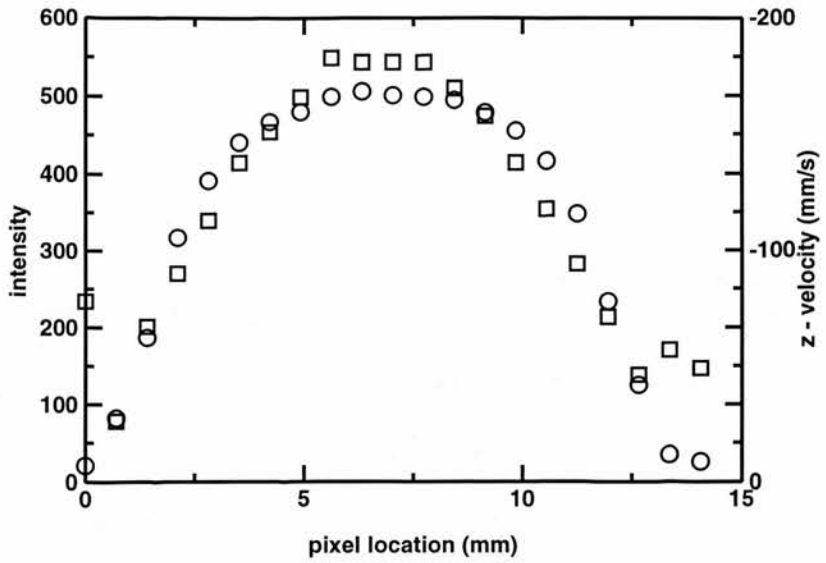

Figure 7.17.: *Line profiles for the straight tube (Figure 7.7). The measured intensity (circles) across the vessel and the measured z - component of the velocity (squares) are shown.*

measurement grid. With the detected (Section 7.3.2) and fitted (Section 7.3.3) wall, the position of the points where the expression has to be evaluated is given. The surface normals can be reconstructed from the surface mesh. This process is very important in 3D computer graphics and a method is provided in **VTK**. The "vtkPolyDataNormals" filter returns the normal for every vertex in the mesh. The list of points is in the same order as for the surface.

The surface points for the wall mesh are not necessarily located on the original measurement grid. However, the fitted velocities and their derivatives are only known on that grid for the segmented fit. The WSR is only calculated at wall points, that lie within 10 % of the original grid in every direction. Rounding errors prevent an equality test and 10 % keeps the error at an acceptable level. There is a trade off between the number of points included and the precision of the WSR calculation.

Wall shear rate has been chosen as the quantity to be calculated, since there is a simple correlation with wall shear stress and it leaves the software independent of the viscosity.

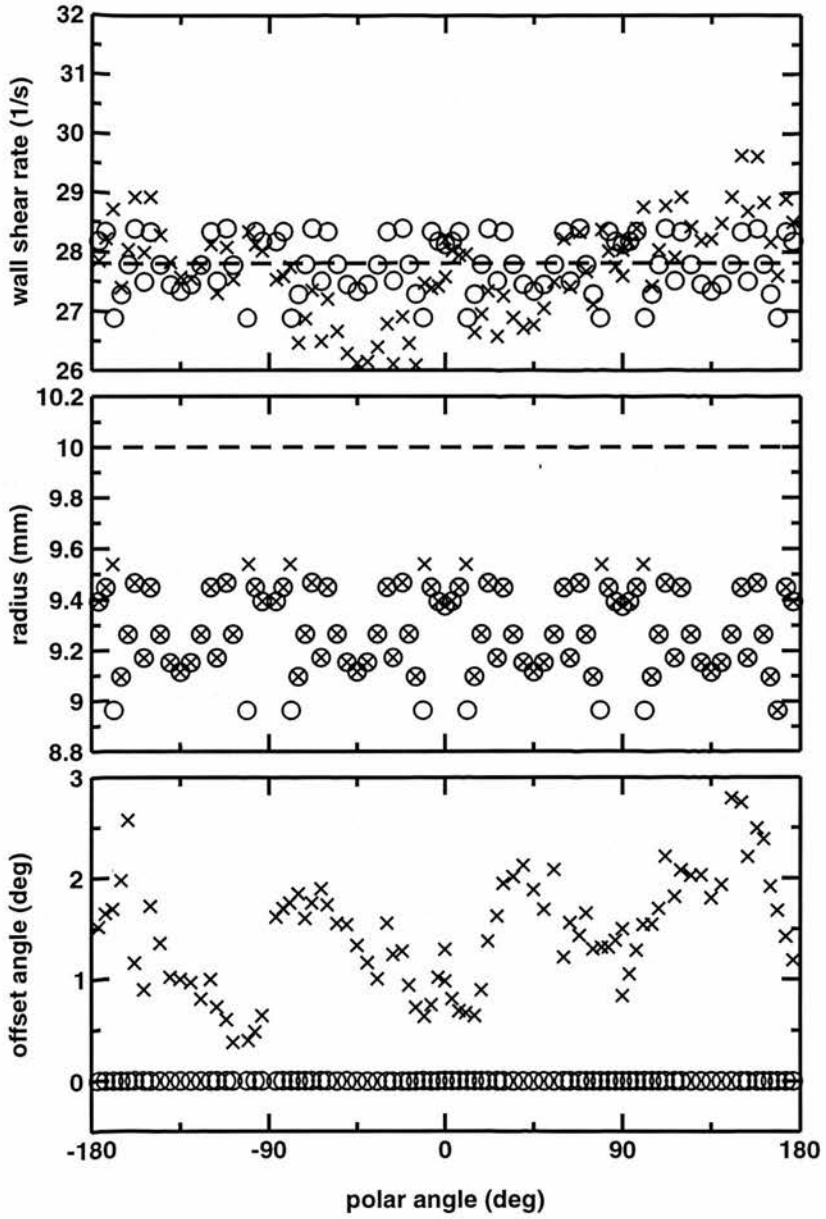

Figure 7.18.: *Wall shear rate calculated for simulated steady flow in a straight tube of 10 mm radius with 0 (circles) and 5 % v_{enc} (crosses) noise added to the velocity data. The wall was reconstructed from the segmented fit of the velocity (Section 7.2.4). The wall shear rate, radius of wall points and the offset angle between calculated WSR and the z - axis are displayed. The dashed line represents the simulated vessel radius and the WSR expected for the mean detected radius. The theoretical WSR was 30 1/s.*

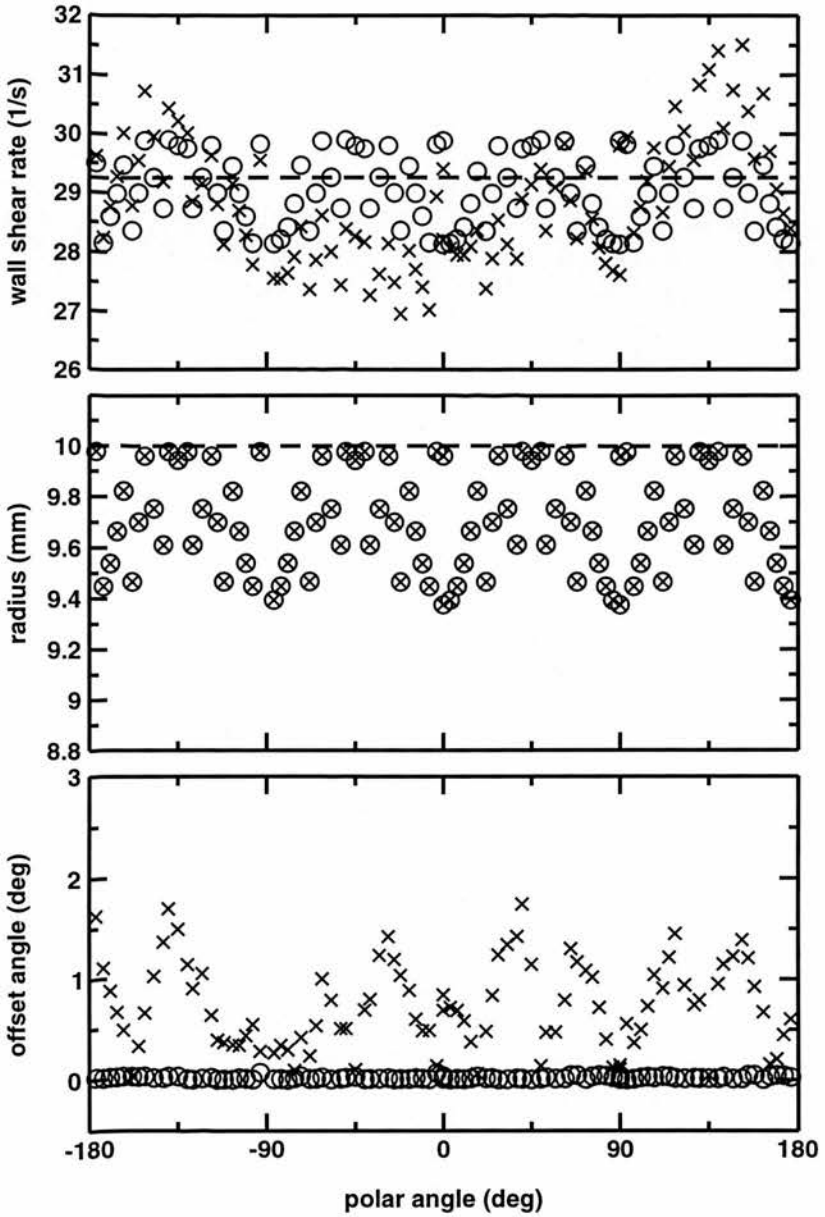

Figure 7.19.: *Wall shear rate calculated for simulated steady flow in a straight tube of 10 mm radius with 0 (circles) and 5 % v_{enc} (crosses) noise added to the velocity data. The wall was reconstructed from the flow points provided (Section 7.3.2). The wall shear rate, radius of wall points and the offset angle between calculated WSR and the z - axis are displayed. The dashed line represents the simulated vessel radius and the WSR expected for the mean detected radius. The theoretical WSR was 30 1/s.*

7.4.2. Validation with Simulated Poiseuille Flow

The theoretical solutions for Poiseuille flow (Section 4.4.3) form the ideal basis for a test of the wall shear rate implementation. To test the robustness of the method, a Gaussian noise function [PTVF92] of increasing width was added to all velocity components. A realistic data set was simulated with the following parameters: 256 columns by 128 rows with a pixel size of 0.59 mm^2 (the best resolution provided by the Elscint scanner). Ten slices were created of 1 mm slice thickness, all containing the same flow information modified by the random noise distribution. An encoding velocity v_{enc} of 180 mm/s is a realistic choice for a maximum velocity of 150 mm/s. Flows in vessels whose radius was 10 or 6 mm were centred in the image.

Figures 7.18 and 7.19 show the results for the large pipe (10 mm radius) for the fitted and detected wall, respectively. The fitted wall in Figure 7.18 underestimates the radius by about one pixel. Interestingly, the simulation with 5 % v_{enc} noise (crosses) produces a slightly better estimate of the radius than the simulation without noise. This underestimate of the radius leads to an underestimate of the wall shear rate. The expected value of 30 $^1/_s$ is underestimated by about 6 %. The wall shear rate calculated for the mean detected radius is shown as a dashed line. Both the simulations with and without noise agree with this prediction. The variation in the simulation with added noise is slightly bigger and the resulting wall shear rate vector deviates up to 3^o from the expected direction along the z-axis.

For the detected wall method (Figure 7.19) the error in radius is due to the pixelisation of the simulation and the smoothing process only. Since the velocity values do not influence the wall detection, the simulation results with and without noise agree in their prediction of the wall positions. The radius is still slightly underestimated, but by a maximum of only half a pixel. This leads to a better value for the WSR (3 % underestimation). No clear improvement in the variation of the wall shear rate magnitude can be seen, but the offset angle seems to be slightly smaller for the fitted wall.

The simulation was repeated for a more realistic 6 mm pipe. The simulations with low noise level can be seen in Figures 7.20 and 7.21 and the higher noise levels in Figures 7.22 and 7.23.

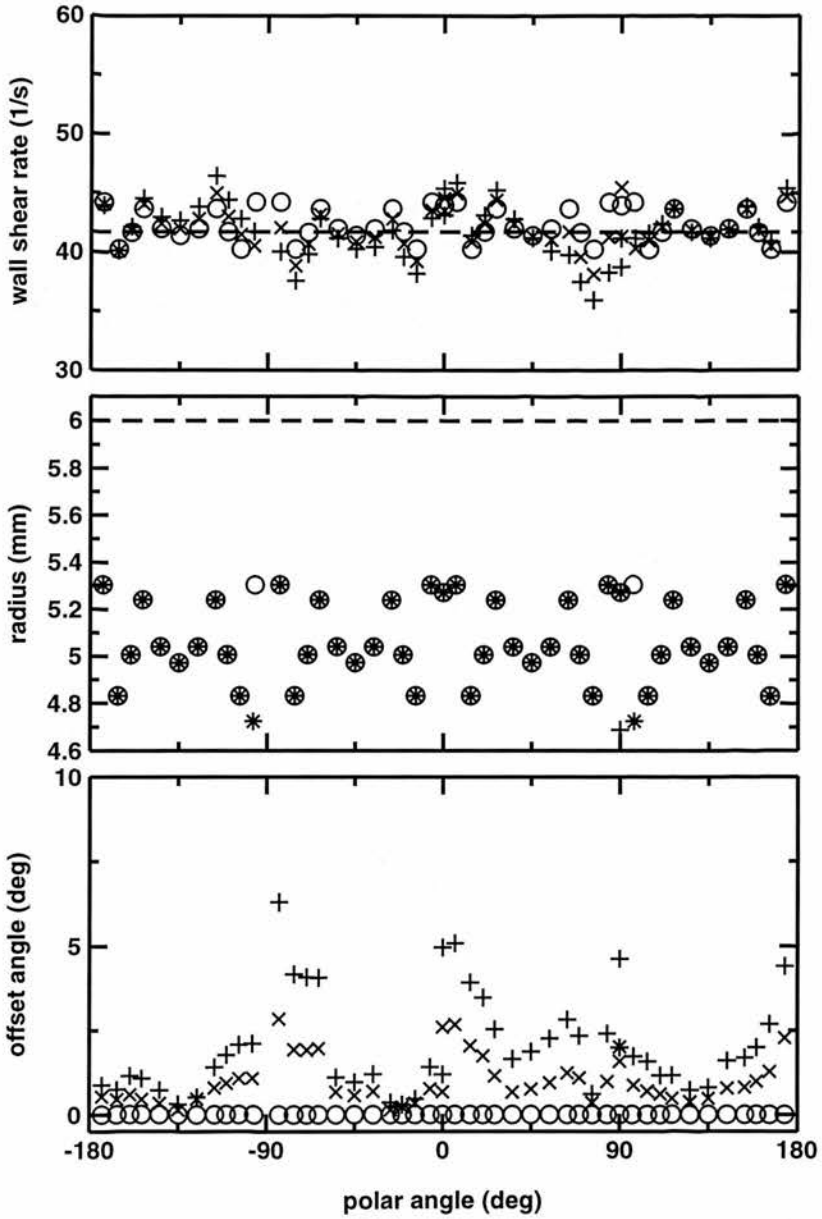

Figure 7.20.: *Wall shear rate calculated for simulated steady flow in a straight tube of 6 mm radius with 0 (circles), 2.5 (crosses) and 5 % v_{enc} (plus signs) noise added to the velocity data. The wall was reconstructed from the segmented fit (Section 7.2.4). The wall shear rate, radius of wall points and the offset angle between calculated WSR and the z - axis are displayed. The dashed line represents the simulated vessel radius and the WSR expected for the mean detected radius. The theoretical WSR was 50 1/s.*

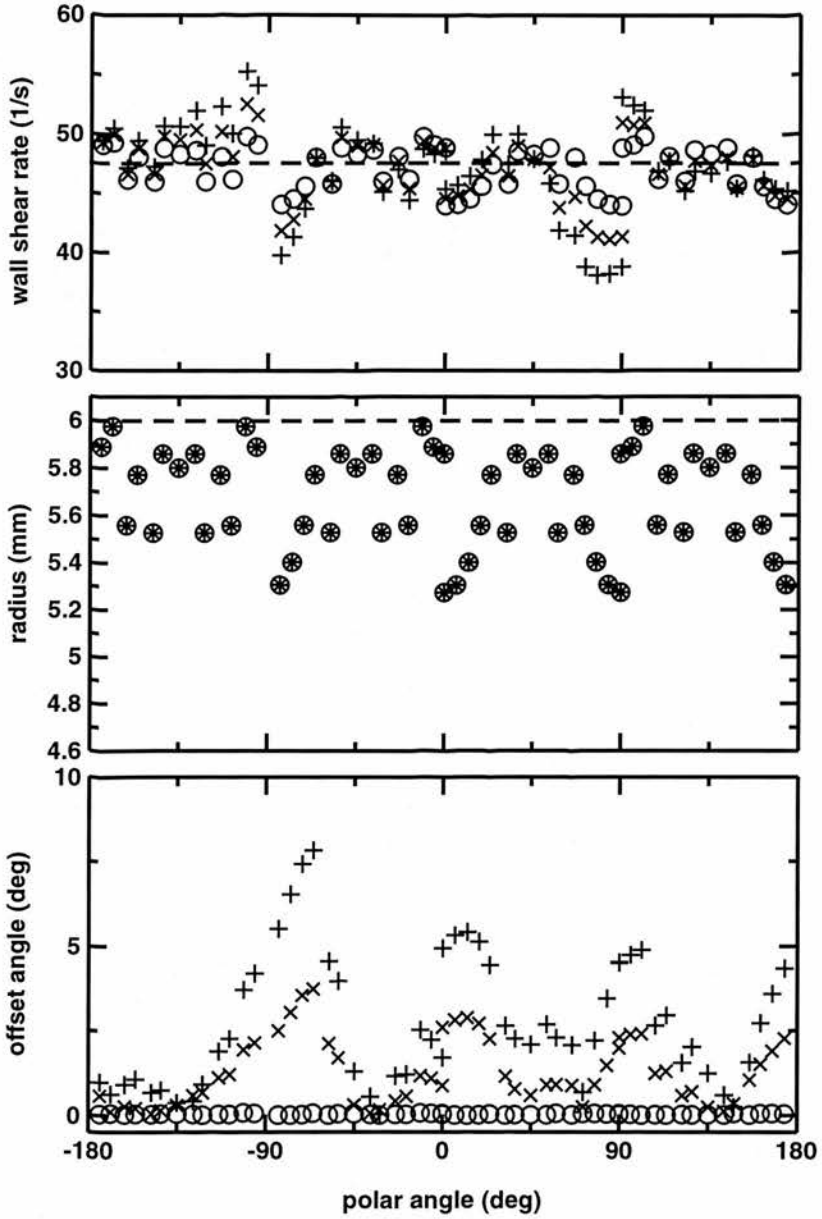

Figure 7.21.: *Wall shear rate calculated for simulated steady flow in a straight tube of 6 mm radius with 0 (circles), 2.5 (crosses) and 5 % v_{enc} (plus signs) noise added to the velocity data. The wall was reconstructed from the flow points provided (Section 7.3.2). The wall shear rate, radius of wall points and the offset angle between calculated WSR and the z - axis are displayed. The dashed line represents the simulated vessel radius and the WSR expected for the mean detected radius. The theoretical WSR was 50 1/s.*

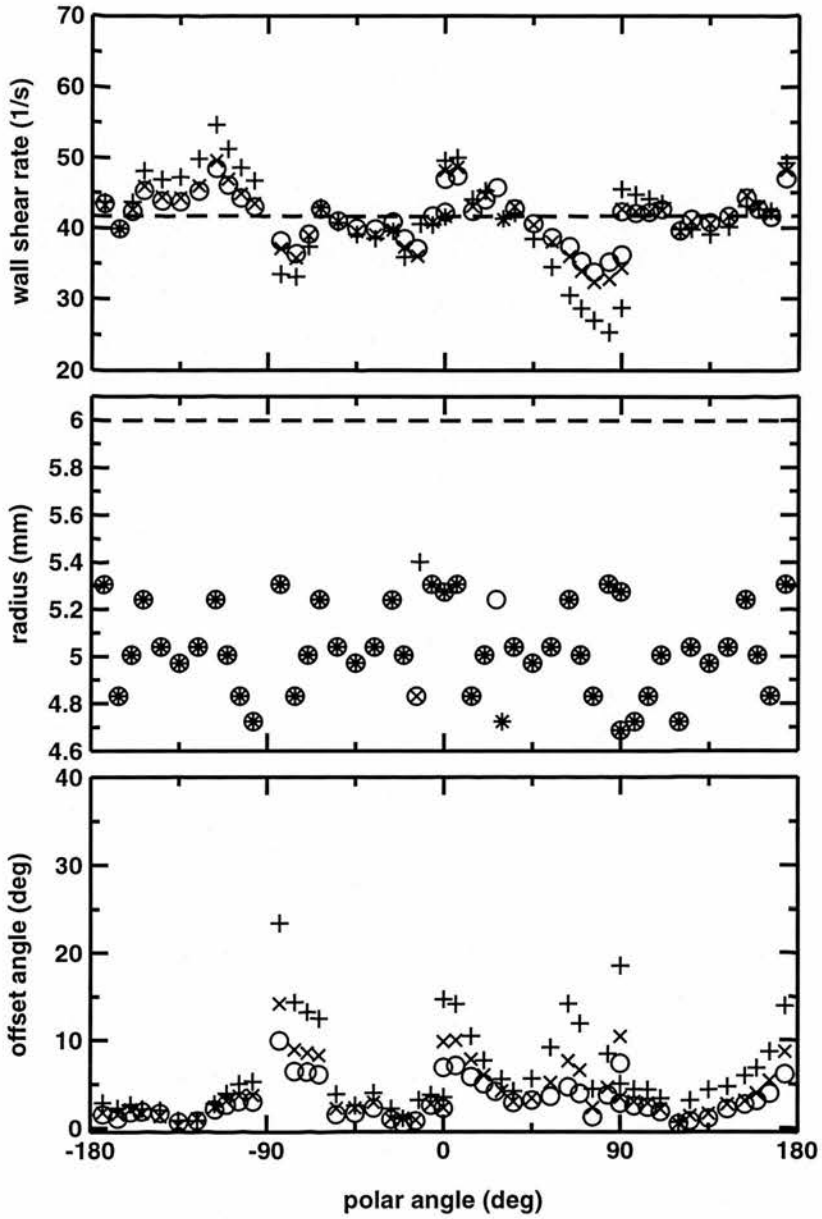

Figure 7.22.: *Wall shear rate calculated for simulated steady flow in a straight tube of 6 mm radius with 7.5 (circles), 10 (crosses) and 15 % v_{enc} (plus signs) noise added to the velocity data. The wall was reconstructed from the segmented fit (Section 7.2.4). The wall shear rate, radius of wall points and the offset angle between calculated WSR and the z - axis are displayed. The dashed line represents the simulated vessel radius and the WSR expected for the mean detected radius. The theoretical WSR was 50 1/s.*

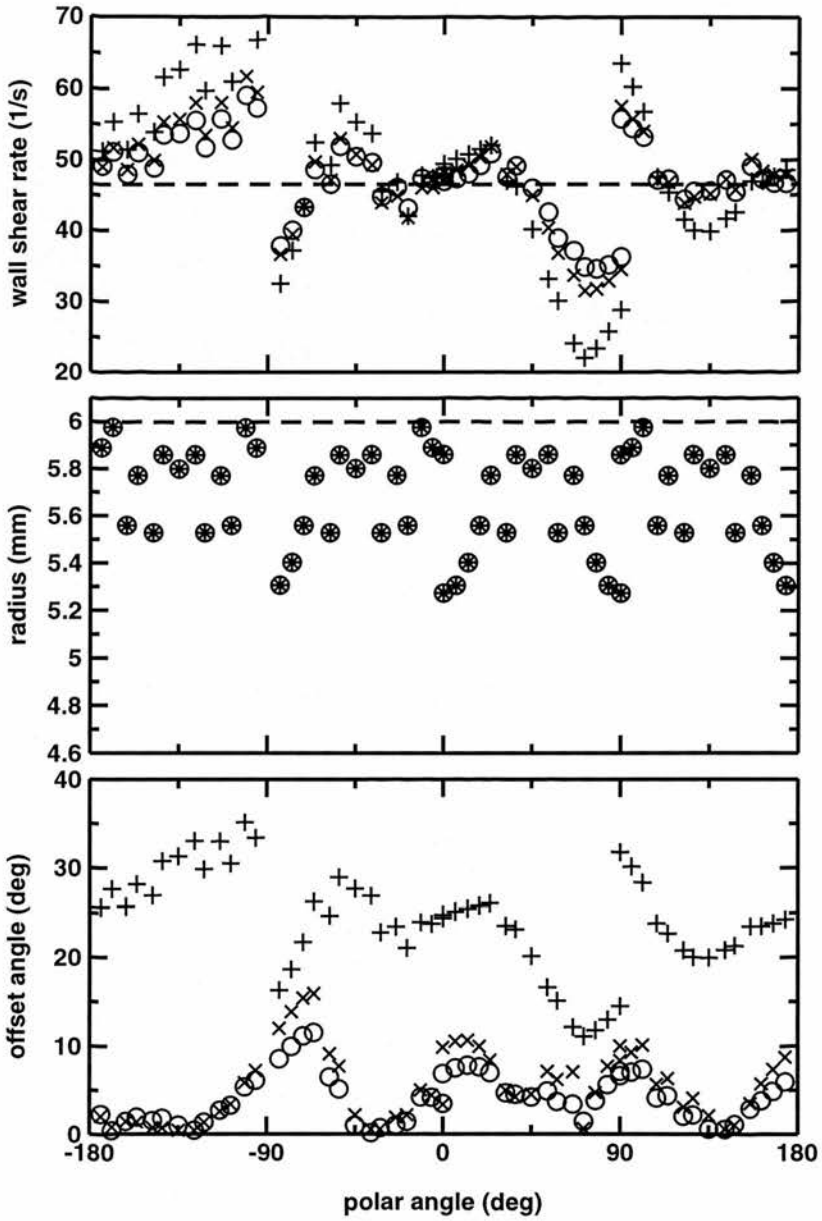

Figure 7.23.: *Wall shear rate calculated for simulated steady flow in a straight tube of 6 mm radius with 7.5 (circles), 10 (crosses) and 15 % v_{enc} (plus signs) noise added to the velocity data. The wall was reconstructed from the flow points provided (Section 7.3.2). The wall shear rate, radius of wall points and the offset angle between calculated WSR and the z - axis are displayed. The dashed line represents the simulated vessel radius and the WSR expected for the mean detected radius. The theoretical WSR was 50 1/s.*

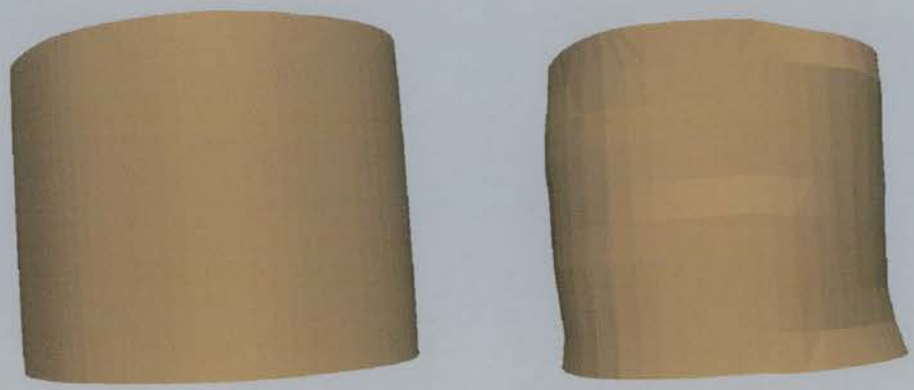

Figure 7.24.: *Vessel wall reconstructed for the highest (15 % v_{enc}) noise level simulated for the straight tube of 6 mm radius. The detected wall is shown on the left and the fitted wall on the right.*

The lower noise levels for the fitted wall (Figure 7.20), demonstrate that the radius is underestimated by slightly more than a pixel. However, the reproducibility of this result for noise levels from zero noise (Figure 7.20, circles) to 15 % (Figure 7.22, pluses) indicates that the pixelisation plays a major role. The mean of the wall shear rate calculated seems to be independent of the amount of noise added and it agrees with the value predicted for the mean radius detected. Only the spread of values increases. The theoretical value of WSR is 50 $^1/_s$ and the method underestimates this value by about 15 %. Although the magnitude of WSR is relatively independent of the noise level, a strong dependence of the offset angle between the z - axis and the calculated WSR can be seen. The relatively distorted wall which was reconstructed for the example with 15 % v_{enc} noise (Figure 7.24, right) easily explains this effect. A deviation of the WSR direction of up to 5° for the noise level expected for PC MRI acquisitions is expectable.

Comparing these results (Figure 7.20) with the values calculated based on the detected wall (Figure 7.21), it is apparent that the offset angle is larger (e.g. 8° for the 5 % v_{enc} noise level expected for PC MRI). The radius, however, is detected to within one pixel and the resulting WSR values underestimated by only 4 %.

The numerical results of these simulations are collected for the fitted wall in Table 7.1 and the detected wall in Table 7.2. Within error bars, the noise has no influence on the mean

Sim. radius (mm)	Noise (% v_{enc})	Mean WSR (1/s)	Std. dev. WSR (1/s)	Mean rad. (mm)	Std. dev rad. (mm)
10	0	27.7	0.4	9.3	0.1
10	5	27.6	0.8	9.3	0.1
6	0	42.2	1.2	5.1	0.2
6	2.5	41.9	1.5	5.1	0.2
6	5	41.7	2.1	5.0	0.2
6	7.5	41.6	3.0	5.0	0.2
6	10	41.4	3.7	5.0	0.2
6	15	41.2	5.9	5.0	0.2

Table 7.1.: *The WSR and* **fitted** *radius results for Poiseuille flow simulations with increasing amounts of noise. The theoretical WSR values was 30 1/s for 10 mm diameter and 50 1/s for 6 mm radius.*

Sim. radius (mm)	Noise (% v_{enc})	Mean WSR (1/s)	Std. dev. WSR (1/s)	Mean rad. (mm)	Std. dev rad. (mm)
10	0	29.2	0.6	9.8	0.2
10	5	29.0	1.1	9.8	0.2
6	0	47.5	1.7	5.7	0.2
6	2.5	47.5	2.5	5.7	0.2
6	5	47.62	3.6	5.7	0.2
6	7.5	47.8	5.3	5.7	0.2
6	10	48.0	6.6	5.7	0.2
6	15	48.5	11.0	5.7	0.2

Table 7.2.: *The WSR and* **detected** *radius results for Poiseuille flow simulations with increasing amounts of noise. The theoretical WSR values was 30 1/s for 10 mm diameter and 50 1/s for 6 mm radius.*

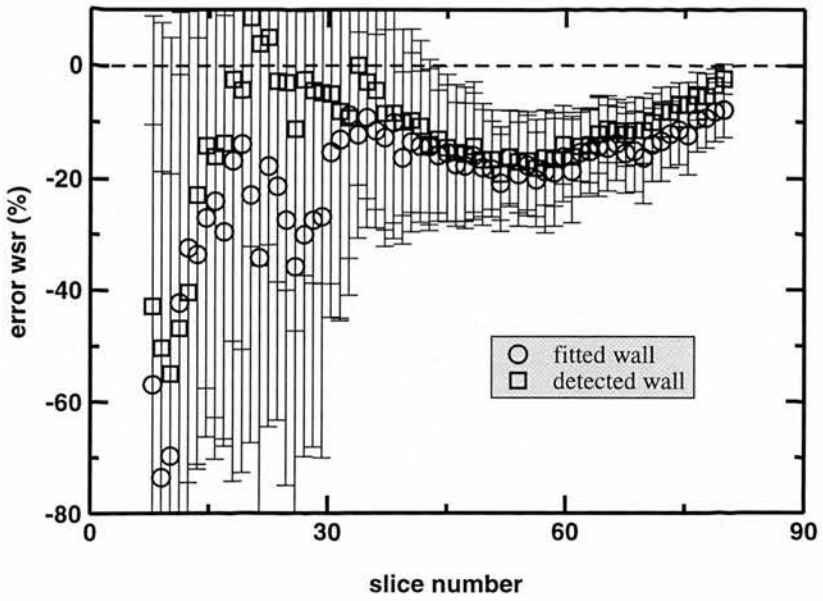

Figure 7.25.: *Wall shear rate calculated in a straight tube of 6 mm radius measured in a straight tube on the GE system.*

WSR magnitude calculated by both methods. Although the detected wall reproduces the simulated radius more accurately, the variation of WSR values calculated is higher.

The simulation based on a straight tube with 6 mm radius with lower noise (Figures 7.20 and 7.21) was studied experimentally with the GE scanner. The data set showed a significant dependence of the flow rate on the slice number as shown in Figure 7.7. However, a simple correction was performed. Assuming Poiseuille flow, the WSR can be calculated from the volume flow rate. The mean and standard deviation of the WSR around the circumference in a single slice was compared with the theoretical WSR, calculated from the volume flow rate in that slice. The results (Figure 7.25) show a systematic underestimation of WSR of about 17 % for the data with slice numbers higher than 30. This compares well to the results predicted by the simulations. As both the detected and fitted wall are based on experimental data, no significant difference between them can be expected. The drop in WSR calculated with the fitted wall below slice number 30 is due to a reconstruction problem. Visual inspection of the fitted wall indicates that the wall detection in that area is unreliable (Figure 7.16). The drop in WSR for the first slices is consistent for both methods and may be due to phase wrapping artefacts or an insufficient correction of the velocity measurement problem on the GE scanner (Figure 7.7).

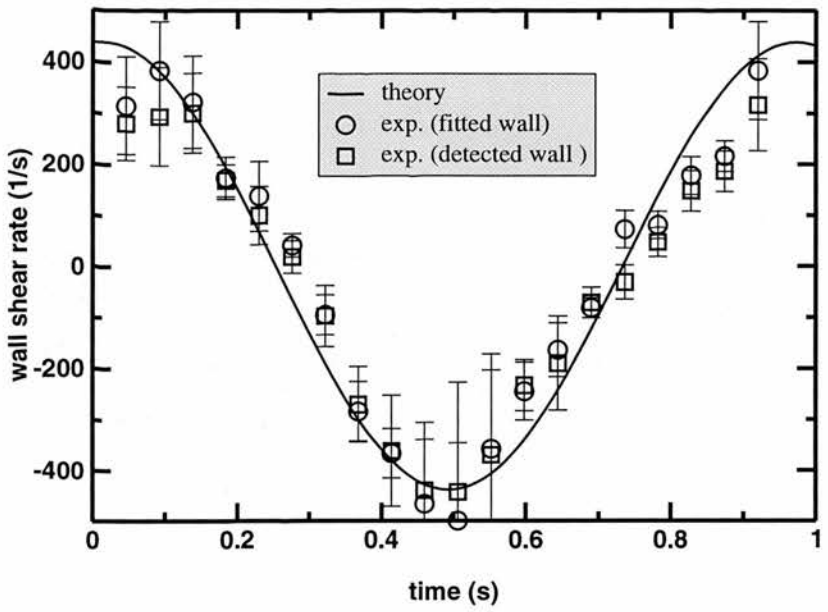

Figure 7.26.: *Wall shear rate in a straight tube of 3.15 mm radius driven with a sinusoidal flow waveform.*

7.4.3. Validation with Gated Womersley Flow

The velocity profile for a sinusoidal flow in a straight tube can be calculated using the Womersley oscillatory theory (Equation 4.60, Section 4.4.3). Fourier transform of the flow rate waveform and addition of the contributions from the individual harmonics allows the simulation of more complex pulsatile flows [RKM99b, RKHM99, RKHM00]. The theoretical data used for this verification was provided by a routine written in Maple (Waterloo, Canada) by my colleague Malcolm Robertson. The experiments were carried out on the Elscint scanner. For every reconstructed time point, the data for the axial slice was replicated for ten equal slices at successive positions in the z - direction. This allowed the direct application of the software developed for this project. The WSR was calculated for the middle slice.

Figure 7.26 shows the results for sinusoidal flow with no forward component. The vessel radius for both simulation and experiment was 3.15 mm and an inlet length of more than 380 radii ensured fully developed flow. The viscosity $\eta = 0.003\,\mathrm{Pa{\cdot}s}$ and density $\rho = 1030\,\mathrm{kg/m^3}$ are the values used to describe the fluid in both the experiments and the simulation. The maximum flow rate was 10 ml/s with a frequency of 1 Hz. The results

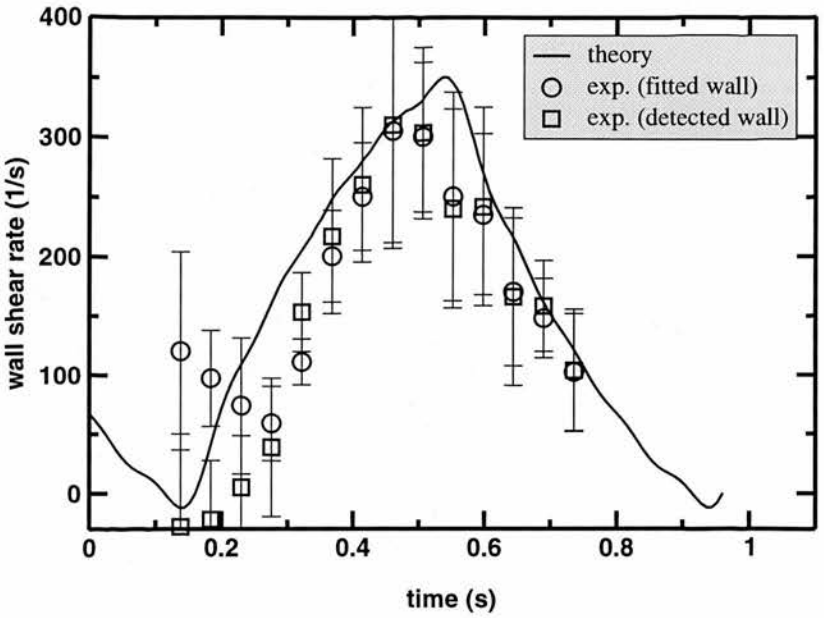

Figure 7.27.: *Wall shear rate calculated in a straight tube of 3.15 mm radius driven with saw-tooth flow.*

of the Womersley calculation are presented in Figure 7.26 as a solid line. The acquisition matrix used on the Elscint scanner was 256×256 for a FOV of 26×26 cm for a 4.2 mm thick slice. The echo time was chosen to be 10.8 ms, the repetition time 23 ms and the flip angle 30°. Only the z - component of the velocity was acquired to improve the time resolution. The results of the WSR calculation using the fitted wall (circles) and the detected wall (squares) agrees within error bars with the theory for most time points. The error bars represent one standard deviation of the distribution of WSR around the circumference of the vessel.

The simulation was repeated for identical parameters using a forward flow triangular saw-tooth waveform with a maximum flow rate of 10 ml/s and a frequency of 1.25 Hz. Again, the theoretical solution is presented in Figure 7.27 as a solid line, while the measured WSR with a fitted wall is represented as circles and detected wall as squares. The limited number of harmonics used for the theoretical calculation explains the slight oscillation in the theoretical WSR. For all time points with a significant velocity, the measured values agree with the theory. However, for the time span from 0 to 0.2 s the flow profile (Figure 7.28) shows very low velocities throughout the vessel. The reconstruction

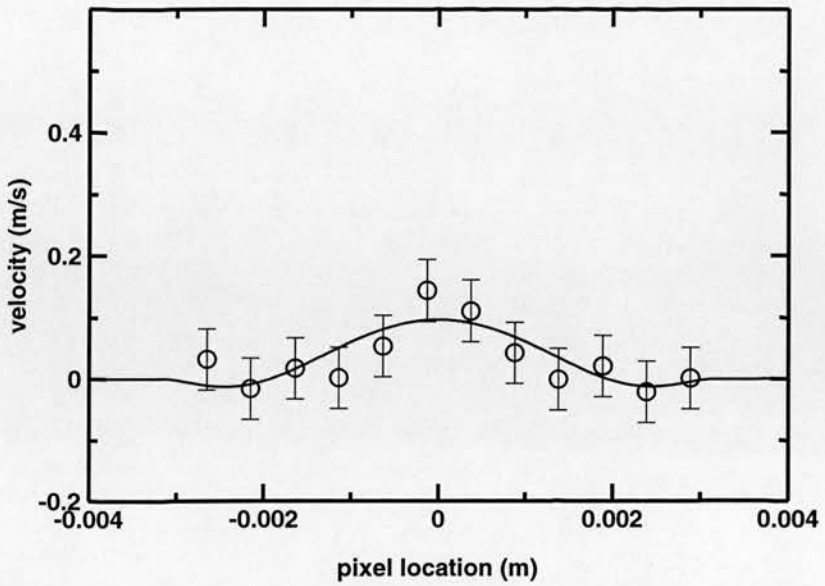

Figure 7.28.: *Velocity profile in a straight tube of 3.15 mm radius driven with a saw-tooth flow calculated at 0.092 s (line) and measured (circles).*

of a wall from these profiles is very difficult, especially when the velocity noise is taken into consideration. The detected wall based calculation (Figure 7.27, squares) works better in this region.

Another possible problem is that the time resolution of the measurement influences the scanner's response function. Higher harmonics are detected with a lower amplitude and different phase. However, the good agreement between the experiment and the theory shows that, for the limited number of harmonics used for these waveforms, the influence of the response function is small.

An additional simulation was performed for a carotid waveform, although no experiment was carried out with this waveform, due to the unsatisfactory precompensation of the flow waveform determined by inspection of the velocity field. This waveform requires more harmonics to be described satisfactorily and hence requires a higher degree of precompensation. Figure 7.29 shows the WSR detected from the simulated flow profiles. The calculation was repeated for a vessel radius reduced by one pixel (dotted line) and increased by one pixel (dashed line). Again the WSR calculated for the fitted wall is represented as circles and the detected wall as squares. For most of the simulations, the

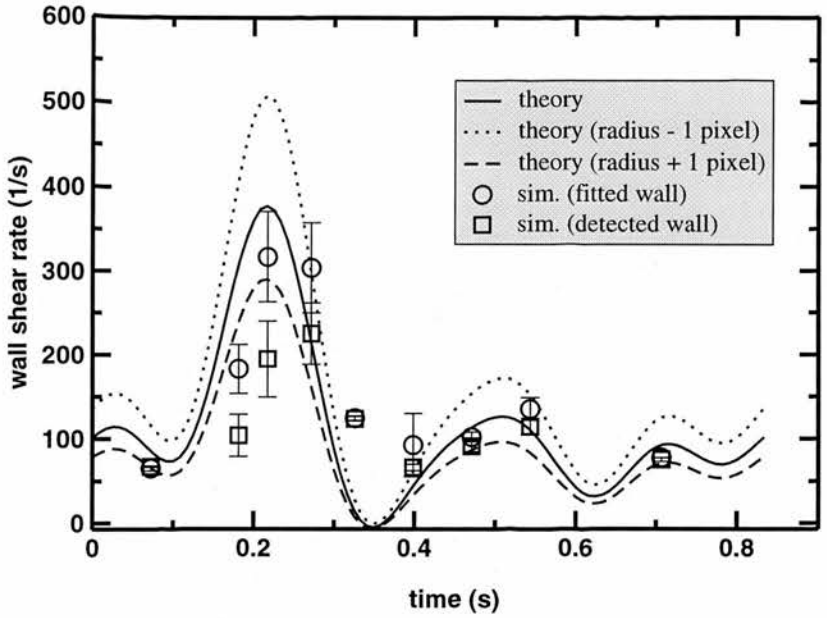

Figure 7.29.: *Wall shear rate calculated in a straight tube of 3.15 mm radius driven with carotid flow.*

fitted wall returns a WSR within error bars of the values predicted by the two offset radii. This simulation also shows the great influence of the wall position on the WSR calculation.

7.4.4. Conclusion

Based on PC MRI measured velocity data for all three velocity components with a high spatial resolution, a method for calculating WSR has been demonstrated. It is applicable to steady or ungated pulsatile flow and can be used with time gated axial slices.

Noise reduction and the calculation of velocity derivatives are based on independent fits of polynomial functions to all velocity components. It was shown that a segmented fifth order fit of the data set delivers the most stable results with the differences between measurement and fit of the order of the expected noise.

For the reconstruction of vessel surfaces, two methods have been proposed. Simulations show that both methods underestimate the vessel area. Experience shows that they complement each other for more complex geometries rather than one being superior.

The fitted surface method minimises errors due to differences in the apparent position of the wall in the fit, while the detected flow ensures a reconstructed surface. Apart from regions with questionable raw data, the method was found to work robustly.

Knowledge of the fit functions and the wall position allowed the wall shear rate to be calculated. Experimental verification and simulation of complex flow profiles showed satisfactory agreement of the results with theoretical predictions. However, the underestimated flow area led to slight underestimation of the WSR. Considering that the noise level in the velocity data is about 5 % v_{enc}, and the considerable number of post-processing steps, an underestimation of this magnitude for WSR is an excellent result.

8. Phantom Results

8.1. 180° Bend

A validation of the wall shear rate (WSR) calculation from MRI measurements using a straight tube phantom has been presented in Chapter 7. A more interesting geometry was provided by the bend phantom where secondary velocities have been observed [Ped80, KYM+93, BHL95, JvTBS96, WWT+98].

The bend phantom was scanned on the GE scanner with the plane of the bend positioned horizontally. Blood mimicking fluid was circulated using the UHDC pump at a steady volume flow rate of 15 ml/s. The size of the acquisition matrix was 256 × 128 × 104 covering a FOV of 18 × 6 × 10.4 cm resulting in a voxel size of 0.703 × 0.703 × 1.0 mm. The echo time T_E= 6.304 ms was fixed by the scanner, a repetition time T_R of 100 ms and a flip angle α of 25° were chosen to minimise saturation effects in the fluid while it progressed through the bend. The 3D slab was placed axially and the encoding velocity v_{enc} of 40 cm/s was determined from preparatory 2D PC velocity MRI acquisitions. All three velocity components were measured.

The resulting velocity field is shown in Figure 8.1 where the velocity at every location of the grid is represented by a vector. This representation is called a "hedgehog". The

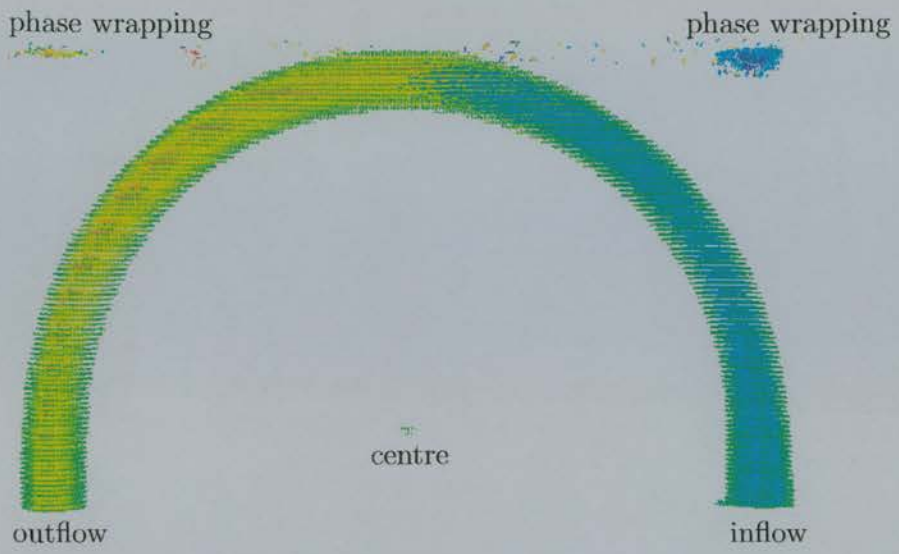

Figure 8.1.: *"Hedgehog" of the velocities in the bend phantom acquired on the GE scanner. The volume flow rate used was 15 ml/s.*

colour scale is proportional to the speed and split in order to show the flow direction. For velocity vectors with a positive z-component, the colour scale ranges from green (no flow) to dark blue (maximum velocity) and for velocity vectors with negative z-component it ranges from yellow (no flow) to (dark red). The velocity field presented in Figure 8.1 is limited to the locations where flow was detected using the *in vitro* algorithm (**Alg. 2**). This algorithm was discussed in detail in Chapter 6. The flow in the bend is segmented reliably with sharp edges and very few additional flows are detected. The one picked out at the centre is due to the vial inserted into the wooden board to mark the centre of the bend. This feature is quite useful to relate slices with respect to the centre of the bend. At the apex of the bend, noise is picked up. By the time the flow reaches the bend the spins have experienced several excitations and the intensity drops. The large tube diameter (12 mm) leads to low velocities and therefore higher saturation effects. It is obvious, that some of the flows which are detected by the algorithm are actually phase wrapped flow information. All this noise was filtered successfully before the segmented fit was executed.

The change in the shape of the velocity profile at different positions in the bend is illustrated (Figure 8.2). The velocity profiles at the entrance (e) are parabolic, but are biased towards the outside wall in all other slices (a,b,c,d). At the exit, parabolic flow

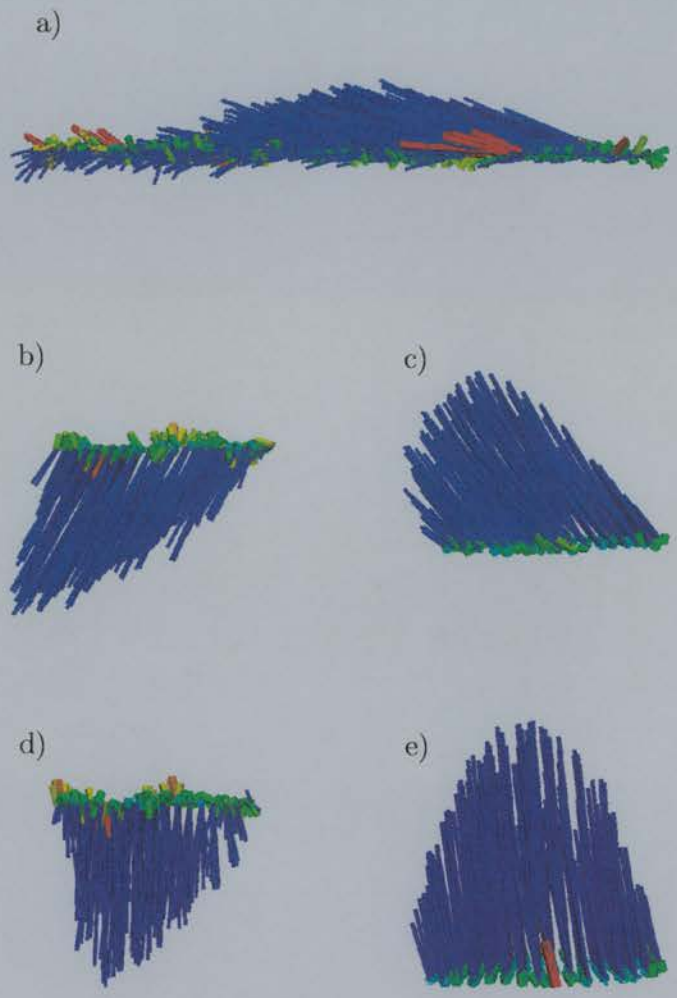

Figure 8.2.: *The measured velocity vectors and fit differences for the segmented fit in the bend phantom (GE scanner). The flow enters the bend in the lower right corner (e), passes the bend 45° at (c), reaches the apex at (a) and passes down another 45° at (b) to reach the exit at (d). The thin blue tubes represent the measured velocity vectors, while the colour coded thicker tubes represent the difference vectors. The colour scale extends from green (no difference) via yellow (5 % v_{enc} difference) to red (more than 10 % v_{enc} difference). The colour is based on the velocity component with the biggest difference at every point. Equal scaling cannot be guaranteed.*

is, however, almost reconstituted. This behaviour has been described in the literature [Ped80, KYM+93, BHL95, JvTBS96, WWT+98]. The fit differences are all within the expected range justifying the use of the segmented fifth order fit (Chapter 7) to describe this velocity field.

The velocity components in the y-direction are shown in Figure 8.3. The phantom was placed in the scanner in such a way that these velocity components vanish for purely forward flow since the plane of the bend was placed horizontally. The development of significant velocities in the y-direction proves the existence of secondary flow components as expected. In the case of the bend, two helical vortices are formed (Figure 8.4) that circulate from the inside wall in both directions away from the symmetry plane towards the outside wall [Ped80, KYM+93, BHL95, JvTBS96, WWT+98]. These can be seen in Figure 8.3 (a-c). The secondary flow components, which form after the entrance slice, have almost vanished by the time the exit is reached.

The wall shear rate (WSR) calculated for the detected wall of the bend is depicted in Figure 8.5. Lower WSR at the inside wall and increased WSR at the outside wall can clearly be seen. The insert in the upper right corner shows the WSR in the inflow in more detail. The WSR drops slightly at the outside of the bend where the two helical vortices meet.

8.2. 60° Bifurcation

A very simple version of the geometry of the carotid bifurcation was provided by the 60° bifurcation phantom.

The 60° bifurcation phantom was scanned successfully twice on the GE scanner. Both acquisitions were performed with blood mimicking fluid for a steady flow rate of 10 ml/s. The common matrix size was 256 × 256 × 124 covering a FOV of 10 × 10 × 9.9 cm resulting in a voxel size of 0.39 × 0.39 × 0.8 mm. The echo time was fixed by the scanner (T_E = 6.88 ms) and a flip angle of 22° was chosen. The first acquisition had a repetition time of 100 ms and the second a shorter repetition time of 50 ms, but four repetitions. The total study time was 1 hour and 45 minutes and 3 hours 32 minutes,

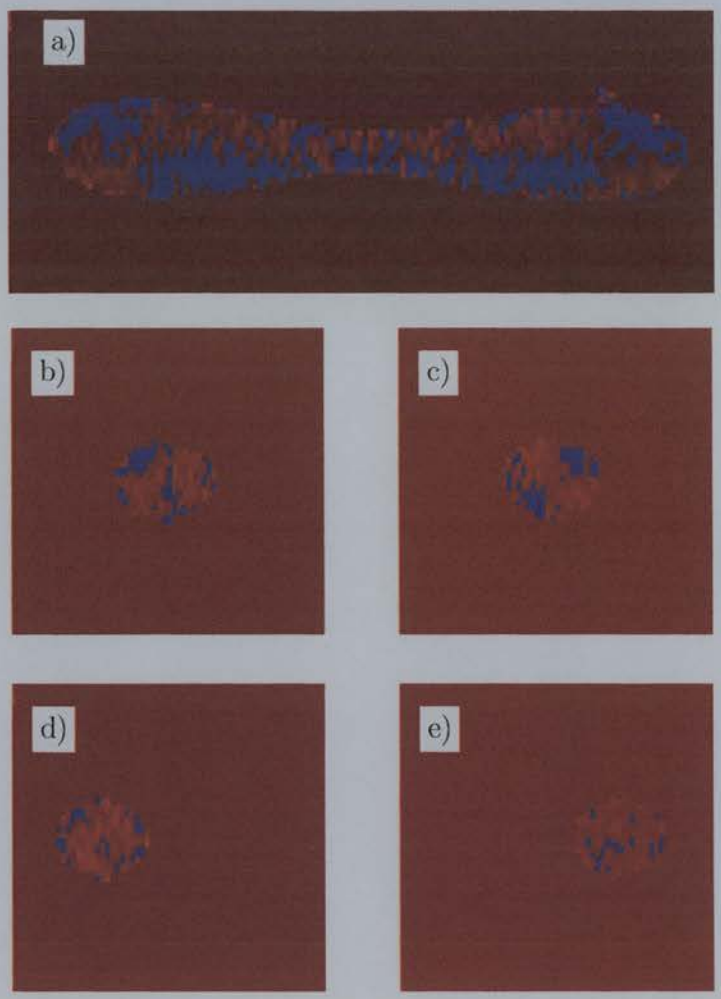

Figure 8.3.: *The y - component of the velocity measured in the bend phantom on the GE scanner. The flow enters the bend in the lower right corner (e), passes the bend 45° at (c), reaches the apex at (a) and passes down another 45° at (b) to reach the exit at (d). The non vanishing values of the y - component of the velocity indicate secondary flows. Image (a) is zoomed less than the rest.*

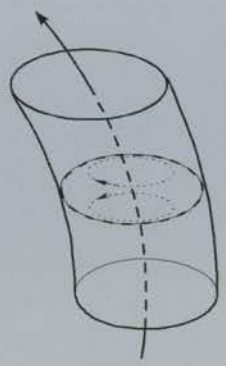

Figure 8.4.: *Illustration of the secondary flow patterns in the bend phantom. Two helical vortices form as indicated by the dotted lines.*

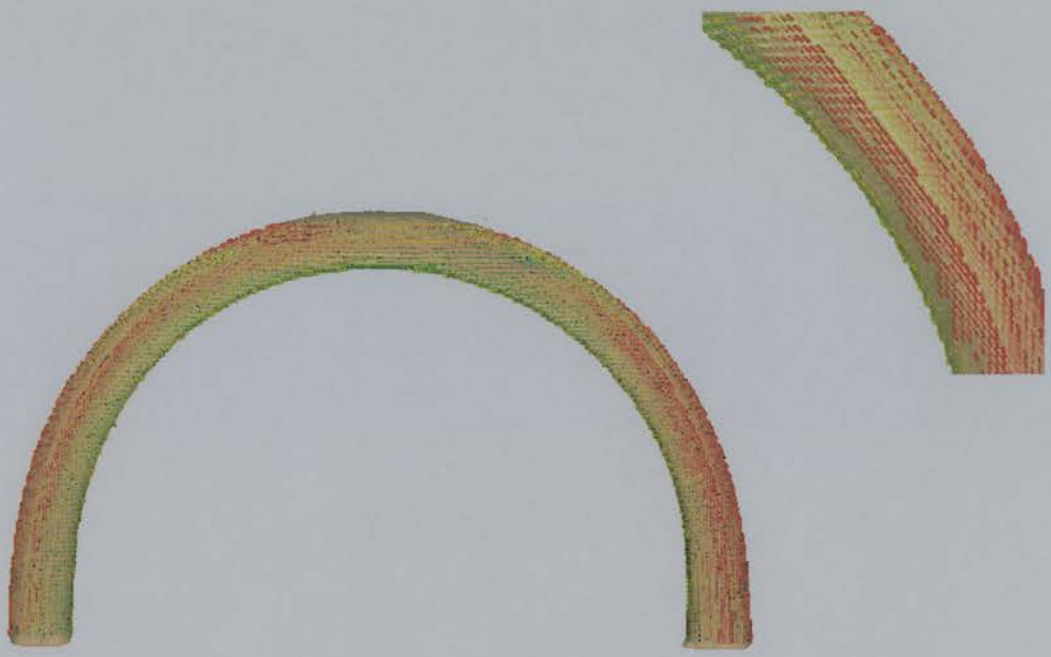

Figure 8.5.: *WSR vectors in the bend phantom calculated from an acquisition with the GE scanner for the detected wall.*

Figure 8.6.: *"Hedgehog" of the velocities in the 60° bifurcation phantom acquired on the GE scanner with $T_R = 100\,ms$. The volume flow rate used was 10 ml/s.*

respectively. The encoding velocity of 140 cm/s was chosen for both studies. All three velocity components were measured.

The velocity field in the 60° bifurcation phantom for the acquisition with a T_R of 100 ms is shown in Figure 8.6 as a "hedgehog". The *in vitro* flow detection algorithm (**Alg. 2** in Chapter 6) filtered out the flow field reliably in all regions apart from the flow divider. A few pixels in the region at the flow divider seem to be missing. With the flow areas of the two branches in very close proximity, the edge detection may be misled on a pixel by pixel basis. However, the regions of complex flow at the outside wall of the flow divider were detected reliably.

The inertia of the fluid drives it towards the inner wall of the flow divider. This can be seen clearly in the measured flow field (Figure 8.6). At the outer wall wall of the flow divider the velocities are lower and the flow field more complex.

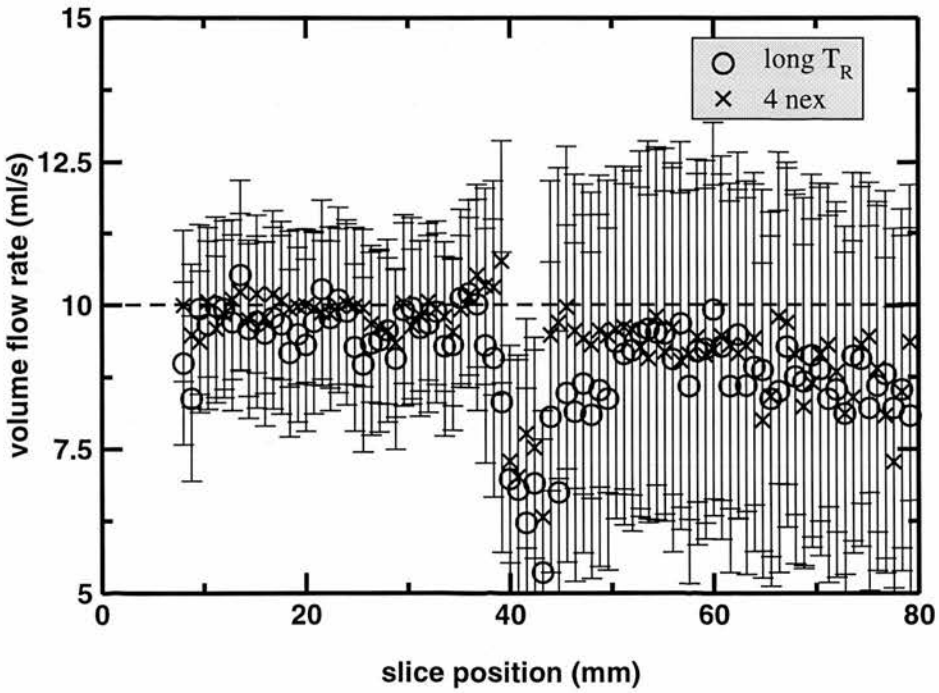

Figure 8.7.: *The dependence of the volume flow rate in the 60° bifurcation phantom on the slice position. The volume flow rate used was 10 ml/s (dashed line).*

The dependence of the measured volume flow rate on the slice position can be seen in Figure 8.7. Away from the bifurcation which begins at 40 mm, both studies agree with

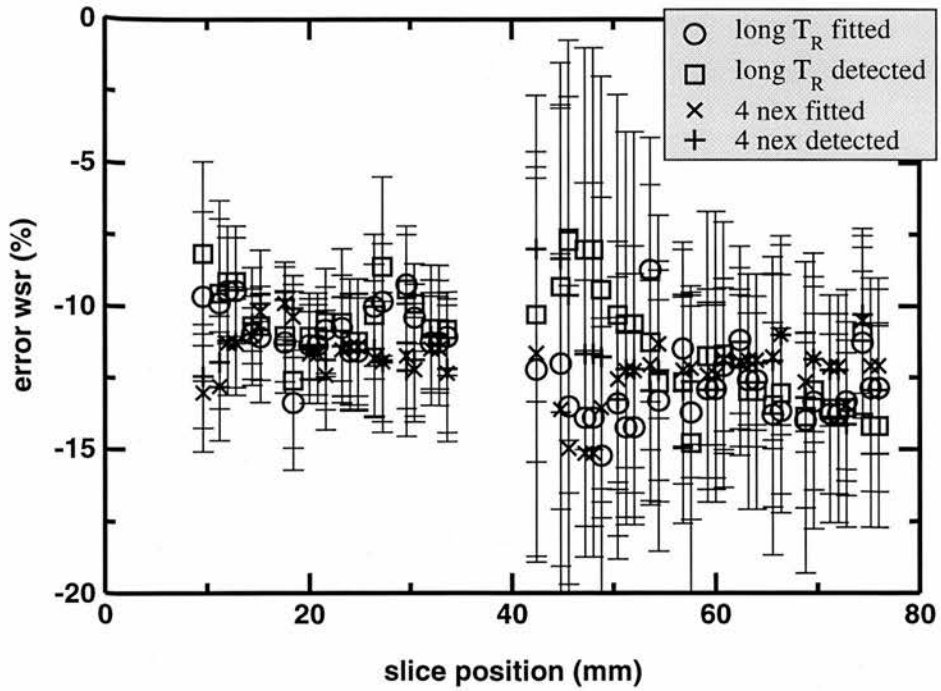

Figure 8.8.: *WSR error for the individual slices in the 60° bifurcation phantom. The velocity field was acquired with a lengthened $T_R = 100\,ms$ and a higher number of repetitions for a T_R of 50 ms.*

the known volume flow rate of 10 ml/s (dashed line). Only a relatively small drop of flow rate with the slice position can be seen in both acquisitions.

Within error bars the branching ratio is 50 %. From this, a theoretical value of the wall shear rate (WSR) can be calculated from the volume flow rate and the known radius of 3 mm. This calculation assumes Poiseuille flow (Chapter 4). The flow rate was taken from the measurement rather than using the known value to avoid the drop in velocity encoding normally seen on the GE scanner (Chapter 7). The error between the measured and calculated WSR can be seen in Figure 8.8. Around the bifurcation, which was located at 40 mm, the flow is not expected to be parabolic. Outside this region, both studies and both methods of wall reconstruction agree. The WSR is underestimated by about 12 %. This underestimation was predicted in Chapter 7 by the conservative estimate of the wall position.

The colour scale used, for the WSR images of this phantom, was fixed to a range from green (0 $^1/_s$) via yellow (450 $^1/_s$) to red (more than 900 $^1/_s$). This achieved a matching colour scale to the computational fluid dynamics (CFD) predictions provided by Quan Long and Yun Xu (Dept. of Chem. Eng. & Chem. Technol., Imperial College, London). The simulation was based on a surface mesh reconstructed from structural MRI scans of the phantom provided by our research group. The results based on a viscosity of 0.01387 Ns/m seemed to describe the measured velocities better than those based on the viscosity quoted by the manufacturer (0.0026 Ns/m^2). By the time the experiment was carried out, the viscosity of the blood mimicking fluid seemed to have changed. Viscosity measurement carried out after the experiments and CFD calculation were completed lead to a viscosity of 0.0206 Ns/m^2 (Section 5.3.3).

A comparison of the velocity derived from the CFD calculation, for the z-component, with the PC MRI measurement can be seen in Figure 8.9. The viscosity had to be estimated to achieve this level of agreement. It is clear that the tendency for the highest velocity to occur at the inner wall of the bifurcation is the same in both data sets, but the line profile shows considerable disagreement at the vessel walls, the area of interest for WSR calculations.

CFD data for the wall shear stress (WSS) has also been provided. The magnitude can be seen in Figure 8.10 and the vectors in Figure 8.11. In all the straight sections of

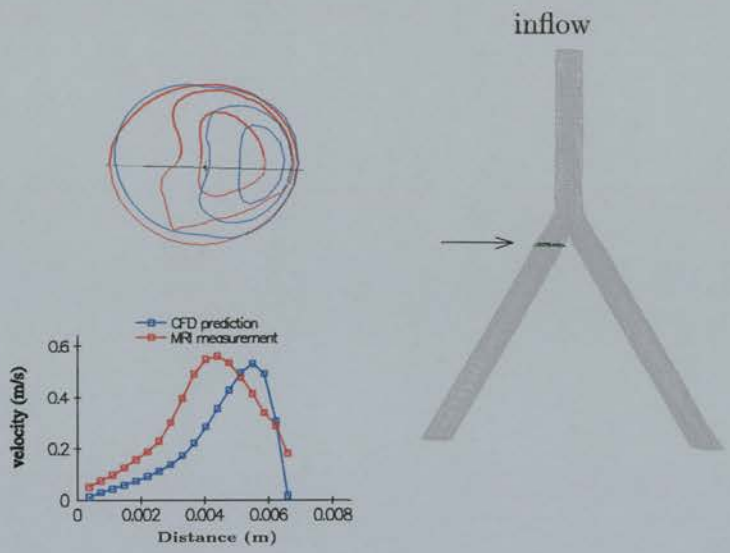

Figure 8.9.: *Example of the velocities measured with PC MRI and calculated using CFD for a volume flow rate of 10 ml/s in the 60° bifurcation phantom. The z-component of the velocity field is displayed as a contour plot and a line profile across the slice marked on the right hand image. The flow direction is from the top of the page down.*

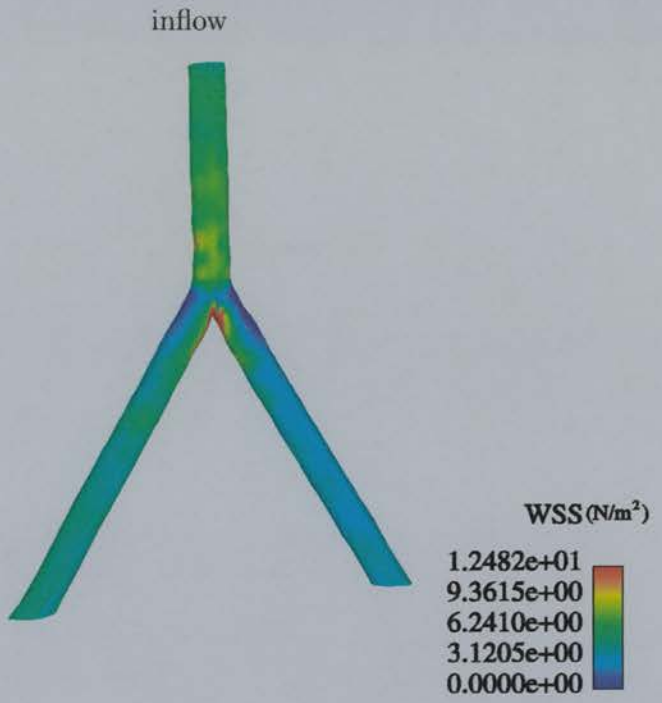

Figure 8.10.: *The magnitude of the wall shear stress as calculated using CFD for the 60° bifurcation phantom. The WSS is colour coded onto the surface. The flow direction is from the top of the page down.*

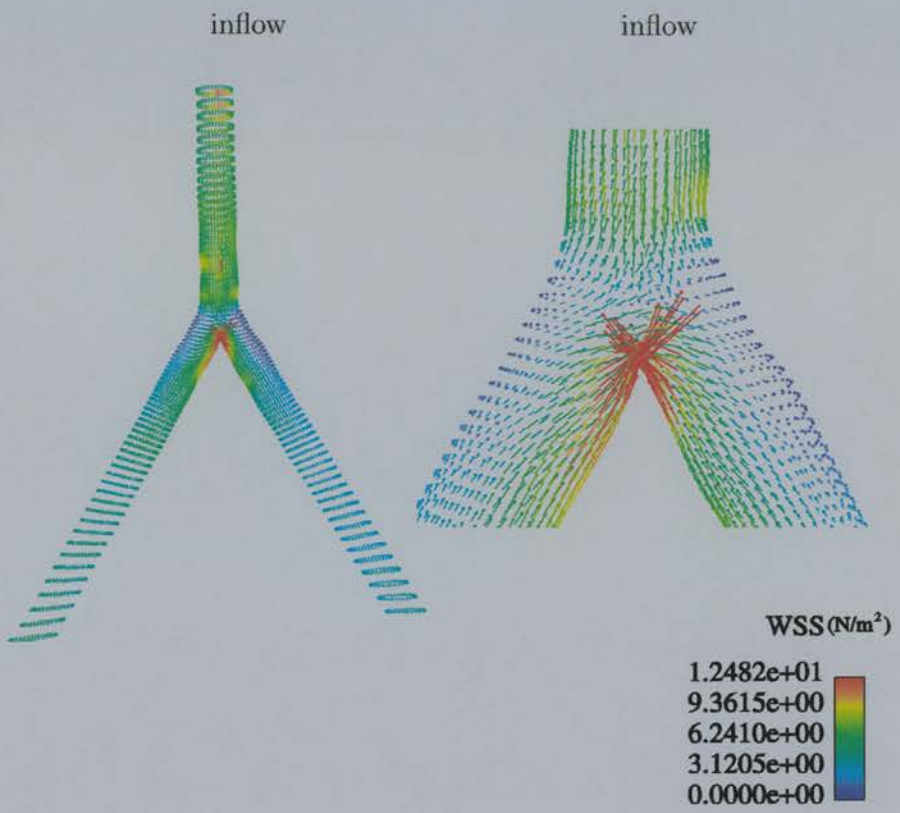

Figure 8.11.: *The wall shear stress vectors as calculated using CFD for the 60° bifurcation phantom. The WSS is presented as colour coded vectors. The flow direction is from the top of the page down.*

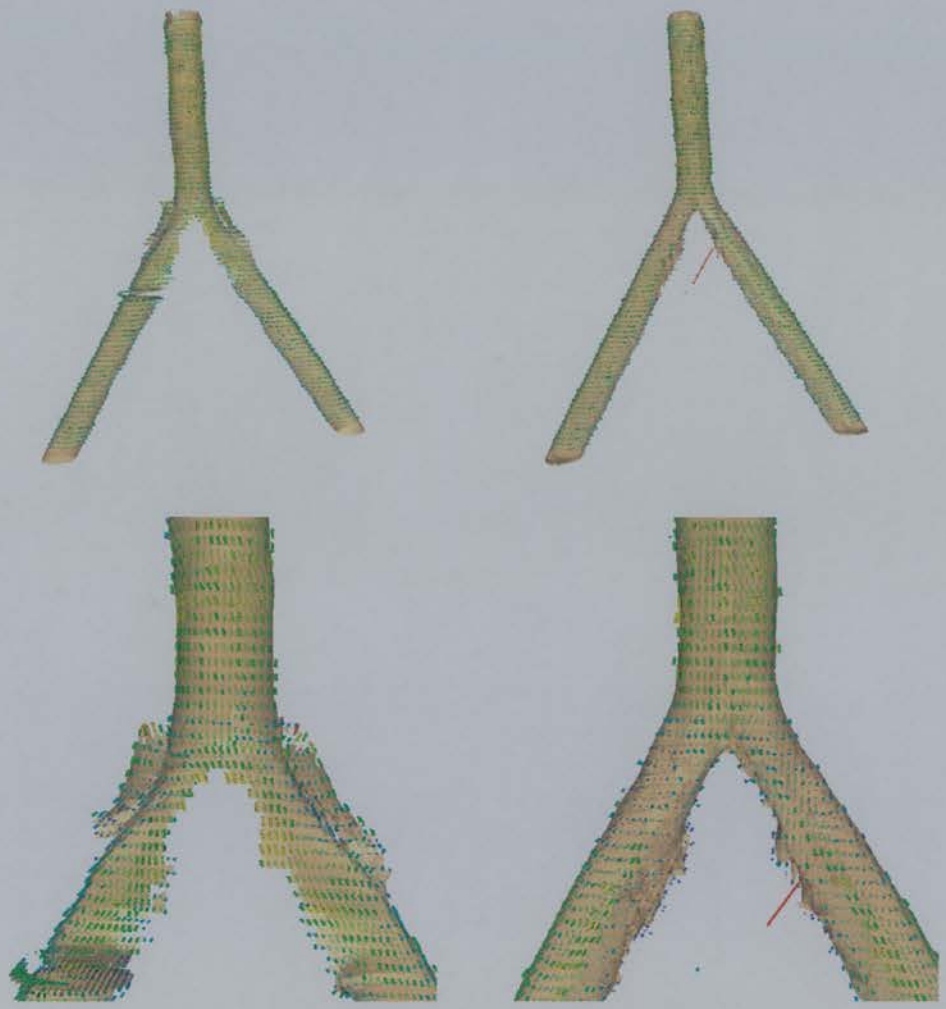

Figure 8.12.: *The wall shear rate vectors as calculated from the PC MRI acquisition with a T_R of 100 ms. The fitted wall was used for the images displayed in the left column and the detected wall in the right. The flow direction is from the top of the page down.*

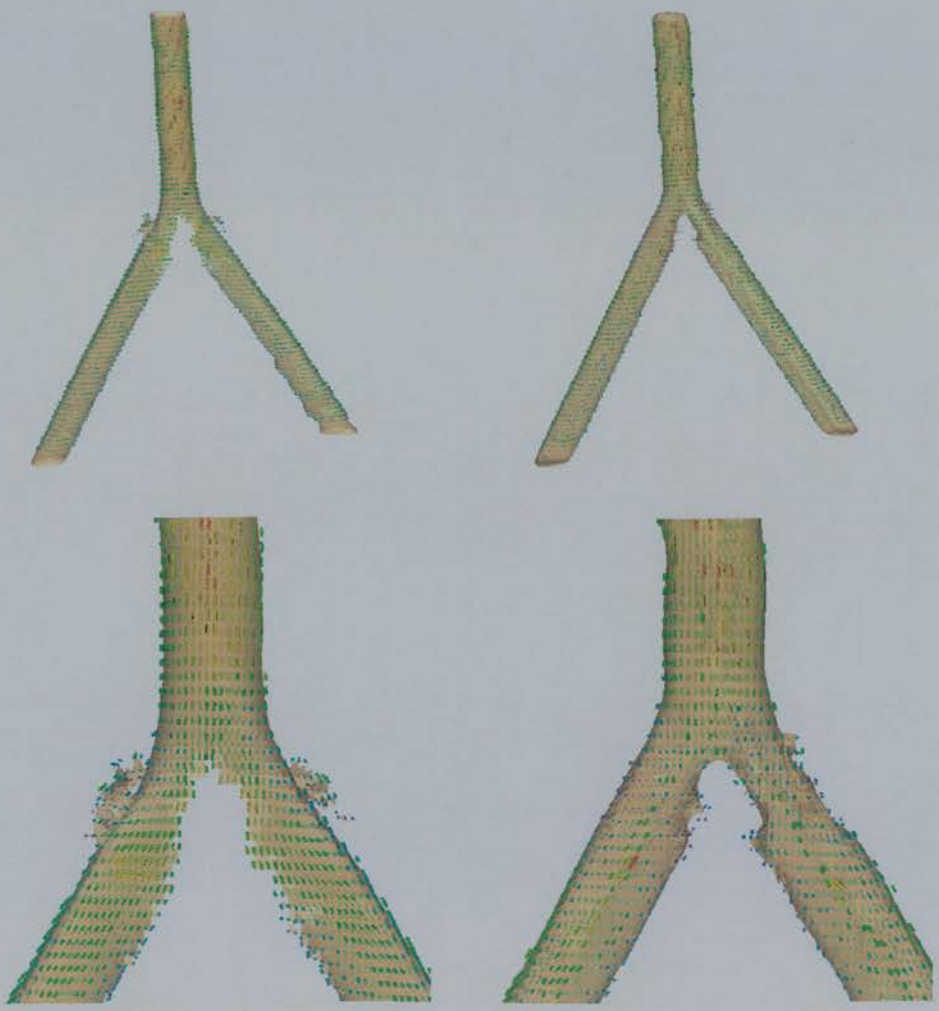

Figure 8.13.: *The wall shear rate vectors as calculated from the PC MRI acquisition with a T_R of 50 ms and four repetitions. The fitted wall was used for the images displayed in the left column and the detected wall in the right. The flow direction is from the top of the page down.*

the phantom, away from the bifurcation, the vectors align with the axis of the flow and remain stable. Around the bifurcation, the outside walls exhibit considerably reduced WSS and the WSS vectors rotate away from the principal axis of the branches.

Figures 8.12 and 8.13 show the WSR calculated from the PC MRI acquisitions with a T_R of 100 ms, and a T_R of 50 ms and four repetitions, respectively. A view similar to that provided in the CFD images was chosen. There are noticeable difficulties in reconstructing the inside surfaces of the bifurcating branches. This is due to the fact that the fit has little incentive to cross zero in this area. Outside this region, both acquisitions show similar trends to those seen in the CFD calculation. The WSR in the inflow vessel is similar and starts to change at the same distance from the bifurcation. The WSR at the outer wall of the bifurcation regions shows a reduction in magnitude. Parabolic flow with the associated behaviour of WSR is reconstituted quickly downstream of the bifurcation. Only the insides of the branches show a lower WSR in the measurements when compared to the CFD calculations. This could be due to difficulties in the surface reconstruction or the differences between measured velocities and the CFD calculation, which can clearly be seen in Figure 8.9. It is always difficult to model sharp edges with smooth surfaces and this difficulty can be observed in all the walls reconstructed from the measurements. Apart from this problem, the measurement of WSR and the predictions of CFD show a good agreement.

The study with a repetition time of 50 ms and four repetitions did not show any improvement over the study with a T_R of 100 ms and one repetition, which had a shorter acquisition time. In phantoms with no stationary background in close proximity to the flow regions, a single repetition with a long T_R was found to deliver the best results.

8.3. Normal Carotid Artery Model

A commonly used *in vitro* model of the human carotid artery (Section 5.3.6) was used to investigate a velocity field that represents the findings *in vivo*.

The human carotid artery phantom was scanned successfully with both the Elscint and the GE scanner. The acquisition matrix on the Elscint was 256 × 32 × 128 covering a FOV of 20 × 2.5 × 10.2 cm with a resulting voxel size of 0.78 × 0.78 × 0.8 mm in an

axial direction. The echo time was fixed at 10.791 ms and the repetition time of 24 ms and the tip angle of 20^o were chosen, leading to a total study time of 7 minutes. The encoding velocity was set to 50 cm/s. All three velocity components were measured.

The matrix on the GE scanner cannot be optimised to the same degree in order to keep the acquisition time down. The matrix used was 256 × 128 × 100. This included a FOV of 12 × 6 × 8 cm leaving the voxel size at 0.47 × 0.47 × 0.8 mm. The slab was oriented axially. The echo time was fixed by the scanner at 6.72 ms, and the repetition time (50 ms) and the flip angle (22^o) were chosen. This left the total acquisition time at 43 minutes. In this case the encoding velocity was adjusted to 60 cm/s. All three velocity components were measured.

The colour scale used for the WSR images of this phantom was fixed to a range from green (0 1/s) via yellow (343 1/s) to red (more than 686 1/s). This achieved a matching colour scale to the CFD calculations provided by Quan Long and Yun Xu (Dept. of Chem. Eng. & Chem. Technol., Imperial College, London). The simulation was based on a surface mesh reconstructed from structural MRI scans of the phantom provided by our group. The results were again based on a viscosity of 0.01387 Ns/m.

The velocity field of the human carotid phantom at a steady flow of 10 ml/s, the flow rate that corresponds to the values found in the volunteer studies (Chapter 9), is represented as a "hedgehog" in Figure 8.14 for the acquisition on the Elscint scanner. The flow detection included no noise in the flow region. The overall appearance of the flow field is rather noisy, but the complex flow pattern in the carotid bulb with low velocities can be seen clearly.

The variation of the volume flow rate for the acquisition of the human carotid phantom with slice position was calculated (Figures 8.15 and 8.16). The flow rates of 5 and 10 ml/s which were used are confirmed in the common carotid artery (< 105 mm). More fluid seems to flow into the internal carotid branch. This is due to the larger radius of the internal (2.775 mm) than the external branch (2.325 mm).

Since the flow rate is known in all branches, the wall shear rate (WSR) can be calculated in the straight section from the volume flow rate and the known radius of 4 mm (common carotid), 2.775 mm (post-sinus internal carotid) and 2.325 mm (external carotid). This calculation assumes Poiseuille flow. The flow rate was taken from the measurement

Figure 8.14.: *"Hedgehog" of the velocities in the human carotid phantom acquired on the Elscint scanner with a volume flow rate of 10 ml/s.*

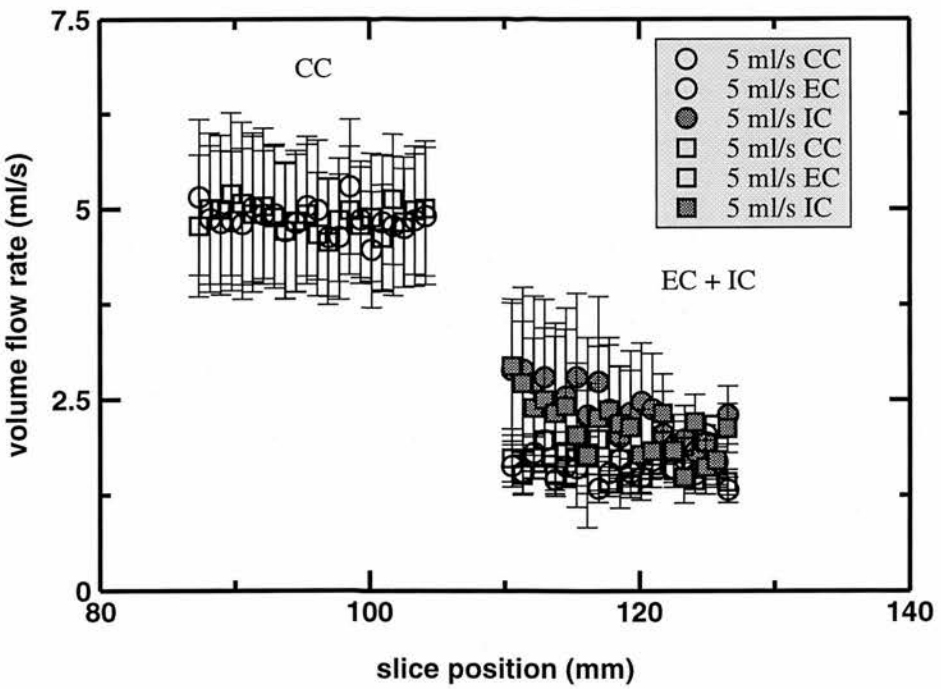

Figure 8.15.: *The dependence of the Volume flow rate (5 ml/s) in the human carotid phantom on the Elscint scanner.*

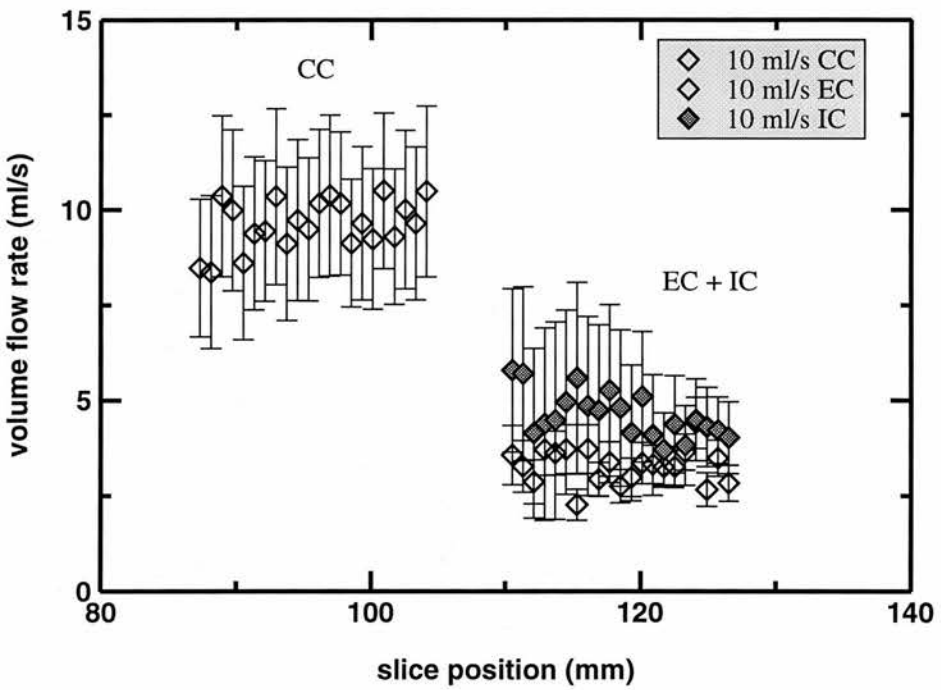

Figure 8.16.: *The dependence of the Volume flow rate (10 ml/s) in the human carotid phantom on the Elscint scanner.*

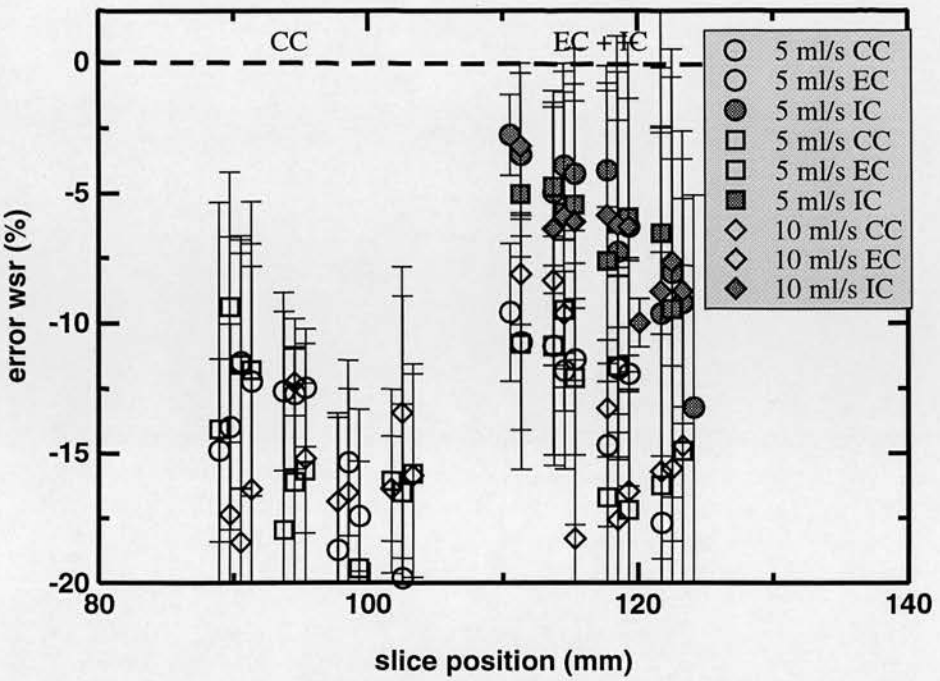

Figure 8.17.: *The error in WSR for the individual slices in the human carotid phantom for the fitted wall.*

rather than using the known volume flow rate to avoid assumptions about the branching ratio. The error between the measured and calculated WSR can be seen in Figure 8.17 for the fitted wall and Figure 8.18 for the detected wall. Around the bifurcation, which was located at 105 mm, the flow is not expected to be parabolic. Outside this region, both studies and both methods of wall reconstruction agree. The WSR is underestimated by about 15 % with slightly better values obtained from the detected wall. The values for the internal carotid branch are significantly better than for the external branch. This underestimation was predicted in Chapter 7 by the conservative estimate of the wall position.

The walls and WSR vectors reconstructed from the acquisition on the Elscint scanner with a volume flow rate of 10 ml/s can be seen in Figure 8.19. The fitted wall reconstruction on the left exhibits some segments outside the wall where the fitted velocity data undergoes a secondary zero crossing in the extrapolated area. In the carotid bulb, two surfaces are reconstructed. The inner surface is located at an inner position with a zero crossing. This surface marks the flow separation in the carotid bulb. At the outside

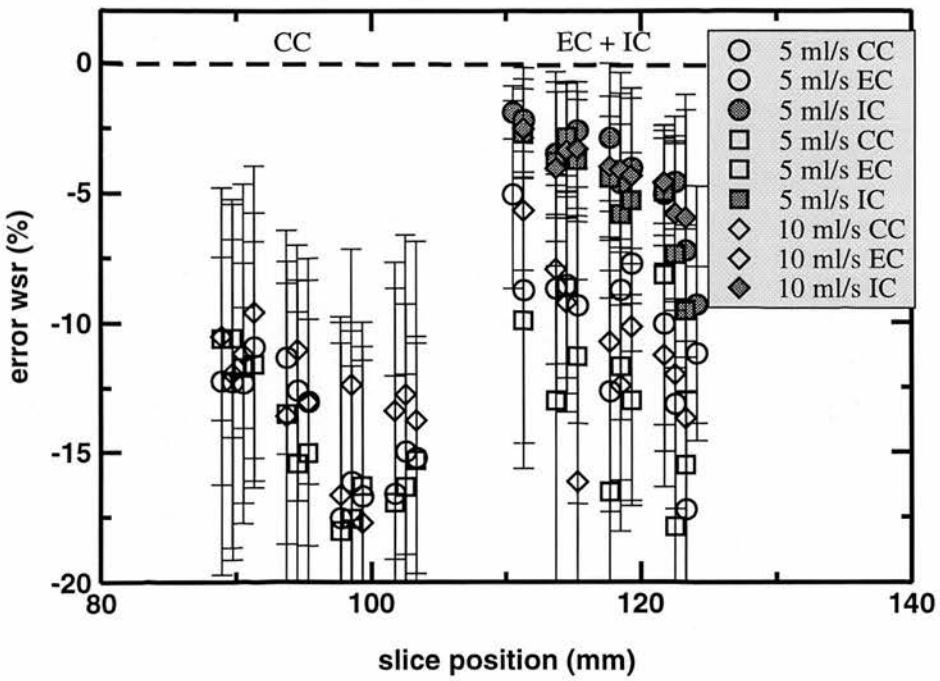

Figure 8.18.: *The error in WSR for the individual slices in the human carotid phantom for the detected wall.*

of the carotid bulb, no surface was reconstructed. This is a result of the fit not having an incentive to cross zero between the branches. The detected wall does not suffer from these problems, but the external carotid branch looks very thin. This is probably due to the smoothing of the surface.

A comparison of the CFD velocity data for the z-component with the PC MRI measurement can be seen in Figure 8.20. Uncertainty in the value of the viscosity meant the properties had to be estimated in the CFD calculation. The results based on a viscosity of 0.01387 Ns/m seemed to describe the measured velocities better than those based on the viscosity quoted by the manufacturer (0.0026 Ns/m^2). By the time the experiment was carried out, the viscosity of the blood mimicking fluid seems to have changed. Viscosity measurement carried out after the experiments and CFD calculation were completed lead to a viscosity of 0.0206 Ns/m^2 (Section 5.3.3). It is clear that the tendency for the highest velocity to occur at the inner wall of the bifurcation is the same in both data sets, but the line profile shows considerable disagreement at the vessel walls.

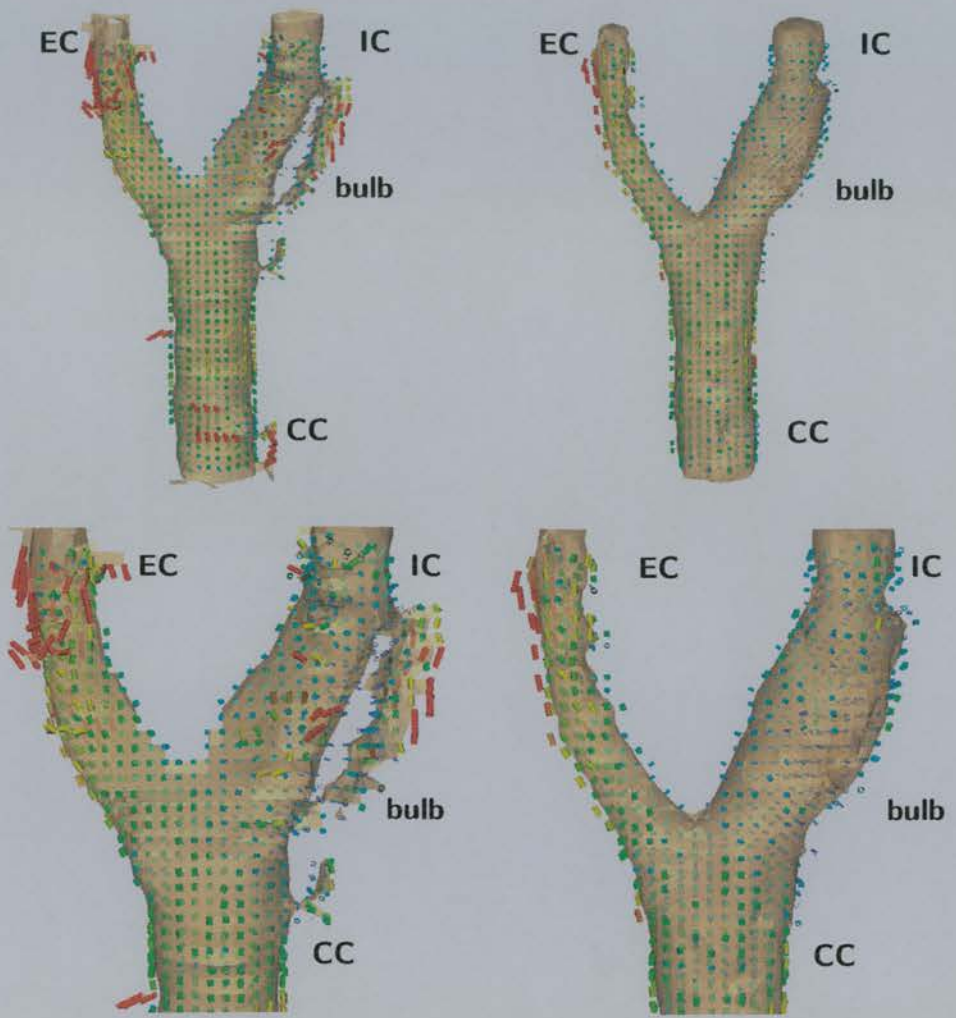

Figure 8.19.: *The wall shear rate vectors as calculated from the PC MRI acquisition on the Elscint scanner. The data which uses the fitted wall is presented in the left column and the detected wall in the right. The data is based on the acquisition with a volume flow rate of 10 ml/s.*

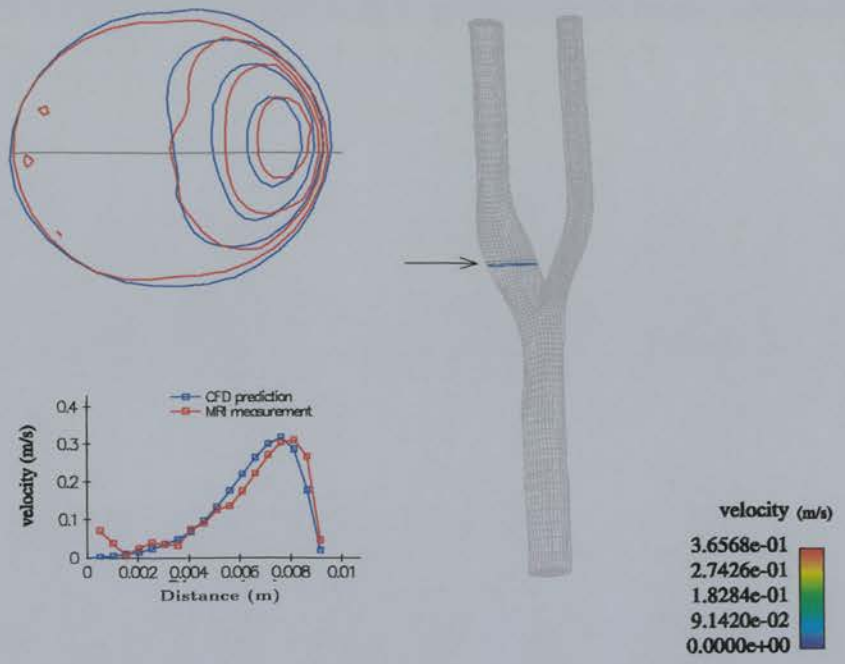

Figure 8.20.: *Example of the velocities measured with PC MRI and calculated using CFD for a volume flow rate of 10 ml/s in the human carotid phantom. The z-component of the velocity field is displayed as a contour plot and a line profile across the slice marked on the right hand image.*

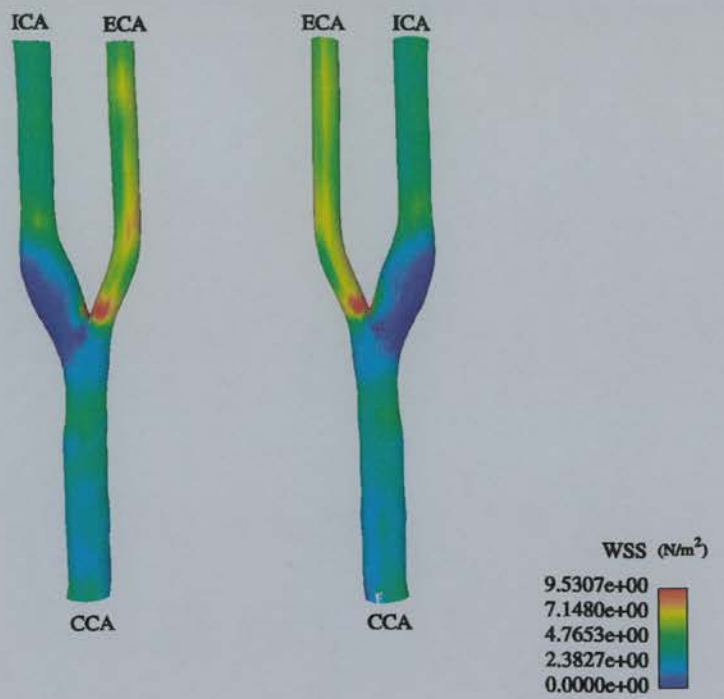

Figure 8.21.: *The magnitude of the wall shear stress as calculated using CFD for the human carotid phantom. The WSS is colour coded onto the surface.*

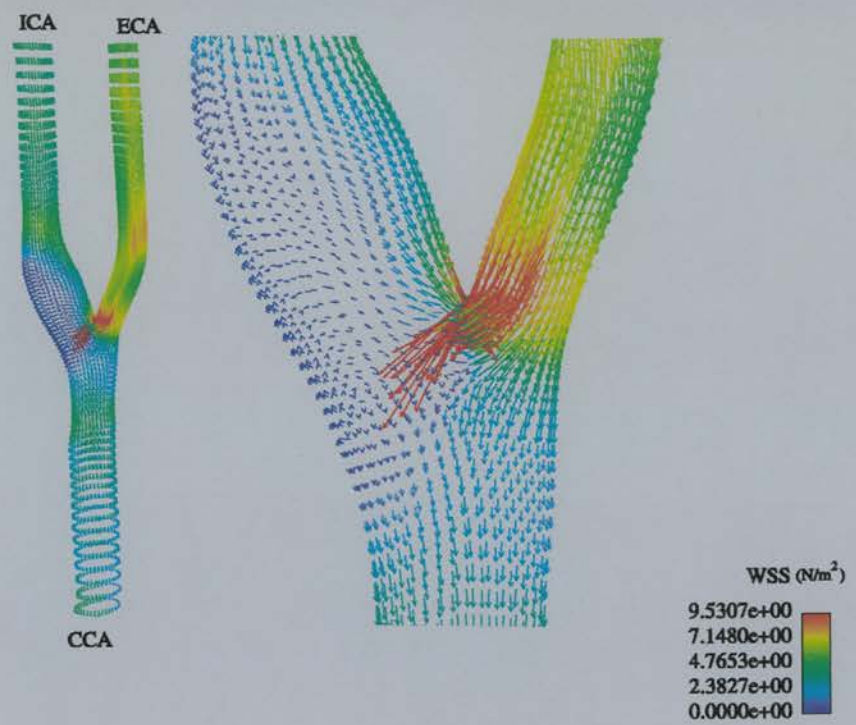

Figure 8.22.: *The wall shear stress vectors as calculated using CFD for the human carotid phantom. The WSS is presented as colour coded vectors.*

The wall shear stress has been calculated using CFD. The magnitude can be seen in Figure 8.21 and the vectors in Figure 8.22. In all the straight sections of the phantom away from the bifurcation, the vectors align with the axis of the flow and remain stable. Around the bifurcation, the outside walls exhibit markedly reduced WSS and the WSS vectors rotate away from the principal axis of the branches.

The reduction of WSR can be seen in the values calculated from the acquisition on the Elscint scanner. There is also good agreement for the common branch (Figure 8.19). The higher WSR in the bifurcation and the lower values at the lateral wall of the external branch, however, cannot be seen clearly in the measured data.

The velocity field acquired on the GE scanner with a steady flow rate of 10 ml/s is presented in Figure 8.23. The detected flow region replicates the geometry of the phantom very well and no noise is included in the flow. At the flow divider, where the inertia of the fluid leads to higher velocities at the inner walls of the phantom, high velocity streams are clearly visible in the internal and external carotid branch. In the bulb the flow field is more complex with lower velocities. Parabolic flow profiles can be found in the common branch close to the bifurcation and reconstitutes only few slices downstream of the bifurcation in both branches. The viscosity of the blood mimicking fluid had increased by the time these experiments were carried out and the exact value remains unknown. It can, however, be estimated at $0.0206\,\mathrm{Ns/m^2}$. The high viscosity leads to a faster reconstitution of parabolic flow profiles.

The variation of the volume flow rate for the acquisition of the human carotid phantom on the GE scanner with slice position can be seen in Figure 8.24. Flow rates of 5 and 10 ml/s were used, which were confirmed in the common carotid artery ($< 35\,\mathrm{mm}$). The branching ratio between the internal and external branch ($> 35\,\mathrm{mm}$) seems to be around 50 %. The measurements for 15 ml/s showed consistent results.

As for the acquisition on the Elscint scanner, the WSR can be calculated from the volume flow rate. The error between the measured and calculated WSR can be seen in Figure 8.25 for the fitted wall and Figure 8.26 for the detected wall. The results are very similar to those for the Elscint scanner (Figures 8.17 and 8.18), although the detected wall does not have an obvious advantage in this case. The values determined for the internal carotid are better, again.

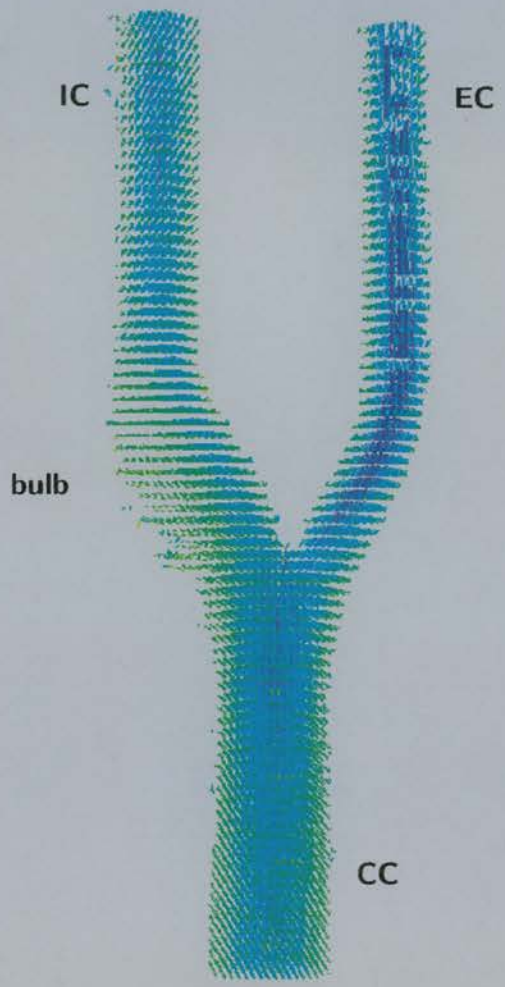

Figure 8.23.: *"Hedgehog" of the velocities in the human carotid phantom acquired on the GE scanner with a volume flow rate of 10 ml/s.*

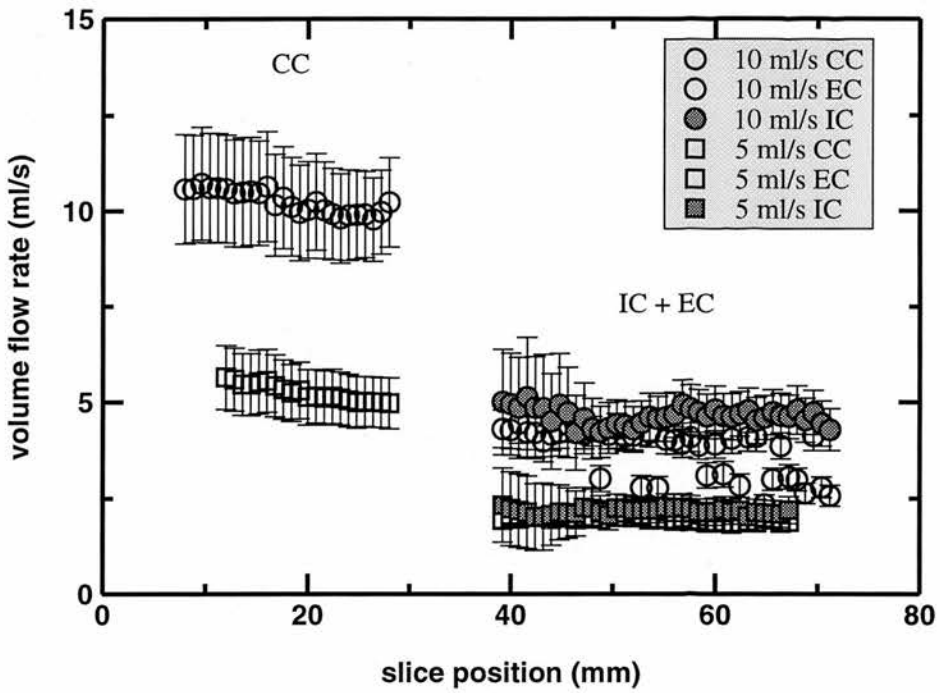

Figure 8.24.: *The dependence of the Volume flow rate in the human carotid phantom on the GE scanner.*

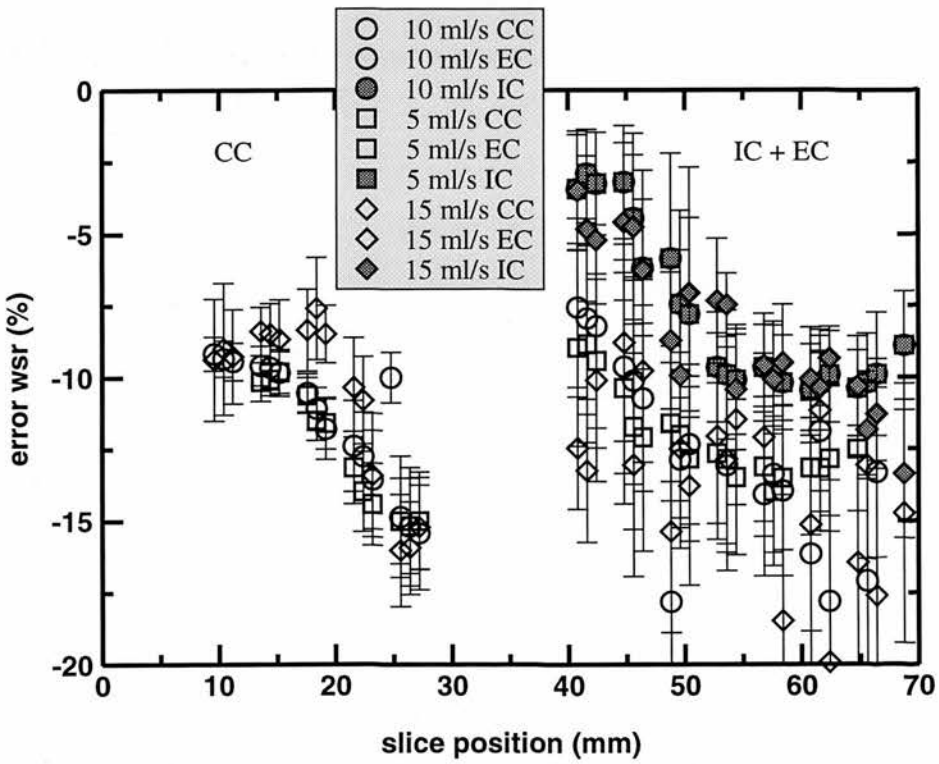

Figure 8.25.: *WSR error for the individual slices in the human carotid phantom for the fitted wall.*

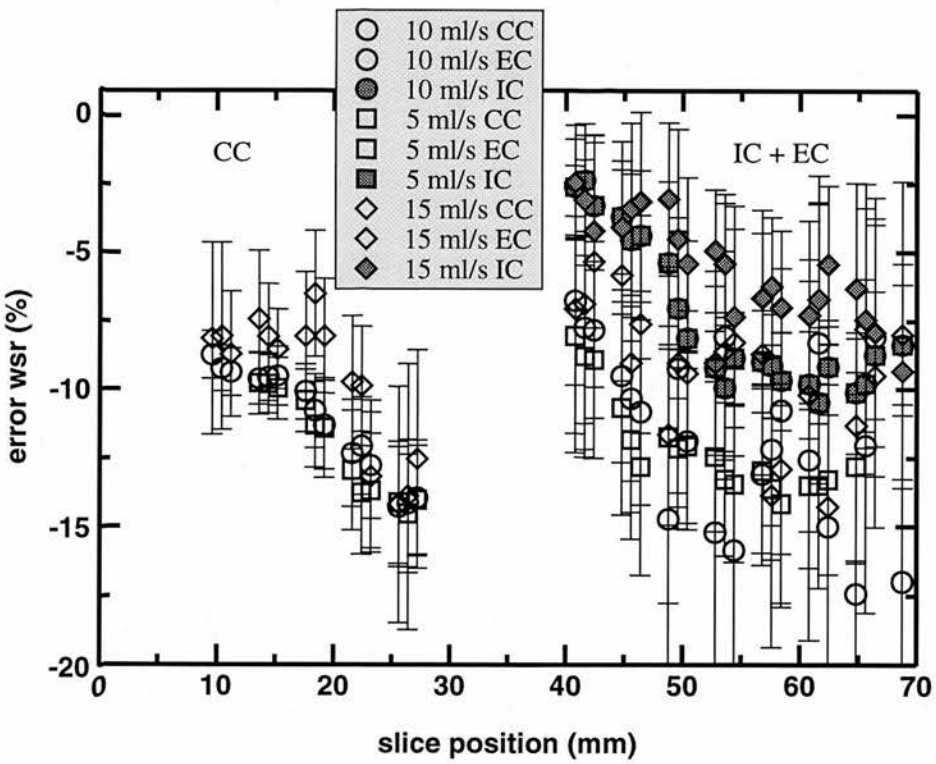

Figure 8.26.: *WSR error for the individual slices in the human carotid phantom for the detected wall.*

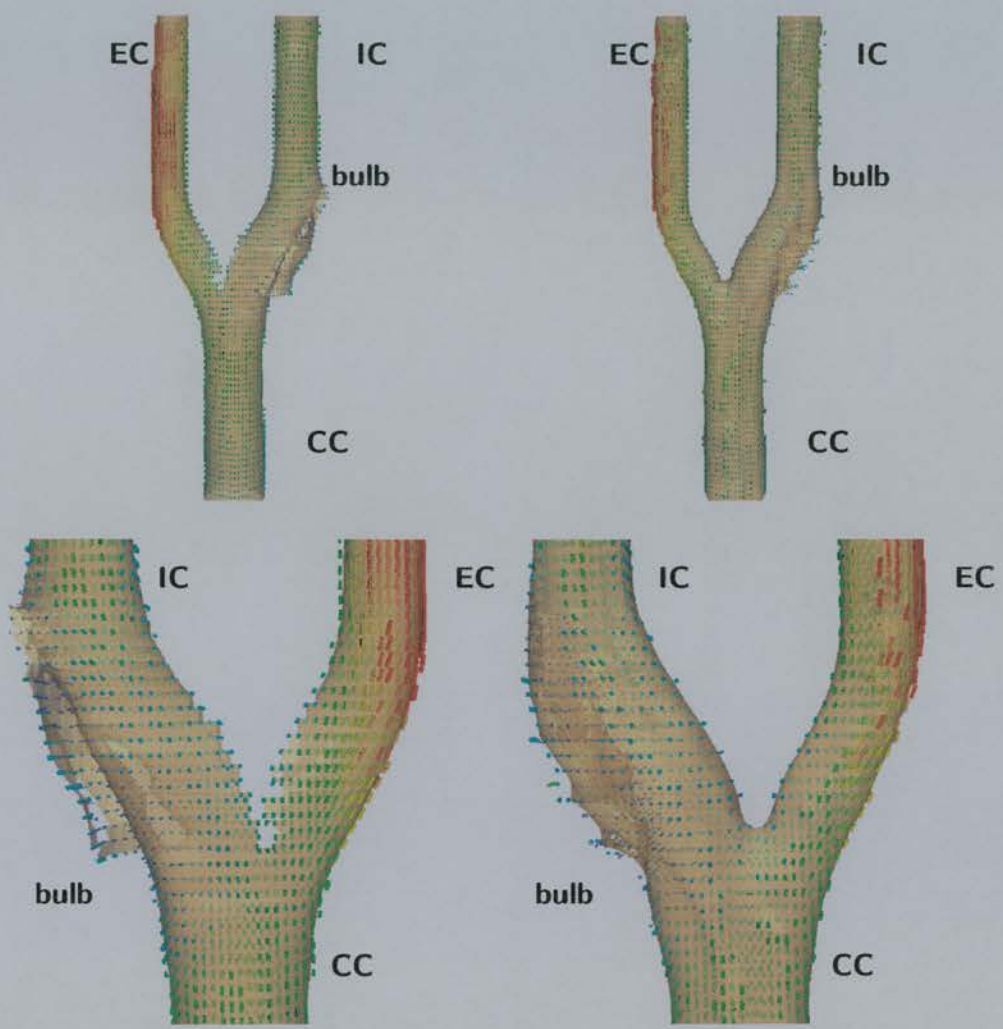

Figure 8.27.: *The wall shear rate vectors in the human carotid phantom at 10 ml/s as calculated from the PC MRI acquisition with a T_R of 50 ms on the GE scanner. The fitted wall was used in the left column and the detected wall in the right.*

The WSR vectors calculated for the fitted and detected wall are presented in Figure 8.27 for the acquisition with a steady flow rate of 10 ml/s and a T_R of 100 ms. Outside the carotid bulb, the geometry of the human carotid phantom is reconstructed closely by both methods of wall reconstruction. The sharp edge of the flow divider is very difficult to describe with a smooth polynomial function and hence no wall was found in that region using the fitted wall. The complex flow field in the carotid bulb possesses a zero crossing inside the vessel due to flow separation. This leads to the reconstruction of an inner wall for the fitted surface. The flow field is too complex in this region to produce absolutely correct surfaces. The detected wall does not exhibit a secondary surface, but the surface is not as smooth as the phantom. The WSR vectors in the bulb show nonetheless the right trend when compared to the CFD calculations (Figures 8.21 and 8.22). The WSR is decreased in the carotid bulb when compared to any other region of the phantom. The high WSR values at the flow divider that were predicted by CFD, however cannot be seen in the values calculated directly from the experiments. The CFD calculation predicts higher values of WSR at the outer wall of the external carotid branch. This effect is also seen in the values calculated from the experiments. Here, the WSR values are even higher. Overall, the agreement between CFD and experiment for WSR calculation is good.

8.4. Discussion and Conclusion

The *in vitro* flow detection algorithm (**Alg. 2** in Chapter 6) was successfully applied to all phantom data sets. No noise was included in the flow region with the correct choice of threshold value. The segmented fifth order fit was sufficient to describe the complete velocity field acquired in the phantom studies. The comparison of the velocity fields acquired using the Elscint and GE scanners showed a significant improvement with the GE scanner except for the slice dependent flow encoding. The increased resolution of 0.018 mm^3 on the GE versus 0.049 mm^3 on the Elscint scanner is the major contribution to this improvement, since the velocity noise does not significantly increase with the enhanced resolution.

The acquisition of the bend phantom shows a limit of the present method. With more than three times as many points included in the flow region, the calculation times on our

computers take about half a day to determine WSR vectors and the interactive display is too slow to be termed truly interactive. The method worked, however, and it would be interesting to compare the WSR results with CFD simulations as soon as these can be provided.

Both the 60^o bifurcation and the human carotid phantom studies were compared with theoretical results, where possible, and the agreement found was good. A 12 % underestimation of the WSR was predicted from simulation results (Chapter 7) and that is the discrepancy found for these comparisons with theory. The human carotid data acquired with the Elscint scanner shows a slight underestimation and higher variation than the results on the GE scanner. This is due to the lower quality (resolution and SNR) of the measured velocity field.

Additional comparison with CFD data was possible for these two phantoms. Both the overall values and the trends for WSR predicted in the CFD results are reflected in the measured WSR data. This agreement is all the more surprising, since the CFD data seems to deviate from the measured velocities at the vessel walls (Figures 8.9 and 8.20). Only the regions at the flow divider show significant disagreement. This can be explained by the difficult modelling of a sharp edge with smooth functions. Overall, the method to calculate WSR worked well for flow in complex geometries.

9. Volunteer Studies

9.1. Introduction

Volunteer studies were initiated on the carotid arteries primarily because of the established collaboration between the MRI group of the Department of Medical Physics and the Stroke Research Group of the Department of Clinical Neurosciences. It also allowed comparison with the *in vitro* data acquired for the anthropomorphic carotid phantom. Another advantage is the fact that the carotid arteries remain relatively stationary during the heart and breathing cycle, thus reducing the effect of movement artefacts.

Three volunteers were recruited each of whom was a young (< 30 years), healthy male who had given informed consent prior to scanning. The long acquisition times of the 3D velocity studies (typically 30 minutes) made them susceptible to EMI on the GE scanner (Section 5.2.2) and movement artefacts. Care was taken to reduce the acquisition time as far as possible, sometimes at the cost of limiting the anatomical coverage. Volunteer 1 was scanned on the Elscint scanner, Volunteer 2 on both the Elscint and GE scanners, and Volunteer 3 on the GE scanner. Several ungated 2D slices were initially acquired to determine the optimum encoding velocity. This was followed by the main scan, an ungated 3D acquisition with high spatial resolution. Since the acquisition was not

synchronised with the heart rate, the resulting data set should represent a time-averaged velocity field.

The colour scale for all wall shear rate (WSR) images that are presented extends from green (0 $^1/_s$) via yellow (150 $^1/_s$) to red (more than 300 $^1/_s$) and the vector length is proportional to the WSR magnitude. This corresponds to wall shear stresses (WSS) ranging from 0 to 0.90 N/m^2 assuming a viscosity $\eta = 0.003$ Ns/m^2 for blood [BHHR95]. The scale was fixed after examination of all available data sets.

9.2. Volunteer 1

An ungated 3D PC study was acquired on the Elscint scanner for Volunteer 1. Using a FOV of 15×15×5.4 cm with a resolution of 256×256×36 resulted in a voxel size of 0.58×0.58×1.5 mm. The 3D slab was placed in an axial orientation centred at the level of the carotid bifurcations. The sequence parameters used the minimum echo time T_E = 10.8 ms, the minimum repetition time T_R = 24 ms in order to keep the acquisition as short as possible and a standard flip angle $\alpha = 30^o$. This kept the total acquisition time about 15 minutes in length. After evaluating a number of 2D PC slices that covered the desired volume, the encoding velocity was chosen as v_{enc} = 50 cm/s. All three velocity components were measured.

Figures 9.1 and 9.2 illustrate the velocity field in the left carotid bulb. The velocity vector at every location of the grid is represented by a line. This representation is called a "hedgehog". The *in-vivo* flow detection algorithm (**Alg. 3**) that was discussed in Chapter 6 separates the flow region without any residual noise. The increase in the velocities around the flow divider and the drop in velocity in the carotid bulb can clearly be seen. The colours range from green (no flow) to the maximum speed (dark blue) over the full range of velocities detected. The same behaviour was found in the human carotid phantom (Figure 8.23). The velocities in a single slice through the bulb are shown as vectors in Figure 9.2 together with the magnitude image of that slice and the detected wall for the complete volume. The magnitude image shows the flow void and the associated reconstruction problem for the detected wall can be seen through the transparent surface. The complex nature of the flow inside the bulb can be observed as a change in orientation of the velocity vectors.

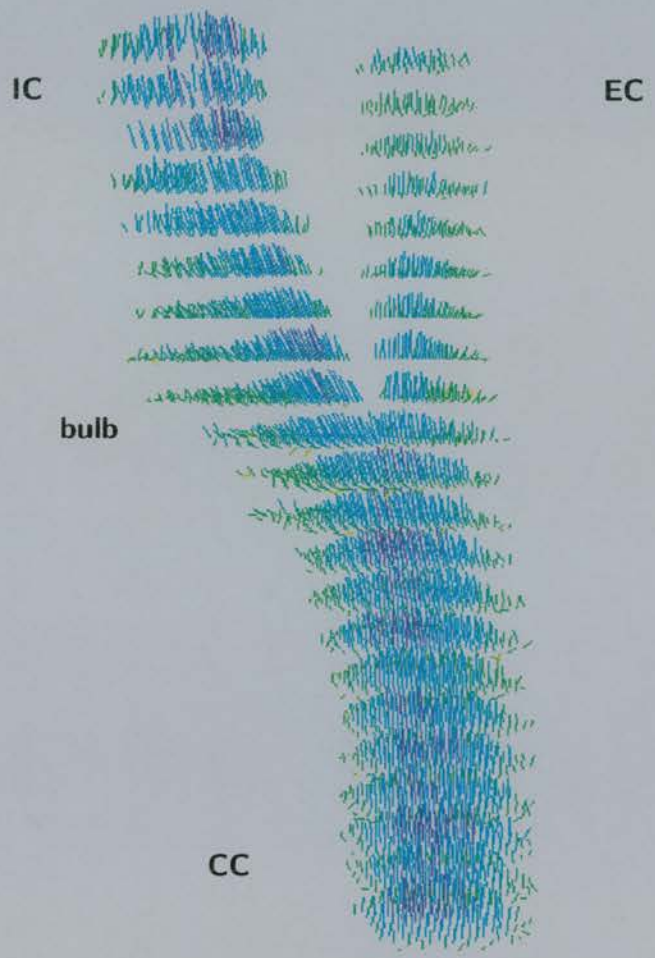

Figure 9.1.: *"Hedgehog" of the velocities in Volunteer 1's left carotid artery. The velocity data was acquired on the Elscint scanner.*

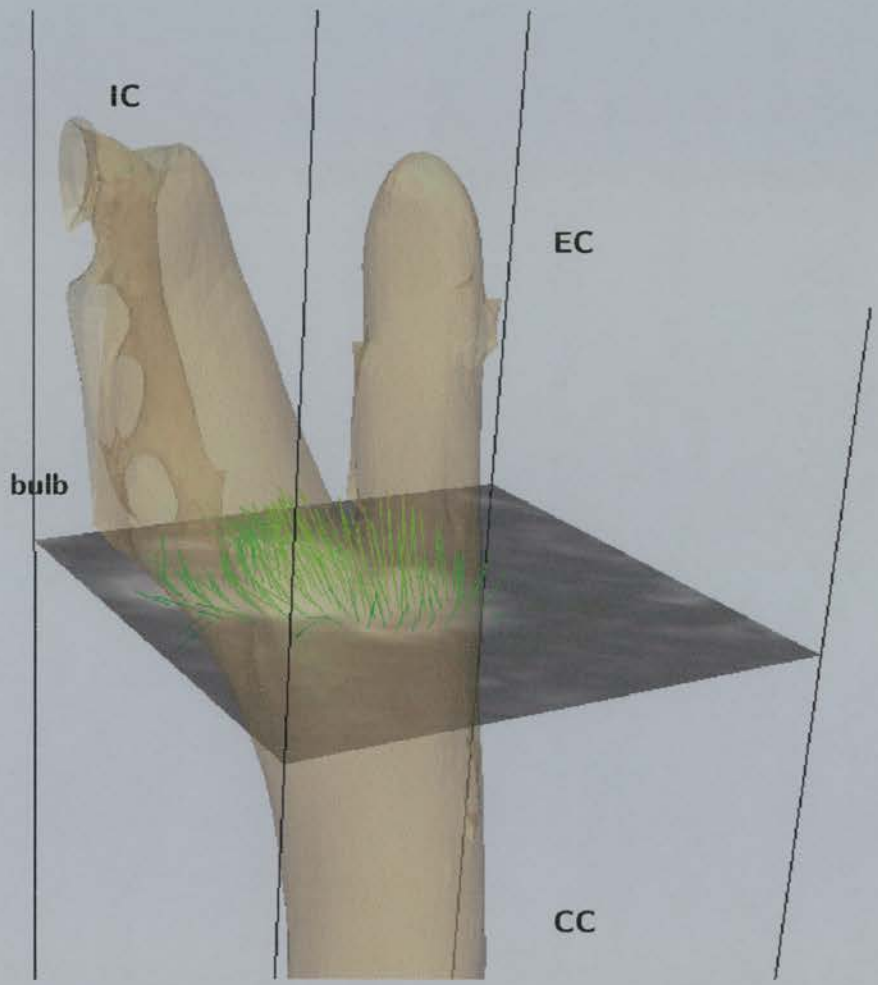

Figure 9.2.: *Velocities in a slice through Volunteer 1's left carotid bulb. The grey scale slice shows the magnitude image of that slice and the vectors represent the measured velocities. The detected wall is shown as a transparent surface. The velocity data was acquired on the Elscint scanner.*

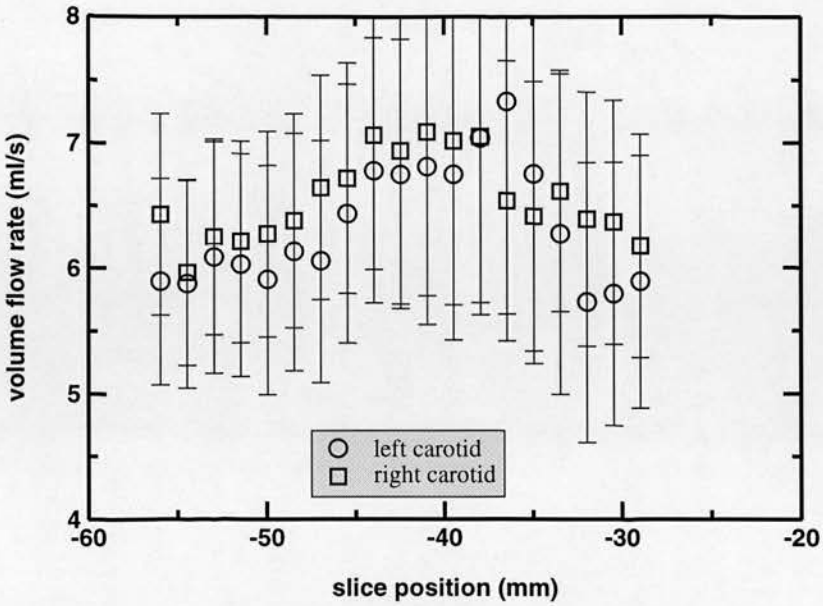

Figure 9.3.: *Dependence of the volume flow rate measured in Volunteer 1's left and right carotid arteries. The velocity data was acquired on the Elscint scanner.*

The detected volume flow rate in the left and right carotid arteries, which includes the common (CC) combined with internal (IC) and external (EC) branches, was calculated (Figure 9.3). Both sides are similar and the volume flow rate remains constant within error bars for most of the slices. The error bars were calculated from the number of flow pixels in a slice and the expected velocity noise of 5 % v_{enc} in each pixel.

The calculated wall shear rates (WSR) in the left carotid artery bifurcation are shown in Figure 9.4 for the fitted and detected wall. The fitted wall does not reconstruct the two branches, and combines them over the whole volume of interest. Within the carotid bulb, the reconstruction fails due to the complex flow field with low velocities. However, the detected wall does distinguish the two branches. It also shows a problem in the carotid bulb. This was associated with the flow void in the magnitude images.

In the complex flow field of the carotid bulb, intra-voxel phase dispersion destroys the signal of the spins and hence the magnitude image appears darker. This effect is illustrated in Figure 9.5, where the central bright region is the carotid bulb. It clearly displays a flow void at the centre of the magnitude image (Figure 9.5(a)). The phase map (Figure 9.5(b)) shows the low velocities in the z-direction associated with this feature.

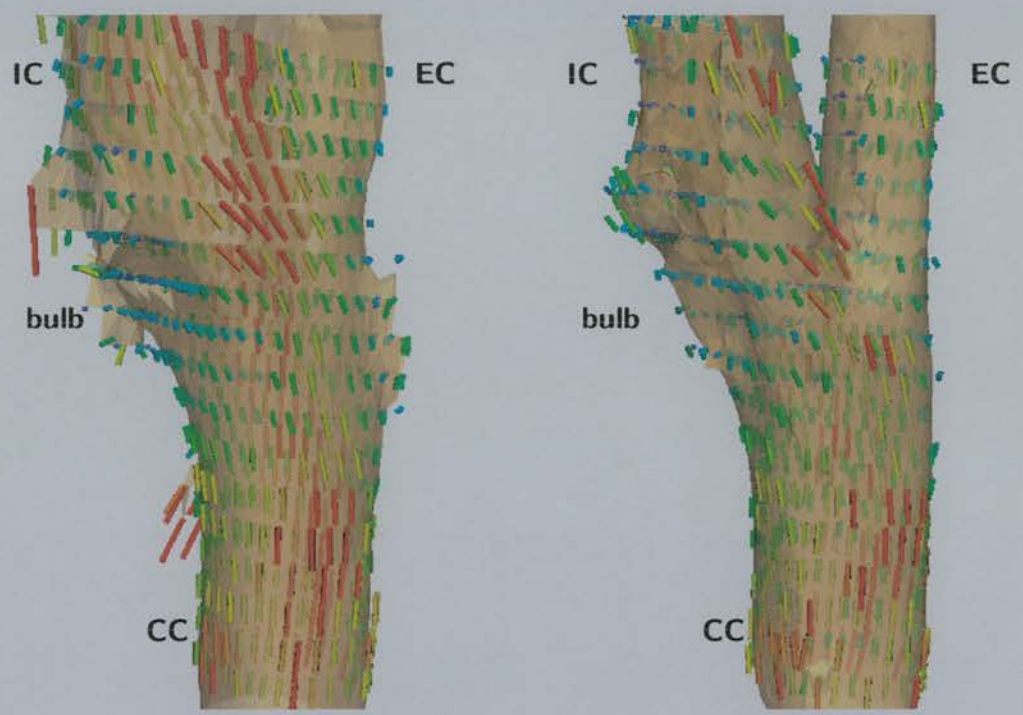

Figure 9.4.: *The wall shear rate in Volunteer 1's left carotid artery calculated from the fitted wall (left) and the detected wall (right). The colour scale ranges from green ($0\,^1/_s$) via yellow ($150\,^1/_s$) to red (more than $300\,^1/_s$), determined from the WSR magnitude. The velocity data was acquired on the Elscint scanner.*

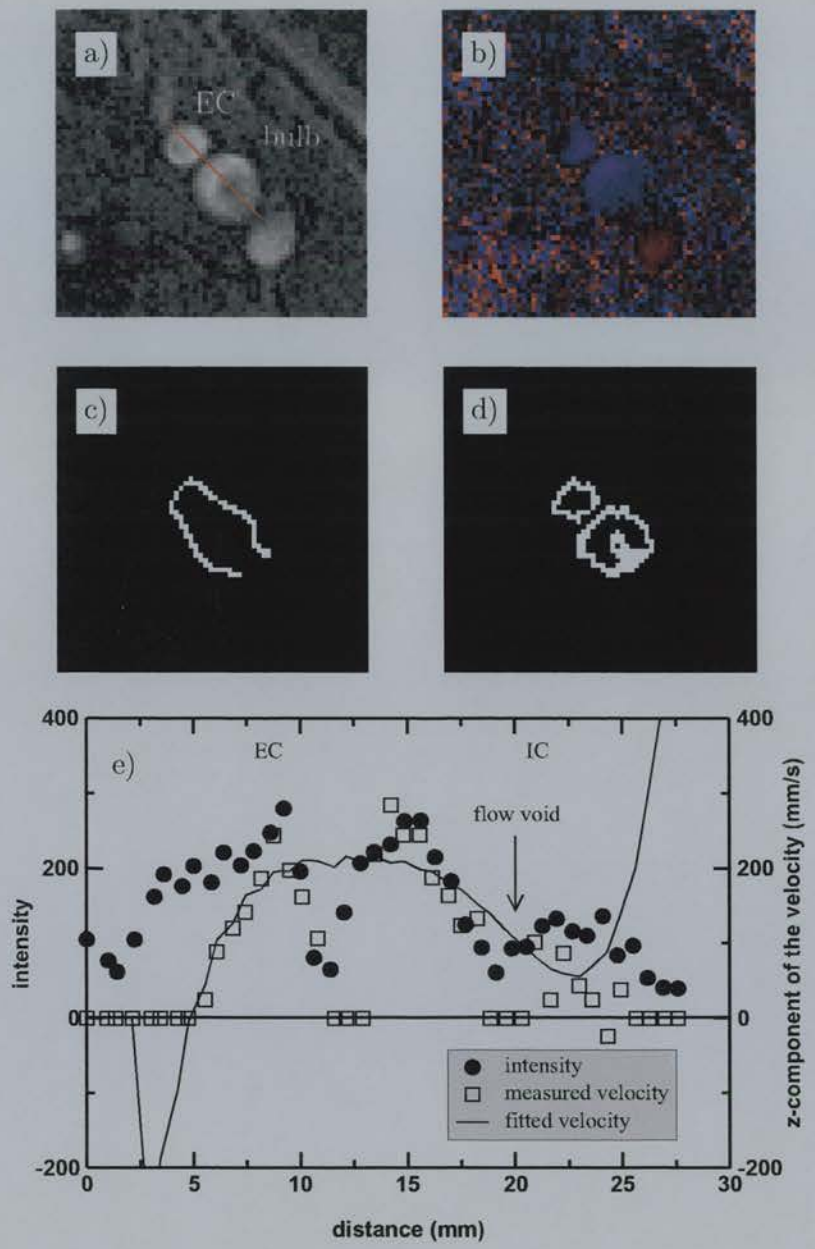

Figure 9.5.: *Illustration of flow voids using the left carotid bulb of Volunteer 1. The magnitude image is displayed in (a) with the external carotid artery, the internal carotid artery and the jugular vein from the top left to the bottom right of the central bright regions. The phase map for the z-direction is presented in (b) and the reconstructed fitted wall (Section 7.3.3) in (c) and the detected wall (Section 7.3.2) in (d). The line profile (e) was taken along a line from the top left of the external carotid to the gap between the internal carotid and the jugular vein. This line is marked in red on image (a). The velocity data was acquired on the Elscint scanner.*

The wall reconstructed from the fitted velocities (Figure 9.5(c)) exhibits a hole in the surface while the detected wall (Figure 9.5(d)) exhibits an inner wall around the pixels that were discarded by the flow detection algorithm. The line profile (Figure 9.5(e)) shows the variation of the intensity and z-component of the velocity along a line from the outside of the external carotid to the outside of the internal carotid. In the external carotid, the velocity decreases more quickly than the intensity. Velocity information for pixels that were discarded by the flow detection are shown with a velocity of zero. In the internal carotid, the drop in intensity is apparent. The velocities in the lateral parts of the bulb are relatively low. The segmented fifth order fit of the velocities works well for the outside of the external carotid and the internal carotid, but near the flow divider, the fit does not decrease in value sufficiently. Hence the extrapolation on the outside of the internal carotid does not cross zero. This is the reason why no fitted wall is reconstructed in the flow divider and at the outside of the carotid bulb. However, in most places, the two methods give comparable results and can be seen to complement each other.

In the carotid bulb, a drop in WSR has been indicated in the formation of plaque (Chapter 1). Examining the right carotid bulb, it is clear that the bulb is modelled more accurately with the fitted wall (Figure 9.6, left) than the detected wall (Figure 9.6, right). The overall agreement between the methods is lower for this side of the neck. Both models seem to produce a slightly higher WSR for the right carotid bulb than the left. All algorithms employed in this project are fully isotropic within a slice and could not introduce such an effect.

To give a better impression of the 3D nature of the results, the view from the outside of the neck towards the right carotid artery is presented (Figure 9.7). The vertebral artery (VA) can be seen in the background. There are, unfortunately, not enough pixels across the vessel at this resolution to provide reliable data for a WSR calculation. The two branches of the carotid artery are separated for the fitted wall (Figure 9.7, left) as well as the detected wall (Figure 9.7, right). Excluding the highest values of WSR calculated, the two methods agree well. All the views presented show a distinct deviation of the WSR vector from the z-direction.

The mean WSR in the common carotid arteries of this volunteer was (231±52) $^1/_s$ corresponding to a WSS of (0.693±0.156) N/m^2 for the fitted wall and WSR = (240±73) $^1/_s$ or

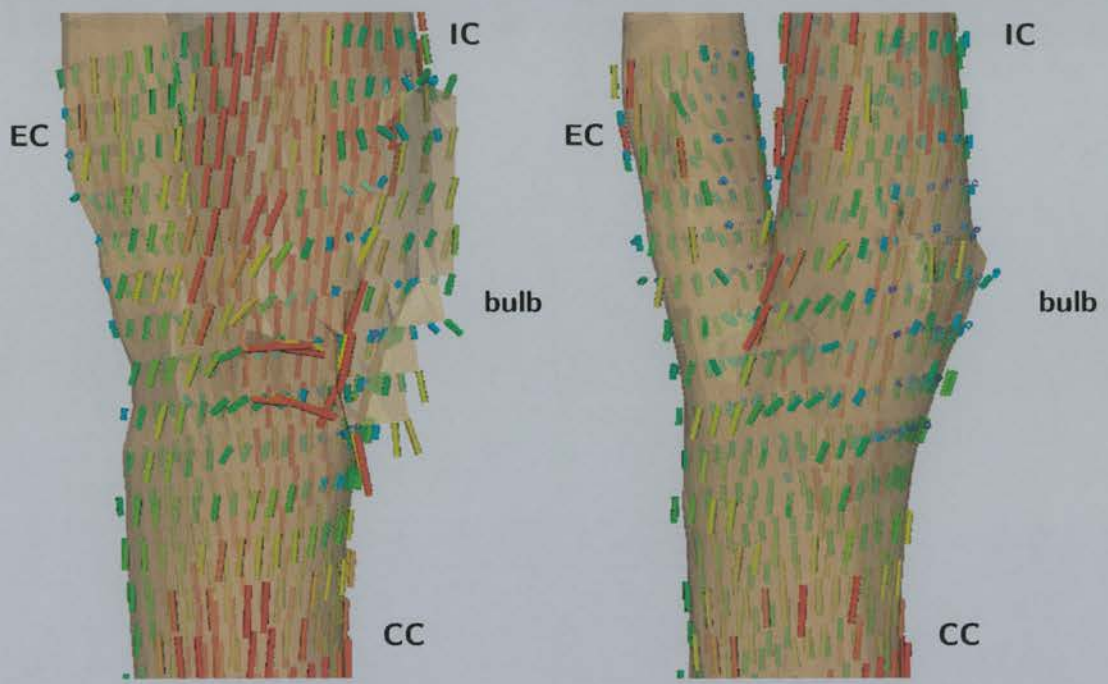

Figure 9.6.: *The wall shear rate in Volunteer 1's right carotid artery calculated from the fitted wall (left) and detected wall (right). The colour scale ranges from green ($0\,^1/_s$) via yellow ($150\,^1/_s$) to red (more than $300\,^1/_s$) determined from the WSR magnitude. The velocity data was acquired on the Elscint scanner.*

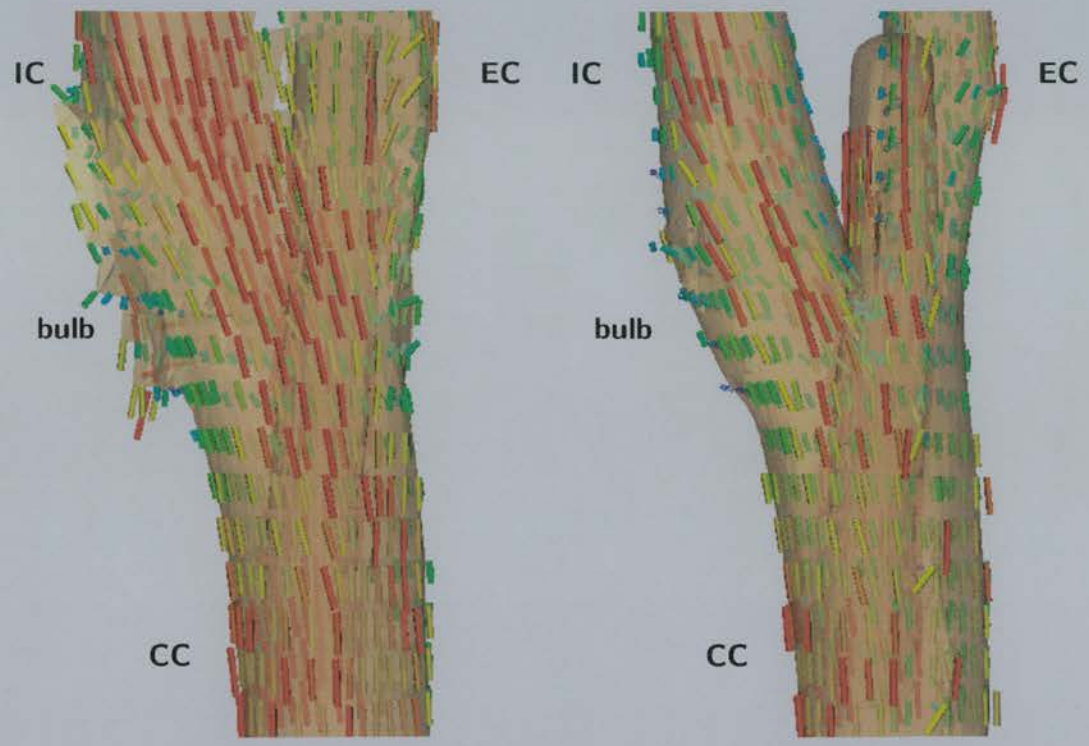

Figure 9.7.: *The wall shear rate in Volunteer 1's right carotid artery calculated from the fitted wall (left) and the detected wall (right). A view from the outside of the neck towards the bifurcation was chosen. The right vertebral artery can be seen in the background. The colour scale ranges from green (0 $^1/_s$) via yellow (150 $^1/_s$) to red (more than 300 $^1/_s$) determined from the WSR magnitude. The velocity data was acquired on the Elscint scanner.*

WSS = (0.72±0.22) N/m^2 for the detected wall. A viscosity of 0.003 Ns/m^2 was used to calculate the WSS from the WSR. These values are slightly lower than 0.95 N/m^2 which was reported for the common carotid [ORP+97, ORK+98]. Assuming the slightly high viscosity of 0.0043 Ns/m^2 which was used [ORP+97, ORK+98], the WSS in Volunteer 1's common carotid was determined as 0.99 N/m^2 for the fitted wall and 1.03 N/m^2 for the detected wall, which is a good agreement.

9.3. Volunteer 2

The first study of Volunteer 2, acquired on the Elscint scanner, created a data set of 256×256×64 points. The FOV covered was 18×18×6.4 cm resulting in a voxel size of 0.703×0.703×1.0 mm. The timing parameters were a fixed echo time of 10.791 ms, a repetition time of 24 ms and a flip angle of 30°. The total acquisition time was 26 minutes. The 3D slab was chosen axially, centred at the level of the carotid bifurcations. Based on the velocities found in preliminary 2D PC MRI scans, the encoding velocity was chosen as 80 cm/s. All three velocity components were measured.

The velocity field of the left carotid bifurcation of Volunteer 2 is examined in detail in Figure 9.8. The detected flow region appears virtually noise free. The complex flow field in the carotid bulb can clearly be seen. Increased velocities at the inside vessel walls, however, is not apparent. High velocities concentrated at the inner walls were observed in the study of the human carotid phantom (Figure 8.23). While the internal carotid artery is well defined, there are obvious holes in the flow regions of the external carotid branch. This branch is difficult to separate using the edge detection based algorithm (Chapter 6) due to the low resolution.

The volume flow rates measured for each slice in the volunteer's carotid arteries are compared in Figure 9.9. Within error bars, the flow rate of the right and left carotid arteries is the same and stays more or less constant. The drop in volume flow rate at a slice position around 15 mm is due to the loss of velocity information in a flow void at the carotid bulb. This leads to an underestimation of the volume flow rate. The flow void in the carotid bulb is discussed in detail in Section 9.2.

Figure 9.8.: *"Hedgehog" of the velocities in Volunteer 2's left carotid artery. The data was acquired on the Elscint scanner.*

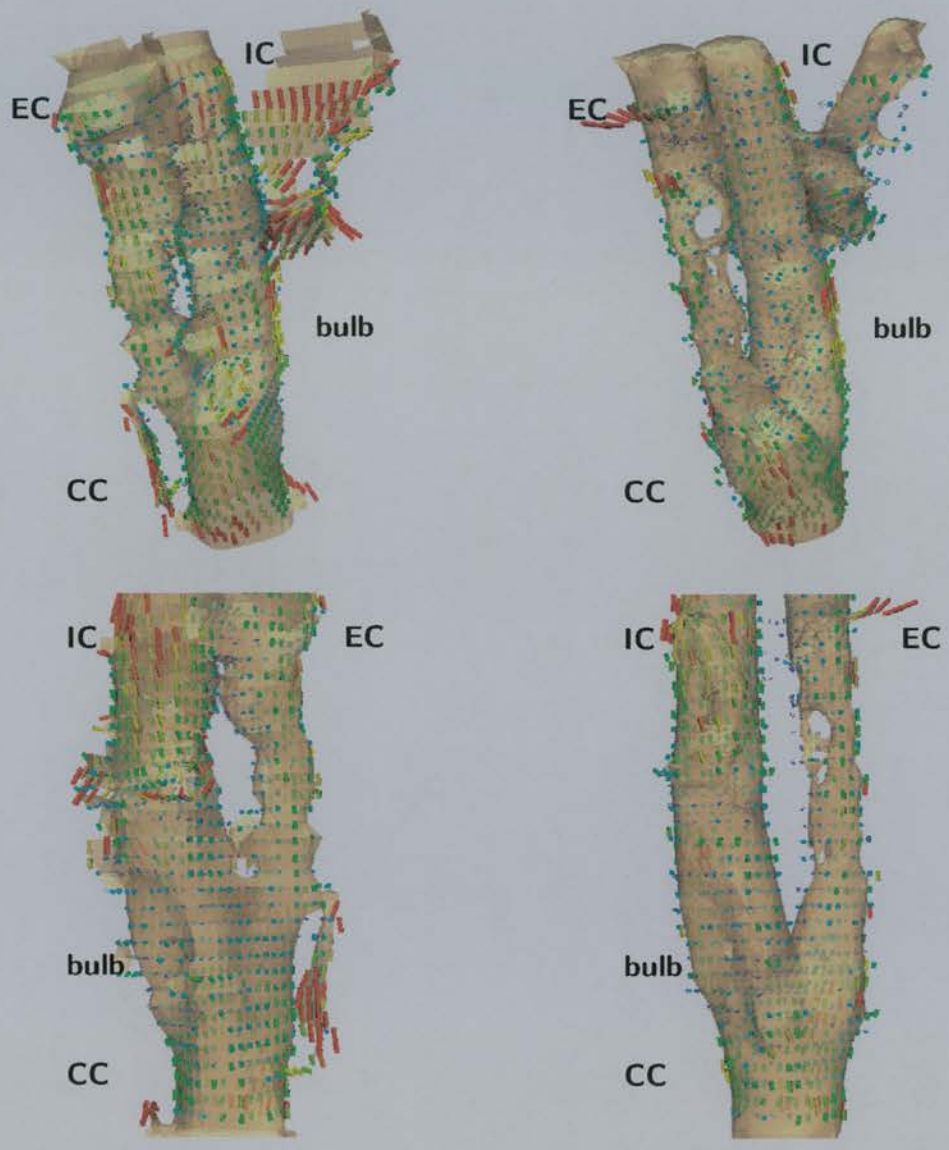

Figure 9.10.: *The wall shear rate in Volunteer 2's left carotid artery calculated from the fitted (left) and detected (right) wall. The top row shows a view from the front of the neck and the bottom row from the back. The velocity data was acquired on the Elscint scanner.*

for the detected walls. The corresponding WSS values calculated were $0.29\,\mathrm{N/m^2}$ and $0.35\,\mathrm{N/m^2}$, which are rather lower than a previously determined value of $0.81\,\mathrm{N/m^2}$ [MFU+99]. A viscosity of $0.003\,\mathrm{Ns/m^2}$ was used to calculate the WSS from the WSR.

A smaller artery was detected downstream of the bifurcation. However, this does not contain enough data for a stable fit and the surface reconstructed from the fit does not resemble the detected artery.

Another successful study on Volunteer 2 was performed on the GE scanner using a slightly bigger matrix of 256×256×84 with a FOV of 16×16×6.7 cm. This resulted in a smaller voxel size of 0.625×0.625×0.8 mm. The slab was acquired axially but centred slightly higher. The sequence parameters were a fixed echo time of 5.96 ms, a repetition time of 18 ms and a tip angle of 25^o. The total acquisition time was 26 minutes. The encoding velocity was chosen to be 80 cm/s. All three velocity components were measured.

The velocity field of the left carotid artery is displayed as a hedgehog in Figure 9.11. Compared with Figure 9.8, the Elscint results that were obtained at a lower resolution, the data from the GE scanner appears smoother and more consistent. The complex flow field in the carotid is detected, together with the increased velocity at the inside vessel walls of both branches. At the lower left of Figure 9.11 an additional artery that is connected to the common and external carotid arteries can be seen. This artery contains downward flow and is therefore presented with a colour scale from yellow to red. At the top right, a small segment of vein can be seen that has a high inflow artefact in the first few slices of the slab. The intensity drops on the way through the slab, since the slow moving blood gets saturated like the surrounding tissue by repeated excitation.

The volume flow rate shows a dependence on the slice position (Figure 9.12) that was discussed earlier (Section 7.1). However, the effect is not linear and is too complex to be corrected easily. Within error bars the results are the same for both arteries.

The WSR results for the fitted wall can be seen in Figure 9.13 in the left column. The camera position was chosen to produce a view similar to that used in Figure 9.10. The two branches of the carotid bifurcation are not separated by the fitted surface for this example. The detected wall discriminates the two branches, but compared to the reconstruction in Figure 9.10 the internal carotid artery seems thinner. The WSR results

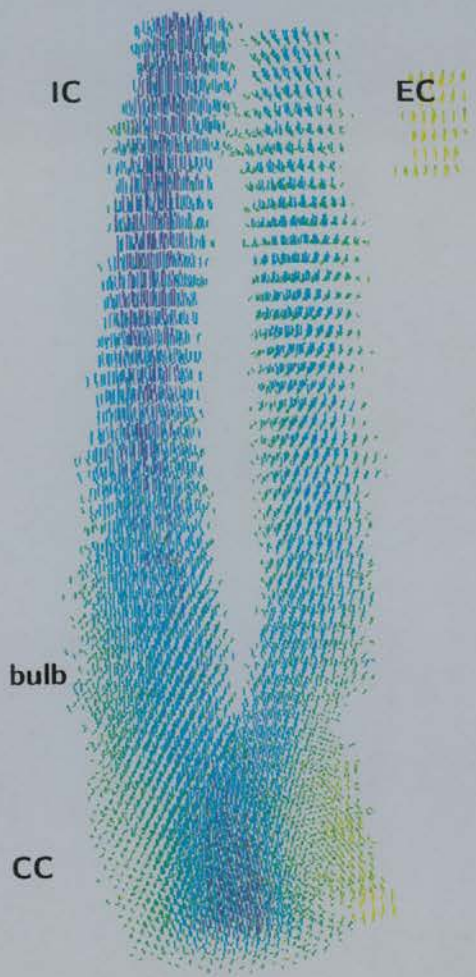

Figure 9.11.: *"Hedgehog" of the velocities in Volunteer 2's left carotid artery. The data was acquired on the GE scanner.*

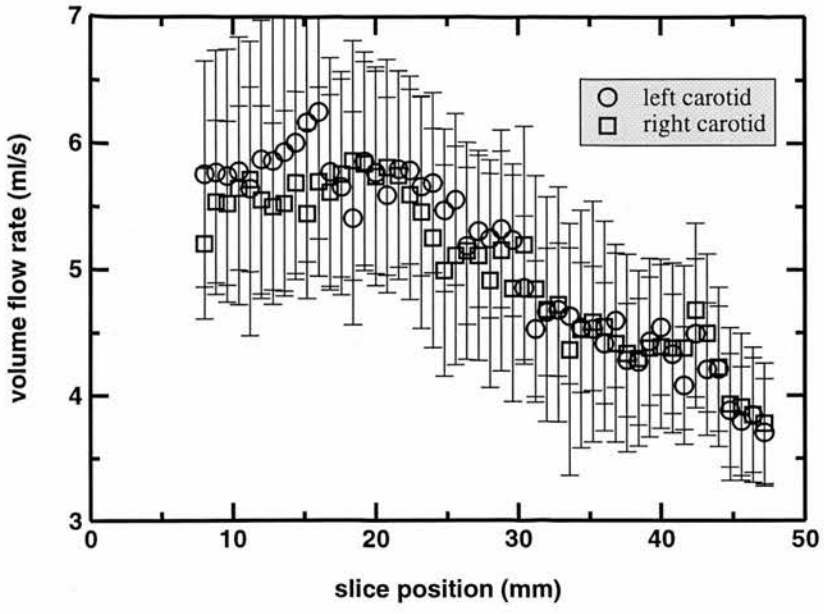

Figure 9.12.: *Dependence of the volume flow rate measured in Volunteer 2's left and right carotid arteries. The velocity data was acquired on the GE scanner.*

show the same trend with low WSR in the carotid bulb. No increase in WSR can be seen in the vicinity of the flow divider. In this reconstruction, higher values of WSR appear on the outside wall of the internal carotid artery.

An average value for the WSR in the common carotid artery could not be obtained from this acquisition. The values in the internal carotid branch outside the bulb, however, were (138±74) $^1/_s$ for the fitted walls and (113±72) $^1/_s$ for the detected walls. These measurements correspond to WSS values of 0.41 N/m^2 and 0.34 N/m^2, which are rather lower than a previously reported value of 0.81 N/m^2 [MFU+99]. A viscosity of 0.003 Ns/m^2 was used to calculate the WSS from the WSR.

The magnitude image acquired in the left carotid bulb of Volunteer 2 with the GE scanner is shown in Figure 9.14. No obvious flow void was observed. This explains the good reconstruction of the bulb's surface for this example.

9.4. Volunteer 3

Volunteer 3 was scanned with an ungated 3D PC velocity MRI sequence on the GE scanner. An acquisition with a resolution of 256×256×84 in a FOV of 18×18×6.7 cm

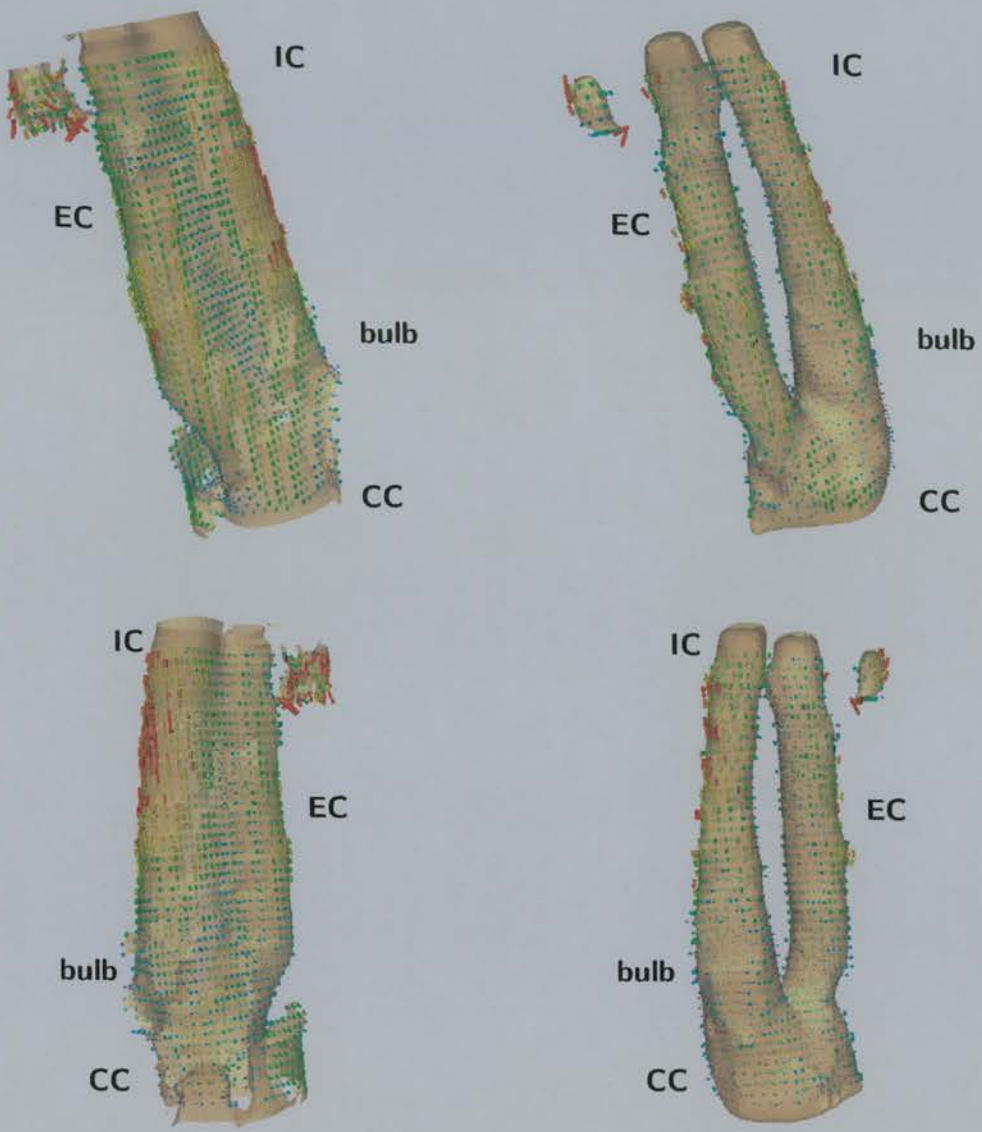

Figure 9.13.: *The wall shear rate in Volunteer 2's left carotid artery calculated from the fitted (left) and detected (right) wall. The top row shows a view from the front of the neck and the bottom row from the back. The data was acquired on the GE scanner.*

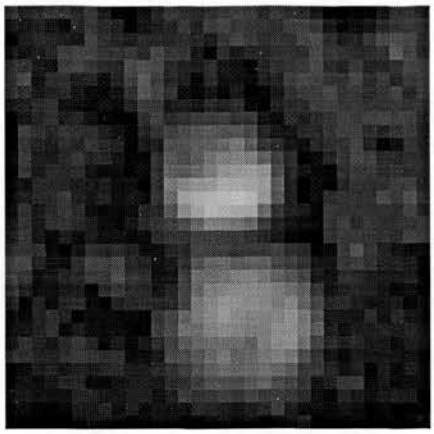

Figure 9.14.: *Magnitude image in the left carotid bulb of Volunteer 2 on the GE scanner. No obvious flow void was observed.*

resulted in a voxel size of 0.7×0.7×0.8 mm. The echo time was fixed at 6.2 ms and the repetition time (T_R = 22 ms) was chosen to minimise the total acquisition time to 32 minutes. Using the values from 2D PC scans, the velocity encoding was set to 50 cm/s. All three velocity components were measured.

The hedgehog of the velocity field acquired for Volunteer 3 (Figure 9.15) on the GE scanner shows the increased velocities near the flow divider and the complex flow patterns in the carotid bulb. This corresponds to the velocity field observed in the human carotid phantom (Figure 8.23). The overall appearance of the velocity field is rather smooth, like the one measured for Volunteer 2 with the same scanner (Figure 9.11). This is due to the increase in spatial resolution compared with the acquisitions on the Elscint scanner. No noise pixels were included in the flow region by the *in vivo* flow detection algorithm (**Alg. 3**) that was discussed in Chapter 6.

The volume flow rate (Figure 9.16) shows a very slight asymmetry in Volunteer 3, however those differences remain within error bars. The typical drop in volume flow rate on the GE scanner (Section 7.1) was clearly shown in this study. However, the effect is not linear and is too complex to be corrected easily.

The WSR results for Volunteer 3 are presented in Figure 9.17. Both his left carotid and vertebral arteries are shown. The vertebral artery includes only a few pixels across the

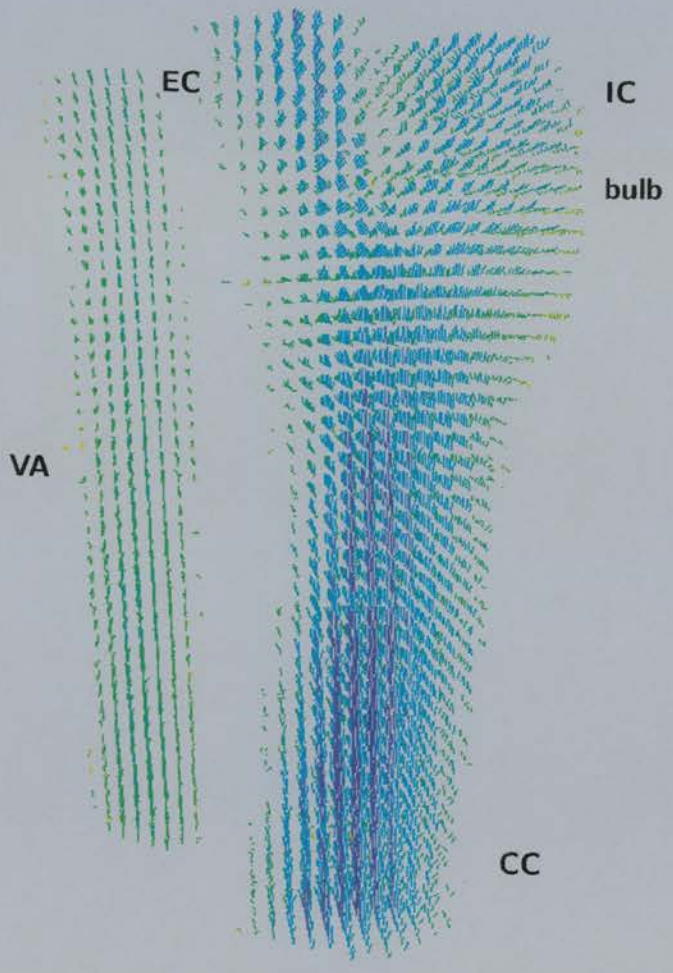

Figure 9.15.: *"Hedgehog" of the velocities in Volunteer 3's left carotid artery. The data was acquired on the GE scanner.*

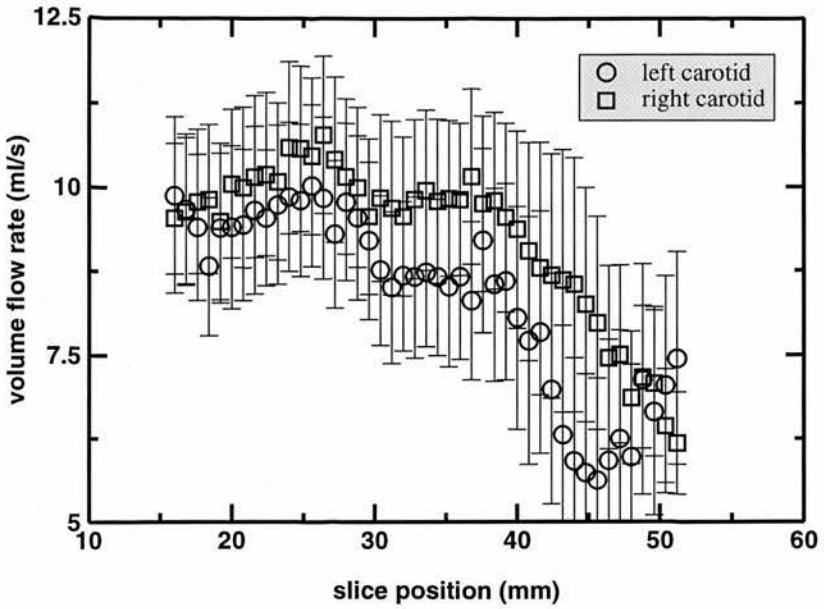

Figure 9.16.: *Dependence of the volume flow rate measured in Volunteer 3's left and right carotid artery. The velocity data was acquired on the GE scanner.*

vessel diameter, but being relatively straight serves as a good test for the *in vivo* WSR measurement. The surface reconstructed from the fitted velocities exhibits additional areas that are clearly outside the arteries. These are caused by the extrapolation of the fit. Outside the areas associated with these problems, the WSR values seem relatively stable with both types of wall reconstruction methods.

In the common carotid artery The WSR results in the common carotid artery with both types of wall are similar. However, the reconstruction of the vessel wall for the two branches immediately downstream of the bifurcation seems to fail for the fitted wall. The characteristic low WSR values in the carotid bulb are clearly observed. An artefact at the outermost wall of the bulb shows the difficulty of producing a stable fit in a region that is dominated by flow voids. The velocities were very low and a zero crossing hard to define. The detected wall distinguishes the two branches and shows the same trends in the carotid bulb.

The frontal view indicates increased values in WSR with both reconstructed surfaces. The overall appearance of the colour scale indicates that the previously reported mean WSS values of $0.95\,\mathrm{N/m^2}$ [ORP+97, ORK+98] in the common carotid and $0.81\,\mathrm{N/m^2}$

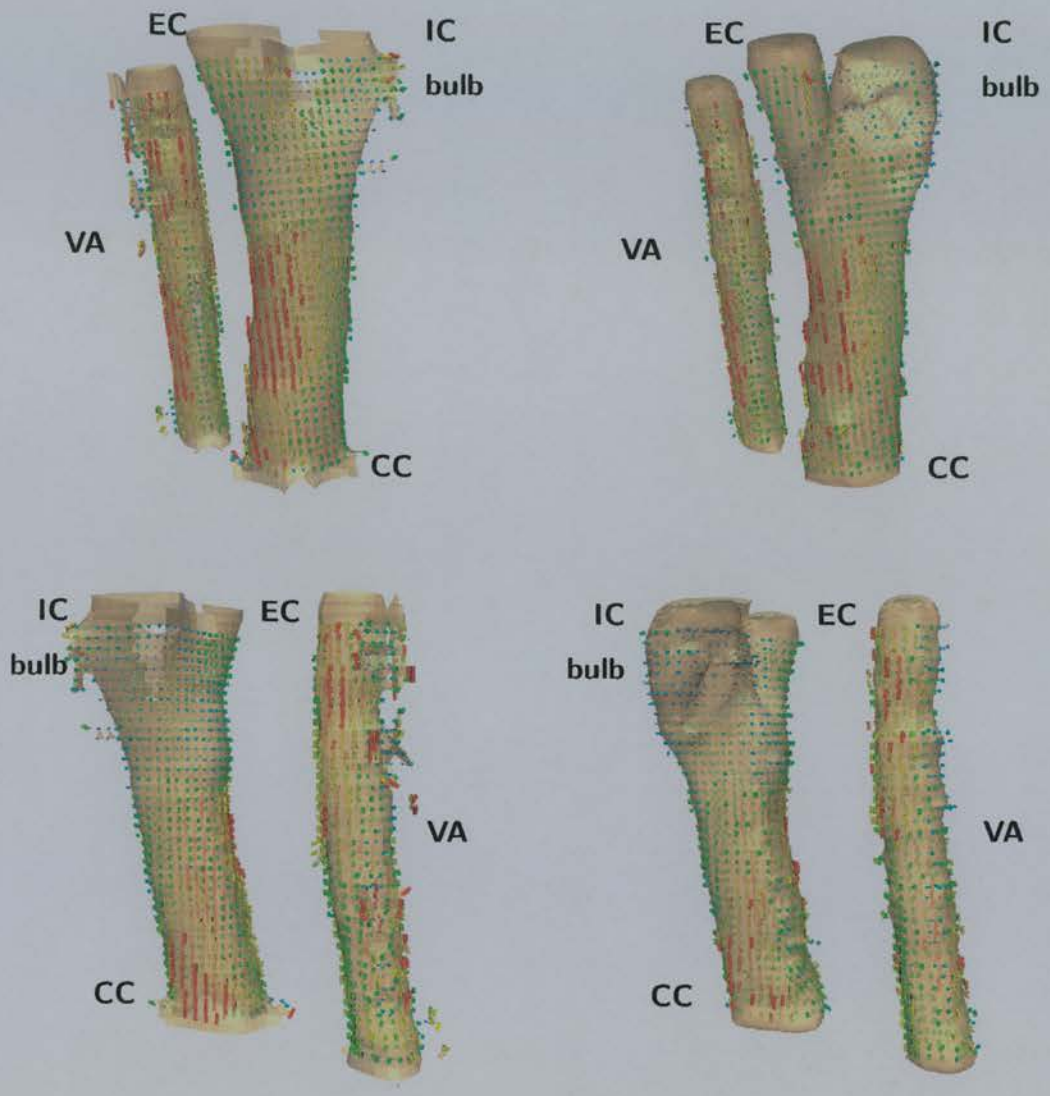

Figure 9.17.: *The wall shear rate in Volunteer 3's left carotid artery calculated from the fitted (left) and detected (right) wall. The top row shows a view from the front of the neck and the bottom row from the back. The velocity data was acquired on the GE scanner.*

[MFU+99] in the internal carotid are slightly higher than the results for this volunteer. The values indicate higher WSR than those measured for Volunteer 1, a result that would be expected from the slightly higher volume flow rate observed in the carotid arteries of this volunteer.

The WSR in the common carotid arteries of Volunteer 3 was (209±72) $^1/_s$ corresponding to a WSS of (0.627±0.21) N/m^2 for the fitted wall and a WSR of (196±74) $^1/_s$ or a WSS of (0.59±0.22) N/m^2 for the detected wall, were slightly lower than 0.95 N/m^2 [ORP+97, ORK+98] in the common carotid. A viscosity of 0.003 Ns/m^2 was used to calculate the WSS from the WSR. Using the higher blood viscosity of 0.0043 Ns/m^2 [ORP+97, ORK+98] the WSS in Volunteer 3's common carotid is 0.90 N/m^2 and 0.84 N/m^2, for the fitted and detected walls respectively. The WSR values in the vertebral arteries are lower: (179±98) $^1/_s$ for the fitted wall and (160±63) $^1/_s$ for the detected wall. They also show a higher standard deviation. This is due to the reduced number of pixels across the vessel.

9.5. Discussion and Conclusion

The study of the dependence of the volume flow rate with the slice number (z-position) showed that the right and left carotid arteries exhibit similar flow rates within error bars. The results show an unexpected symmetry, since one of the vertebral arteries cannot be detected in most volunteers. It seems to be perfectly normal for a healthy subject to show significant blood flow in only one vertebral artery. For the GE scanner, a strong dependence of the volume flow rate on the z-position was demonstrated. However, it appears to be non-linear and cannot be corrected easily. This effect could be due to overlapping gradient pulses (Section 3.3.4) or eddy currents, but this is currently under investigation.

The velocity fields acquired for Volunteer 1 and 3 and the GE acquisition of Volunteer 2 show similar behaviour to the velocities seen in the study of the human carotid phantom (Figure 8.23). The volume flow rates found *in vivo* are similar to those studied *in vitro*: i.e. 5 - 10 ml/s. The fluid is driven by its inertia and remains close to the flow divider and the inner vessel walls. A complex flow field was observed in the carotid bulb in all cases studied.

The average WSR in the common carotid arteries of Volunteer 1 and Volunteer 3 agreed with the values for WSS reported in the literature when the same viscosity was applied. The difference was about 10 % and within error bars. The WSR calculated for Volunteer 2 in the internal carotid branch was lower than the value reported in the literature [MFU+99]. The underestimation was as much as 50 %. However, from the simulation results presented in Chapter 7 an underestimation of WSR is expected. This effect should increase with lower numbers of pixels across the vessel. The internal carotid branch of Volunteer 2 measured only about 7 pixels across. Since average WSS is seldom reported, it is difficult to compare the results with the literature. Both [ORP+97, ORK+98] with 7 and [MFU+99] with 6 volunteers are based on limited number of volunteers.

The velocity fields measured *in vivo* showed all the characteristics of the velocity field found for the carotid phantom. The resulting WSR values found for the common carotid arteries agreed well with previously published values.

10. Conclusion

10.1. Magnetic Resonance Imaging

10.1.1. Pulse Sequence Performance

Phase contrast pulse sequences on the Elscint and GE scanner have been used in this project. Both deliver ungated 3D velocity field measurements with approximately 5 % v_{enc} velocity noise per pixel (Chapter 7). The errors for the central slice of the 3D acquisitions might be slightly smaller on the GE scanner than those measured with the Elscint scanner. However, a strong dependence of the measured velocity on the slice position for the GE scanner has been demonstrated for reference measurements (Chapter 7), and *in vitro* (Chapter 8) and *in vivo* (Chapter 9) studies. The nature of this velocity distortion is currently under investigation. Maxwell terms of the gradients or eddy currents could lead to this effect. Assuming a linear relationship between the slice number and the z-component and no influence on the x- and y-components, this distortion produces an additional contribution to the x- and y-component of the wall shear rate. This component would be independent of the position in the x-y-plane and rotate WSR vectors.

Overall, the pulse sequence on the GE scanner provided two improvements. The echo time T_E is less than 7 ms while it was about 11 ms on the Elscint scanner. The complex

flow patterns in the carotid bulb show a flow void where the phase coherence in a voxel is destroyed by varying velocities of the spin isochromats. The importance of a short echo time, low gradient strength and short gradient durations on flow voids in magnetic resonance angiography have been discussed in the literature [ERT+93, SOPK95, SOPK97]. It was noted that this effect is reduced for the volunteer studies (Chapter 9) on the GE scanner. The other improvement is the enhanced resolution that was discussed in detail for the human carotid phantom (Chapter 8) and Volunteer 2 (Chapter 9).

With the phantom studies (Chapter 8), the acquisition time for high resolution studies can be longer than three hours. While this is acceptable for phantom studies, it is the limiting factor for high resolution *in vivo* studies with adequate coverage. Faster pulse sequences should improve this situation. These are discussed in the following sections.

10.2. Flow Detection

The 3D studies of phantoms often have about 100 slices and volunteer studies have about 60 slices. The edge detection based image segmentation algorithms described in Chapter 6 have been used successfully for all the studies (Chapters 7, 8 and 9). Flow in arteries and phantoms is reliably detected when it exhibits an area with a diameter larger than 6 pixels and produces a bright inflow effect. For complex flows, a method has been developed that employed velocity information to stabilise the results. The only variable parameter, the threshold setting for the region filling, is insensitive, since it produces the same results over a wide range of settings (Chapter 6).

One advantage of the automatic flow detection is the almost complete elimination of inter- and intra-operator variability, since the only adjustable parameter proved insensitive. However, the results still need to be checked by a human observer. That task is made easier by the fact that the algorithm has so far either given a reasonable or drastically wrong result. The later case is very obvious and the algorithm should be reapplied using an appropriately adjusted threshold value.

The use of more complex image smoothing algorithms (e.g. structure adaptive filtering [YBFU96] or a local orientation detector (LOD) [MYB+92] that correlates the expected velocity at a location, as given by neighbouring values, with the measured value might

improve the algorithm. Higher resolution and SNR will improve the performance of this method. A dedicated surface coil may be used to achieve this.

This flow detection method enables the use of high resolution acquisitions by eliminating the time consuming process of image segmentation by hand and provides a fully reproducible flow detection method.

10.3. Wall Shear Rate (WSR) Calculation

Polynomial fits of velocity fields have been introduced to reduce the influence of noise and provide a method for a reliable derivative calculation. The segmented fifth order fit was sufficient to describe the most complex velocity fields encountered in both *in vitro* (Chapter 8) and *in vivo* (Chapter 9) studies. The algorithm takes a conservative approach to flow detection to avoid the inclusion of wall pixels that suffer from partial volume effects.

Two methods were developed to reconstruct the surface of the vessel wall. One is based on the flow region segmented by the flow detection algorithm and the second is based on the zero crossing in the fitted velocity field. The latter one is based on the non-slip surface condition. The first method returns a surface reliably for all flow fields. This surface might be distorted by the conservative approach adopted in the flow detection algorithm. The second approach to wall reconstruction is mathematically more elegant, but suffers some draw-backs in regions of complex flow. These regions sometime exhibit reverse flow and a secondary surface is reconstructed inside the true vessel wall. In addition, the extrapolation of the velocity field towards the wall sometimes fails to cross zero and therefore no wall is reconstructed. Both methods complement each other in regions of complex flow and deliver very similar results in other regions.

Based on the knowledge of the stress tensor from the velocity derivatives, the surface position and the surface normals, the wall shear rate can easily be calculated. This calculation has been verified using simulations (Chapter 7) and phantom experiments (Chapter 8). A slight underestimation is predicted from the simulations, which has been associated with the underestimation of the vessel radius. Otherwise, the results are stable and agree well with theoretical predictions. Computational fluid dynamics

calculation provided a second WSR calculation for comparison. Apart from the flow dividers in the bifurcations, both methods agreed well. The description of the sharp edge of a flow divider by a smooth polynomial function makes the accurate description of the wall and flow field in the vicinity of the flow divider very difficult.

Apart from minor drawbacks, the method to calculate WSR from 3D MRI velocity data proved stable and reliable. Higher resolution and SNR would improve the results, since the fit of velocities and the wall reconstruction would get better.

10.4. Summary

It has been argued [CFGS71] that the velocity field of blood flow in an artery can be regarded as consisting of a mean and an oscillatory component, which are closely comparable in magnitude. It is the steady component of the arterial flow that may cause spatial variations of wall shear, typically associated with boundary-layer growth. Fluctuating shears associated with the oscillatory component would be expected to be much less strongly dependent on the position [CFGS71]. The knowledge of the time averaged WSR will contribute to the understanding of stenosis formation.

The method developed in this project provides the means to study the steady component of the wall shear with high spatial resolution. It also provides the full shear vector. The effects of secondary flows on the wall shear rate are often ignored. The measurement of all three velocity components increases the complexity of the acquisition and hence the previous measurements are often restricted to just the major velocity component. It was shown in this study that the wall shear vectors deviate clearly from the axis of the major velocity component and a significant underestimation of the wall shear rate results from ignoring the secondary velocity components. The time resolved acquisition of the 3D velocity field would improve the understanding of the wall shear in arteries even further, but neither the Elscint nor the GE scanner were capable of this acquisition. This study would also take several hours for a volunteer or patient and more effective phase contrast pulse sequences are necessary to undertake such a study. Another problem can be seen in the amounts of data generated. The ungated volunteer studies were difficult to handle on a Workstation with 745 MB of RAM and a time resolved study would generate approximately 15 times more data.

The slight problems with the underestimation of WSR and the reconstruction of the vessel wall that could not be resolved in this work are expected to improve significantly with higher resolution and a better signal to noise ratio. The use of dedicated surface coils would enable the improvement of both and could be achieved in the near future. The software developed as part of this project is perfectly able to handle these improved data sets.

A detailed knowledge of the vessel geometry and the behaviour of blood flow, especially the velocity profile near the vessel wall, may provide a quantitative method for estimating the risk of development and progression of atherosclerosis; growth and rupture of cerebral aneurysms; and hypertension and haemorrhage associated with malformations in the arterial and venous system. Although the method as been applied to the carotid artery as part of this project, it can be applied to to any of the major periferal arteries. The method developed in this project significantly enhances the available methods of *in vivo* velocity field and wall shear measurement.

10.5. Future Development

10.5.1. Fast Imaging Sequences: EPI and Spiral

Pulse sequences that acquire k-space more efficiently may be used to shorten the acquisition time. Standard pulse sequences gather information by traversing k - space (frequency space) one straight line (horizontal or vertical) at a time. Sequences like echo planar (EPI) [Man78] traverse k - space much faster. All the information for an image is acquired in one repetition time with the echo planar technique by jumping from one line to the next between the multiple echos.

Echo planar imaging has been used for fast magnetic resonance angiography (MRA) and phase contrast MRI for 2D and multi-shot 3D acquisitions [SST98]. These methods provide fast, high quality information on the vascular structure, but the reliability for quantitative studies remains to be proven. One way of avoiding the misregistration and intra-voxel phase dispersion artefacts due to the long effective echo time may be the use of segmented k-space sampling, e.g. multi-shot EPI. In this method, several lines of k-space are sampled per excitation, but not the complete image. It reduces the effective

echo time, but lengthens the total acquisition time. The GE scanner is capable of EPI scanning, but the phase contrast EPI sequence would have to be developed, optimised and validated.

An earlier proposal uses an even more rigorous approach [IN95]. Based on the same idea, i.e. the highest intensities are measured around the origin of k - space, the acquisition of data is performed on a non-rectangular array. Various acquisition methods have been proposed, e.g. stack of elliptical spirals, shells, spherical stacks of elliptical spirals, cones, yarn, etc [IN95]. The raw data has to be placed on a grid to take advantage of the fast Fourier transform (FFT) algorithm, a process called regridding. This process is time intensive, but the acquisition time can be reduced considerably. Even with a reduced number of data points far away from the origin of k - space, the image resolution is adequate. Nowadays, specialised hardware is used in commercial scanners to speed up the regridding. The artefacts created by flow in a spiral acquisition appear different to those in conventional imaging [NIM95]. An elliptical centric phase encoding order has also been proposed for fast data acquisition [WR97]. In essence the points acquired are ordered according to their distance from the origin of k - space. The outer regions of k - space might be neglected leading to a shorter acquisition.

Both elliptical acquisition methods could be implemented on the GE scanner. The reconstruction would have to be done offline on the Suns without the dedicated hardware on the scanner. This process is too time-consuming in order to make this approach feasible.

10.5.2. Ultrafast Imaging using Smash and Sense

Higher acquisition speeds, under the limitations of equipment and safety considerations, can only be achieved by acquiring several lines of k-space simultaneously. Using several receiving coils the signal from the sample can be sampled at different spatial locations of the coil and with differing levels of sensitivity for each coil. These signals can afterwards be reassigned to their original location using the spatial sensitivity of the coils. With SMASH [SM97], an approximation for linear arrays coils, and SENSE [PWSB99], an exact reconstruction, these sensitivities have to be known in advance. In contrast PILS [GJN+00] will measure the sensitivity with a short preparatory sequence allowing the

use of flexible body coil arrays. Here every surface coil is described by its centre and width of sensitivity in the FOV. Both parameters can be deduced from a Gaussian fit to a magnitude profile.

Since multichannel ADCs are not available on the GE scanner at present, none of these methods could be implemented in the near future.

A. Post-processing

A.1. Design Principle of the Post-processing Software

It was evident from the project aims that considerable effort was required in the development of post-processing software. Important design decisions were needed prior to commencement of programming. The aim was to create a software package that would fulfil the following requirements:

1. Application: it should be easy to use within routine clinical practice.
2. Maintenance: support of the program should be easy as several people might have to contribute to the code.
3. Testing: components of the program should be able to be decoupled and tested separately.
4. Extension: it should be easy to extend the functionality of the software while maintaining the current level of functionality.
5. Platform independence: the program should be capable of running on a variety of operating systems. The main development platforms were Linux and SunOS.

6. Cost: any libraries used should ideally be free and preferably be Open Source.

A graphical user interface is absolutely necessary for an image based system. Concomitantly the system should carry out any repetitive tasks. The processing steps need to be optimised for two reasons: the amount of data acquired is large (several hundred megabytes), which makes the resulting calculations time consuming (typically up to several hours). There has to be a trade-off between processing speed and use of working memory that commercial mathematical or image processing packages do not allow. In addition, conventional imaging software does not usually permit the handling of six or seven dimensional data, and support for flow detection is often not available.

Maintainability and decoupling of software blocks is best achieved with object oriented programming languages. The most common at the time of the start of the project was **C++**. The basics of object-oriented programming are explained in the next section. It will become clear that it allows several developers to contribute to a project while minimising possible sources of errors.

C++ is increasingly well supported with free and open source libraries. However, for some of the libraries free use is restricted to non-commercial users. All libraries used in this project are platform independent and open source. The last point proved very important, since solutions or "work-arounds" for severe compiler bugs could be included in the source code. Portability included the support for several scanners from different manufacturers. This limited the choice of input file format to the most commonly used format for medical equipment.

A.2. Object-Oriented Programming

The major difference between object-oriented systems and conventional, procedural programming systems is the way the two approaches treat data abstraction. Conventional systems limit abstraction to data typing, while object-oriented systems create abstractions for both the data and the operations that can be applied to the data. In fact, an object-oriented system keeps the data and operations together in one programming construct called an object.

Objects are the dominant concept in an object-oriented approach. Objects are abstractions that encapsulate the properties and behaviour of the entities within a system. Each object has an identity that distinguishes it from other objects in the system. Often, the distinguishable aspect between different identities of an object is obvious. However, even two objects that share all the same characteristics may still have different identities. Programming systems that deal with multiple entities require an identity mechanism to distinguish objects in a system. A pointer to allocated memory or a variable name in a system-managed symbol table is often used for this purpose.

Together, the data and operations comprise an object's properties. When an operation is applied to an object, the programming language's dynamic binding mechanism executes the procedure that is appropriate for that object. This is not the case in procedure oriented systems; the programmer must supply logic to decide which procedure to call.

Good introductory texts for object-oriented programming and **C++** are [LL98, Str97].

A.2.1. Objects

An object is an abstraction that models the state and behaviour of entities in a system. Abstraction is a concept that extracts the essential aspects of a situation for a particular purpose. Entities are discernible elements in the system that have identity.

The state of an object is described by its attributes (also called instance variables) and it defines its behaviour by the operations that can be applied to it. Attributes have a name, a data type, and a data value. The data type of an attribute may be a primitive type in the programming language or another object.

Operations are functions or transformations that can be applied to an object. Operations define the behaviour of the object. The operations for a particular object are implemented in procedures, called methods.

Together, the attributes and operations of an object comprise its properties. As an example, a two-dimensional line graph could have attributes that include an x and y axis, a legend and a connected set of points. This graph has methods that draw the graph in a window. It also has methods that let the user specify the axes, data to draw and legend to use.

Objects that share the same properties can be grouped using the process of classification. An object class, usually just called class, specifies the properties which all objects in that class possess. The class only specifies the names, not their specific values. Different classes can have properties with names that exist in other classes.

A.2.2. Inheritance

Inheritance is a programming mechanism that simplifies adding new classes to a system when they differ in small ways from the currently existing classes. The notion of inheritance is adopted from the observation that most systems can be specified using a hierarchical classification system.

Organising objects into an inheritance hierarchy provides many benefits. Properties of a general classification are also properties of its children's classification. From the software point of view this means any instance variables and methods of a superclass are automatically inherited by its subclass. This allows changes to be made to a number of objects simultaneously by modifying their subclass. Furthermore, existing functionality can easily be duplicated to add a new class to the hierarchy. It is only necessary to differentiate the two classes by adding new instance variables or overloading existing methods.

Classes that exist only to act as superclasses for their subclasses are called abstract classes. Instance creation of an abstract class is generally prohibited. Abstract classes are useful for gathering attributes and methods that all subclasses will use. They can also define protocols for behaviour of their subclasses. A major advantage of the use of abstract superclasses is the fact that methods tested for the superclass do not have to be tested again for the subclasses.

A.2.3. Templates

Often classes will act exactly the same regardless of the type of their instance variables. A list class for example will treat a float the same as an integer or a more complex class. To avoid the need to write a different list class for all possible instance variable types, templates can be used. A template is an abstract class that will take the type of one or more instance variables as a parameter. This parameter is passed when an instance of the class is created and the compiler will generate the class for the specific instance type when the program is compiled. Templates are often used in programming libraries. They reduce the programming effort and make testing easier, since tests on one kind of variable type are sufficient for all possible variations.

A.2.4. Program Design

The design of object-oriented systems is quite different from that of procedural programs. It helps to think of a program as a collection of objects that are interacting with each other rather then a linear succession of programming steps. This is very important for graphic user interfaces (GUI) where the order of events is dictated by the user. The right choice of object structure will aid the programming process enormously and allows for easy extensions. However, the complete functionality of the system needs to be known from the start. Often, as was the case in this project, concepts change and it is only fortuitous that the original choice of objects supports the new concept. By adding new objects rather than changing existing ones, the functionality of the system up to that point can be maintained. New objects can also inherit most of their functionality from existing classes.

Although it is sometimes easier, direct access to instance variables within a class should not be allowed. When the access is restricted to member functions the implementation of the functionality of a class does not need to be known. In fact, the implementation of one class can be changed completely without changing any other part of the system. This feature helped in this project when the implementation of the flow data structure had to be changed.

Books that introduce the concepts of object-oriented program design using **C++** include [Mey98, Mey96].

A.3. Programming Libraries

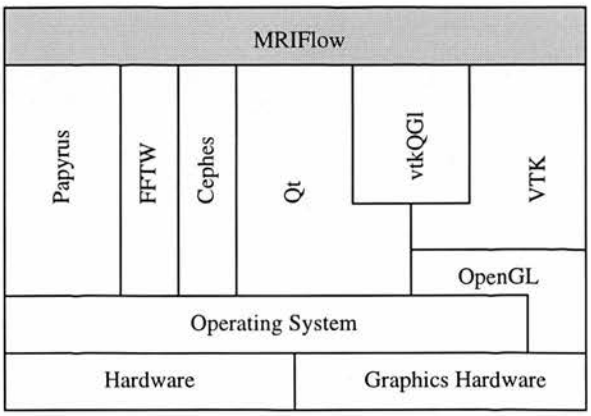

Figure A.1.: *An illustration of the programming libraries used for the* **MRIFlow** *project.*

The parts of software that manage a specific task can be separated and handled as a tool once they have been completed and tested. Subsequently, this part does not need to be compiled when other sections of the software have been altered or added. These parts are known as software libraries. Libraries for many programming issues have been made public and can aid with the development of new software packages. The program designed for this project, **MRIFlow**, builds on a number of libraries. The basic structure can be seen in Figure A.1. The operating system and **OpenGL** are provided with the Sun computers on purchase. For PCs the free operating system Linux and the free **OpenGL** implementation **Mesa** were used. **OpenGL** is a *de facto* standard for computer graphics developed originally by Silicon Graphics Inc. It allows platform independent graphics programming and supports, depending on the implementation, hardware acceleration in modern graphics cards. All the other libraries were specifically chosen and installed for this software project and details are given in the following sections.

A.4. Reading Scanner Data

A common file format used by MRI scanner manufacturers is "DICOM" (Section B.1.1). Two choices of free libraries which read "DICOM" files were determined after a search on the Internet. David Clunie's **DICOM tools** [Clu98a] is very comprehensive. However, due to an error in the Makefile, it did not compile on either the department's Sun computers or my Linux machine. This left **PAPYRUS 3** [PAP97] from the University Hospital Geneva as the only readily available option. Its big advantage is the ability to handle compressed images. This was important, since the image data is "Lossless RICE" compressed after saving on the OmniPro, a workstation provided with the Elscint scanner. "Osiris", a widely used free medical image package, is based on this library. **PAPYRUS**, however only reads little-endian (byte order, see Section B.1) encoded files. The conversion from big- to little-endian can be handled by the OmniPro for each slice.

An error in the flow acquisition program on the Elscint scanner meant FIDs had to be read directly. These, however, cannot be handled by the OmniPro. At this point, the error in the Makefile for David Clunie's **DICOM tools** was found and subsequently fixed. One program out of that package, **dccp** (DICOM copy), is able to copy a file from one format to the other leaving private elements untouched by default. This is not a problem, since the **PAPYRUS** library was extended to read the information from private elements. Together with workarounds of serious bugs in the Sun's **C++** compiler, this is documented along with the source code of the package.

A short program (`ElscintSort`) was implemented, that copies all the files downloaded from the scanner to little-endian. Additionally it deletes the original files and the velocity and phase maps that cannot be used quantitatively under Version 2 or 3 of the Elscint scanner software due to a software error.

Handling data from the GE scanner is somewhat easier. The only pre-processing necessary is the reordering of the files according to the image number using the **Perl** script `GESort.pl`. Although the computer used to handle the data on the scanner is big-endian, the file format is converted to network- (little-) endian before transmission. All filtering of phase contrast data can be switched off using the scanner software and there is no need to read raw data files.

Group	Tag	Module Element	Description
0x0008	0x0060	GeneralSeries papModalityGS	Modality of acquisition ("MR")
0x0020	0x0011	GeneralSeries papSeriesNumberGS	Series or study number
0x0008	0x0070	GeneralEquipment papManufacturerGE	Manufacturer name
0x0018	0x1020	GeneralEquipment papSoftwareVersionGE	Software number
0x0018	0x1312	MRImage papPhaseEncodingDirection	Encoding direction
0x0010	0x0020	Patient papPatientIDP	Patient number
0x0020	0x0013	GeneralImage papImageNumberGI	Image number
0x0028	0x0030	ImagePlane papPixelSpacing	Pixel size in mm
0x0018	0x0050	ImagePlane papSliceThickness	Slice thickness in mm
0x0020	0x0032	ImagePlane papImagePositionPatient	Position of lower left corner of first image in the absolute coordinate system in mm
0x0020	0x0037	ImagePlane papImageOrientationPatient	Normal vectors along the first row and first column in the absolute coordinate system
0x0028	0x0010	ImagePixel papRows	Number of rows
0x0028	0x0011	ImagePixel papColumns	Number of columns
0x0028	0x0101	ImagePixel papBitsStoredIP	Number of significant Bits (wrong for GE data)

Table A.1.: *A list of all "DICOM" tags extracted and their* **PAPYRUS** *equivalents. Both private and standard tags are listed with a short description.*

Group	Tag	Module Element	Description
0x0018	0x0089	MRImage papNumberofPhaseEncodingSteps	Number of phase encoding steps
0x00E1	0x1040	ElscintPrivateInformation papImageLabelEPI	"hom" for homogenised magnitude
0x0207	0x102E	ElscintPrivateInformation papMaximumVelocityEPI	Encoding velocity in cm/s
0x0223	0x1027	ElscintPrivateInformation papReconstructedImageEPI	Image type
0x0207	0x1030	ElscintPrivateInformation papFlowDirectionEPI	"VIEW/ENCD/SLCE" or only one of those
0x0207	0x101F	ElscintPrivateInformation papScalingFactorEPI	Magnitude scaling factor
0x0207	0x1012	ElscintPrivateInformation papViewPointsEPI	Number of columns for FIDs
0x0207	0x1017	ElscintPrivateInformation papZXPlanesEPI	Averages=zxplanes/encodingsteps for FIDs
0x0207	0x1014	ElscintPrivateInformation papNumberZPhaseEncodingsEPI	Number of slices for FIDs
0x0018	0x1062	MRImage papNominalIntervalMRI	RR interval in ms
0x0018	0x0080	MRImage papRepetitionTime	T_R in ms
0x0215	0x1043	ElscintPrivateInformation papCineTimeOffsetTableEPI	Time offset for the repeated acquisitions of a specific line of k-space. Details are unknown to Elscint.
0x0215	0x1044	ElscintPrivateInformation papCineNumberOfFramesTable-EPI	Number of acquisitions for a specific line of k-space.

Table A.2.: *A list of all private Elscint "DICOM" tags extracted and their* **PAPYRUS** *equivalents. Both private and standard tags are listed with a short description.*

Group	Tag	Module Element	Description
0x0021	0x104F	GEPrivateInformation papLocationsInAcquisitionGEPI	Number of slices
0x0019	0x10CC	GEPrivateInformation papMaximumVelocityGEPI	Encoding velocity in mm/s
0x0043	0x1030	GEPrivateInformation papFlowDirectionGEPI	3 for R/L, 4 for A/L, 5 for I/S

Table A.3.: *A list of all private GE "DICOM" tags extracted and their* **PAPYRUS** *equivalents. Both private and standard tags are listed with a short description.*

Within **PAPYRUS** the data read from "DICOM" files is reorganised slightly into modules. These modules collect the information by topic. Tables A.1, A.2 and A.3 list all the tags used for this work. Image data is contained in <0x7FE0, 0x0010> and Elscint FID data in <0x72FF, 0x0041>.

The way retrospective gating is executed on the Elscint scanner is reflected in the structure of the raw data in the FID files. Every line of k-space is scanned several times and the scan moves on to the next line when a trigger has been received. The number of times one k-space line was scanned can be found in tag <0x0215,0x1044>, while an offset time relative to the trigger event is stored in <0x0215,0x1043>. Despite serious effort neither we nor Elscint were able to interpret this time correctly. It seems to be clear that it records the time when the acquisition of a new line of k-space starts in relation to the previous or next trigger event. However, times of the order of magnitude of 600 ms seem excessive and the image information can only be reconstructed relative to some unknown time offset.

From a study into the effect of interpolation on retrospectively gated PC MRI [FR93] it is clear that linear interpolation is the best approach in generating k-space information. The maximum number of time points and their duration follows from the absolute T_R and the RR interval (the time between two heart beats). The data is accordingly regridded into k-space arrays interpolated for each of those time points. This is done for each of the velocity encoding acquisitions. These are executed in a sequence depending on the choice of flow encoding directions made by the operator. Interpolating the different encoding data sets minimises the errors introduced by subtracting flow information recorded at different times during the heart cycle.

A.4.1. Frames of Reference (Coordinate systems)

For some applications, it is necessary to know the absolute position of a pixel and its vector components in a common coordinate system. To emulate ultrasound data for example, it is desirable to cut vessels at a right angle. This requires two sets of images in a bifurcation that have to be combined later. The image centred coordinate system has to be transformed into some common base. The "NEMA" [Nem98] documentation refers to coordinate system as "Frames of Reference", due to the wide variety of modalities covered.

The coordinate system used in MRI handbooks has x increasing to the right, y down and z forward when looking from the patient's feet to the head. To avoid ambiguities, the frame of reference in the "DICOM" standard is patient centred, i.e. x to the patient's left, y to the posterior and z from the feet towards the patient's head. For almost all applications on the Elscint scanner, this is the same coordinate system described previously.

Information on the slice position is stored in tag <0x0020, 0x0032>. It contains three numbers representing a vector in the above coordinate system to the upper left hand corner pixel (0, 0) of the image measured in mm. Combining this with the information on image orientation, tag <0x0020, 0x0037>, allows the absolute position of every pixel to be calculated. That tag contains six numbers representing a unit vector along the first row and the first column, respectively. Pixel size or pixel spacings can be found in tag <0x0028, 0x0030> as two numbers measured in mm for the row spacing and the column spacing, respectively.

The following expression calculates the absolute position of a pixel (row, col):

$$\vec{x} = \vec{P} + \vec{R} * col * rowscale + \vec{C} * row * colscale \tag{A.1}$$

with $\vec{P}$ representing the image position vector, $\vec{R}$ the image orientation vector along the first row, $rowscale$ the pixel spacing in the row direction. Respective descriptions hold for the column variables ($\vec{C}$ and $colscale$). The addition of 0.5 shifts the value to the centre of the pixel rather than the upper left hand corner.

To determine the position of a voxel in a 3D dataset, the slice thickness (tag <0x0018, 0x0050>) and the slice number k have to be taken into account:

$$\vec{x} = \vec{P} + \vec{R} \cdot col \cdot rowscale + \vec{C} \cdot row \cdot colscale + (\vec{R} \times \vec{C}) \cdot k \cdot slicethickness. \quad \text{(A.2)}$$

To rotate a vector expressed in slice centred coordinates into this general frame of reference a multiplication with a rotation matrix constructed from the column vectors $\vec{R}$, $\vec{C}$ and $\vec{R} \times \vec{C}$ is required:

$$\vec{v}_{abs} = \begin{pmatrix} \vdots & \vdots & \vdots \\ \vec{R} & \vec{C} & \vec{R} \times \vec{C} \\ \vdots & \vdots & \vdots \end{pmatrix} \vec{v} \quad \text{(A.3)}$$

It remains to be noted that two vectors are needed to describe the slice orientation namely the row and column vector. When the picture is constructed there is no influence of the encoding direction on the rows and columns. Normal images are always saved correctly, but FIDs might have to be turned depending on the encoding direction.

A.4.2. Reading Elscint FIDs

Phase contrast MR FIDs from the Elscint scanner are saved in a similar format as the reconstructed images. The subsequent description is restricted to these, because sequences with a different ordering in k-space may be saved slightly differently.

The file format is a big-endian "DICOM 3" format with a lot of tags missing, that have to be read from the reconstructed images. The FIDs follow in the last tag <0x72FF, 0x0041>. The real and imaginary parts of the FID data are stored in sequence for every point. Otherwise the order is the same as for images. There is no averaging for PC MRI (tag <0x0018, 0x0022> == "AVEEXT"), hence all the repeated acquisitions are stored in one file. There are "Number of View Points" <0x0207, 0x1012> points in a line and "Number of ZX Planes" <0x0207, 0x1017> lines of data. Each point is made up from the real and imaginary part stored in 16 bits each. "Number of ZX Planes" is "Number of Phase Encoding Steps" <0x0018, 0x0089> multiplied by the number of acquisitions.

To reconstruct the image, the data is read, sorted into arrays containing the real (Figure A.2 (a)) and imaginary (Figure A.2 (b)) parts. Initially, the values for every point in

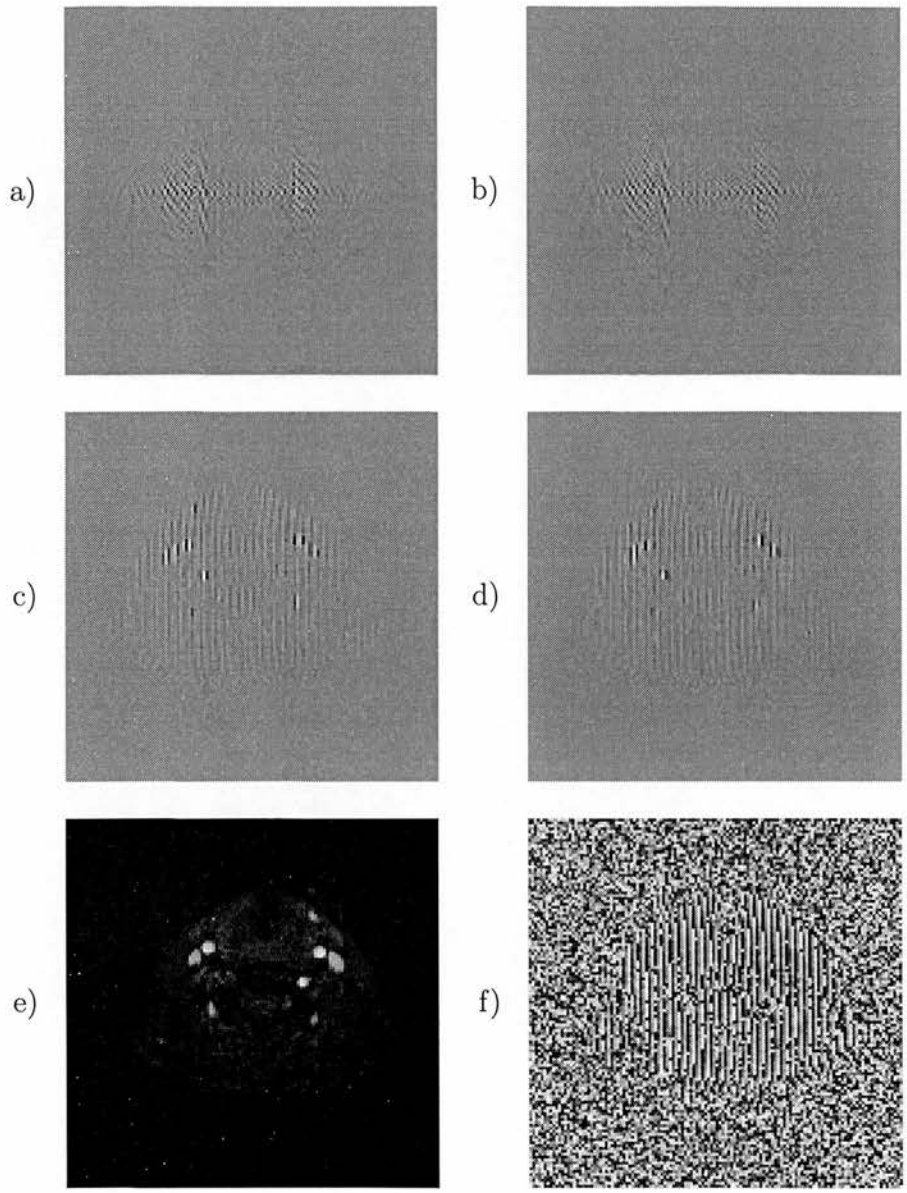

Figure A.2.: Image reconstruction from FIDs. The real (a) and imaginary (b) data after the first Fourier transformation is read from the file. Following the second Fourier transform, the real (c) and imaginary (d) values are reconstructed and the magnitude (e) and phase image (f) calculated. The FID was created with horizontal ("ROW") phase encoding and no rotation is necessary.

the image are added up from all the acquisitions and then divided by the number of acquisitions to implement a sensible form of averaging.

The scanner is equipped with a digital signal processor (DSP). These are chips designed to handle common signal transformations very effectively. The Fourier transformation within the lines is "done on the fly" by the DSP card and the data is saved after the first Fourier transform. To reconstruct the image from that data set, single columns are selected from the real and imaginary array and passed on to a double precision Fast Fourier Transform (FFT). The results are columns in new arrays containing the real (Figure A.2 (c)) and imaginary (Figure A.2 (d)) part of the data points after the transformation. If the encoding direction is "ROW", the matrices are then rotated by 90^o. The conventional magnitude (Figure A.2 (e)) and the phase (Figure A.2 (f))

$$\varphi = \text{atan2}(\Im, \Re) = \arctan \frac{\Im}{\Re}$$

of the complex data points $(\Re + i\Im)$ is finally stored in the arrays used for further processing.

Since many tags are missing in the FID files, it is always necessary to read a magnitude image reconstructed by the scanner, to supply the missing information.

A.4.3. Reconstructing Flow Information

For Elscint FIDs, as mentioned above, it is necessary to check a magnitude image generated by the scanner. When this is found, the phase maps (one for the reference scan and one for each encoded velocity component) that were reconstructed from the FIDs are located and the velocity maps calculated by subtracting the velocity encoded phase map from the reference phase map.

In the literature, the general term "subtraction" is used for this process. This is not quite accurate. Since the values in the maps are only unique within a total range of 2π, the resulting phase difference must be folded back into this range (see Figure A.3 (a) and (b)). In Figure A.4 (c) and (d) this effect shows up as "Salt and Pepper" noise in the simple subtraction (Figure A.4 (c)). The values covered by the 2π range can be adjusted in situations with one dominant velocity component. In the case of flow measurements,

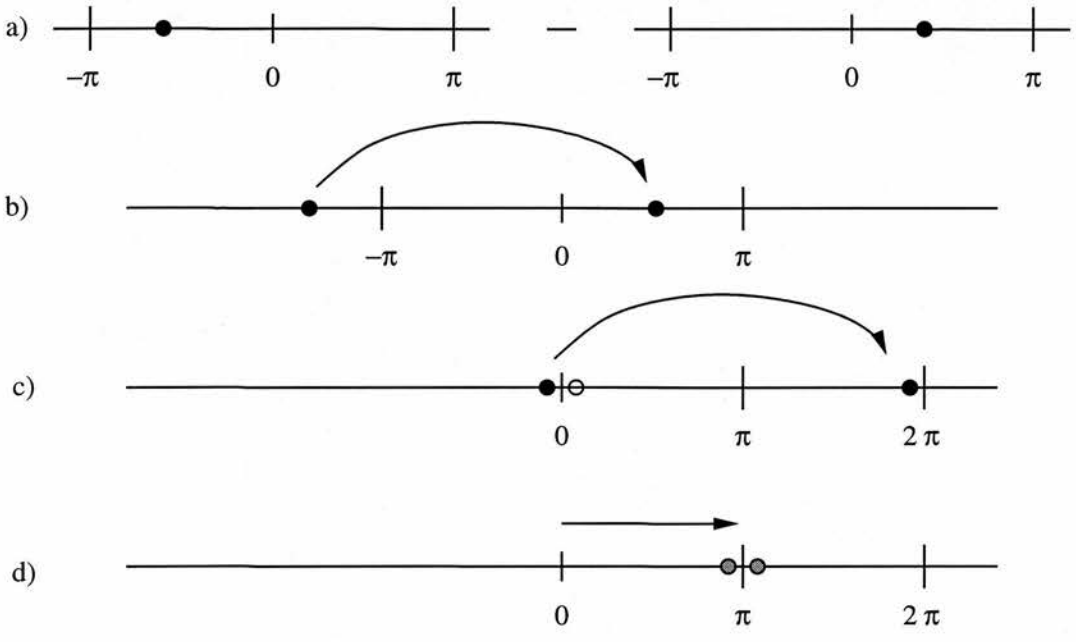

Figure A.3.: Phases must be folded back to $]-\pi, \pi]$. The velocity encoded and reference values are shown in (a), with the result in (b) folded back. The problem with grey scale pictures is shown in (c) where two small velocities of different direction give completely different appearance. This effects vanishes when the values are shifted by some reasonable amount first, as can be seen in (d).

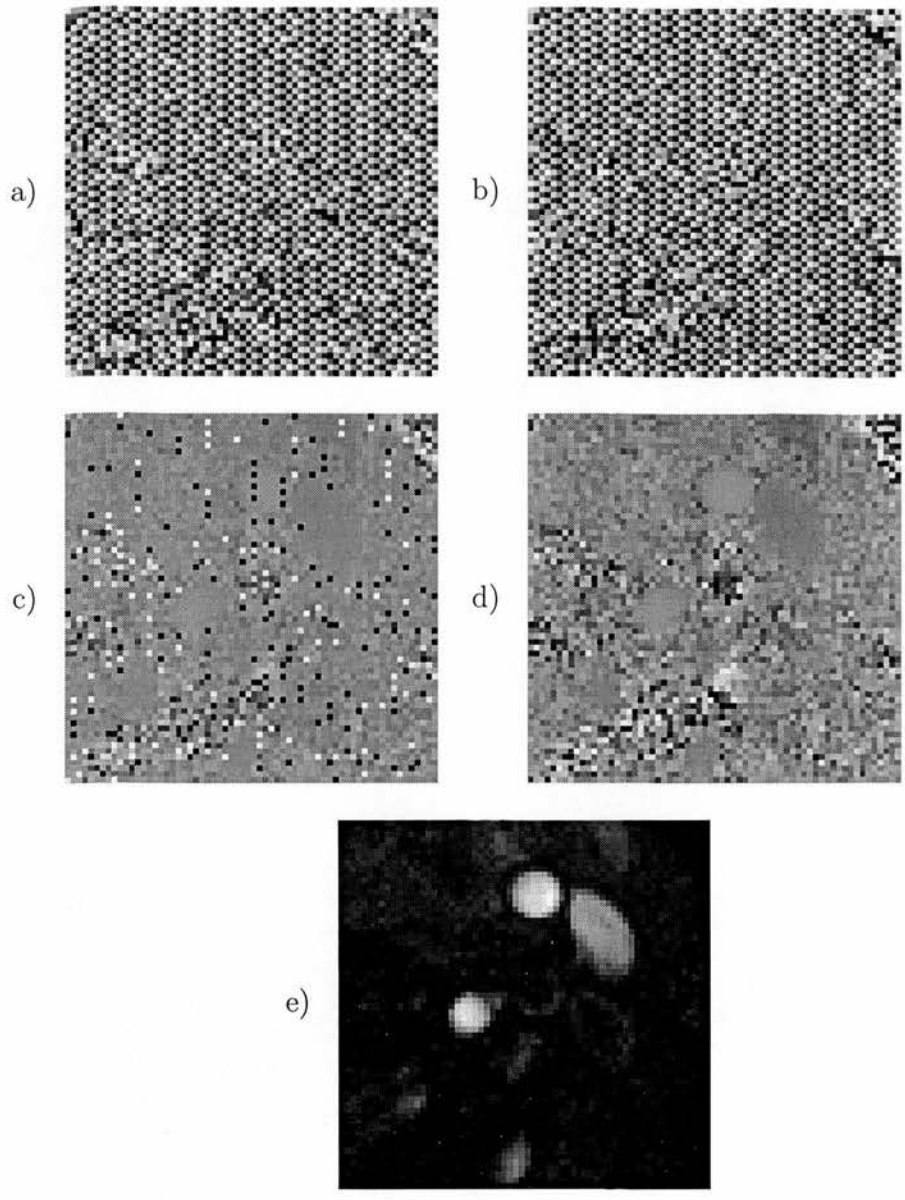

Figure A.4.: A region of interest of the same acquisition as in Figure A.2 is used to illustrate the problems connected with straight forward phase subtraction. The reference (a) and velocity encoded (b) phase information is presented as well as the simple subtraction (c) and the wrapped phase subtraction (d). A magnitude image (e) is shown for orientation. The wrapping problem is clearly visible in the flow regions of (c) that stand out bright in (e). Both differences are corrected for grey scale printing.

only velocities in the range of $2v_{enc}$ can be measured uniquely. Conventionally this range is chosen to be $]-v_{enc}; v_{enc}]$. However, the post processing software used on the SIEMENS scanner uses two different ranges according to the dominant velocity direction in the region of interest: either $]-0.5v_{enc}; 1.5v_{enc}]$ or $]-1.5v_{enc}; 0.5v_{enc}]$. When generating grey scale images, however, it is important to offset the resulting phases before folding them back. Since only positive values are allowed in this case, a small positive velocity would otherwise be represented by a small number, whereas a small negative number would be folded back to a number just smaller than 2π. The sensible convention, however is to place stationary values at π (or some other non-zero value on the SIEMENS). This situation is demonstrated in Figure A.3 (c) and (d). The formula for the simple grey scale phase difference indicating velocities is therefore[1]

$$\varphi = \left\{ \left[(\varphi_{vel} - \varphi_{ref}) + \left(\frac{min}{2\pi} + 1 \right) \cdot 2\pi + \underline{\pi} \right] \bmod 2\pi \right\} \tag{A.4}$$

with φ_{vel} the phase in the velocity encoded image, φ_{ref} the phase in the reference image, "min" the minimum value of the resulting difference and "mod" the division remainder. The underlined $\underline{\pi}$ actually shifts the phase originating from stationary spins. SIEMENS uses $\frac{3\pi}{4}$ or $\frac{\pi}{4}$ for this shift to increase the dynamic range. The data is represented as unsigned long integers, so 2π will thus be represented by $2\pi \equiv 1 << BitsStored = 2^{BitsStored}$, where $BitsStored$ is the number of significant bits in the data set and $<<$ is the bitshift operator to the left. Since the software developed for this project can handle negative integers, the 2π range is centred around zero:

$$\varphi = \left\{ \left[(\varphi_{vel} - \varphi_{ref}) + \left(\frac{min}{2\pi} + 1 \right) \cdot 2\pi + \pi \right] \bmod 2\pi \right\} - \pi. \tag{A.5}$$

The velocity component in the flow encoding direction is then simply calculated:

$$v = \frac{\varphi \cdot v_{enc}}{\pi} \tag{A.6}$$

since v_{enc} is the velocity encoding at π.

When the red/blue scale is used to present the velocities, the mapping from velocity value to colour intensity is straight forward, while the shift of values has to be taken

[1]The difference is the other way round for Elscint images.

into account for the grey scale representation. In that case, the middle grey value represents no flow.

Any velocities outside the $2 \cdot v_{enc}$ range are wrapped into the interval. This poses a problem for some applications. When simply summing up velocity values to determine average velocities or volume flow rates, the velocities must be unwrapped to their true values. A number of papers have been published on the topic of phase unwrapping in the MRI literature and other fields that use phase measurements. These methods are explained in he following paragraphs.

Most authors base their algorithm on the phase unwrapping condition that the phase difference between adjacent pixels is less then π. Ignoring noise, the unwrapping process would be simply based on the addition or subtraction of multiples of 2π to match this condition. Any path that covers the region of interest can be chosen. In the presence of noise, however, the process becomes more complex. The phase unwrapping condition might be violated due to noise and the corrected phase value might be dependent on the chosen path. A simple test for these violations, called residues [GZW88], is the validation of the condition that the sum of phase differences along any arbitrary path within the region must be zero, as mentioned in [GZW88, HR92, SNPG95]. The obvious test involves four neighbouring pixels that all are marked as residue in case the unwrapping condition is violated. Temporal changes during the cardiac cycle have been used to eliminate further residual errors [YBK+96].

Three different ways of unwrapping phases were developed: the first and perhaps simplest is known as path following. In the absence of residues in the region of interest, the phase can be corrected by following an arbitrary path and correcting the values, so that the difference to the previous pixel is less than π. The under-determined phase of the start pixel serves as a reminder that the absolute phase value in an image cannot be measured. This simple approach has been adopted [AM89], whereas another approach [HR92] splits the image into consistent areas (objects) and unwraps the phase between objects later. An even more elaborate approach was presented [GZW88]. They cannot split the image up into objects and need to make sure they reconstruct as much of the image as possible. For this purpose they test the image for the presence of residues. The original uniquely linked area is then cut between those residues to create a multiple

linked area. As long as an arbitrary path does not cross any cut, the reconstruction above holds. To minimise the losses, the cuts are taken to be as short as possible.

A second approach [SNPG95] reduces the phase unwrapping problem to a discrete Poisson equation and uses fast Poisson solvers to unwrap the phase.

The third approach uses an extension of the unwrapping condition. The change in phase over the image is approximated by a smooth function. The parameters of the function are then fitted to the data and the phase is corrected accordingly. In one case [Lia96] the approximation is a combination of a polynomial and residual.

In the present work, only subregions of the image, the flow regions, which are determined from the magnitude values, are of specific interest. Hence, there is no requirement to describe the rest of the image. The phase (velocity) at the border of the region can safely be assumed to be about zero, so the need for intra-object phase unwrapping does not exist. Lastly, no residues have been found. When no residues are detected in any of the velocity components, a connected path through the flow region is followed and the phases are corrected. The shape of the path does not matter in this case. This path following is repeated, until no more corrections are found in one cycle.

From my experience with laminar flow, regions with flows up to approximately $1.7 \cdot v_{enc}$ can be unwrapped. This can be linked to the fact that the velocity changes very quickly at the vessel wall. For non-laminar flow, the change at the vessel wall is even higher and is lower in the middle of the flow region (plug flow).

A.5. Graphical User Interface

The graphical user interface (GUI) is the most system dependent part for many programs. A number of packages have been developed that allow for easier, platform independent systems. Of the freely available packages, **Qt** ("cute" by Trolltech, Oslo, Norway, www.troll.no), is the most complete and widely supported. It is implemented in C++ and supports a wide variety of operating systems. A comprehensive handbook in HTML format is provided with the library and a book has been published [Dal99]. An easy introduction is provided in the form of a tutorial.

Graphical user interfaces operate using objects that are called widgets. For **Qt** these objects are implemented in an object-oriented programming language. The alternative widget set **Motif**, on the other hand, mimics the structure in **C**. The basic widgets can be combined into more complex ones by either a fixed structure or a container widget that allows for flexible placements of its contents when it is resized. All widgets contain code to handle resize, move, hide, draw and other events that are created by the underlying windowing system.

Unlike **Motif**, information in **Qt** is passed back from widgets via a signal/slot mechanism rather than callback functions. This allows programs to be structured in a clearer way. A pushbutton widget will, when the button is pressed (i.e. the left mouse button is pressed and released over the widget), generate a "clicked()" signal that can be connected to any slot in the program that accepts void signals. It can also be connected to more than one slot or alternatively no slot. This mechanism is implemented via a precompiler that will add the necessary mechanisms to the program.

The core of every program built with a graphical user interface is the application widget. This object continously listens for events generated by the windowing system. Once an event has been received, it is passed on to the widget concerned by checking the screen coordinates associated with every event. All widgets have to be registered with either the application or a higher order widget. This way the event can be handed down the widget hierarchy until a widget is found that will accept and handle it. If no widget is found to handle the event, it is ignored.

A.6. Data Visualisation

The aim of data visualisation is not the production of a photo-realistic image, but rather to aid the understanding of complex datasets. Streamlines are a good example. They are not real, but improve the understanding of very complex data. While the geometric projection of 3D objects onto the screen has to be absolutely correct, effects like shadows, ambient lighting and fog can be ignored or approximated. This allows for far faster graphics systems. This in itself aids the understanding, since the interactive manipulation of a 3D model on the screen increases the impression of depth.

There are a number of commercial tools available that help with data visualisation such as AVS, Irix Explorer, and IBM Data Explorer. All of these are very expensive and designed for high performance hardware. The programming interface is visual, i.e. a representation of the data flow (the visualisation pipeline) is drawn on the screen. This approach has two major drawbacks. The first is a limit in data import modules, although this might be provided by the user. The second is more serious. These packages cannot be integrated into a software system and all the data processing would have to take place within the visualisation package. These packages are, however, not optimised to incorporate user friendly interfaces.

VTK (Kitware, Clifton Park, NY, www.kitware.com/vtk.html) follows a different approach. The software is free and the source code is freely available. The software is also a library that is designed to be included into software projects. For rapid prototyping, a number of wrappers are provided for scripting languages like **TCL**, **TK** and **Python**. The computational concepts are comprehensively described [SML97] and a large number of examples are provided with the source code. The documentation is unclear, however, and it is advisable to go to the examples in case of problems.

It is useful to think of visualisation programs in terms of a pipeline. The commercial packages allows the user to place modules, like import functions, filters or renderers, on the screen and draw the pipeline between them. In **VTK**, the pipeline is implemented using pointers. The pointer to a module's input is set to the pointer of another module's output. One obvious advantage of this approach is the fact that all the conventional elements of the **C++** programming language for conditional executions are available, e.g. loops, conditional clauses, etc.

A visualisation pipeline involves many time-consuming steps. The data has to be read, filtered, mapped as polygons and then rendered. It is therefore very important to keep track of the changes within the pipeline. This allows for conditional re-execution of the limited part of the pipeline affected by a change. Conventional packages like **AVS** use an explicit executive that keeps track of changes and dependencies. **VTK** uses an implicit model. All objects keep track of their modification time and when the renderer requests the object data, it asks all its input modules in the pipeline if they have been modified which in turn ask their input modules. This is done until all the starting modules are

reached and the direction is reversed. All modules pointed to by the output pointer are executed if they have been modified and the new data is passed down the pipeline. When changing any of the data in the pipeline without the use of a filter provided by, or based on, **VTK** care has to be taken to execute the relevant modules explicitly.

VTK provides a number of data structures with varying degrees of memory and execution optimisation. These data structures are based on the abstract representation of the data in memory rather than the representation in space. A structured grid, for example, contains data vertices that can be addressed as an array. A vertex is a point with a position, normal and colour assigned to it, each of which is a three element vector. The geometric representation of the vertices and cells, however, can have any shape.

There are some problems when combining the **VTK** library and **Qt**. These are rooted deep in the handling of **OpenGL** structures. A tool from Jan Ehrhardt called **vtkQGL** (www.medinf.uni-luebeck.de/ ehrhardt/vtkQGL/vtkQGL.html) makes the necessary adjustments. It supplies a widget **VTK** renders into while all events are handled by **Qt** and the necessary actions initiated in **VTK**.

A.7. Mathematical Libraries

The direct evaluation of a discrete Fourier transform scales with $O(n^2)$. This can be an extremely time consuming process. However, the discrete Fourier transform can be split into two discrete Fourier transform for even n and recursed further for data sets with a power of 2 data points. This leaves just a sum of Fourier transform with just one element. Clever reordering and summing up the elements of the data array can reduce the scale of the problem to $O(n \log(n))$. Details are described in [BS79, PTVF92].

The **FFTW** (Matteo Frigo and Steven G. Johnston, Massachusetts Institute of Technology, www.fftw.org, Fastest Fourier Transform in the West) combines this technique with a host of others to create the fastest general function available. For special cases, a version from Japan is faster. **FFTW** guesses or measures the performance of certain elements of the hardware to find the optimal algorithm to use. Since this project is concerned with relatively few Fourier transforms of the same kind (number of rows and

columns) at a time, the guessed version performs well. It can also handle data of any number of rows and columns.

The non-linear fitting in the project is based on a modified Levenberg-Marquardt approach. The algorithm is described in [PTVF92], but the implementation is not stable. The function **lmdatafit**, supplied as part of the **Cephes** library (www.netlib.org/cephes), will minimise the sum of squares for any function depending on a set of parameters. This procedure continues iteratively until a certain difference is achieved or the fit fails to improve over several iterations. This implementation is a translation to **C** from **Fortran** by Steve Moshier and was originally part of the Argonne National Laboratories **MINPACK**.

A slight modification to the function call was made to pass the data to the function. The function that will be minimised is passed to **lmdatafit**. It is called as part of the algorithm to supply an array of function values evaluated at a certain number of points for a given set of parameters. To fit a given set of data points, these points had to be passed to the function evaluation. To enable 3D weighted fitting, the data points are passed in a 1D vector that contains the data point coordinates, the weight and the measured value for each of the points.

A.8. The MRIFlow Program

A.8.1. Choice of Data Structures

For the image data, the choice of data structure is straight forward: a 2 or 3 dimensional array. In C++ these have to be simulated using a linear address scheme. The linear address of a cell (i, j, k) 3D array is $k \cdot rows \cdot columns + j \cdot columns + i$. **Qt** provides an array class that checks all input and output functions and avoids overstepping the array, as well as providing memory reservation functions.

Representing the flow data is somewhat more difficult. Firstly, to enable the presentation of the data under the cursor in real time, the absolute coordinates and velocity components have to be stored in addition to the values in slice coordinates. Secondly, most of the volume acquired does not contain any flow points. Hence, arrays (Figure A.5) would store redundant information. Thirdly, a data structure is required for each

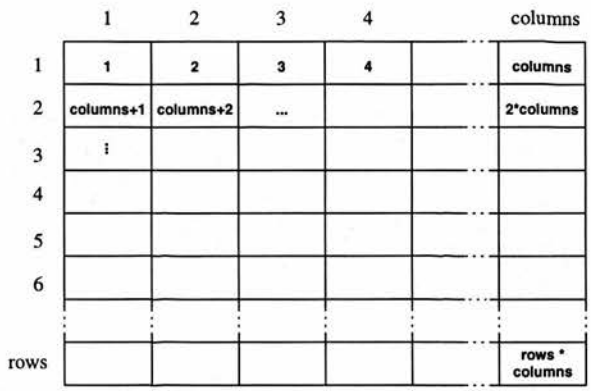

Figure A.5.: *Illustration of the organisation of an array.*

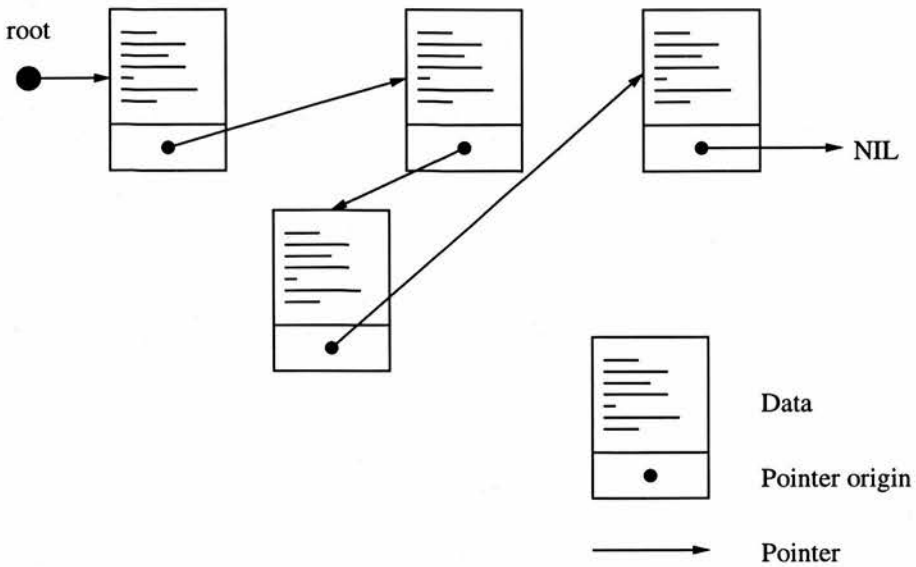

Figure A.6.: *Illustration of the organisation of a linked list.*

flow in the image. That would mean a huge array per flow storing redundant information. Fourthly, when fitting, the points outside the flow cannot be represented as having zero flow velocity. In these regions the flow function is not defined and the extrapolation can adopt any value. Finally, the number of flow points is not known *a priori*. The data structure should therefore handle flexible amounts of data. The simplest choice was a linked list (Figure A.6). **Qt** provides a template class for this structure. It grows dynamically and, if it is not sorted, with constant time (insertion at the beginning or end). Searching an unsorted linked list, however, involves comparing the search element against every member of the list. This process has to be undertaken numerous times during program execution and takes a lot of time since it scales with $O(n)$. Storing the bounding box of the flow (maximum and minimum x-, y- and z-coordinates) avoids searches for elements outside the bounding box. The complexity of a search in a linked list reduces to $O(n/2)$ when the list is sorted. In this case, however, list growing is of complexity $O(n/2)$, instead of $O(1)$ for the unsorted list. The data structure handling flows only contains a few elements and was implemented as a list. For a flow that contained up to 50 000 flow points, a simple list was found to be far too inefficient.

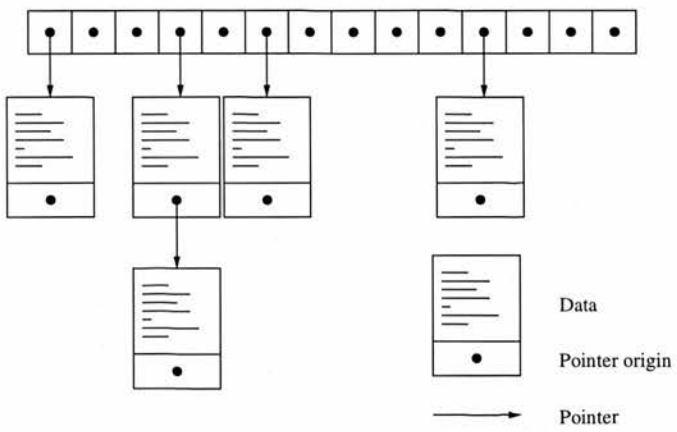

Figure A.7.: *Illustration of the organisation of a hash table.*

The abstraction of data in classes allowed the data structure of flows to be changed with a limited amount of risk. A different data structure had to be chosen that consumes less memory than arrays and less time than lists. Hash tables are just such a structure

(Figure A.7). In a hash table, elements are stored in short lists that are stored in an array (in fact, only the root element of every list is stored in that array). The index of the array element that contains the list is calculated in a random, unique way. The function should be random to distribute the elements evenly throughout the table to keep the lists as short as possible. A hash table has a performance critical value, which is the length of the array. If the array is approximately as long as the expected number of elements, then every list only has one element and the hash table guarantees, on average, the same performance as an array. Although the elements in a hash table are not sorted, searching for this case is of complexity $O(1)$. The problem is the correct choice of array length. Often, this is difficult to predict and for this software project a value of 9973 was chosen. Most acquisitions contain between 2 000 and 50 000 flow points and the hash function used by the **Qt** hash table class works best for prime numbers. It is important to remember that the elements of a hash table are not returned in any specific order. The particular hash table chosen for flow data maps integer values. The linear array address of the flow point is used. This ensures a simple correspondence between the data structure for the original image data and the flow points.

A number of values are stored for every flow point. The pixel coordinates are stored as integers, the absolute coordinates as floats in mm, the velocity components in the pixel coordinate system as floats in mm/s, the same parameters phase unwrapped and both of these in the absolute coordinate system. In addition, the pixel intensity of the magnitude image and a weight are stored. The weight will be 2 for core flow regions and 1 for flow points close to the wall. Altogether there are 5 integers and 12 floats stored for every flow point. This is a lot, but it allows for very fast access to all the important data. Later, it also turned out to be exactly the number required to store the segmented data fit points. In that case the pixel coordinates are accompanied by the fitted flow at that point in mm/s, and the derivatives of the x-, y-, and z-velocity components with respect to x, y, and z.

A.8.2. Program Structure and Dialogs

The software project is made up of one main program and two short support scripts. The support scripts are written in **C++** and **Perl**. The scripts order the data received from the scanners and in the case of the Elscint scanner also converted the data from big- to little-endian (Section B.1.1). These two scripts are called `ElscintSort` and `GESort.pl`. This step has to be done only once and was therefore separated from the main program.

All other processing steps are included in one program called `MRIFlow`. This program was originally designed for clinical use and therefore includes a graphical user interface. Three main tasks can be differentiated:

1. User interaction.
2. Management of scanner data.
3. Post-processing.

There are two main classes that handle user interactions in the program. `UKMRIFlow` provides a framework for the user interface with all global settings, the menu structure, the help bar and an information bar (Figure A.8). All data structures are collected in the class `UKCanvas` (Figure A.8). Here, images are represented for all 2D and 3D data sets on a rectangular grid and the lists of the various data types are managed. This class handles mouse press and mouse move events to select or deselect a data structure and allows for binary data set operations (accessible via a pop-up menu when pressing the middle mouse button). When a dataset operation is selected in the menu structure provided in `UKMRIFlow` it will operate on all selected data sets of the appropriate type. This is arranged by keeping lists for 2D and 3D scanner data sets, flow data, segmented flow fit data and wall data sets. Within the workspace provided by `UKCanvas` all data sets are represented by 2D slices. For all 3D data sets the middle slice is shown. This avoids wasting the available space with hundreds of images.

Images can be zoomed in `UKCanvas` by a factor of two at a time. This avoids distorting the image by interpolation. Once the zoom menu point is selected, the first highlighted image is presented in the upper left corner and the cursor changes to a blue rectangle

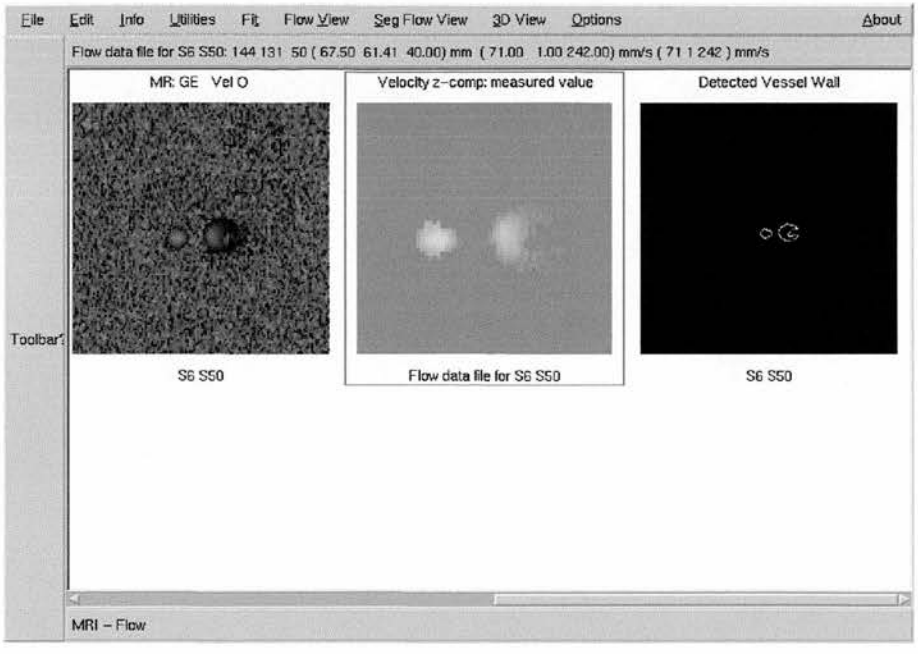

Figure A.8.: *The basic appearance of the* `MRIFlow` *program. The frame with the menu functionality is provided by the* `UKMRIFlow` *class while the* `UKCanvas` *(white background) class manages the datasets. A velocity map (S/I component), the detected velocities (selected, S/I component) and the detected wall are presented for the middle slice with the velocity map zoomed once and the masked velocity zoomed twice. The cursor (not captured in the screen shot) was positioned in the right hand side of the masked flow and the velocity data is presented together with the pixel and absolute coordinates in the information bar. The detected velocities have been rotated into the laboratory frame.*

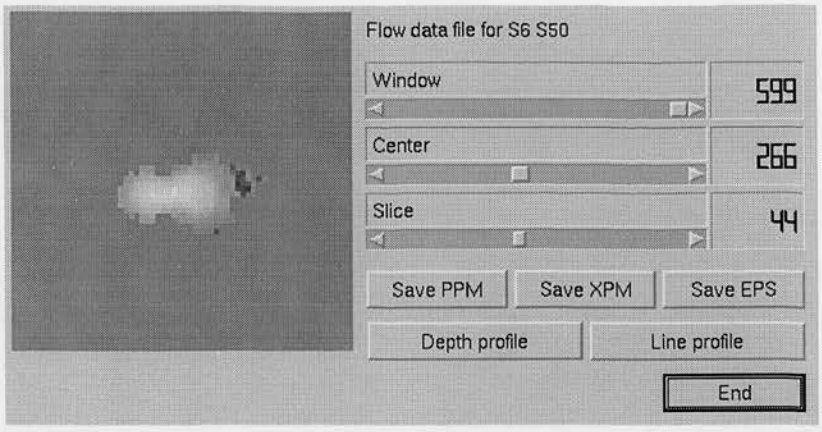

Figure A.9.: *The masked flow dataset from Figure A.8 as displayed by the* `UKSliceViewWindow` *dialog. Windowing and selection of a specific slice are provided in this dialog.*

when entering the image. This rectangle represents the part of the image that appears zoomed. During this process the values under the cursor are still represented in the information bar. This allows the reproduction of the process. The zoom information is then applied in the same way for all remaining images that are highlighted.

The `UKSliceViewWindow` class provides windowing for positive, as well as positive and negative, data sets (Figure A.9). In addition the ability to quickly select a specific slice for 3D data sets is provided. The part of the image currently displayed in `UKCanvas` is selected in `UKSliceViewWindow`. For data structures containing positive as well as negative values a grey scale representation with null as mid-grey and a colour version with blue and red scales are provided. Both `UKCanvas` and `UKSliceViewWindow` will capture mouse move events and display the value under the cursor in the information bar of `UKMRIFlow`. This needs fast access data structures but proves a valuable tool. Images in various file formats can be saved in both `UKCanvas` and `UKSliceViewWindow`. Standard graphic formats are created using the functionality of `QPixmap` (part of **Qt**), but a new function was written to save images as Encapsulated PostScript images. All pixels are actually saved as coloured squares to avoid any interpolation by the print driver.

Arbitrary line profiles can be drawn across any slice in both `UKCanvas` and `UKSliceViewWindow` and depth (temporal or spatial) lines can be drawn in `UKSliceViewWindow`

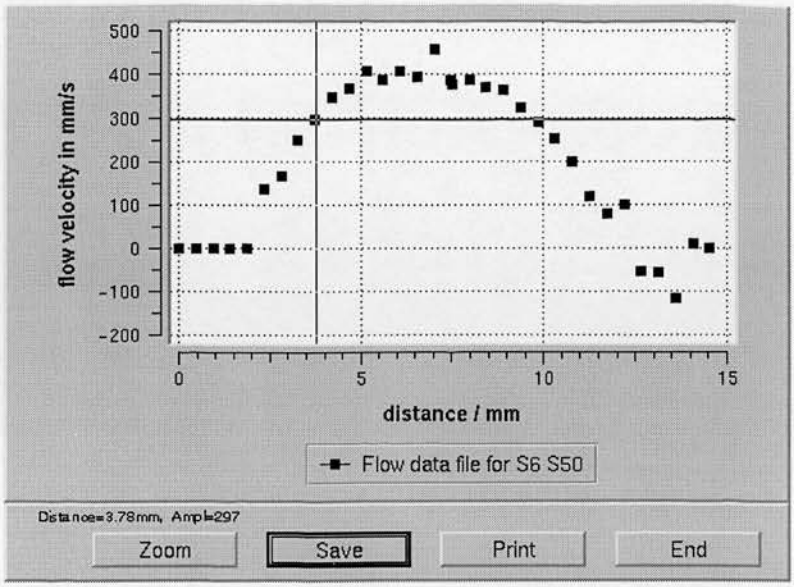

Figure A.10.: *Arbitrary line profiles can be sampled across any data set using* `UKLineProfileWin`. *The data can be saved in ASCII format and printed. Basic zooming and presentation of the cursor position are implemented. The data shows the velocity values across the flow presented in Figure A.9 for the S/I component.*

using `UKLineProfileWin` (Figure A.10). All values can be printed, saved in various graphics file formats or stored as ASCII files for further processing. The approximation of a line on a discrete grid follows the algorithm presented in [OO94]. This class is based on ideas from the **Qwt** widget set by Josef Wilgen.

To compare two slices of equal dimensions, a **UKCompWin** dialog can be launched that provides split window representation with either a horizontal or vertical split (Figure A.11). This split can be continuously manipulated by the operator using scrollbars. Once a view is accepted it is transferred to `UKCanvas` where small triangles mark the split. Again, the part of the image that is currently displayed in `UKCanvas` is used. This enables exact pixel by pixel comparisons between images.

Data sets are loaded using a variety of methods. To load "DICOM" slices, a special dialog was developed: `UKDiComLoadDialog` (Figure A.12). This dialog contains the usual means to select a subdirectory and a widget to display thumbnails of any "DICOM" files found in that directory. When Elscint FIDs are encountered, only an icon representing the type of FID (2D, 3D, Cine) is shown, since the necessary Fourier transform to reconstruct the

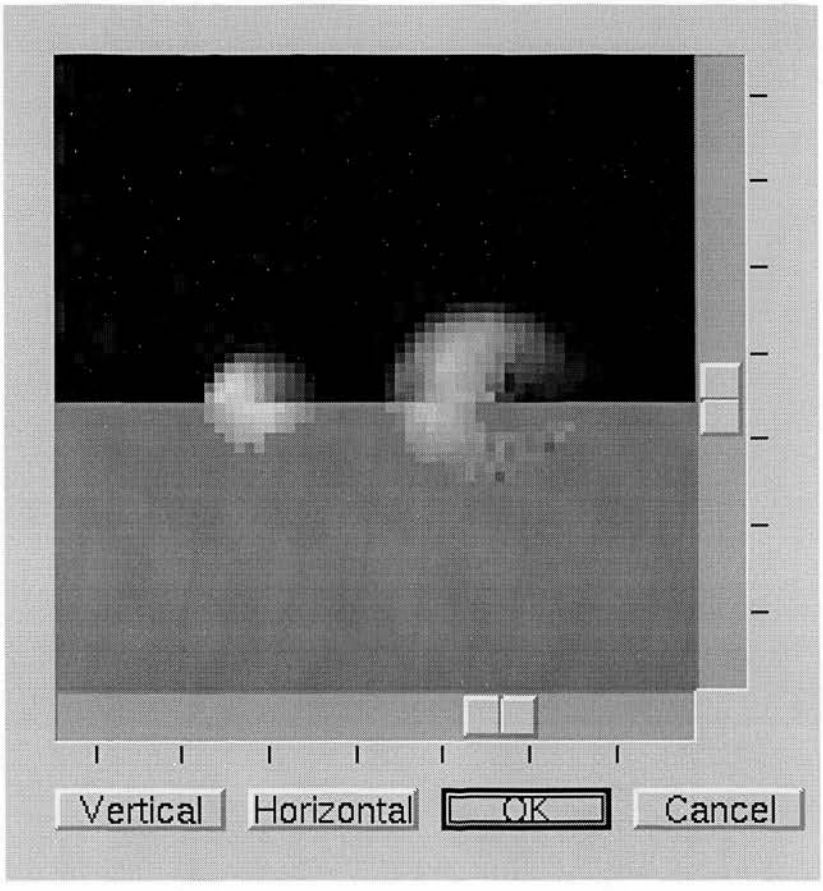

Figure A.11.: *Comparison of two images with a horizontal split The data shows magnitude image (top) and masked flow presented in Figure A.9 for the S/I component.*

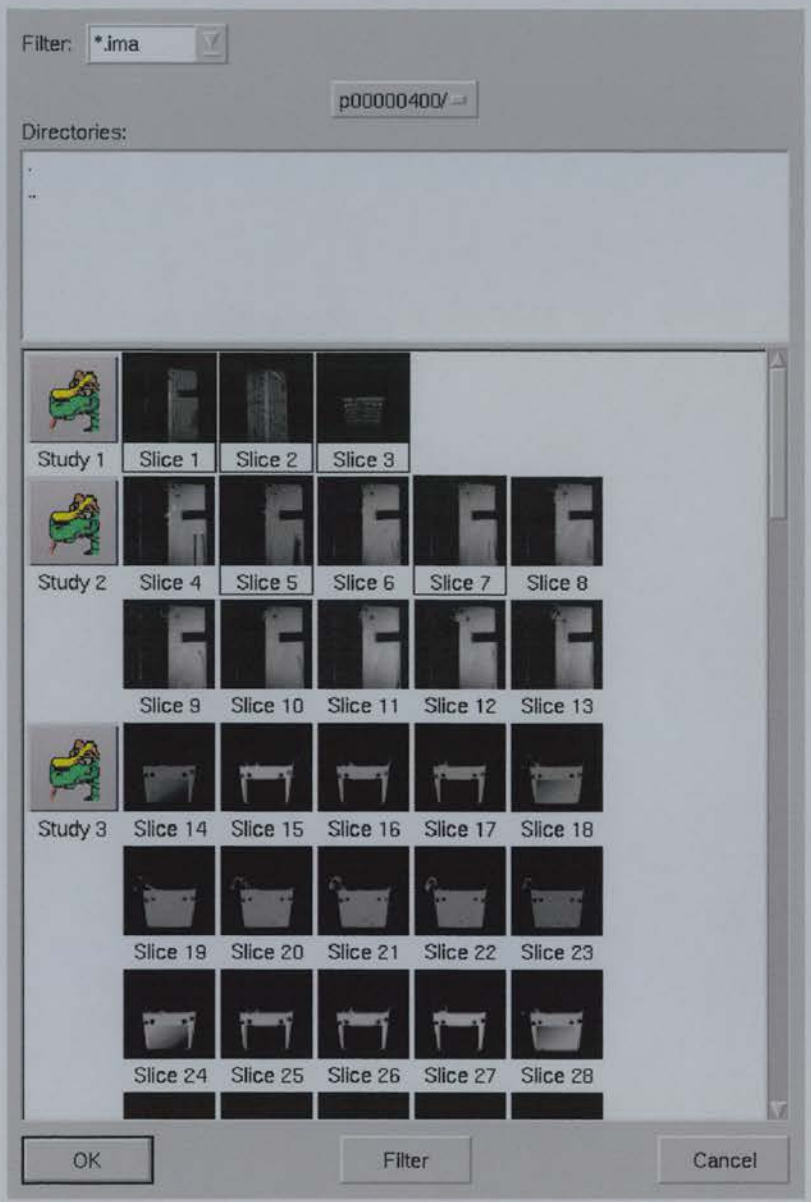

Figure A.12.: *"DICOM" slices are read via the* `UKDiComLoadDialog`. *Shown is the contents of a subdirectory from the SIEMENS scanner containing several studies. The header information can be called up by clicking the header icon generated for every study. A number of slices have been selected prior to loading.*

image is relatively time consuming. While reading the "DICOM" files, the dialog keeps track of the study number and sorts the files into studies each beginning with a new line and a header icon. This feature was primarily designed for the SIEMENS scanner, where all slices for one patient appear in one subdirectory without differentiating the studies into subdirectories. Left clicking this icon will select the whole study while right clicking this icon will pop up a `UKDiComInfoWin`.

3D and Cine studies on the GE scanner are saved as individual slices. It is useful to combine these into one 3D object when loading the data. Two functions have been created. The first loads all the slices in a subdirectory into a 3D slab and the second sorts out the different types of maps created with PC MRI into individual 3D slabs. Both functions rely on standard **Qt** directory selection dialogs.

Flow and wall data sets are not represented as thumbnails and the standard **Qt** file selection dialogs can be used to identify the file to use. Both functions can differentiate between the types of flow and wall data sets (Section B.1).

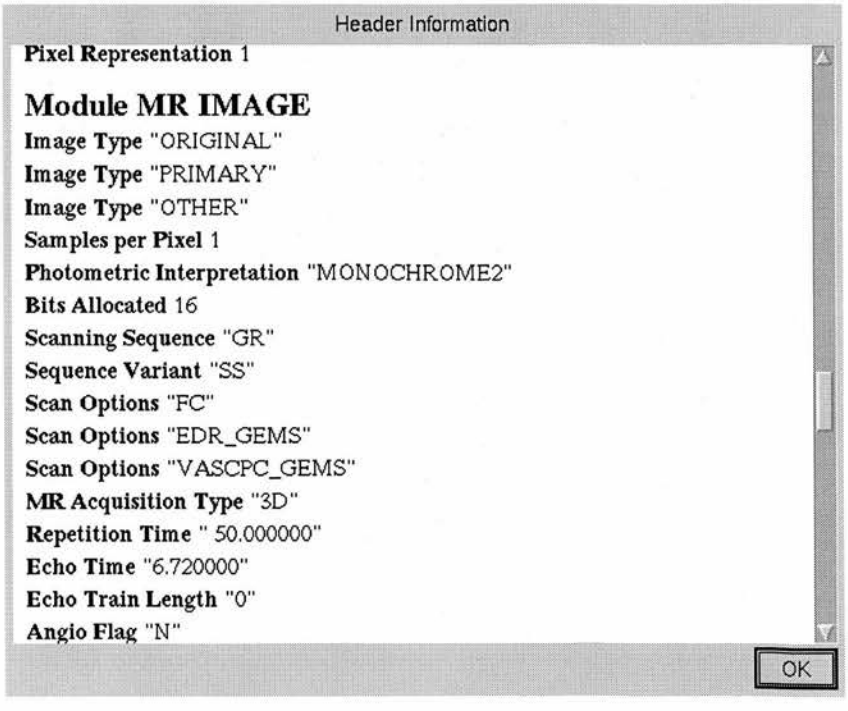

Figure A.13.: *The contents of the "DICOM" header information displayed in* `UKDiComInfoWin` *dialogs.*

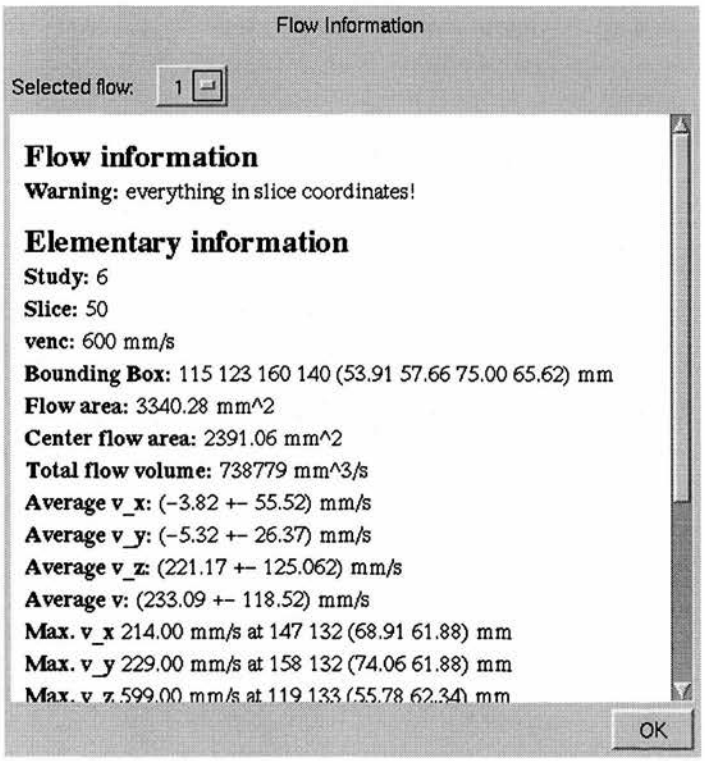

Figure A.14.: *Information on the first flow in the list displayed in a* `UKFlowInfoWin` *dialog.*

By either right clicking a header icon in `UKDiComLoadDialog` or selecting the header info menu point, a `UKDiComInfoWin` dialog (Figure A.13) is launched that presents the "DICOM" header info for the appropriate slice and study. This information is presented in **PAPYRUS** modules. For MR images, the relevant subset is shown whereas for other modalities all available information is presented. A similar dialog exists for flow information implemented in `UKFlowInfoWin` (Figure A.14). However, since the information required for flows varies a great deal, this feature was later replaced by a short **Perl** scripts that act on the flow data files. These can easily be adapted to the specific situation.

The thresholding filter and flow detection are the only functions that expect parameters which are stored globally. These can be changed via two simple dialog windows (`UKFlow-DetectionOptionsWin` (Figure A.15) and `UKThresholdOptionsWin`) which allow the parameters to be set via scrollbars.

A number of different 3D Views can be created for flow, wall and wall shear stress information. The basic functionality is provided by the parent class `VTKQTWidget` (Figure A.16).

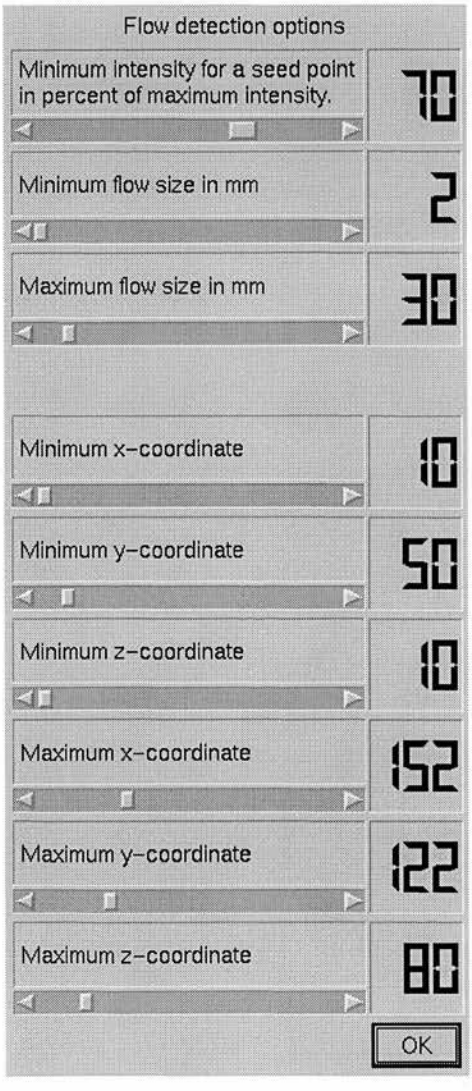

Figure A.15.: *Parameters for the flow detection algorithm are chosen in the* `UKFlowDetectionOptionsWin` *dialog.*

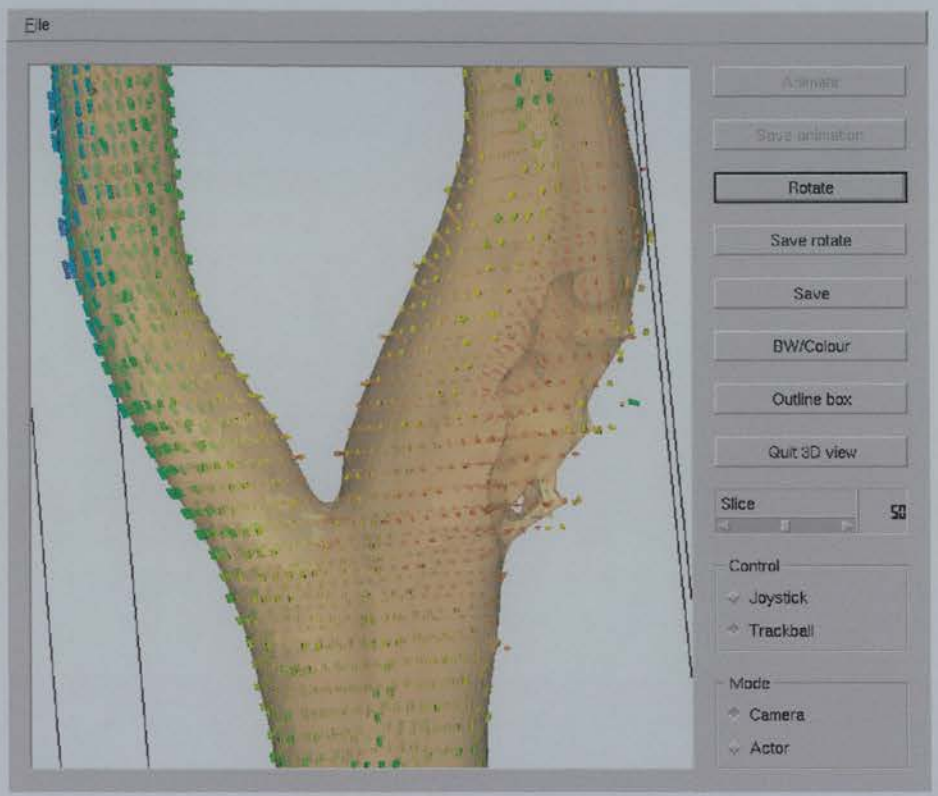

Figure A.16.: *3D views of data sets are presented in subclasses of the* `UKVTKQTWidget` *dialog. In this case, the surface and wall shear stress vectors for a flow in a normal carotid artery model are rendered. The camera position may be saved and restored via the file menu. For representations that include a specific slice this can be chosen interactively using the slider bar and animated to cycle through all slices. This animation may be saved as a series of individual pictures. The same may also be applied for rotations around the vertical axis of the current view. Individual views can be saved in PNG format. The bounding boxes can be toggled and the view can be switched between colour and grey scale.*

B. Programming Details

B.1. File Formats

B.1.1. "DICOM" 3

To generate absolute spatial and velocity information, it is necessary to read "DICOM" files directly from the MRI scanner. As an aid, comprehensive information on medical image formats can be found in the "Frequently Asked Questions" [Clu98b] document by David Clunie. Most of the principle information following here is taken from that document.

A variety of information has to be stored in the image files:

- image data, which might be compressed,
- patient identification,
- technique information about the exam, series and slice,
- timings in the case of gated examinations,
- and details of contrast agents.

Generally, there are several families of file formats in use:

- fixed format, where layout is identical in each file (very inflexible),
- block format, where the header contains its own length,
- tag based format, where each item contains its own length.

The American College of Radiologists (ACR) and the National Electrical Manufacturers Association (NEMA) recognised some time ago the need for standards to facilitate multi-vendor connectivity to promote the development of Picture Archiving and Communication System (PACS). Their up-to-date standard was released as a draft during 1992-1993 as ACR/NEMA Standards Publication PS3, also referred to as Digital Imaging and Communications in Medicine ("DICOM") 3 [Nem98].

The example *par excellence* of the tag based format is the ACR/NEMA style of data stream, which, though never intended as a file format *per se*, has proven useful as a model. In the process of being accepted by "DICOM" as an extended standard, a media interchange format is included. ACR/NEMA style tags are each self-contained and self-describing (with the appropriate data dictionary), and contain their own length, so if a tag cannot be interpreted it can be skipped.

ACR/NEMA 1.0 and 2.0 define a mechanism along the lines of a layered ISO-OSI (Open Systems Interconnect) model, with physical, transport/network, session, and presentation and application layers. Unless one actually wants to physically connect to a device that supports the unique 50 pin point-to-point electrical interface, then one really only needs to be aware of how ACR/NEMA implements the presentation and application layers, which are described in terms of a "message format". This message format is important, not because anyone seriously wants to connect devices in the limited fashion envisaged by these early standards, but because many proprietary formats and other *de facto* standards have adopted the ACR/NEMA message format and its corresponding data dictionary and extension mechanisms.

A message consists of a series of "data elements", or tags, each of which contains a piece of information. Each element is described by an "element name" consisting of a pair of 16 bit unsigned integers <"group number", "data element number">. The data stream

is ordered by ascending group number, and within each group by ascending data element number. Even numbered groups describe elements defined by the standard (can be found in the data dictionary). Odd numbered groups are available for use by vendors or users, but must keep the same structure as standard elements. To avoid confusion, these groups contain, as one of the first elements, a tag containing a manufacturer specific string, e.g. "`ELSCINT1`". Following the <"group number", "data element number"> pair is a length field that is a 32 bit unsigned even integer that describes the number of bytes from the end of the length field to the beginning of the next data element.

The last part of a data element is its value, which is defined by the data dictionary to be ASCII (numeric AN or text AT) or binary value (BI 16 bit or BD 32 bit). The values may be single or multiple. Multiple ASCII values are delimited by backslash (0x05C) character. Odd length ASCII values are padded with a space (0x020).

The electrical interface is a 16 bit one, and hence even though 32 bit binary values are defined to be transmitted least significant word first, there is no mention in the standard as to how to encapsulate the message in an 8 bit world, hence different users and vendors have chosen little- or big-endian schemes, complicating the exchange of files. Endianess refers to the ordering of bytes within a 16 bit word. In decimal this would be the difference between "500 000" and "000 500". However, the order of bytes in a string remains the same in both byte orders. This makes it impossible to convert information from one byte order to the other without the detailed knowledge of the data interpretation. The term can be traced back to *Swift's Gulliver's Travels* see [Ray94]. Big-endian refers to "big end first". The new "DICOM" standard assumes a default little-endian representation which seems to be the most appropriate considering the old definition for 32 bit words, which specified that the least significant 16 bit word be transmitted first.

It is important to note that the native byte order may become important when reading 32 or 64 bit binary values. This has been accounted for in the version of the library used for this project. It contains code that is compiled depending on the specific platform.

B.1.2. The Flow File Format

The format of files storing flow information was defined as part of this project. One objective was to avoid any problems with endianess of the computers used and ease of inclusion in subsequent post-processing software, i.e. Matlab and IDL. Certain information about the original images has to be stored to allow for later use. This information is stored in strings following a clear text description that starts with the general Unix comment character "#". The convention agreed on UNIX systems is to start the file with a few identification bytes, the magic number. Flow files start with the string "FlowData". For Cine data sets, the table of cardiac times is stored in the block of descriptive data.

This general description is followed by a data block for every flow region in the list of flows for the acquisition. Each of these blocks is started by the line "FlowInformation" followed by the bounding box of the flow.

For polygonal fits of the whole flow, the flow data is preceded by a block of data with parameters for every fit executed. This block starts with the line "FlowFit:" followed by an indication if it is a 2D or 3D fit, the number of parameters and an indicator if the wall pixels were included. The parameters describing the fit of the x- component in the absolute coordinate system starts with the line "ParametersX:". This is repeated for the y and z - components. One of these blocks is saved for every fit executed.

Following the fit parameters, all the flow points are listed one per line. First the pixel coordinates are saved followed by the velocity components in pixel coordinates (mm/s) and similarly the phase unwrapped data. The values in absolute coordinates start with the absolute coordinates of the voxel (mm), the velocity components in the absolute coordinate system (mm/s) and the same for the phase unwrapped data. The intensity of the voxel on the magnitude image is stored at the end together with a weight of 1 for a wall pixel and 2 for a pixel in the core flow region.

Segmented fifth order fits have a second flow data block following every data flow that contains the fitted values instead of the fit parameters. In this flow block the pixel coordinates are followed by the fitted velocity values at that point (mm/s) and the derivatives of the y - component of the velocity in all three directions (1/s). This is followed by the absolute coordinates (mm), the derivatives of the x and z - component of the velocity in all three directions (1/s). There are more points in this second, fitted flow than the original flow, since values outside the original region are saved for extrapolations.

This information structure is repeated for every flow in the flow list.

B.1.3. The Wall File Format

Storing the geometry of the wall involves the vertex coordinates and the geometric relationship between them. All this is handled in the **VTK** library. The important additional information needed to reconstruct the wall information is stored in the 256 bit descriptive string that **VTK** includes. The study and slice number, the fit order and the number of rows, columns and slices are stored as integers, followed by floats of the voxels size, the maximum velocity and the position, and row and column vectors in the absolute coordinate system. For detected walls this will be preceded by the string "Detect ". **VTK** handles all the writing and reading of the polygonal data of the wall, for representation purposes this is regridded to be displayed along with the flow information. The location of all vertices is stored followed by the triangle faces and the vector and scalar values associated with the vertices.

B.2. File Structure of the Software Project

Rather then describing the detailed implementation (45 000 lines of **C++**) of list handling and the management of data structures, the relevant mathematics are described in this thesis. In this section all of the header files are described in detail. To understand the workings of an object orientated program it is sufficient to know the interface definition for most of the objects in order to use or extend the functionality of a specific object. This interface definition is made public in **C++** through header files. The header files collect similar objects in one place. All objects defined in a header file are explained together with a list of the implementation files.

"ukmriflow.h": This file provides the interface for the `UKMRIFlow` class. This class provides the menu bar, the status line and info bar. However, the tool bar is unused at present. The status line at the bottom provides usage information, whereas the info bar provides information on the current pixel position and the interpretation of that pixel. All menu events are coordinated in this class and then passed on to the instance of a `UKWorkspace` widget contained in this widget. The current version of **Qt** provides a container class similar to this one. The implementation of the class is found in "ukmriflow.cpp".

The only instance of the `UKMRIFlow` class is defined in the "Main.cpp" file. In this file an instance of `QApplication` is created and an instance of `UKMRIFlow` is connected to it as the main widget. `QApplication` provides the basic interaction with the window system and starts an event loop.

"ukcanvas.h": The `UKWorkSpace` class is defined in this file. It inherits from `QTableView` and serves two main functions. The representation image of the data sets have to be displayed and the lists of data sets maintained. The images are arranged in a rectangular grid that grows its column and row size according to the biggest item currently stored in it. It is important to be able to assign mouse events to the element the mouse currently resides over. A pop up menu is provided for binary operations on compatible data sets. These are executed for every marked data set and the one the mouse event was created in, by pressing the middle mouse button. One instance of the template class `QList` is managed for every class defined in "uk2d.h". This is needed to call functions specific to some of these data structures. The appearance of the mouse changes with context and the current mode is stored in this class. Requests to change the status or information bar contents from one of the children widgets are passed through to `UKMRIFlow` by this widget. The implementation is located in "ukcanvas.cpp" (mainly event handling and list management), "ukfilter.cpp" (mathematical filters for image processing and flow detection algorithms) and "ukvtk.cpp" (initialisation of 3D views).

"uk2d.h": A number of classes are defined in this file that handle all the main data structures used in the program. The main functionality of a data structure to be handled by `UKWorkSpace` is defined in the abstract parent class `UK2D`. This class defines a common interface only, and steps were taken to ensure that no instance of it can be created. In essence, every class derived from `UK2D` can be selected, contains a pixmap and knows its dimensions and the location relative to this widget. This class is also able to print the pixmap or save it in various data formats including EPS, stores its zoom state, knows its position within the grid of `UKWorkSpace`, is able to return a specific value from the pixmap, issue a request for a pop up menu and for the pixel information in the information bar to be changed. It also handles a variety of mouse and repaint events. A descriptive text is displayed below the pixmap, if provided. A number of specialised classes are derived from this class (Figure B.1).

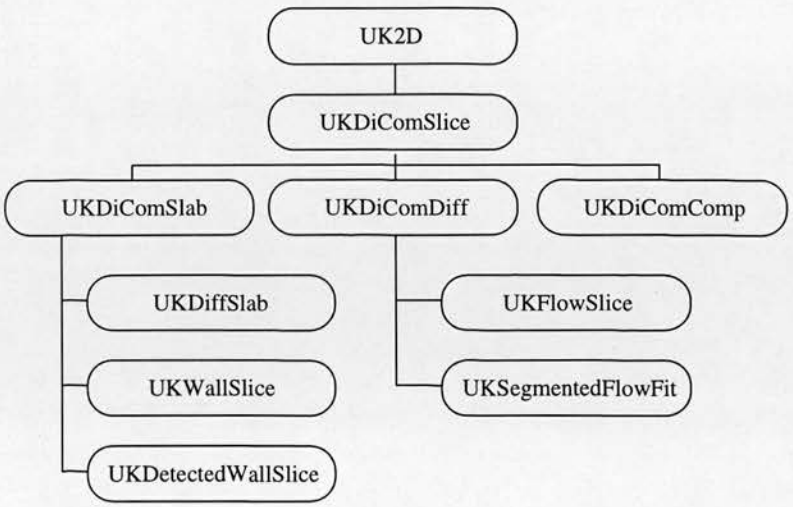

Figure B.1.: *The structure of classes derived from* `UK2D`.

The `UKDiComSlice` slice class handles 2D slices. It was mainly designed to handle medical images, but could be used for any data set that contains positive integer values arranged in an array. This class adds a number of additional elements to `UK2D` and forms the actual parent of all other classes in this file. A second descriptive text is displayed on top of the image and a filename is stored for later reference. The value array is stored in a `QArray<int>`. Its values are available via linear or two value addresses. A number of additional parameters can be stored: the number of stored bits in the original data, the slice and study numbers, a special direction, the image position and orientation in scanner coordinates. Additional values are the manufacturer identification string, the encoding direction, the patient identification number, the image type, the normalisation type, the image scale, the maximum velocity, the cardiac time and the software version from the scanner. A constructor, a function that allocates memory for and initialises the variables of an object, is provided that parses "DICOM" files, and another that takes a data array as an initialisation parameter. The grey scale image displayed always covers the whole range of values with a linear gradient of grey values.

A `UKDiComSlab` is derived from a `UKDiComSlice` and provides another 3D array in which to store positive integers. The displayed image is constructed from the middle slice of the slab. For Cine data, the cardiac times are stored as a table.

For positive and negative integer data sets `UKDiComDiff` is derived from `UKDiComSlice` and `UKDiffSlab` from `UKDiComSlab`. The display may be either monochrome or colour with red for negative and blue for positive values.

To store the results from the `UKCompWin` dialog, `UKDiComComp` is derived from `UKDiComSlice`. The pixmap is copied from the two original images according to the chosen split. However, the stored data array does not make sense in all conceivable cases. This class is for display and printing purposes only.

To handle flow data `UKFlowSlice` is derived from `UKDiComDiff`. The flow information is stored in a `UKFlowList` instance and the data array is created according to the chosen view. The velocity components may be displayed in either absolute or slice coordinates with and without phase unwrapping. When fit information (Section 7.2.3) is stored in the `UKFlowList`, the differences for the various fit orders and velocity components can be be displayed. Of course, all other member functions have to be made aware of the currently chosen view to avoid information loss by using the integer data array (all functions operate on the list of flows). For Cine data, the cardiac times can be stored as a table.

The reconstructed walls (see Sections 7.3.2 and 7.3.3) are stored in `vtkUnstructuredGrids`, but for simple display and saving purposes, `UKWallSlice` was derived from `UKDiComSlab`. Since the calculated coordinates of wall points can be located between grid points, the data array is constructed by setting a grid point to 1 if a wall point is found within 10 % of the grid location and 0 otherwise. 10 % was chosen to minimise errors in subsequent calculations (see Section 7.4.1). The walls in this structure are constructed from fit results rather than the walls stored in the otherwise equivalent `UKDetectedWallSlice` where the detected flow points are used to construct a wall that is subsequently smoothed. To avoid associating walls and fits of different order, the fit order is stored in this object.

As an alternative fitting process, segmented fits were introduced (Section 7.2.4). The results of these are stored in `UKSegmentedFlowFit` (derived from `UKDiComDiff`). In these, one flow list stores the original data and a second, the fit list, stores the results of the fit evaluated at grid points and all the required derivatives of the velocity components. For Cine data, the cardiac times can be stored as a table.

Since the creation of `UKFlowSlice`, `UKSegmentedFlowFit`, `UKWallSlice` and `UKDetectedWallSlice` consumes considerable amounts of time, all of these have special file formats associated with them (Section B.1).

The implementation of these classes can be found in "uk2d.cpp" and "uksegmentedfit.cpp".

"ukflow.h": All classes connected to flow data and fits thereof are collected in this file with the exception of the segmented fit. The velocity information for every pixel that has been detected as being part of a flow is stored in a `UKFlowPoint` object. It stores the pixel coordinates of the voxel as integers and the absolute coordinates in mm as floats, the velocity components in pixels and absolute velocities in mm/s as floats, as well as the phase unwrapped values of the velocity components in both coordinate systems. The image intensity of the voxel in the magnitude image and a weight (1 for a suspected wall pixel and 2 for the core flow region) are also stored as integers. Storing all these values avoids recalculating them every time they are needed. This is especially important for the pixel information generated for the current cursor position.

Instances of `UKFlowPoint` are collected in `UKFlow`, a derivative of `QIntDict<UKFlowPoint>`. A bounding box (the maximum and minimum numbers in the pixel coordinate system) is stored for every flow together with the dimension of the original grid and the voxel size. Functions to test two flows for intersecting bounding boxes and connection is provided, together with functions to mark wall pixels and eliminate obvious noise pixels. The detection of residuals and phase unwrapping functions are also defined in this class.

All flows detected in an acquisition are collected in a `UKFlowList`, a derivative of `QList<UKFlow>`. Again, a bounding box that contains all the individual flows is provided. Search functions are provided that locate the `UKFlowPoint` associated with specific pixel coordinates. `UKFlow` objects can be merged in case they touch and the absolute values of the velocity and location variables for all flow points are calculated for the whole flow list.

For polynomial fits that operate on complete flow data sets, a common class is provided, `UKFlowFit`, since the fits can be distinguished by the chosen fit order. The constructor will execute the fit of the data `UKFlow` given the order of the polynomial and information on whether or not to incorporate wall pixels. The resulting fit parameters for every

velocity component are stored and the fitted velocities may be requested for a voxel given in pixel coordinates. The various possible fit orders are collected by `UKFlowFitList`. One of these is part of every `UKFlow` which holds possible fits.

The `UKFlowPoint`, `UKFlow` and `UKFlowList` classes are implemented in "ukflow.cpp", while the `UKFlowFit` and `UKFlowFitList` classes are implemented in "ukflowfit.cpp".

"lmdatafit.h": This file defines the adapted function calls to the **lmdatafit** function from the **Cephes** library. The function call was modified to accept one more array, which contains the data and is subsequently passed to the function evaluation. The implementation of the functions can be found in "lmdatafit.c".

"polyfit.h": 2D and 3D polynomials of up to fifth order are defined in this file. Basing all polynomial evaluations on one function ensures a consistent interpretation of the parameters. A function that returns the array needed by **lmdatafit** is provided together with a function executing the fit after initialising all parameters. For 3D polynomials, the derivatives with respect to every coordinate are provided as a function.

"ukVTKQTWidget.h": The appearance of all the 3D view windows is defined by the `VTKQTWidget` class that is derived from `QDialog`. It provides the menu, push buttons and scroll bar that can be activated by the derived classes. These have to define the visualisation pipeline and also redefine the `SliceChanged(int)` slot, `animate()` and `saveanimate()` functions. The slice selection scroll bar displays the cardiac time when Cine data is used.

The implementation of these classes can be found in "ukVTKQTWidget.cpp".

"uksliceviewwin.h": The slice view dialog is defined in this file using two classes. `UKSliceViewInputFrame`, derived from `QFrame`, provides the user interaction whereas `UKSliceViewWindow`, derived from `QDialog`, uses `UKSliceViewInputFrame` and handles the various possible input data sets. These classes are implemented in "uksliceviewwin.cpp".

"uklineprofilewin.h": The line profile window dialog is, again, defined by a frame in order to handle user interaction (`UKLineProfileInputFrame`, derived from `QFrame`)and a class using the frame and displaying the data (`UKLineProfileWin`, derived from `QDialog`). The graph itself is drawn by an instance of `QwtPlot`. The data points

are generated by the classes derived from `UKDiComSlice`. This dialog is implemented in "uklineprofilewin.cpp".

"ukcompwin.h": The comparison of two pixmaps using a split window is defined by the class `UKCompWin`, a derivative of `QDialog`. It stores the two pixmaps and displays the part of each that is defined by the position of the horizontal or vertical slider bar. A push button is integrated to switch between the two modes. The implementation of this class can be found in "ukcompwin.cpp".

"ukdicomloaddlg.h": The dialog for loading "DICOM" files is defined in the class `UKDiComLoadDialog` that is derived from `QDialog`. This class provides the usual user interaction elements for a file load dialog and an instance of `UKDiComIconTable` that manages the display of the icons representing the files. The implementation can be found in "ukdicomloaddlg.cpp".

"ukdicomicon.h": A parent class for the icons representing the files and the header information (`UKDiComIcon`, derived from `QWidget`), handles the display of text, the pixmap and stores the filename. This class is specialised into `UKDiComSliceIcon`, a class displaying thumbnails of the images and `UKDiComFIDIcon`, `UKDiComCINEFIDIcon`, `UKDiCom3DFIDIcon` and `UKDiComHeaderIcon` that use predefined icons to represent data sets that cannot be transformed to thumbnails very quickly. These objects are arranged on a regular grid that is managed by `UKDiComIconTable`, a class that inherits from `QTableView`. These classes are implemented in "ukdicomicon.cpp".

"ukdicominfo.h": The window that displays the header information for "DICOM" files is defined in `UKDiComInfoWin`, derived from `QDialog`. It handles the user interaction and uses `UKDiComInfoField`, derived from `QWidget`, to display the data. It takes two kinds of strings, one representing a module name printed in bold and one representing the elements. These are arranged in a list that can be scrolled under the control of `UKDiComInfoWin`. The implementation of these classes can be found in "ukdicominfo.cpp".

"ukflowinfo.h": The setup of the flow information window is similar to the container class `UKFlowInfoWin` and the information field `UKFlowInfoField`. Due to the more complex information extracted out of 3D velocity data sets, this class was replaced with external **Perl** scripts. The implementation can be found in "ukflowinfo.cpp".

"uksupportwin.h": A couple of global variables can be changed using the two classes defined in this file. `UKFlowDetectionOptionsWin`, derived from `QDialog`, allows the setting of the threshold values, the minimum and maximum size of the flow object and the bounding box to be considered for the flow detection algorithms. It uses a number of `QLabel`, `QScrollBar` and `QLCDNumber` combinations that are quite useful.

The minimum and maximum value for the thresholding filter can be changed using the similar class `UKThresholdOptionsWin`. Both classes are implemented in "uksupportwin.cpp".

B.3. Adding Private Tag Information to PAPYRUS 3.5

Extending the software library **PAPYRUS 3.5** to handle private "DICOM" tags involves two major steps:

1. At least one **PAPYRUS** group and one module have to be created to hold the additional tags.
2. The new tags have to be added to the new groups and modules as **PAPYRUS** elements.

Adding new private tags for a specific machine involves step 2 only.

All changes to the original **PAPYRUS** 3.5 source are documented and are commented with my name. The simple UNIX command `grep Uwe *.h *.c` should indicate all the changes and the details of the implementation may be found in the source code files.

B.3.1. The Characteristics of the Data Structures Involved

The "DICOM" standard allows for the definition of proprietary or private tags by the manufacturer. These tags are collected in private groups. To simplify the detection of private information and avoid conflicting definitions, the group numbers of private tags have to be odd. In addition, a unique manufacturer identifier has to be included at the start of every private group.
The beginning of a private group in a GE "DICOM" file might look like this when being investigated using **dcdump**:

```
(0x0019,000000) UL Group Length          VR=<UL>   VL=<0x0004>  [0x000004b4]
(0x0019,0x0010) LO PrivateCreator        VR=<LO>   VL=<0x000c>  <GEMS_ACQU_01>
(0x0019,0x100f) DS Horizontal Frame Of Reference   VR=<DS>   VL=<0x000a> ...
(0x0019,0x1011) SS Series Contrast       VR=<SS>   VL=<0x0002>  [000000]
(0x0019,0x1012) SS Last Pseq     VR=<SS>   VL=<0x0002>  [0x0004]
(0x0019,0x1017) SS Series Plane          VR=<SS>   VL=<0x0002>  [0x0002]
(0x0019,0x1018) LO First Scan RAS        VR=<LO>   VL=<0x0002>  <I >
(0x0019,0x1019) DS First Scan Location   VR=<DS>   VL=<0x000a>  <-32.900002>
(0x0019,0x101a) LO Last Scan RAS         VR=<LO>   VL=<0x0002>  <S >
(0x0019,0x101b) DS Last Scan Location    VR=<DS>   VL=<0x000a>  <85.599998 >
```

Where Elscint provided a unique identifier (`ELSCINT1`), GE provides one per group. This introduces additional problems when reading the private groups with **PAPYRUS**.

PAPYRUS groups and modules are dynamic arrays of type ELEMENT. These elements are referred to via enumerator identifiers and the length id given by an additional (the last) element of the enumeration. Descriptive strings are stored for every element and can be used as labels when printing out the information.

B.3.2. Adding a New Group and Module

The following describes all the steps taken to add the tags <0x0019, 0x10cc> and <0x0043, 0x1030>. To make the description of the two steps for creating groups and modules and subsequently adding the tags clearer, the groups will remain empty at this point. The following steps are implemented:

- `PapyEnumGroups3.h`: Add `Group19GE` and `Group43GE` to the enumeration.

- `PapyEnumModules3.h`: Add `GEPrivateInformation` to the enumeration.
- `PapyEnumMiscGroups3.h`: Add an enumeration for `Group19GE` and `Group43GE`. The enumeration should start with element 2 (nill and one are used for the group length and the private group identifier) and end in `papEndGroup**GE`.
- `PapyEnumMiscModules3.h`: Add an enumeration for `GEPrivateInformation` ending with `papEndGEPrivateInformation`.
- `PapyInitModules3.h`: Add function declarations `init_group**GE()` and `init_GE-PrivateInformation()`.
- `Papyrus3.h`: Reserve space for the module name string and the module's element labels.
- `PapyInit3.c`:
  - `InitGroupNbandSize3()`: Add the commands for the new groups.
  - `InitModuleSize3()`: Add the module length for the new module.
  - `InitGroup3(...)`: Add the correct calls for the new groups.
  - `InitModule3(...)`: Add the correct call for the new module.
  - `InitModulesLabels3()`: Add the module label.
- `PapyInitGroups3.c`: Add init functions for the new groups with an element for the group length and an element for the group identifier (e.g. `GEMS_ACQU_01` for group 19).
- `PapyInitModules3.c`: Add init function for the new module (no elements are included at present).
- `PapyFiles3.c`: Add the identifiers for private groups (e.g. `GEMS_ACQU_01` for group 19 in `papy3FileOpen(...)`).

At this point it is advisable to rebuild (using `make`) and test the library (e.g. with `PapyScreenDump`). It will not do anything new, but debugging the library is a very complex undertaking, which is best avoided.

B.3.3. Adding a New Tag

Once the groups and modules have been defined, adding new tags is relatively straight forward. The procedure is shown for tag <0x0019, 0x10cc>. Information about the tag numbers and data type needs to be confirmed by the manufacturer. The special case of several units of data of the same type is documented in the source code.

- `PapyEnumMiscGroups3.h`: Add an identifier for this tag to the enumeration of the group, ensuring the first element has number 2 (e.g. `papMaximumVelocity19GE = 2`).
- `PapyEnumMiscModules3.h`: Add an identifier for this tag to the enumeration of the module (e.g. `papMaximumVelocityGEPI`).
- `PapyInit3.c`: In function `InitModulesLabels3()` add a desciptive string for the new tag: `label_GE_Private_Information[papMaximumVelocityGEPI] = ''Maximum Velocity'';`.
- `PapyInitGroups3.c`: Add the element in the init function of the group. Possible values for `vr` are listed in `Papyrus3.h`.
- `PapyInitModules3.c`: Add the element in the init function of the module. Possible values for the parameter `vr` (the value representation) are listed in `Papyrus3.h`.

The choice of data type is critical for the working of the library. A wrongly chosen data type will lead to the element or module not being filled. This problem is very difficult to debug.

C. List of Publications

C.1. Papers

Robertson MB, **Köhler U**, Marshall I. Reduction of Electromagnetic Interference from a Commercially Available MR-compatible Flow Simulator, Journal of Medical Engineering and Technology; 24(1); (2000); 28 - 31

Robertson MB, **Köhler U**, Hoskins PR, Marshall I. Quantitative Analysis of PC MRI Velocity Maps: Pulsatile Flow in Cylindrical Vessels, submitted to Journal of Magnetic Resonance Imaging

Köhler U, Robertson MB, Marshall I. An Edge - Detection based Approach to Flow Identification in Magnetic Resonance Angiography, submitted to Magnetic Resonance in Medicine

C.2. Conference Proceedings

Köhler U. Fully Automated MRA Flow Detection, in Proc. ISMRM; 2006 (1999)

Robertson MB, **Köhler U**, Marshall I. Reduction of Electromagnetic Interference from a Commercially Available MR-compatible Flow Simulator, in Proc. ISMRM Workshop on Flow and Motion in Cardiovascular MRI; 119 (1999)

Köhler U. Fully Automated PC - MRA Flow Detection using Phase and Magnitude Information: ¡I¿In Vitro¡/I¿, in Proc. ESMRMB; 416 (1999)

Köhler U. Magnitude and Phase based ¡I¿In Vivo¡/I¿ PC - MRA Flow Detection, in Proc. ESMRMB; 417 (1999)

Robertson MB, **Köhler U**, Marshall I. Analytical Model of Pulsatile Flow using Fourier Analysis, in Proc. ESMRMB; 419 (1999)

Robertson MB, **Köhler U**, Marshall I. Reduction of Interference from a MR-compatible Flow Simulator, in Proc. ESMRMB; 418 (1999)

Robertson MB, **Köhler U**, Hoskins PR, Marshall I. Quantitative Analysis of PC MRA Velocity Maps of Sinusoidal Flow, in Proc. ESMRMB; 420 (1999)

Robertson MB, **Köhler U**, Hoskins PR, Marshall I. Quantitative Analysis of PC MRI Velocity Maps for Pulsatile Flow in Cylindrical Vessels, in Proc. ISMRM; 1669 (2000)

Köhler U, Robertson MB. Segmented Fifth-Order Fit of 3D PC-MRI Flow Data, in Proc. ESMRMB; 540 (2000)

Köhler U, Robertson MB, Marshall I, Hoskins PR. Calculation of the Wall Shear Stress Vector from 3D PC-MRI Flow Data, in Proc. ESMRMB; 542 (2000)

Abbreviations

2D — 2 dimensional
3D — 3 dimensional

ADC — analogue to digital converter

CC — common carotid artery
CFD — computational fluid dynamics
CV — control variable (GE)

DANTE — delays alternating with nutations for tailored excitation
DSP — digital signal processor

EC — external carotid artery
EMI — electromagnetic interference
EOS — equation of state
EPI — echo planar imaging
EPS — encapsulated PostScript

FID — free induction decay
FISP — fast imaging with steady-state precession
FFT — fast Fourier transform
FOV — field of view
FWHM — full width at half maximum

GUI — graphical user interface

IC — internal carotid artery
ISO — international standards organisation

LoG — Laplacian of Gaussian
LDA — laser Doppler anemometry
LDL — low density lipoprotein
LOD — local orientation detector

MRI — magnetic resonance imaging
MRA — magnetic resonance angiography

NMR — nuclear magnetic resonance
NSE — Navier-Stokes equation

OSI — oscillatory shear index

PC — phase contrast
PILS — partially parallel imaging with localised sensitivities
PNG — portable network graphics

RF — radio frequency

SENSE — sensitivity encoding

SMASH — simultaneous acquisition of spatial harmonics

SNR — signal to noise ratio

T_1 — longitudinal relaxation time

T_2 — transverse relaxation time

$T_2^\star$ — total transverse relaxation time

T_E — echo time

T_R — repetition time

TOF — time of flight

v_{enc} — encoding velocity

VA — vertebral artery

WSR — wall shear rate

WSS — wall shear stress

Acknowledgement

I am extremely grateful to my parents and my brother for their support during the last years that enabled me to undertake a PhD abroad. I am sorry for not making it home for Christmas three years in a row and for not being around when they needed me.

I would like to thank the German Government (German Academic Exchange Council) and the European Commission for the provision of the funding the enabled me to undertake a PhD abroad.

I would like to thank my supervisors Dr. Ian Marshall and Dr. Peter R. Hoskins (Dept. of Medical Physics) for providing support during the course of this work and the initial concept of trying to measure wall shear stress from 3D MRI acquisitions. I would also like to thank Dr. Malcolm B. Robertson (Dept. of Medical Physics) for his close collaboration and constructive criticism. Without him this work could not have been completed. My thanks to Dr. Mark Bastin (Dept. of Medical Physics) for constructive criticism and Dr. Joanna Wardlaw (Dept. of Clinical Neurosciences), to whom I am extremely grateful for her help with the clinical background.

I would also like to thank the other members of the research group who have provided much needed advice at times of distress, particularly Jim Wild and Paul Armitage, and Jim Cannon and Evelyn Cowie for organising scan time. I am also grateful to

the secretarial stuff, Irene Craig (Dept. of Medical Physics) and Ann Deary (Dept. of Clinical Neurosciences) for much appreciated assistance.

I would also like to acknowledge the help and support of the following people and groups:

Prof. Norman McDicken: For providing advice and support.
Martin Connell: For comprehensive UNIX support and help with **VTK**.
David Perry: For providing PC support.
Jerry Williams: For providing advice throughout the course of this work as part of the departments 'Mentor' system.
Quan Long and Yun Xu: For their help with fluid dynamics and their CFD calculations.
Rob Blundel: For his help with fluid dynamics.
George Campbell: For his help with the construction of the phantoms.
Medical Illustration: For providing high quality slides.
Robert Hebel: For suggesting PDF as a document format.
Vanessa Robertson: For being a Superhero and help defeat Magneto.

I would like to express my gratitude to the SHEFC Brain Imaging Research Centre for Scotland for providing access to the MRI scanner and associated facilities and the EPSRC for the funding of equipment and scanner time.

Finally I would like to thank the many friends who have contributed to making my time in Edinburgh so enjoyable and supported me during the sometimes difficult time I had: Aillen, Alex, Andy, Andy, Becky, Clemens, Chen, Chrissie, Dave, Dave, Doug, Elke, Els, Fin, Florian, Franz, George, HeiJo, Hugh, Ian, Karen, Kirsty, Klaus, Ksenjia, Martin, Michaela, Michaela, Mike, Nick, Nicole, Nicole, Paul, Rachel, Ray, Robert, Ross, Stefan, Stefan, Steve, Theda, Tony, Udo, Ulrich, Wendy and all the staff in DCN X-ray.

Declaration

I hereby declare that this thesis has been written, and the work performed, by myself. Where the work is published that has been performed by other people, either associated with the research group or elsewhere, an appropriate acknowledgement is made in the text.

Uwe Köhler

Bibliography

[AJG+94] A. S. Anayiotos, S. A. Jones, D. P. Giddens, S. Glagov, and C. K. Zarins. Shear Stress at a Compliant Model of the Human Carotid Bifurcation. *J. Biochem. Eng.*, **116** (1994) 98 – 106.

[Ale95] R. W. Alexander. Hypertension and Pathegenesis of Atherosclerosis. *Hypertension*, **25**(2) (1995) 155 – 161.

[AM89] L. Axel and D. Morton. Correction of phase wrapping in magnetic resonance imaging. *Med. Phys.*, **16**(2) (1989) 284 – 287.

[ASJK84] H. V. As, T. J. Schaafsma, P. A. D. Jager, and J. M. Kleijn. Flow Imaging by Nuclear Magnetic-Resonance. *Ann. Radiol.*, **27**(5) (1984) 405.

[Bat68] J. H. Battocletti. Magnetic Resonance Flowmeter for LNG an LPG. *Pipe Line Industry*, **29** (1968) 61 – 64A.

[BFWE92] D. J. Burkart, J. P. Felmlee, R. L. Wolf, and R. L. Ehman. Adaptive Histogram Method of Vessel Edge Detection to Improve Reliability of Cine Phase Contrast Flow Analysis. *Radiology*, **185** (1992) 203.

[BHHR95] P. J. Brands, A. P. G. Hoeks, L. Hofstra, and R. S. Reneman. A Noninvasive Method to Estimate Wall Shear Rate Using Ultrasound. *Ultrasound Med. and Biol.*, **21**(2) (1995) 171 – 185.

[BHL95] M. M. Black, D. R. Hose, and P. V. Lawford. The Origin and Significance of Secondary Flows in the Aortic Arch. *J. Med Eng. Technol.*, **19**(6) (1995) 192 – 197.

[BK59] R. L. Bowman and V. Kudravcev. Blood flowmeter utilizing nuclear magnetic resonance. *IRE Trans. Med. Electron?*, **6** (1959) 267 – 269.

[BPFL84] D. J. Bryant, J. A. Payne, D. N. Firmin, and D. B. Longmore. Measurement of Flow with NMR Imaging using a Gradient Pulse and Phase Difference Technique. *J. Comp. Assist. Tomogr.*, **8**(4) (1984) 588.

[BRS+00] R. Botnar, G. Rappitsch, M. B. Scheidegger, D. Liepsch, K. Perktold, and P. Boesiger. Hemodynamics in the Carotid Artery Bifurcation: A Comparision between numerical simulations and in vitro MRI measurements. *J. Biomech.*, **33** (2000) 137 – 144.

[BS79] I. N. Bronstein and K. A. Semendjajew. *Taschenbuch der Mathematik.* Verlag Harri Deutsch, Thun und Frankfurt/Main, 1979.

[BS95] M. A. Brown and R. C. Semelka. *MRI - Basic Principles and Applications.* John Wiley & Sons, Inc., New York, NY, 1995.

[Buo98] M. H. Buonocore. Visualizing Blood Flow Patterns Using Streamlines, Arrows, and Particle Path. *Magn. Reson. Med.*, **40** (1998) 210 – 226.

[BZKG97] M. A. Bernstein, X. Zhou, K. F. King, and A. Ganin. Shading Artifacts in Phase Contrast Angiography Induced by Maxwell Terms: Analysis and Correction. In *Proc. ISMRM*, p. 110, 1997.

[BZP+98] M. A. Bernstein, X. J. Zhou, J. A. Polzin, et al. Concomitant Gradient Terms in Phase Contrast MR: Analysis and Correction. *Magn. Reson. Med.*, **39** (1998) 300 – 308.

[Cal91] P. T. Callaghan. *Principles of Nuclear Magnetic Resonance Microscopy.* Oxford Science Publications, Oxford, 1991.

[CFGS71] C. G. Caro, J. M. Fitz-Gerald, and R. C. Schroter. Atheroma and Arterial Wall Shear - Observation, Correlation and Proposal of a Shear Dependent Mass Transfermechanism for Atherogenesis. *Proc. Roy. Soc. Lond. B.*, **177** (1971) 109 – 159.

[Clu98a] D. Clunie. DICOM Tools. David Clunie, GE Medical Systems - Integrated Imaging Solutions - Global Connectivity Center, 800 Business Center Drive, Mt. Prospect, Il 60056, USA, 1998. email: david.clunie@med.ge.com, homepage: http://idt.net/~clunie, mirror: http://www.ba-karlsruhe.de/faqlib/medical-image/toc.html.

[Clu98b] D. Clunie. Medical Image Format FAQ. David Clunie, GE Medical Systems - Integrated Imaging Solutions - Global Connectivity Center, 800 Business Center Drive, Mt. Prospect, Il 60056, USA, 1998. email: david.clunie@med.ge.com, homepage: http://idt.net/~clunie, mirror: http://www.ba-karlsruhe.de/faqlib/medical-image/toc.html.

[CP54] H. Y. Carr and E. M. Purcell. Effects of Diffusion on Free Precession in Nuclear Magnetic Resonance Experiments. *Phys. Rev.*, **94** (1954) 630 – 638.

[CPSS78] C. G. Caro, T. J. Pedley, R. C. Schroter, and W. A. Seed. *The Mechanics of the Circulation.* Oxford Medical Publications, Oxford, 1978.

[Dal99] M. K. Dalheimer. *Programming with Qt.* O'Reilly, Köln, 1999.

[DDGQ98] J. G. Diodati, N. Dakak, D. M. Gillian, and A. A. Quyyumi. Effect of Atherosclerosis on Endothelium-Dependent Inhibition of Platelet Activation in Humans. *Circulation*, **98** (1998) 17 – 24.

[DH86] C. L. Dumoulin and H. R. Hart. Magnetic-Resonance Angiography. *Radiology*, **161** (1986) 717.

[Dij84] P. V. Dijk. Direct cardiac NMR imaging of the heart wall and blood flow in arteries. *J. Comp. Assist. Tomogr.*, **8**(3) (1984) 429 – 436.

[DSHA91] C. L. Dumoulin, S. P. Souza, C. J. Hardy, and S. A. Ash. Quantative Measurement of Blood Flow Using Cylindrically Localized Fourier Velocity Encoding. *Magn. Reson. Med.*, **21** (1991) 242 – 250.

[EMKS89] R. R. Edelman, H. P. Mattle, J. Kleefield, and M. S. Silver. Quantification of Blood Flow with Dynamic MR Imaging and Presaturation Bolus Tracking. *Radiology*, **171**(2) (1989) 551 – 556.

[Eng85] F. Engelke. *Aufbau der Moleküle.* Teubner Studienbücher, Stuttgart, 1985.

[ERT+93] A. J. Evans, D. B. Richardson, R. Tien, et al. Poststenotic Signal Loss in MR Angiography: Effects of Echo Time, Flow Compensation, and Fractional Echo. *Am. J. Neuro. Rad.*, **14** (1993) 721 – 729.

[FCS+85] D. A. Feinberg, L. E. Crooks, P. Sheldon, J. Hoenninger III, J. Watts, and M. Arakawa. Magnetic Resonance Imaging the Velocity Vector Components of Fluid Flow. *Magn. Reson. Med.*, **2** (1985) 555 – 566.

[FGR+93] R. Frayne, L. M. Gowman, D. W. Rickey, et al. A Geometrically Accurate Vascular Phantom for Comparative Studies of X-Ray, Ultrasound, and Magnetic Resonance Vascular Imaging: Construction and Geometrical Verification. *Med. Phys.*, **20**(2) (1993) 415 – 425.

[FNK+87] D. N. Firmin, G. L. Nayler, R. H. Kilpstein, S. R. Underwood, R. S. O. Rees, and D. B. Longmore. *In Vivo* Validation of MR Velocity Imaging. *J. Comp. Assist. Tomogr.*, **11**(5) (1987) 751 – 756.

[FNKL90] D. N. Firmin, G. L. Nayler, P. J. Kilner, and D. B. Longmore. The Application of Phase Shifts in NMR for Flow Measurement. *Magn. Reson. Med.*, **14** (1990) 230 – 241.

[FR93] R. Frayne and B. K. Rutt. Frequency Responce of Retrospectively Gated Phase-Contrast MR Imaging: Effect of Interpolation. *JMRI*, **3** (1993) 907 – 917.

[Gar74] A. N. Garroway. Velocity measurements in flowing fluids by NMR. *J. Phys. D*, **7** (1974) 159 – 163.

[GIC+97] A. Gnasso, C. Irace, C. Carallo, et al. In Vivo Association Between Low Wall Shear Stress and Plaque in Subjects With Asymmetrical Carotid Atherosclerosis. *Stroke*, **28**(5) (1997) 993 – 998.

[GJN+00] M. A. Griswold, P. M. Jakob, M. Nittka, J. W. Goldforb, and A. Haase. Partially Parallel Imaging with Localised Sensitivities (PILS). In *Proc. Intl. Soc. Mag. Resn. Med. 8*, p. 156, 2000.

[GK87] D. P. Giddens and D. N. Ku. A Note on the Relationship Between Input Flow Waveform and Wall Shear Rate in Pulsatile, Separating Flows. *J. Biomech. Eng.*, **109** (1987) 175 – 176.

[GS71] T. Grover and J. R. Singer. NMR Spin - Echo Flow Measurements. *J. Appl. Physiol.*, **42** (1971) 938 – 940.

[GSW88] G. T. Gullberg, M. A. Simons, and F. W. Wehrli. A Mathematical Model for Signal from Spins Flowing During the Application of Spin Echo Pulse Sequences. *Magn. Reson. Imaging*, **6** (1988) 437 – 461.

[GZG93] D. P. Giddens, C. K. Zarins, and S. Glagov. The role of fluid mechanics in the localisation and detection of artherosclerosis. *J. Biomech. Eng.*, **115**(4 PtB) (1993) 588–594.

[GZGK88] S. Glagov, C. K. Zarins, D. P. Giddens, and D. N. Ku. Haemodynamics and atherosclerosis - insights and perspectives gained from studies of human arteries. *Arch. Pathol. Lab. Med*, **112**(10) (1988) 1018–1031.

[GZW88] R. M. Goldstein, H. A. Zebker, and C. L. Werner. Satellite radar interferometry: Two-dimensional phase unwrapping. *Rad. Sci.*, **23**(4) (1988) 713 – 720.

[Hah50] E. L. Hahn. Spin Echoes. *Phys. Rev.*, **80** (1950) 580.

[Hah60] E. L. Hahn. Detection of sea-water motion by nuclear precesion. *Geophys. Res.?*, **65** (1960) 776 – 777.

[Ham94] C. A. Hamilton. Correction of Partial Volume Inaccuracies in Quantitative Phase Contrast MR Angiography. *Magn. Reson. Med.*, **12**(7) (1994) 1127–1130.

[Har85] R. K. Harris. *Nuclear Magnetic Resonance Spectroscopy.* Longman Scientific & Technical, New York, 1985.

[HBV98] R. M. Hoogeveen, C. J. G. Bakker, and M. A. Viergever. Limit to the Accuracy of Vessel Diameter Measurement in MR Angiography. *J. Magn. Reson. Imaging*, **8** (1998) 1228–1235.

[Hee93] R. H. Heethaar. *The Physics of Heart and Circulation*, chapter Atherosclerosis and Blood Flow, pp. 321 – 334. IOP Publishing, Bristol, 1993.

[HFMM98] P. R. Hoskins, P. J. Fish, W. N. McDicken, and C. Moran. Developments in Cardiovascular Ultrasound. Part 2: Arterial applications. *Med. Biol. Eng. Comput.*, **36** (1998) 1 – 11.

[HFS+94] P. R. Hoskins, A. Fleming, P. Stonebridge, P. L. Alan, and D. Cameron. Scan-plane Vector Maps and Secondary flow motions in arteries. *Eur. J. Ultrasound*, **1** (1994) 159 – 169.

[HH93] P. E. Hughes and T. V. How. Quantitative Measurement of Wall Shear Rate by Pulsed Doppler Ultrasound. *J. Med Eng. Technol.*, **17**(2) (1993) 58 – 64.

[HMBF88] J. Henning, M. Mueri, P. Brunner, and H. Friedburg. Fast and Exact Flow Measurement with the Fast Fourier Flow Technique. *Radiology*, **166** (1988) 237.

[Hos96a] P. R. Hoskins. Accuracy of Maximum Velocity Estimates made using Doppler ultrasound systems. *Brit. J. Radiol.*, **69**(818) (1996) 172 – 177.

[Hos96b] P. R. Hoskins. The Sonogram in Doppler Ultrasound. *Ultrasound Int.*, **2**(3) (1996) 134 – 144.

[Hos97] P. R. Hoskins. Peak Velocity Estimation in Arterial Stenosis Models Using Colour Vector Doppler. *Ultrasound in Med. & Biol.*, **23**(6) (1997) 889 – 897.

[HR92] M. Hedley and D. Rosenfeld. A New Two-Dimensional Phase Unwrapping Algorithm for MRI Images. *Magn. Reson. Med.*, **24** (1992) 177 – 181.

[HRC+98] Y.-L. Hu, W. J. Rogers, D. A. Coast, C. M. Kramer, and N. Reichek. Vessel Boundary Extraction based on a Global and Local Deformable Physical Model with Variable Stiffness. *Magn. Reson. Imaging*, **16**(8) (1998) 943–951.

[HVvR+95] M. B. M. Hofman, F. C. Visser, A. C. van Rossum, G. Q. M. Vink, M. Sprenger, and N. Westerhof. *In Vivo* Validation of Magnetic Resonance Blood Volume Flow Measurements with Limited Spatial Resolution in Small Vessels. *Magn. Reson. Med.*, **33**(6) (1995) 778 – 784.

[IK98] S. G. Imbesi and C. W. Kerber. Why Do Ulcerated Atherosclerotic Carotid Artery Plaques Embolize? A Flow Dynamics Study. *Am. J. Neuroradiol.*, **19** (1998) 761 766.

[IN95] P. Irarrazabal and D. G. Nishimura. Fast Three Dimensional Magnetic Resonance Imaging. *Magn. Reson. Med.*, **33**(5) (1995) 656 – 662.

[JKS95] R. Jain, R. Kasturi, and B. G. Schunck. *Machine Vision.* Computer Science Series. McGraw-Hill, Singapore, international editions edition, 1995. ISBN 0-07-113407-7.

[JvTBS96] L.-D. Jou, R. van Tyen, S. A. Berger, and D. Saloner. Calculation of the Magnettization Distribution for Fluid Flow in Curved Vessels. *Magn. Reson. Med.*, **35** (1996) 577 – 584.

[KFU+87] R. H. Klipstein, D. N. Firmin, S. R. Underwood, R. S. O. Rees, and D. B. Longmore. Color Display of Quantitative Blood-Flow and Cardiac Anatomy in a Single Magnetic-Resonance Cine Loop. *British Heart Journal?*, **58**(4) (1987) 316 – 323.

[KG87] D. N. Ku and D. P. Giddens. Laser Doppler anemometer measurements of pulsatile flow in a model carotid bifurcation. *J. Biomech. Eng.*, **115** (1987) 407 – 421.

[KGZB97] K. King, A. Ganin, X. Zhou, and M. Bernstein. Effect of Maxwell Fields in Spiral Scans. In *Proc. ISMRM*, p. 1917, 1997.

[KGZG85] D. N. Ku, D. P. Giddens, C. K. Zarins, and S. Glagov. Pulsatile flow and atherosclerosis in the human carotid bifurcation - positive correlation between plaque location and low and oscillating shear stress. *Atherosclerosis*, **5**(3) (1985) 293–302.

[KHS95] M. Kouwenhoven, M. B. M. Hofman, and M. Sprenger. Motion Induced Phase Shifts in MR: Acceleration Effects in Quantitative Flow Measurement - A Reconsideration. *Magn. Reson. Med.*, **33**(6) (1995) 766 – 777.

[KKKW00] D. W. Kaandorp, K. Kopinga, M. Kouwenhoven, and P. F. F. Wijn. Dealing with the Subvoxel Vessel Position Relative to the Reconstruction Voxel Grid in 2D MR Quantitative Flow Measurement. *Magn. Reson. Imaging*, **18** (2000) 49–58.

[KNN+95] R. S. Keynton, R. E. Nemer, Q. Y. Neifert, R. S. Fatemi, and S. E. Rittgers. Design, Fabrication, and *In Vitro* Evaluation of an *In vivo* Ultrasonic Doppler Wall Shear Rate Measuring Device. *IEEE Trans. Biomed. Eng.*, **42**(5) (1995) 433 – 441.

[Köh99a] U. Köhler. Fully Automated MRA Flow Detection. In *Proc. ISMRM*, p. 2006, 1999.

[Köh99b] U. Köhler. Fully Automated PC - MRA Flow Detection using Phase and Magnitude Information: *In Vitro*. In *Proc. ESMRMB*, p. 416, 1999.

[Köh99c] U. Köhler. Magnitude and Phase based *In Vivo* PC - MRA Flow Detection. In *Proc. ESMRMB*, p. 417, 1999.

[Kol96] H. Kolem. Studienbrief 0018 - Kernspintomographie und Kernspinspektroskopie. Universität Kaiserslautern, ZFUW, Erwin-Schrödinger-Straße, 67663 Kaiserslautern, Germany, 1996.

[Kon96] E. Konecny. Studienbrief 0005 - Medizintechnik. Universität Kaiserslautern, ZFUW, Erwin-Schrödinger-Straße, 67663 Kaiserslautern, Germany, 1996.

[KR00] U. Köhler and M. B. Robertson. Segmented Fifth-Order Fit of 3D PC-MRI Flow Data. In *Proc. ESMRMB*, p. 540, 2000.

[KRM] U. Köhler, M. B. Robertson, and I. Marshall. An Edge - Detection based Approach to Flow Identification in Magnetic Resonance Angiography. sunmitted to Magn. Reson. Med.

[KRMH00] U. Köhler, M. B. Robertson, I. Marshall, and P. R. Hoskins. Calculation of the Wall Shear Stress Vector from 3D PC-MRI Flow Data. In *Proc. ESMRMB*, p. 542, 2000.

[KWO+97] R. Krams, J. J. Wentzel, J. A. F. Oomen, et al. Evaluation of Endothelial Shear Stress and 3D Geometry as Factors Determining the Development of Atherosclerosis and Remodeling in Human Coronary Arteries in Vivo. *Arteriosclerosis, Thrombosis, and Vascular Biology*, **17**(10) (1997) 2061 – 2065.

[KYM+93] P. J. Kilner, G. Z. Yang, R. H. Mohiaddin, D. N. Firmin, and D. B. Longmore. Helical and Retrograde Secondary Flow Patterns in the Aortic Arch Studied by Three-Directional Magentic Resonance Velocity Mapping. *Circulation*, **88** (1993) 2235 – 2247.

[Lia96] Z.-P. Liang. A Model-Based Method for Phase Unwrapping. *IEEE Trans. Med. Imaging*, **15**(6) (1996) 893 – 897.

[LKT95] M. Lei, C. Kleinstreuer, and G. A. Truskey. Numerical Investigation and Prediction of Atherogenic Sites in Branching Arteries. *J. Biomech. Eng.*, **117** (1995) 350–357.

[LL98] S. B. Lippman and J. Lajoie. *C++ Primer.* Addison Wesley, Reading, Massachusetts, third edition edition, 1998.

[LM84] D. Liepsch and S. Moravec. Pulsatile Flow of Non-Newtonian Fluid in Distensible Models of Human Arteries. *Biorheology*, **21** (1984) 571 – 586.

[LMB92] D. Liepsch, S. Moravec, and R. Baumgart. Some Flow Visualization and Laser-Doppler Measurement in a True-to-Scale Elastic Model of a Human Aortic Arch — a New Model Technique. *Biorheology*, **29** (1992) 563 – 580.

[LPOP95] J. Laustsen, W. P. Paaske, S. Oyre, and E. M. Pedersen. Dynamic Quantification, Visualisation and Animation of Blood Velocities and Flows in Infrarenal Aortic Aneurysms *in vivo* by Three-Dimensional MR Phase Velocity Encoding. *Eur. J. Vasc. and Endovasc. Surg*, **9** (1995) 383 – 388.

[Man78] P. Manfield. Multi-Planar Image Formation Using NMR Spin Echoes. *J. Phys. C*, **10** (1978) L55.

[Mar96] E. A. Martin, editor. *Oxford Concise Colour Medical Dictionary.* Oxford University Press, Oxford, UK, 1996.

[Mat82] R. T. Mathie, editor. *Blood Flow Measurement in Man.* Castle House Publications Ltd., Tunbridge Wells, Kent, 1982.

[MB92] J. P. Mugler III and J. R. Brookeman. The design of Pulse Sequences Employing Spatial Presaturation for the Suppression of Flow Artifacts. *Magn. Reson. Med.*, **23**(2) (1992) 201 – 214.

[Mey96] S. Meyers. *More Effective C++.* Addison Wesley, Reading, Massachusetts, 1996.

[Mey98] S. Meyers. *Effective C++*. Addison Wesley, Reading, Massachusetts, second edition edition, 1998.

[MF78] G. A. Morris and R. Freeman. A DANTE Tagging Sequence for the Evaluation of Transitional Sample Motion. *Magn. Reson. Med.*, **29** (1978) 433.

[MFU+99] A. M. Masaryk, R. Frayne, O. Unal, E. Krupinski, and C. M. Strother. In Vitro and In Vivo Comparision of Three MR Measurement Methods for Calculating Vascular Shear Stress in the Internal Carotid Artery. *Am. J. Neuroradiol.*, **20** (1999) 237 – 245.

[MHJ97] S. E. Meier, O. Heid, and F. A. Jolesz. Flow Calibration of an Open MR System. In *Proc. ISMRM*, p. 1872, 1997.

[MK84] T. Mayer-Kuckuk. *Kernphysik*. Teubner Studienbücher, Stuttgart, 1984.

[MK91] C. P. Markou and D. N. Ku. Accuracy of Velocity and Shear Rate Measurements using Pulsed Doppler Ultrasound: A Comparision of Signal Analysis Techniques. *Ultrasound Med. and Biol.*, **17**(8) (1991) 803 – 814.

[Mor82] P. R. Moran. A Flow Velocity Zeugmatographic Interlace for NMR Imaging in Humans. *Magn. Reson. Imaging*, **1** (1982) 197 – 203.

[MWS98] B. Massey and J. Ward-Smith. *Mechanics of Fluids*. Stanley Thornes (Publishers) Ltd, Cheltenham, 1998.

[MXG+94] J. E. Moore Jr., C. Xu, S. Glagov, C. K. Zarins, and D. N. Ku. Fluid wall shear stress measurement in a model of the human abdominal aorta: oscillatory behavior and relationship to atherosclerosis. *Atherosclerosis*, **110** (1994) 225–240.

[MYB+92] R. H. Mohiaddin, G. Z. Yang, P. Burger, D. N. Firmin, and D. B. Longmore. Automatic Enhancement; Animation, and Segmentation of Flow in Peripheral Arteries from MR Phase-Shift Velocity Mapping. *J. Comput. Assist. Tomogr.*, **16**(2) (1992) 176 – 181.

[MYK94] R. H. Mohiaddin, G. Z. Yang, and P. J. Kilner. Visualization of Flow by Vector Analysis of Multidirectional Cine MR Velocity Mapping. *J. Comp. Assist. Tomogr.*, **18**(3) (1994) 383 – 392.

[Nem98] Digital Imaging and Communications in Medicine (DICOM), Part 3: Information Object Definitions (Draft Standard). National Electrical Manufacturers Association, 1300 N. 17th Street, Rosslyn, Virginia 22209 USA, 1998. ftp://ftp.nema.org/medical/dicom/1998/98_03dr.pdf.

[NFL86] G. L. Nayler, D. N. Firmin, and D. B. Longmore. Blood Flow Imaging by Cine Magnetic Resonance. *J. Comp. Assist. Tomogr.*, **10**(5) (1986) 715 – 722.

[NGD+97] B. Newling, S. J. Gibbs, J. A. Derbyshire, et al. Comparision of Magnetic Resonance Imaging Velocimetry With Coumputational Fluid Dynamics. *J. Fluids Eng.*, **119** (1997) 103 – 109.

[NIM95] D. G. Nishimura, P. Irarrazabal, and C. H. Meyer. A Velocity k-Space Analysis of Flow Effects in Echo-Planar and Spiral Imaging. *Magn. Reson. Med.*, **33** (1995) 549 – 556.

[NO90] W. W. Nichols and M. F. O'Rourke. *McDonald's Blood Flow in Arteries.* Edward Arnold, London, 3 edition, 1990.

[O'D85] M. O'Donnell. NMR Blood Flow Imaging using Multiecho, Phase Contrast Sequences. *Med. Phys.*, **12**(1) (1985) 59 – 64.

[OO94] M. Oberdorfer and R. Oberdorfer. *Graphikprogrammierung unter XWindows.* Franzis, Poing, Germany, 1994.

[OP00] S. Oyre and E. M. Pedersen. Determination of Wall Shear Stress and Subpixel Lumen Area in the Right Coronary Arteries using MRI. In *Proc. ISMRM*, p. 1655, 2000.

[OPR+97] S. Oyre, E. M. Pedersen, S. Ringgaard, P. Boesinger, and W. P. Paaske. *In vivo* Wall Shear Stress Measurement by Magnetic Resonance Velocity Mapping in the Normal Human Abdominal Aorta. *Eur. J. Vasc. and Endovasc. Surg*, **13** (1997) 263 – 271.

[ORK+98] S. Oyre, S. Ringgaard, S. Kozerke, et al. Quantitation of Circumferential Subpixel Vessel Wall Position and Wall Shear Stress by Multiple Sectored Three-Dimensional Paraboloid Modeling of Velocity Encoded Cine MRI. In *Proceedings of the International Society for Magnetic Resonance in Medicine Sixth Scientific Meeting and Exhibition*, p. 44, Sydney, Australia, 1998.

[ORP+97] S. Oyre, S. Ringgaard, E. M. Pedersen, et al. Accurate *in vivo* quantitative determination of wall shear stress and vessel wall position. In *Proceedings of the International Society for Magnetic Resonance in Medicine Fifth Scientific Meeting and Exhibition*, p. 1879, Vancouver, BC, Canada, 1997.

[PAP97] PAPYRUS 3.0. Digital Imaging Unit, University Hospital of Geneva, 24, rue Micheli-du-Grest, 1211 Genève 14, Switzerland, 1997. http://expasy.hcuge.ch/www/UIN/UIN.html.

[Ped80] T. J. Pedley. *The Fluid Mechanics of Large Blood Vessels.* Cambridge University Press, Cambridge, UK, 1980.

[PLEO96] F. Peeters, R. Luypaert, H. Eisendrath, and M. Osteaux. Interpretation of Flow Encoding and Quantification in MRI: Time Domain Versus Frequency Domain. *Magn. Reson. Med.*, **36**(5) (1996) 758 – 766.

[Poi46] J. L. M. Poiseuille. Recherches experimentales sur le mouvement des liquids dans les tubes de tres petits diametres. *Mem. Savant Etrangers*, **9** (1846) 433 – 544.

[Poz97] C. Pozrikidis. *Introduction to Theoretical and Computational Fluid Dynamics.* Oxford University Press, Oxford, 1997.

[Pra78] W. K. Pratt. *Digital Image Processing.* John Wiley & Sons, New York, 1978.

[Pri94] M. Prince. Gadolinium-Enhanced MR Aortography. *Radiology*, **191**(1) (1994) 155–164.

[PSE+91] N. J. Pelc, F. G. Sommer, D. R. Enzmann, L. R. Pelc, and G. H. Glover. Accuracy and precision of phase contrast flow measurements. *Radiology*, **181(P)** (1991) 189.

[PSL+94] N. J. Pelc, F. G. Sommer, K. C. P. Li, T. J. Brosnan, and D. R. Enzmann. Quantitative Magnetic Resonance Flow Imaging. *Magn. Reson. Qua.*, **10**(3) (1994) 125 – 147.

[PTVF92] W. H. Press, S. A. Teukolsky, W. T. Vetterling, and B. P. Flannery. *Numerical Recipes in C - The Art of Scientific Computing.* Cambridge University Press, Cambridge, 1992.

[PWF+00] E. M. Pedersen, P. Walker, A. Ferrandez, S. Wu, S. Oyre, and T. David. Comparision of Computerized Fluid Dynamics and High Resolution Phase Contrast MRI for Wall Shear Stress Estimations In Vivo. Preliminary Results. In *Proc. ISMRM*, p. 1654, 2000.

[PWSB99] K. Pruessmann, M. Weiger, M. B. Scheidegger, and P. Boesiger. SENSE: Sensitivity Encoding for Fast MRI. *Magn. Reson. Med.*, **42** (1999) 952–962.

[PYK+93] M. Prince, E. Yucel, J. Kaufman, D. Harrison, and S. Geller. Dynamic Gadolinium-Enhanced 3-Dimensional Abdominal MR Arteriography. *J. Magn. Reson. Imaging*, **3** (1993) 877–881.

[Ray94] E. S. Raymond. *The New Hacker's Dictionary.* The MIT Press, Cambridge, Masschusetts, USA, 2nd edition, 1994.

[RKHM99] M. R. Robertson, U. Köhler, P. R. Hoskins, and I. Marshall. Quantitative Analysis of PC MRA Velocity Maps of Sinusoidal Flow. In *Proc. ESMRMB*, p. 420, 1999.

[RKHM00] M. B. Robertson, U. Köhler, P. R. Hoskins, and I. Marshall. Quantitative Analysis of PC MRI Velocity Maps for Pulsatile Flow in Cylindrical Vessels. In *Proc. ISMRM*, p. 1669, 2000.

[RKM99a] M. B. Robertson, U. Köhler, and I. Marshall. Reduction of Electromagnetic Interference from a Commercially Available MR-compatible Flow Simulator. In *Proc. ISMRM Workshop on Flow and Motion in Cardiovascular MRI*, p. 119, 1999.

[RKM99b] M. R. Robertson, U. Köhler, and I. Marshall. Analytical Model of Pulsatile Flow using Fourier Analysis,. In *Proc. ESMRMB*, p. 419, 1999.

[RKM99c] M. R. Robertson, U. Köhler, and I. Marshall. Reduction of Interference from a MR-compatible Flow Simulator. In *Proc. ESMRMB*, p. 418, 1999.

[RKM00] M. R. Robertson, U. Köhler, and I. Marshall. Reduction of Electromagnetic Interference from a Commercially Available MR-compatible Flow Simulator. *J. Med. Eng. and Techol.*, **24**(1) (2000) 28 – 31.

[RNJH84] T. W. Redpath, D. G. Norris, R. A. Jones, and M. S. Hutchinson. *Phys. Med. Biol.*, **29**(7) (1984) 891 – 895.

[RS86] J. P. Ridgeway and M. A. Smith. A Technique for Velocity Imaging using Magnetic Resonance Imaging. *Brit. J. Radiol.*, **59** (1986) 603 – 607.

[Sch79] H. Schlichting. *Boundary Layer Theory.* McGraw-Hill, New York, USA, 7th edition, 1979.

[SE71] L. A. Solberg and D. A. Eggen. Localisation and sequence of development of atherosclerotic lesions in the carotid and vertebral artries. *Circulation*, **43** (1971) 711–724.

[SKC97] K. E. Sorensen, I. B. Kirstensen, and D. S. Celermajer. Atherosclerosis in the Human Brachial Artery. *J. Am. Coll. Cardiol.*, **29**(2) (1997) 318 – 322.

[Sli78] C. P. Slichter. *Principles of Magnetic Resonance.* Springer - Verlag, Berlin, 1978.

[SM97] D. K. Sodickson and W. J. Manning. Simultaneous Acquisition of Spatial Harmonics (SMASH): Fast Imaging with Radiofrequency Coil Arrays. *Magn. Reson. Med.*, **38** (1997) 591–603.

[SML97] W. Schroeder, K. Martin, and B. Lorensen. *The Visualization Toolkit.* Prentice Hall PTR, Opper Saddle River, NY 07458, 2nd edition, 1997.

[SMS+86] K. Shimizu, T. Matsuda, T. Sakurai, et al. Visulization of Moving Fluid: Quantitative Analysis of Blood Flow Velocity Using MR Imaging. *Radiology*, **159**(1) (1986) 195 – 199.

[SNPG95] S. M.-H. Song, S. Napel, N. J. Pelc, and G. H. Glover. Phase Unwrapping of MR Phase Images Using Poisson Equation. *IEEE Trans. Im. Pro.*, **4**(5) (1995) 667 – 676.

[SOPK95] J. M. Siegel, Jr., J. N. Oshinski, R. I. Pettigrew, and D. N. Ku. Comparision of Phantom and Computer-Simulated MR Images of Flow in a Convergent Geometry: Implications for Improved Two-Dimensional MR Angiography. *J. Magn. Reson. Imaging*, **5** (1995) 677 – 683.

[SOPK96] J. M. Siegel, Jr., J. N. Oshinski, R. I. Pettigrew, and D. N. Ku. The Accuracy of Magnetic Resonance Phase Velocity Measurements in Stenotic Flow. *J. Biomech.*, **29**(12) (1996) 1665 – 1672.

[SOPK97] J. M. Siegel, Jr., J. N. Oshinski, R. I. Pettigrew, and D. N. Ku. Computational Simulation of Turbulent Signal Loss in 2D Time-of-Flight Magnetic Resonance Angiograms. *Magn. Reson. Med.*, **37** (1997) 609 – 614.

[SPL+90] C. E. Spritzer, N. J. Pelc, J. N. Lee, A. J. Evans, H. D. Sostman, and S. J. Riederer. Rapid MR Imaging of Blood Flow with a Phase-Sensitive, Limited-Flip-Angle, Gradient Recalled Pulse Sequence: Preliminary Experience. *Radiology*, **176**(1) (1990) 255 – 262.

[SRFR96] R. F. Smith, B. K. Rutt, A. J. Fox, and R. N. Rankin. Geometric Characterisation of stenosed Human Carotid Arteries. *Acad. Radiol.*, **3** (1996) 898 – 911.

[SST98] F. Schmidt, M. K. Stehling, and R. Turner. *Echo - Planar Imaging (Theory, Technique and Application)*. Springer, Berlin, Germany, 1998.

[ST65] E. O. Stejskal and J. E. Tanner. *J. Chem. Phys.*, **42** (1965) 288.

[Str92] J. P. Strong. Atherosclerotic lesions - natural history, risk factors and topography. *Arch. Pathol. Lab. Med*, **116**(12) (1992) 1268–1275.

[Str97] B. Stroustrup. *The C++ Programming Language*. Addison Wesley, Reading, Massachusetts, third edition edition, 1997.

[SWB+97] S. K. Samijo, J. M. Willigers, P. J. Brands, et al. Reproducibility of Shear Rate and Shear Stress Assessment by Means of Ultrasound in the Common Carotid Artery of Young Human Males and Females. *Ultrasound in Med. & Biol.*, **23**(4) (1997) 583 – 590.

[TBP93] C. Tang, D. D. Blatter, and D. L. Parker. Accuracy of Phase-Contrast Flow Measurements in the Presents of Partial-Volume Effects. *J. Magn. Reson. Imaging*, **3** (1993) 377–385.

[UFK+87] S. R. Underwood, D. N. Firmin, R. H. Klipstein, R. S. O. Rees, and D. B. Longmore. Magnetic-Resonance Velocity Mapping - Clinical-Applications of a New Technique. *British Heart Journal?*, **57**(5) (1987) 404 – 412.

[vdGNvdW+98] R. J. van der Geest, R. A. Niezen, E. E. van der Wall, A. de Ross, and J. H. C. Reiber. Automated Measurement of Volume Flow in the Ascending Aorta Using MR Velocity Maps: Evaluation of Inter- and Intraobserver Variability in Healthy Volunteers. *J. Comp. Assist. Tomogr.*, **6**(22) (1998) 904–911.

[vMF71] R. von Mises and K. O. Friedrichs. *Fluid Dynamics.* Springer-Verlag, New York, 1971.

[WEAF+99] L. Wigström, T. Ebbers, M. K. A. Fyrenius, J. Engvall, B. Wranne, and A. F. Bolger. Particle Trace Visualization of Intracardiac Flow Using Time-Resolved 3D Phase Contrast MRI. *Magn. Reson. Med.*, **41** (1999) 793 – 799.

[WERR93] R. L. Wolf, R. L. Ehman, S. J. Riederer, and P. J. Rossman. Analysis of Systematic and Random Error in MR Volumetric Flow Measurements. *Magn. Reson. Med.*, **30**(1) (1993) 82 – 91.

[WR97] A. H. Wiman and S. Riederer. Performance of an Elliptical Centric View Order for Signal Enhancement and Motion Artifact Suppression in Breath-hold Three-Dimensional Gradient Echo Imaging. *Magn. Reson. Med.*, **38** (1997) 793 – 802.

[WRS+00] S. P. Wu, S. Ringgard, R. Stokholm, S. Oyre, M. S. Hansen, and E. M. Pedersen. 250 μm Resolution MRI Wall Shear Stress Measurement In Vivo shows Difeerence between Femoral, Brachial and Carotid Artery Wall Shear Stresses. In *Proc. ISMRM*, p. 1656, 2000.

[WSW96] L. Wigström, L. Sjöqvist, and B. Wranne. Temporally Resolved 3D Phase-Contrast Imaging. *Magn. Reson. Med.*, **36** (1996) 800 – 803.

[WWT+98] S. J. Weston, N. B. Wood, G. Tabor, A. D. Gosman, and D. N. Firmin. Combined MRI and CFD Analysis of Fully Developed Steady and Pulsatile Laminar Flow through a Bend. *J. Magn. Reson. Imaging*, **8** (1998) 1158 – 1171.

[XC94] X. Y. Xu and M. W. Collins. Studies of Blood Flow in Arterial Bifurcations using Computational Fluid Dynamics. In *Proc. Instn. Mech. Engrs.*, pp. 163 – 174, 1994.

[XLC+99] X. Y. Xu, Q. Long, M. W. Collins, M. Bourne, and T. M. Griffith. Reconstruction of Blood Flow paterns in Human Arteries. *Proc. Instn. Mech. Engrs..*, **213** (1999) 411 – 421.

[YBFU96] G. Z. Yang, P. Burger, D. N. Firmin, and S. R. Underwood. Structure Adaptive Anisotropic Image Filtering. *Image Vis. Comput.*, **14**(2) (1996) 135 – 145.

[YBK+96] G. Z. Yang, P. Burger, P. J. Kilner, S. P. Karwatowski, and D. N. Firmin. Dynamic range extemsion of cine velocity measurements using motion-registered spatiotemporal phase unwrapping. *J. Magn. Reson. Imaging*, **6**(3) (1996) 495 – 502.

[YBP86] I. R. Young, G. M. Bydder, and J. A. Payne. *Magn. Reson. Med.*, **3**(1) (1986) 175 – 179.

[YCGN88] Y. Yoshida, C. G. Caro, S. Glagov, and R. M. Nerem. *The role of flow in atherogenesis*, pp. 153–162. Springer-Verlag, Tokyo, 1988.

[ZXC+99] S. Z. Zhao, X. Y. Xu, M. W. Collins, A. V. Stanton, A. D. Hughes, and S. A. Thom. Flow in carotid bifurcations: effect of the superior thyroid artery. *Med. Eng. Phys.*, **21** (1999) 207 – 214.

[ZYC98a] S. Z. Zhao, X. Y. Yu, and M. W. Collins. The Numerical Analysis of Fliud-Solid Interactions for Blood Flow in Arterial Structures – Part 1: A Review of Models for Arterial Wall Behaviour. *Proc. Instn. Meh. Engrs.*, **212** (1998) 229 – 239.

[ZYC98b] S. Z. Zhao, X. Y. Yu, and M. W. Collins. The Numerical Analysis of Fliud-Solid Interactions for Blood Flow in Arterial Structures – Part 1: Development of Coupled Fluid-Solid Algorithmns. *Proc. Instn. Meh. Engrs.*, **212** (1998) 241 – 251.